IUSS
Scuola Universitaria Superiore Pavia

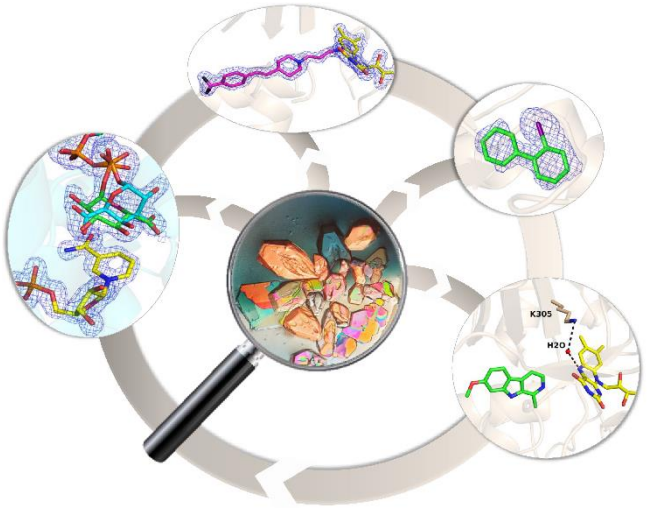

Scuola Universitaria Superiore IUSS Pavia

Biochemical and structural studies on Monoamine Oxidases and UPD-Glucuronic acid 4-epimerase

A Thesis Submitted in Partial Fulfilment of the Requirements
for the Degree of Doctor of Philosophy in

BIOMOLECULAR SCIENCE AND BIOTECHNOLOGY

by

Luca Giacinto Iacovino

January, 2021

Scuola Universitaria Superiore IUSS Pavia

Biochemical and structural studies on Monoamine Oxidases and UPD-Glucuronic acid 4-epimerase

A Thesis Submitted in Partial Fulfilment of the Requirements

for the Degree of Doctor of Philosophy in

BIOMOLECULAR SCIENCE AND BIOTECHNOLOGY

by

Luca Giacinto Iacovino

Supervisors: Prof. Mattevi Andrea, Dep. of Biology and Biotechnology "L. Spallanzani", University of Pavia

Co-Supervisor: Prof. Binda Claudia, Dep. of Biology and Biotechnology "L. Spallanzani", University of Pavia

January, 2021

OUTLINE

My doctoral thesis describes the work carried out in the Structural Biology laboratory at University of Pavia, under the supervision of Prof. Mattevi Andrea and Prof. Binda Claudia. The core of my research activities was the study of two enzymes by a combination of X-ray crystallography and enzymology approaches: the human biomedical target Monoamine Oxidase (MAO; Chapter 1) and the biocatalytically-relevant UDP-Glucuronic acid 4-epimerase (BcUGAepi; Chapter 2). Along the thesis, the Chapters will mainly summarize the results achieved during my PhD and their scientific implications, while a detailed analysis of the experimental work is reported in the articles attached at the end of each Chapter. The work on MAOs was organized in three distinct projects that are described in sections 1.2, 1.3 and 1.4, as detailed below.

Human Monoamine Oxidases A and B (MAO-A and MAO-B) are mitochondrial enzymes involved in the regulation of catecholamines and other biogenic amines. They have been widely studied for their role in neurological diseases but, in the last years, an increasing number of studies highlighted the involvement of MAO-A and hydrogen peroxide (secondary product of oxidases during the catalytic turnover) in heart diseases and cardiac senescence. The aim of the project was the biochemical characterization of engineered "oxygen inert" variants of human MAO-A, which were concomitantly tested in cellular studies by the group of Prof. Angelo Parini at the Institute of Metabolic and Cardiovascular Diseases (Toulouse, France) to probe their effects on ageing mechanisms. The aim of this project was to explore the correlation of altered enzyme levels, imbalanced metabolism, and reactive oxygen species (ROS) generation with mitochondrial damage, cell degeneration, and ageing.

Human MAOs are established neurological targets and many studies are focused on the development of new and selective MAO-A and MAO-B inhibitors. In collaboration with Prof. Stanislav Gobec at the University of Ljubljana (Slovenia) and his team, we studied a new class of MAOs inhibitors with the general scaffold of 1-propargyl-4-styrylpiperidines. Based on cis/trans stereoisomers we aimed at selectively targeting the two isoforms of the MAOs. Interestingly, while the cis isomers have shown MAO-A selectivity, the trans analogues were potent MAO-B inhibitors. The reaction mechanism of these compounds was studied by kinetic analysis, UV-Vis spectrum measurements and X-ray crystallography. This represented a unique case of stereoselective activity of cis/trans isomers able to discriminate between structurally related enzyme isoforms.

Diphenylene iodonium (DPI) is a potent inhibitor of a large number of heme- and flavoenzymes, widely employed in cellular experiments as a probe for ROS-depending processes. In our laboratory, we performed a structural and biochemical analysis of DPI with both MAO-A and MAO-B, as these enzymes play an active role in ROS systems. We proved that DPI is a reversible and competitive inhibitor of both isoforms of MAOs, these

findings should be carefully considered whenever DPI is used as a modulator of ROS signalling and oxidative stress.

The second part of my PhD was focused on the elucidation of the reaction mechanism of UDP-Glucuronic acid 4-epimerase from *Bacillus cereus* (BcUGAepi). Besides their importance in cell biology, the sugar nucleotide syntheses from UDP-Glucuronic acid (UDP-GlcA) are of considerable interest for mechanistic enzyme research. This enzyme belongs to the well-known Short Chain Dehydrogenases/Reductases (SDR) protein superfamily. Despite the protein members of this family share important catalytic features, the reaction mechanism of BcUGAepi has never been explored in detail so far. The aim of this project was based on the identification and analysis of the catalytic residues involved in the substrate and product recognition and a structural comparison with other epimerases and decarboxylases of the same SDR family. In this context, Prof. Bernd Nidetzky of the University of Graz and his team performed mutagenesis, kinetic studies and synthesis of ligands, while in our laboratory we carried out the crystallographic analysis of BcUGAepi.

TABLE OF CONTENTS

LIST OF FIGURES

LIST OF SYMBOLS

k_{cat} = Turnover number

K_m = Michaelis constant

K_i = Inhibition constant

1. Monoamine Oxidases

1.1 Introduction

In 1928 the biochemist Mary Bernheim during her doctorate research at the University of Cambridge conducted the first experiment on tyramine oxidases. These enzymes will be known in the future as monoamine oxidases (MAOs). Her discovery has been referred to as "one of the seminal discoveries in twentieth century neurobiology" (Slotkin 1999). MAOs and their role in the metabolism of neurotransmitters and neuroactive molecules have been extensively studied in the central nervous system (CNS). The distribution of the two isoforms MAO-A/MAO-B is tissue-specific and immunohistochemical studies demonstrated that MAO-A is mostly expressed in noradrenergic and dopaminergic neurons, while MAO B is more abundant in serotoninergic ones and in glia cells (Westlund, Denney et al. 1985, Shih, Chen et al. 1999). During aging, MAO-B levels in the human brain increase ~4−5-fold. Pharmacologically, inhibition of MAOs lead to a global increase of neurotransmitter levels, resulting in improved brain activities.

MAOs represent an important pharmaceutical target widely studied in neurological disorders (Binda, Mattevi et al. 2011, Müller, Riederer et al. 2017). In particular, MAO inhibitors are clinically used for depression and Parkinson's disease. (Youdim, Edmondson et al. 2006). The latter is prevented by the maintenance of adequate levels of dopamine, which allows to delay the L-3,4-dihydroxyphenylalanine (L-DOPA) treatment and its long-term effects. Extending the rationale to Alzheimer's disease (AD), MAOs have been used in association with cholinesterase inhibitors (licensed treatment for AD) due to their neuroprotective effect. In addition, MAOs regulate the levels of neurotransmitters also in peripheric districts. Recent papers highlight a new emerging role of MAOs also in non-neurological diseases. For instance, MAOs are highly expressed in prostate cancer and are supposed to be involved in other tumorigenesis events (Gaur, Gross et al. 2019). All these aspects underline that a new branch of research is looking for potential lead compounds suitable into MAOs non-correlated neurological diseases. In this regard, the isoform-selective modulation of neurotransmitters still represents a medicinal chemistry challenge.

1.1.1 Monoamine Oxidases in Parkinson's disease

Neurodegenerative diseases (ND) are disorders in the central nervous system (CNS) characterized by the progressive loss of brain cells. The inability of neurons to regenerate on their own after severe damage results in abnormal function and, ultimately, cell death. ND such as Alzheimer's (AD), Parkinson's (PD) and Huntington's disease, are associated with misfolding and dysfunctional trafficking of proteins. In addition, mitochondrial dysfunction, oxidative stress, and/or environmental factors have also been implicated in neurodegeneration (Sheikh, Safia et al. 2013). In spite of the considerable efforts to define the molecular mechanisms underlying neurodegeneration, many features of these pathologies remain unclear.

Current therapies for ND are only palliative and fail to modify and/or halt disease progression. Accordingly, the discovery of new and effective drugs with disease-modifying capacity is a pressing and unmet clinical need for ND. Originally described in 1817 by the English physician James Parkinson, PD is the second-most common neurodegenerative disorder (Pfeiffer 2013). PD is clinically characterized by bradykinesia, tremor, rigidity, flexed posture, postural instability and freezing of gait. Additionally, PD is also associated with many non-motor features such as cognitive deficits, ranging from memory impairment to dementia and emotional changes such as depression, anxiety and sleep disturbance. These symptoms contribute to the reduced quality of life and the disability associated with PD (Chaudhuri, Healy et al. 2006, Langston 2006, Chaudhuri and Schapira 2009). Moreover, PD is pathologically characterized by the loss of dopaminergic neurons in the substantia nigra (SN), leading to loss of dopamine in the striatum. Symptoms are only clinically noticeable when approximately 50-60% of the nigral neurons are lost and about 80-85% of the dopamine content of the striatum is depleted (Marsden 1996, Fahn, Oakes et al. 2004).

Epidemiologically, age, gender, occupation, residence and family history are important risk factors for PD (Pfeiffer 2013). Moreover, the disease is uncommon before age 50 and affects 1% of the population above 60 years old (de Lau and Breteler 2006, Tysnes and Storstein 2017). European studies based on populations above 55 or 65 years old showed relatively little incidence variation, with overall rates between 410 and 529 per 100,000 person-years (Wirdefeldt, Adami et al. 2011). A study which reports data from six European prevalence studies estimated the number of individuals above the age of 50 with PD at between 4.1 and 4.6 million in 2005. By 2030 the number was projected to increase up to 8.7 and 9.3 million (Wirdefeldt, Adami et al. 2011). Furthermore, several studies have reported the existence of a lower prevalence of PD in Africa, Asia and South America, when compared to Europe (Wirdefeldt, Adami et al. 2011). Genetic factors are known to

cause PD in small numbers of patients with a familial form of the disorder, however two theories are often considered in order to explain the sporadic form of PD, namely the environmental theory and the genetic theory (Schapira 2007).

Neuropathological hallmarks of PD include the presence of Lewy bodies (FH 1912) (proteinaceous insoluble bodies) containing α-synuclein (α-syn) aggregates (Spillantini, Schmidt et al. 1997). α-Syn is a presynaptic neuronal protein that seems to contribute to PD pathogenesis, particularly in its abnormal soluble oligomeric conformations, termed protofibrils. These toxic aggregates disrupt cellular homeostasis by interference with various intracellular targets, ultimately causing neuronal death. Furthermore, α-syn may exert harmful effects on neighbouring cells, thus contributing to disease propagation (Stefanis 2012).

Another hallmark of the disease consists of the loss of melanin-containing neurons in the midbrain (Oertel 2017). The number of neuromelanin is reduced by about 20% in the elderly when compared with age-matched controls, and in PD there is a greater reduction in the amount of melanin in the cells of the SN (less than 15%). As a result, the neurodegeneration of melanin-containing dopaminergic neurons in the SN leads to a marked dopamine deficit in the striatum (Mann and Yates 1983, Oertel 2017). Moreover, oxidative stress plays a role in the loss of dopaminergic neurons in PD (Linert, Herlinger et al. 1996, Kienzl, Jellinger et al. 1999, Kim, Koh et al. 1999), with hydrogen peroxide (H_2O_2) degrading neuromelanin (Zecca, Tampellini et al. 2001), and reactive oxygen species increasing α-syn aggregation (Levin, Högen et al. 2011). However, and despite the significant progresses, the exact process that triggers the loss of neuromelanin-containing dopaminergic neurons in the SN remains unknown. Nonetheless, it is consensual that mitochondrial dysfunction, α-syn aggregation, dysfunction of protein degradation, endoplasmic reticulum stress, neuroinflammation, excitotoxicity, apoptosis and oxidative stress (Figure 1) are all involved in neurodegenerative processes.(Carlsson 1959, Kienzl, Jellinger et al. 1999, Herrera, Muñoz et al. 2017)

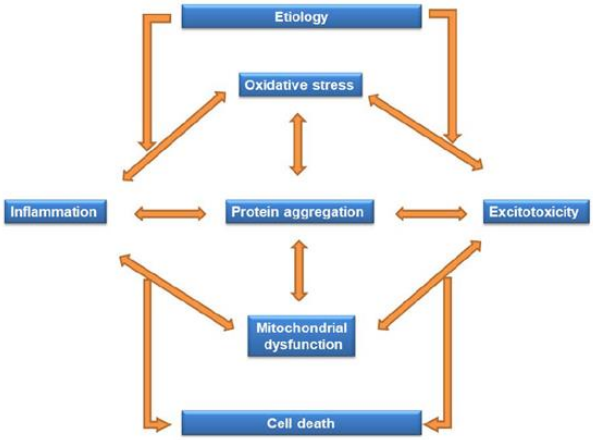

Figure 1. Etiology and pathogenesis in Parkinson's Disease. (Adapted from Harrison's Principles of Internal Medicine)

Dopamine (DA) is a precursor of noradrenalin and adrenaline (Beaulieu and Gainetdinov 2011). The main function of DA is the transmission of signals between brain cells (Emerit, Edeas et al. 2004). Neurons communicate with other cells through a synaptic cleft via transmission of electric signals, in which neurotransmitters such as DA are involved. After neurotransmitter molecules are released from the presynaptic dopaminergic neuron into the synaptic cleft, they consequently diffuse to the postsynaptic neuron, where they can then bind to a special receptor on the membrane of the postsynaptic neuron (Figure 2) (Mason 2011). After its reuptake by presynaptic neurons, DA can be recycled and stored in vesicles, or converted to 3,4-dihydroxyphenylacetaldehyde (DOPAL) by the action of monoamine oxidase-B, followed by the formation of dihydroxyphenylacetic acid (DOPAC), by aldehyde dehydrogenase (ALDH) (Figure 2). On the other hand, within glial cells, DA is converted into homovanillic acid (HVA) by the action of catechol-O-methyltransferase (COMT), MAO-B and ALDH (Figure 2). The reabsorption of DA is achieved through a high-affinity transporter, named dopamine transporter.

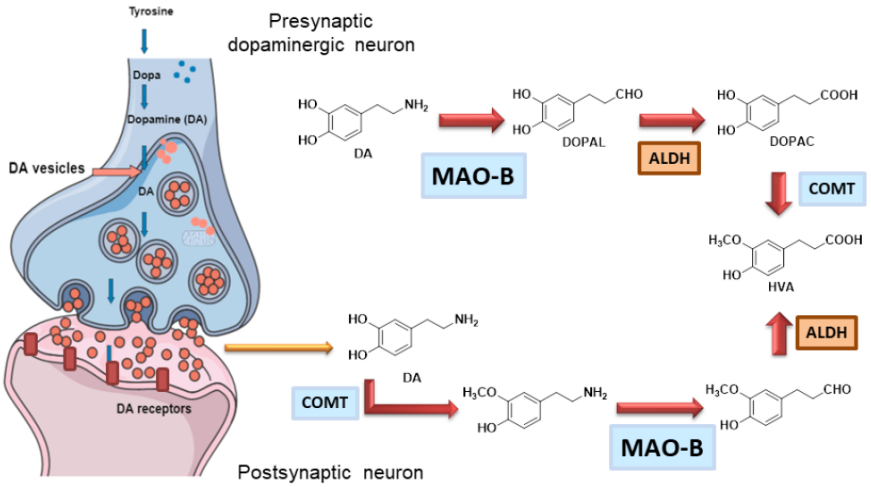

Figure 2. Dopamine metabolism and neurotransmission.

1.1.2 Monoamine Oxidase A in cardiac physiology and oxidative stress

Monoamine oxidases play an active role in the degradation of the neurotransmitters serotonin, dopamine and norepinephrine. In particular, serotonin is mainly oxidized by MAO-A, dopamine by MAO-B whereas catecholamines are metabolized by both isoforms. Besides their functions in the central nervous system, a growing interest aroused on the role of these enzymes in the regulation of neurotransmitters in the peripherical tissues, in particular in the heart. Cardiovascular diseases (CVDs) are the major causes of death in the western world and a lot of efforts are invested to discover new druggable targets for the cardiovascular drug market that raised more than $92.5 billion in 2019. Although both isoforms are present in the heart, it is reported that the expression of MAO-A in cardiomyocytes increases in different pathological situations including cardiac hypertrophy or hypertension (Pino, Failli et al. 1997, Manni, Zazzeri et al. 2013). MAO-A might contribute triggering these cardiac diseases through two principal mechanisms: the first is represented by the regulation of norepinephrine and serotonin concentration, the second is the intracellular production of reactive oxygen species (ROS).

The release of norepinephrine by cardiac sympathetic nerve has a positive chronotropic and inotropic effects, thus the increase in the sympathetic nervous system (SNS) activity has been reported in heart failure (HF) combined with a reduced re-uptake by neuronal

norepinephrine transporter (NET) (Eisenhofer, Friberg et al. 1996). Even serotonin can be produced by coronary endothelial cells and mouse cardiomyocytes (Pönicke, Gergs et al. 2012, Rouzaud-Laborde, Hanoun et al. 2012) regulating different cardiac functions. Remarkably, it is reported that the concomitant increase of serotonin and 5-hydroxyindole acetic acid (5-HIAA) levels was corelated with different pathological events in the heart. The relationship between increase in substrate concentrations and MAO-A activity is particularly evident in the case of cardiac ischemia–reperfusion where both MAO-A substrates norepinephrine (Akiyama and Yamazaki 2001) and serotonin (Du, Zhan et al. 2017) and their respective products 5-HIAA and dihydroxyphenylglycol (DHPG) increased significantly. The overexpression of MAO-A represents a mechanism of compensation due to higher levels of these neurotransmitters. However, this phenomenon might be responsible for the overproduction of hydrogen peroxide (H_2O_2) and subsequent oxidative stress. Substrate concentration and/or MAO-A overexpression could promote an increase of the hydrogen peroxide levels and these situations can coexist in the same pathology.

In physiological situations, H_2O_2 acts as a molecular signalling but the overproduction can trigger a variety of adverse effects. Only recently it has been demonstrated that MAO-A activity and subsequent ROS overproduction is associated with cardiac aging. (Maurel, Hernandez et al. 2003, Villeneuve, Guilbeau-Frugier et al. 2013, Manzella, Santin et al. 2018). The physiologic changes of human cardiac aging mainly include left ventricular hypertrophy, diastolic dysfunction, increased cardiac fibrosis and this condition is strongly associated with mitochondrial disfunction. All these effects were observed with high levels of MAO-A activation and H_2O_2 generation leading to cell death or heart failure. Alternatively, cells exposed to sublethal doses of oxidative stress can undergo another type of response called "senescence"(Childs, Baker et al. 2014). Cell senescence is a process characterized by irreversible cell-cycle arrest, resistance to apoptosis, and release of bioactive factors (cytokines, chemokines and proteases) known as the senescence-associated secretory phenotype (SASP). Thus, depending on the level of ROS production, MAO-A can initiate different types of cellular responses in cardiomyocytes (Manzella, Santin et al. 2018) (Fig. 3). The p53 protein seems to be a major mediator of MAO-A-dependent response in these contexts, being at the hub of many signalling pathways, p53 could either drive senescence or necrosis, based on the intensity of MAO-A activation.

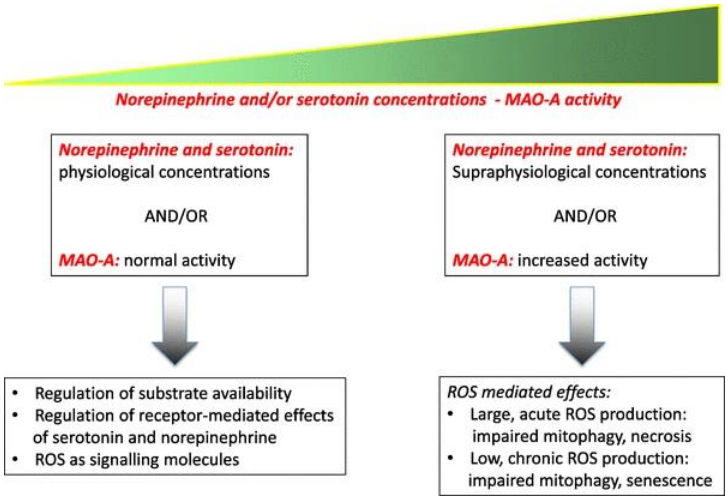

Figure 3. MAO-A activity effects in physiological and pathological situations (Mialet-Perez, Santin et al. 2018)

1.1.3 The crystal structure of Monoamine Oxidases

In general, the FAD_{ox} oxidizes the amine substrate by hydride transfer and the resulting FAD_{red} is then re-oxidized by molecular oxygen which represents the final electron acceptor, converted into hydrogen peroxide. The resulting imine is non-enzymatically hydrolysed into the corresponding aldehyde after its release from the enzyme. Thus, the final products of the reaction are the aromatic aldehyde, NH^{4+} and H_2O_2 (Fig. 4).

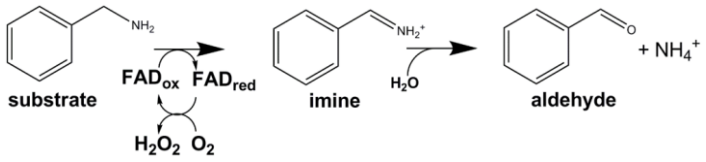

Figure 4. Scheme of the enzymatic reaction catalyzed by MAOs. Benzylamine is showed as substrate model.

Monoamine oxidases are 60-kDa monotopic flavoenzymes anchored to the outer part of the mitochondrial membrane. MAO-A and MAO-B share the 70% of sequence identity, both enzymes catalyze the oxidation of primary, secondary and tertiary amine substrates

through an FAD-dependent mechanism where the final electron acceptor is oxygen which is converted into hydrogen peroxide (Ramsay and Albreht 2018). When the substrate is located in the active site within the "aromatic cage" of the two tyrosine located perpendicularly to the FAD co-factor (Li, Binda et al. 2006), the amine group is perfectly oriented toward the N5 atom of the flavin cofactor. The latter is covalently bound through an 8α-thioether linkage to Cys397 (MAO-B) or Cys406 (MAO-A). Compared to other flavoenzymes, the MAO flavin ring exists in "bent" conformation rather than the more common planar configurations about the N(5)−N(10) axis (Edmondson, Binda et al. 2009). This peculiar conformation has a higher redox potential enabling the oxidation of the low-reactive C-N bond.

In 2002 the first crystal structure of human MAO-B was determined, and much progress has been made to identify the main catalytic features of these enzymes. In the review attached at the end of section 1.1 ("The structure of monoamine oxidases: past, present, and future" published on Journal of Neural Transmission) we describe in detail the structural properties of MAOs. In addition to the active site, a thorough analysis is reported on MAO dimeric organization and on the interaction with the membrane. This aspect is also discussed in relation to the usage of detergents not only for the protein extraction but also for the crystallization conditions. We also analysed how the development of new detergents has had a huge impact in the resolution of membrane protein crystallographic structures.

Journal of Neural Transmission
https://doi.org/10.1007/s00702-018-1915-z

NEUROLOGY AND PRECLINICAL NEUROLOGICAL STUDIES - REVIEW ARTICLE

The structure of monoamine oxidases: past, present, and future

Luca Giacinto Iacovino[1] · Francesca Magnani[1] · Claudia Binda[1]

Received: 19 June 2018 / Accepted: 11 August 2018

Abstract
The first crystal structure of mammalian monoamine oxidases (MAOs) was solved in 2002; almost 65 years after, these FAD-dependent enzymes were discovered and classified as responsible for the oxidation of aromatic neurotransmitters. Both MAO A and MAO B feature a two-domain topology characterized by the Rossmann fold, interacting with dinucleotide cofactors, which is intimately associated to a substrate-binding domain. This globular body is endowed with a C-terminal α-helix that anchors the protein to the outer mitochondrial phospholipid bilayer. As monotopic membrane proteins, the structural elucidation of MAOs was a challenging task that required the screening of different detergent conditions for their purification and crystallization. MAO A and MAO B structures differ both in their oligomerization architecture and in details of their active sites. Purified human MAO B and rat MAO A are dimeric, whereas human MAO A was found to be monomeric, which is believed to result from the detergent treatments used to extract the protein from the membrane. The active site of MAOs consists of a hydrophobic cavity located in front of the flavin cofactor and extending to the protein surface. Some structural features are highly conserved in the two isozymes, such as a Tyr–Tyr aromatic sandwich in front of the flavin ring and a Lys residue hydrogen-bonded to the cofactor N5 atom, whereas a pair of gating residues (Phe208/Ile335 in MAO A; Ile199/Tyr326 in MAO B) specifically determines the different substrate and inhibitor properties of the two enzymes.

Keywords Amine oxidase · Membrane protein · Mitochondrial membrane · Enzyme active site · Inhibitor · Drug design · Flavin

Abbreviations

MAO	Monoamine oxidase
FAD	Flavin adenine dinucleotide
ROS	Reactive oxygen species

Introduction

Eight decades have passed, since monoamine oxidase (MAO) was classified by Zeller as a specific enzyme capable of oxidizing a number of aromatic primary amines such as benzylamine, tyramine, and adrenaline (Zeller 1938). Twenty years later, MAO was serendipitously found to be an antidepressant drug target as molecules of the hydrazine class of inhibitors showed mood elevating effects in tuberculosis patients (Bailey et al. 1959). The subsequent development of propargylamine inhibitors allowed two isoforms of mammalian MAO to be distinguished: clorgyline and deprenyl selectively bind to MAO A and MAO B, respectively (Fowler et al. 1981). Both enzymes (about 70% sequence identity) catalyze the oxidative deamination of substrates through an FAD-dependent mechanism that releases hydrogen peroxide and ammonia together with the aldehyde product (Ramsay and Albreht 2018). MAO A and MAO B are expressed, at different levels, in many organs (Shih and Chen 2004; Tipton 2018), and their roles in the metabolism of neurotransmitters and neuroactive molecules have been extensively studied in the central nervous system. Although the usage of MAO inhibitors for the treatment of depression has been limited and overwhelmed by other drugs with a different mechanism of action, during the 1980s drugs that specifically targeted MAO B were found to ameliorate the symptoms of Parkinson's disease. Deprenyl was the first MAO inhibitor to be used in combination with L-dopa to treat this disease (Lees et al. 1977), and since then, a large bunch of research was dedicated to find new compounds with improved efficacy for neurodegenerative disorders (Riederer and Muller 2017; Binda et al. 2011). It is important to remark that the action of

✉ Claudia Binda
claudia.binda@unipv.it

[1] Department of Biology and Biotechnology, University of Pavia, 27100 Pavia, Italy

Published online: 24 August 2018

propargylamines in Parkinson's disease and other neurodegenerative pathologies represents a multi-target mechanism, because these compounds were found to promote neuronal survival independently of MAO inhibition (Tatton et al. 2003; Youdim et al. 2014). As regards MAOs, the neuroprotective action exerted by inhibitors is not only related to modulation of the levels of specific neurotransmitters, but also to reduction of hydrogen peroxide levels produced by the enzyme reaction. This is particularly relevant in age-related diseases, because MAO A and MAO B expression significantly increases with ageing, which contributes to elevate reactive oxygen species (ROS) derived from the hydrogen peroxide side-product (Edmondson and Binda 2018). This aspect has been thoroughly investigated in the central nervous system, whereas more recently several studies have proved a role of MAOs (more specifically MAO A) in cardiovascular diseases (Mialet-Perez et al. 2018).

Although the clinical relevance of MAOs has been recognized since the 1960s, it was only at the beginning of this century that the first crystal structures of these enzymes were determined (Binda et al. 2002; Ma et al. 2004). This delay was mainly due to the difficulties in handling both mammalian MAO A and MAO B, since they are membrane proteins; more precisely, they are bound to the outer mitochondrial membrane through a C-terminal helix (Fig. 1). MAOs belong to the class of flavoenzymes featuring the so-called Rossmann-fold domain involved in stable binding of the FAD cofactor. Within this class, MAOs share 20–30% sequence identity with other flavin-dependent amine oxidases, such as polyamine oxidase, the fungal MAO N, and lysine-specific demethylases LSD1/LSD2 (Forneris et al. 2009). The active sites of all these enzymes feature a lysine residue on the top of the flavin which is supposed to favor oxygen binding and an aromatic pair (partly conserved in LSD1/LSD2) in front of the cofactor creating the niche for substrate oxidation. The peculiarity of MAO A and MAO B resides in the membrane subcellular localization as, during evolution, the conserved amine oxidase domain acquired a C-terminal extension that interacts with the phospholipid bilayer. As discussed in more detail later in this article, membrane proteins are intrinsically difficult to handle experimentally and, particularly, to crystallize. Moreover, as they are associated with mitochondria, over-expression of MAOs in their recombinant forms required a eukaryotic heterologous system such as *Saccharomyces cerevisiae* or *Pichia pastoris* (Newton-Vinson et al. 2000), the latter also proving successful for other membrane proteins (Byrne 2015). This review will provide a historical perspective of the structural characterization of MAOs, focusing on their properties both as membrane proteins and as validated drug targets.

Overall structure of mammalian MAOs

Protein structure determination not only contributes greatly to our understanding of the mechanisms underlying the biological process in which a specific protein is involved, but also provides a molecular scaffold for drug design strategies. There have been many biochemical and pharmacological studies concerning the MAOs (see, e.g., Cesura and Pletscher 1992; Shih 1991; Weyler et al. 1990). The relatively large sizes of these enzymes (MAO A and MAO B are 527 and 520 residues long, respectively, with a molecular mass of about 60 kDa) ruled out the use of NMR methods in structural studies, leaving X-ray crystallography as the only technically feasible approach.

The first MAO crystal structure, human MAO B in complex with the irreversible inhibitor pargyline, was determined by our group in 2002, at 3.0 Å resolution (Binda et al. 2002) (Fig. 1a). This was followed by the elucidation of the other homologous isozyme (both rat and human MAO A; Fig. 1b–d), as described below. This was achieved when Edmondson and coworkers managed to develop an efficient expression system of human and rat recombinant MAOs using *Pichia pastoris* as heterologous host (Li et al. 2002; Newton-Vinson et al. 2000). Proteins were extracted from the mitochondrial membrane and purified as detergent-solubilized preparations that were enzymatically active and homogeneous, which is an essential prerequisite for crystallographic studies. In particular, human MAO B showed a monodisperse elution profile in gel filtration chromatography and resulted in the first positive hits in crystallization experiments. Notably, these crystals were highly reproducible and after optimization their quality was greatly improved reaching a maximum X-ray diffraction resolution of 1.6 Å (Reis et al. 2018). The crystal structure revealed that human MAO B is dimeric with about 15% of the monomer surface involved in oligomerization (Fig. 2a), similar to what was later found for rat MAO A (Fig. 2b). The interaction within the dimer is stabilized by a network of hydrogen bonds extending from the top to the bottom of the main globular body of the protein (Fig. 2a; Table 1). Each monomer is composed of the FAD-binding domain in the apical portion of the dimer, the substrate-binding domain harboring the active site cavity, and a C-terminal segment that folds into an α-helix emerging from the bottom of the soluble body (Figs. 1a, 3a). This helix is highly hydrophobic and its orientation with respect to the overall structure is consistent with its role of membrane anchor. In particular, although the two C-terminal helices are not involved in dimerization, they are parallel to each other and to the dimer twofold axis (Fig. 1a). This suggested a putative model for insertion into the membrane, which is also supported by the position

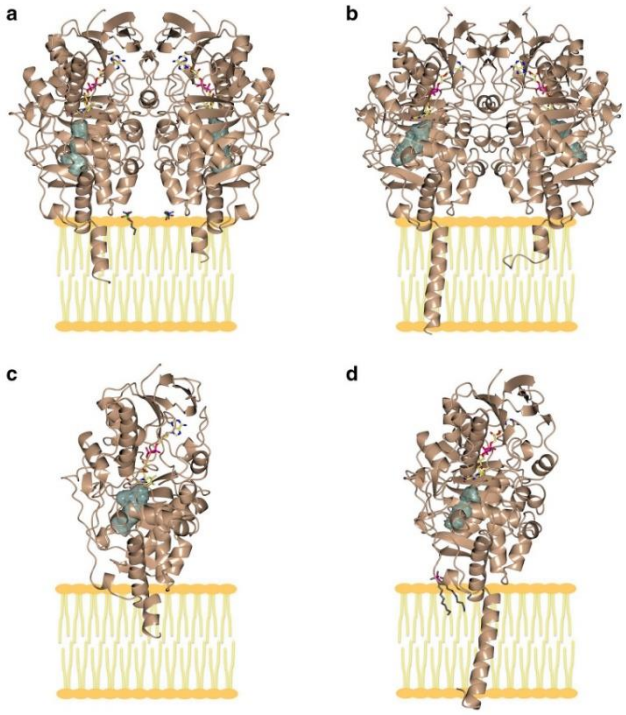

Fig. 1 Overall crystal structure of mammalian MAOs represented as brown ribbon diagram. The FAD cofactor is drawn as stick model with carbon, nitrogen, oxygen, phosphor, and sulphur atoms in yellow, blue, red, magenta, and green color code, respectively. Detergent molecules (the visible part of their aliphatic chains is drawn) are depicted with dark gray carbon atoms. The active site cavity is represented as light blue surface. The putative mode of insertion into the membrane (phospholipid bilayer model in yellow) is showed. All structural figures in this review were produced using the CCP4mg software (McNicholas et al. 2011) and the UCSF Chimera package (Pettersen et al. 2004). **a** Human MAO B crystal structure at 1.6 Å resolution (PDB code 6fw0; (Reis et al. 2018). MAO B structure was first determined in complex with pargyline at lower resolution (Binda et al. 2002). Two ordered molecules of the detergent used in the crystallization conditions (zwittergent 3–12) were found associated with the crystal structure. **b** Rat MAO A in complex with clorgyline at 3.2 Å resolution (PDB code 1o5w; (Ma et al. 2004). **c** Human MAO A in complex with clorgyline at 3.15 Å resolution (PDB code 2bxs; (De Colibus et al. 2005). **d** Human MAO A in complex with harmine at 2.2 Å resolution (PDB code 2z5x; (Son et al. 2008). Two ordered molecules of the detergent used in the crystallization conditions (decyl-dimethyl-phosphine oxide) were found associated with the crystal structure. This human MAO A structure, though being overall similar to that of Fig. 1c, belongs to a distinct crystalline form and is bound to a different and non-covalent inhibitor. Moreover, the higher resolution allowed to better visualize structural features such as the C-terminal membrane-binding α-helix

adopted by a few detergent molecules that bind with the zwitterionic head at the base of the soluble body of the protein and the hydrophobic chain elongating parallel to the C-terminal membrane helix (Figs. 1a, 3a). In all MAO B crystal structures, the C-terminal helices are not fully visible (up to residue 501 and residue 496 in the two monomers), which raised the question whether they may not traverse the phospholipid bilayer entirely as occurs for other monotopic membrane proteins (see section "MAOs are membrane proteins").

Despite the high sequence identity with the B isozyme, crystallization of human MAO A turned out to be much

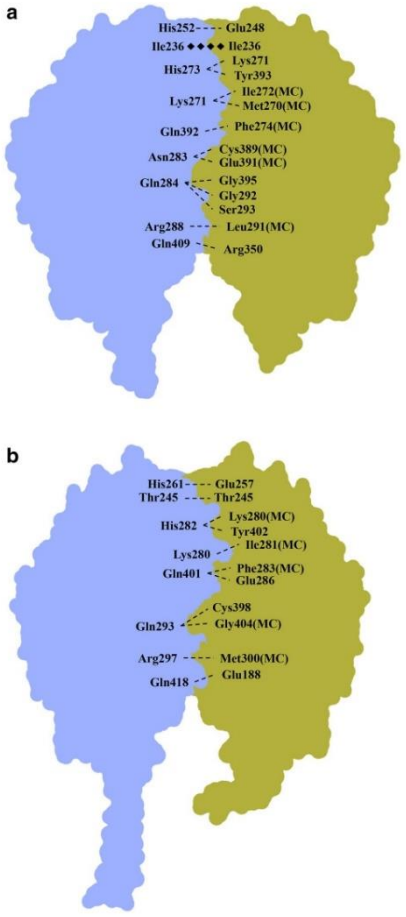

Fig. 2 Scheme of the monomer–monomer interactions listed in Table 1 mapped on the dimeric structure profile of **a** human MAO B and **b** rat MAO A. The orientation of the macromolecules is the same as in Fig. 1a, b, respectively. The two monomers in each dimer are colored in a different way (light blue and greenish) to highlight the dimer interface. As specified in the note underneath Table 1, all interactions are reciprocal, i.e., each pairwise interaction is observed in either monomer-to-monomer direction. MC indicates that main chain (rather than side chain) atoms of the indicated residue are involved in the interaction. Dashed and bold dotted lines indicate hydrogen bonds and hydrophobic interactions, respectively

Table 1 Interactions that stabilize the dimeric structures of rat MAO A and human MAO B

Rat MAO A		Human MAO B	
His261	**Glu257**	His252	**Glu248**
Thr245	**Thr245**	Ile236	**Ile236**
His282	**Lys280(MC)**	His273	**Lys271(MC)**
	Tyr402		**Tyr393**
Lys280	**Ile281(MC)**	Lys271	**Ile272(MC)**
	[Ala279]		**Met270(MC)**
Gln401	**Phe283(MC)**	Gln392	**Phe274(MC)**
	Glu286		**[Pro277]**
[Asn292]	**[Cys398]**	Asn283	**Cys389(MC)**
	[Glu400]		**Glu391(MC)**
Gln293	**Cys398**	Gln284	**[Cys389]**
	Gly404(MC)		**Gly395**
	[Gly301]		**Gly292**
	[Ala302]		**Ser293**
Arg297	**Met300(MC)**	Arg288	**Leu291(MC)**
Gln418	**Glu188**	Gln409	**[Glu179]**
	[Asp359]		**Arg350**

For each dimer structure (either rat MAO A or human MAO B), the left column displays residues of one monomer interacting with residues of the other monomer reported in bold in the right column. All interactions are reciprocal, i.e., each pairwise interaction is observed in both chain A-to-B and chain B-to-A directions. MC stands for main chain, indicating that either the amide nitrogen or the carbonyl oxygen is involved in the specified interaction. Square brackets are used to indicate that the interaction is not existing (though the residue number is reported to be compared with that in the homologous enzyme: in some cases, residue is conserved, whereas the interaction is not)

more difficult. This behavior was ascribed to the higher heterogeneity of the protein samples that was observed in different detergent conditions. In 2004, Tsukihara and coworkers published the crystal structure of rat MAO A (expressed in *Saccharomyces cerevisiae*) in complex with clorgyline at 3.2 Å resolution (Ma et al. 2004) (Figs. 1b, 2b). This work revealed that rat MAO A has a dimeric structure that is similar to that of human MAO B. The crystals contained four molecules in the asymmetric unit, which are organized in two independent dimers with the C-terminal helices pointing in opposite directions (i.e., this arrangement is likely to be due to crystal packing rather than being functionally relevant). The domain organization of each monomer is also conserved, with the main differences being found in the enzyme active site cavity, as discussed in "The active site of MAOs". Results from our more detailed comparative analysis of the human MAO B and rat MAO A dimers are summarized in Fig. 2 and Table 1). The overall architecture of the two dimers is highly similar with a protein surface area involved in monomer–monomer interface that is only slightly lower in rat MAO A (about 11%) than that

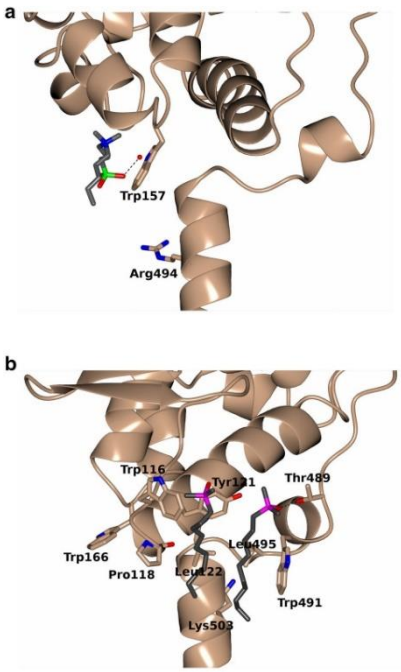

Fig. 3 Zoomed view of the **a** human MAO B and **b** human MAO A membrane-binding domain (these structures were chosen, because ordered detergent molecules were visible in the electron density). The structures correspond to those showed in Fig. 1a, d: for the sake of clarity, only one subunit of human MAO B is showed approximately in the same orientation as the right monomer in Fig. 1a, whereas human MAO A structure has been rotated of about 90° around the vertical axis with respect to that in Fig. 1d. The orientation was chosen to highlight the pocket that interacts with detergent molecules. Color code is as in Fig. 1 (water molecules drawn as red spheres) and hydrogen bonds are represented as dashed lines

found for human MAO B (15%). Both dimers are stabilized by a network of hydrogen bonds except for a hydrophobic interaction in human MAO B (Ile236-Ile236, corresponding to Thr245-Thr245 H-bond in rat MAO A; Table 1). Some interactions are fully conserved, in particular those involving His261, His282, and Arg297 in rat MAO A corresponding to His252, His273, and Arg288 in human MAO B, respectively. Other interactions are established by the same residue but involve different amino acids on the other monomer. This may occur, because either the residue adopts a different conformation (like Gln418 and Gln293 in rat MAO A corresponding to Gln409 and Gln284 in human MAO B, respectively) or is not conserved at all (for example Glu286, whose side chain in rat MAO A is H-bonded with Gln401, is replaced by Pro277 in the B isozyme). Notably, the interaction of Asn283 with Cys389 and Glu391 in human MAO B, located approximately in the middle part of the dimer interface, is completely missing in rat MAO A (Fig. 2a, b; Table 1). In both enzymes, the adenosine moiety of the FAD cofactor, though being well embedded by the protein matrix, is located in proximity of His282 (rat MAO A) and His273 (human MAO B) that are engaged in a conserved interaction (Table 1). However, it is unlikely that dimerization may be essential to stabilize FAD binding, because, in both isozymes, the cofactor is covalently linked to a cysteine residue. Moreover, the active site in each monomer is independent from that in the other subunit (Fig. 1a, b) and, as better described below, human MAO A in its recombinant purified form is enzymatically active, though displaying a monomeric structure.

In 2005, our group managed to obtain diffracting crystals of human MAO A in complex with clorgyline at 3.15 Å resolution (Fig. 1c; De Colibus et al. 2005). The overall domain architecture is highly similar to the previously published structures and the active site cavity resembles that of rat MAO A (sequence identity between rat and human MAO A is 88%), but having a smaller volume and a different shape from that found in human MAO B. A striking peculiarity was that human MAO A crystal structure, contrarily to the rat enzyme, is clearly monomeric. However, a few years later, Tsukihara and coworkers published the crystal structure of human MAO A in complex with the reversible inhibitor harmine at 2.2 Å resolution (Fig. 1d; Son et al. 2008). Though belonging to a different crystal form with respect to that obtained by our group in 2005, this new structure of human MAO A is also monomeric. Since these groups worked independently and also used different protein constructs as well as purification and crystallization conditions, it was unclear whether this monomeric structure of human MAO A is functionally significant or due to a purification artifact. Edmondson and coworkers demonstrated by pulsed EPR techniques that both MAO A and MAO B are dimers when bound to the mitochondrial membrane (Upadhyay and Edmondson 2009), which probably undergo disruption after extraction and detergent solubilization. Superposition of the monomeric structure onto each subunit of either human MAO B or rat MAO A dimers resulted in a dimeric model of human MAO A that most likely corresponds to that bound to the membrane (Edmondson and Binda 2018). In support to this hypothesis, it is important to note that all residues involved in the monomer–monomer interactions in rat MAO A (Table 1) are strictly conserved.

In both rat and human MAO A structures, it was possible to model the C-terminal α-helices in its full-length form (Fig. 1b, d): this domain extends straight from the base of the protein main body for a length of about 37 Å, indicating that MAOs are monotopic membrane-spanning proteins. In the case of human MAO B, human MAO A in complex with harmine showed a few ordered detergent molecules to be bound at the base of the globular body of the protein and with the aliphatic chain running parallel to the membrane α-helix (Figs. 1d, 3b). Their position with respect to the protein and the interactions established with it differ with respect to MAO B (Fig. 3a, b), but, in both cases, this finding supports the hypothesized membrane-binding mode depicted in Fig. 1. Interestingly, in both MAO A and MAO B, there is a basic residue at the beginning of the membrane α-helix (Lys503 in MAO A and Arg494 in MAO B; Fig. 3a, b) and two conserved Trp residues at the interface between the globular body and the C-terminus (Trp116/Trp166 corresponding to Trp107/Trp157 in MAO B). The next section will deal in more detail with the interaction of MAOs with the membrane and on methodological aspects related to it.

MAOs are membrane proteins

Membrane proteins are classified depending on the extent of their interaction with the phospholipid bilayer. This section is focused on the aspects of MAO structures related to their subcellular localization on the outer mitochondrial membrane (Fig. 4). We will apply the simpler classification, into two groups, which has been used in the database of Membrane Proteins of Known 3D Structures (http://blanco.biomol.uci.edu/mpstruc/): monotopic (interacting at least with one lipid leaflet and the bulk of the protein is not located within the lipid bilayer) and transmembrane (with one or more transmembrane segments). Although the overall number of membrane protein structures has been growing in a nearly exponential fashion, monotopic structure determination has followed an almost linear growth over the years (Fig. 5). In particular, the first crystal structure of MAOs in 2002 was determined when the total number of monotopic membrane structures was less than 20 (compared to the 65 structures currently solved). Since 2007, a range of novel methodologies have contributed to the structure determination of increasingly challenging membrane proteins: protein engineering by mutagenesis or insertion of a crystallizable chaperone (Cherezov et al. 2007; Magnani et al. 2016), lipid cubic phases (Caffrey 2015), nanobodies, and monoclonal antibodies fragments (Manglik et al. 2017; Hunte and Michel 2002). More recently, improvements in cryo-electron microscopy (Kuhlbrandt 2014), which requires no crystals and only small amounts of purified protein, introduced an additional and significant contribution to this field.

Membrane proteins require detergents for their extraction and solubilization from the lipid membrane. Detergents mask hydrophobic regions of the protein, thus preventing aggregation in solution. Protein stability upon extraction from the membrane and consequent degree of delipidation depends strictly on the detergent used. The choice of

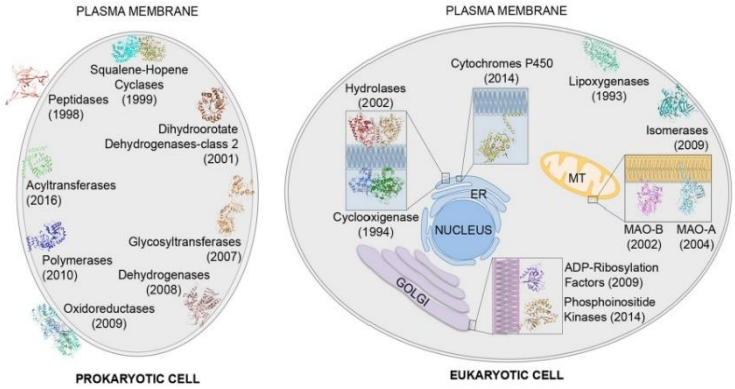

Fig. 4 Distribution of monotopic membrane protein structures. First solved structure of each family of monotopic membrane protein (source: Membrane Proteins of Known 3D Structures, http://blanco.biomol.uci.edu/mpstruc/) is depicted within its native membrane compartment, either in the prokaryotic (left) or in the eukaryotic (right) cell

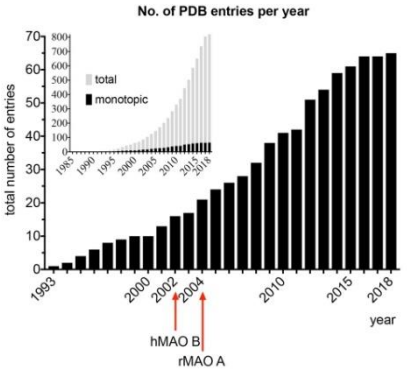

Fig. 5 Number of annual entries of membrane protein structure deposited in the Protein Data Bank (http://www.rcsb.org). The graph represents the number of monotopic membrane protein structures deposited in the PDB as listed in Membrane Proteins of Known 3D Structures (http://blanco.biomol.uci.edu/mpstruc/). Red arrows indicate the year when the first MAO B and MAO A three-dimensional structures have been determined: human MAO B (PDB code 1gos, (Binda et al. 2002) and rat MAO A (PDB code 1o5w, (Ma et al. 2004). The inset shows the total number of membrane protein structures solved (in gray) together with the corresponding number of monotopic membrane protein structures (in black)

detergent, which depends on the structure and its membrane environment, is determined empirically. Sometimes, inclusion of specific lipids together with the detergent is necessary to maintain the protein folding and activity. Detergents (and annular lipids) interact so intimately with the protein that they can be observed as ordered molecules in crystal structures, as occurred in the case of MAOs (Fig. 3). Unfortunately, detergents are not perfect mimics of the lipid bilayer and sometimes they do not fully support protein activity; in addition, disordered detergent molecules can hinder crystal formation, particularly for transmembrane proteins. However, for monotopic membrane proteins, this is usually not an issue, since they are solvated by few detergent molecules, and thus, detergents do not form large micelles as seen for transmembrane proteins. In any case, these amphipathic reagents affect the quality of crystal diffraction, so it is a good practice to screen a range of different detergents either as additives in the crystallization screen or by exchanging them in the latter phases of protein purification (e.g., during the washing step of the affinity purification prior to protein elution, or during gel filtration: beware that the latter does not guarantee a complete detergent exchange). In our lab, the best diffracting crystals for the human MAO B were obtained by solubilizing the *Pichia pastoris* membranes with 0.5% Triton X-100, which was then exchanged during purification to either lauryldimethylamine oxide (LDAO) or zwittergent 3–12, triggering different space groups (Binda et al. 2002). The large number of detergents that have now become available increases the chances of finding one that is appropriate for a specific membrane protein. So far, the crystallization of monotopic membrane proteins has seen the use of both non-ionic and zwitterionic detergents (Table 2). This probably mirrors the broad distribution of those monotopic proteins whose structure has been solved so far (Fig. 4), both in prokaryotic and almost in all subcellular organelles of eukaryotic cells. The lipid compositions of the various cell compartments differ from one another; for instance, cardiolipin is absent from the plasma membrane, but constitutes about 11% of total phospholipids in mitochondria (de Kroon et al. 1997). In mitochondria, the inner membrane is richer in proteins, whereas the outer membrane is richer in lipids and contains phosphatidylcholine and phosphatidylethanolamine (both zwitterionic), phosphatidylinositol (important lipid for various cell signaling cascades, whose sugar head group can be phosphorylated at several of its hydroxyl groups), and only traces of cardiolipin, a negatively charged phospholipid abundant in the inner mitochondrial membrane (de Kroon et al. 1997).

Soluble proteins form crystal contacts through their polar regions (type II crystals). On the other hand, membrane proteins have a polar region and one (monotopic) or two (transmembrane) non-polar regions, and can form type I crystals. These are stacks of bi-dimensional crystals, with the hydrophobic surface of the protein providing most of the contacts. Then, multiple 2D layers stack against each other to form a 3D crystal via polar contacts between protein molecules of neighbor layers. MAOs' crystals contain both polar and non-polar crystal contacts, as shown in Fig. 6. To mask the hydrophobic surface from the solvent, monotopic membrane proteins often arrange their non-polar region in a head-to-toe arrangement, as observed for one crystalline form of human MAO A (Fig. 6c). The limited hydrophobic surface available for crystal contacts in MAO A results in a non-perfect type I crystal arrangement, particularly evident in some other MAO crystals, such as human MAO B (Fig. 6a) and rat MAO A (Fig. 6b).

MAOs bind to the mitochondrial outer membrane through their C-termini. Inspection of MAO B structure and mutagenic studies indicates that residues 99–112, 157 and 481–488 also interact with the lipid bilayer (Binda et al. 2002; Rebrin et al. 2001). Additional interactions with the lipid bilayer can be provided by basic residues, such as Arg494 in MAO B and Lys503 in MAO A, which can engage with the membrane through electrostatic interactions with the negatively charged phosphate groups of phospholipids (Fig. 3). These interactions with the negatively charged phosphate head groups probably help the enzyme to align

Table 2 List of monotopic membrane proteins showed in Fig. 4, including cell localization and type of detergent(s) used for crystallization. (Source: Membrane Proteins of Known 3D Structures, http://blanco.biomol.uci.edu/mpstruc/)

PDB code	Monotopic protein class	Cell compartment	Detergent	Type of detergent
1PRH	Cyclooxygenases	Endoplasmic reticulum, lumen	βOG	Non-ionic
1B12	Peptidases	Bacterial Gram-negative, inner membrane, periplasm side	Triton X-100	Non-ionic
1GOS	Monoamine oxidase B	Mitochondria, outer membrane, cytosol side	LDAO Anzergent 3–12	Zwitterionic
1J79	Dihydroorotate dehydrogenases	Bacterial Gram-negative inner membrane, cytosol side	None	None
1MT5	Hydrolases	Endoplasmic reticulum, cytosol side	CHAPS	Zwitterionic
1O5W	Monoamine oxidase A	Mitochondria, outer membrane, cytosol side	FC12 + DMDPO	Zwitterionic + non-ionic
2K5U	ADP-ribosylation factors	Golgi, cytosol side	None (protein is myristoylated)	None
2OLV	Glycosyltransferases	Bacterial Gram-negative, inner membrane, cytosol side	LDAO	Zwitterionic
2QCU	Dehydrogenases	Bacterial Gram-negative, inner membrane, cytosol side	βOG	Non-ionic
2SBL	Lipoxygenases	Plasma membrane, cytosol side	None	Non-ionic
2SQC	Squalene-Hopene Cyclases	Bacterial Gram-positive, inner membrane, cytosol side	C8E4	Non-ionic
3FSN	Isomerases	Endoplasmic reticulum, cytosol side	C8E4	Non-ionic
3HYW	Oxidoreductases	Gram-negative bacteria, inner membrane, periplasm side	DDM	Non-ionic
3L7I	Polymerases	Gram-negative bacteria, inner membrane, cytosol side	CHAPS	Zwitterionic
4LXJ	Cytochromes P450	Endoplasmic reticulum, lumen	DM	Non-ionic
4PLA	Phosphoinositide Kinases	Golgi, cytosol side	None (palmitoylation motif replaced with T4 lysozyme)	None
5KN7	Acyltransferases	Gram-negative bacteria, inner membrane, cytosol side	DDM	Non-ionic

βOG octyl-β-D-glucopyranoside, *C8E4* *n*-octyltetraoxyethylene glycol ether), *DDM* *n*-dodecyl-β-D-maltoside, *DM* *n*-decyl-β-D-maltoside, *LDAO* Lauryldimethylamine oxide, *FC12* fos-choline 12, *DMDPO* dimethyldecylphosphine oxide

with the membrane surface. The distribution of these interfacial amino acids was noted already in the first structure of a membrane protein, the photosynthetic reaction center from the purple bacterium *Rhodopseudomonas viridis* (Deisenhofer and Michel 1989) and it is in accordance with statistical analysis of the membrane–water interface where Lys and Arg are often found pointing away from the lipid bilayer, whereas aromatic residues (Trp and Tyr) point toward it. In fact, as already described above, near Arg494 in MAO B (Lys503 in MAO A), there is an aromatic residue Trp157 (Trp166 in MAO A) that points toward the lipid bilayer (Fig. 3). While the conformation of membrane α-helix is conserved on the side of the main body of the protein in both MAO A and MAO B, the C-terminal portion is not well defined and might differ in the two enzymes. The C-termini of MAO A (either rat or human) traverses the bilayer entirely, as shown by the fact that the full-length α-helix is visible in the electron density and that the C-terminus includes a few Tyr-Lys sites (Lys519-Tyr520 and Lys521-Tyr522 in human MAO A; Lys519-Tyr520 in rat MAO A) which may contribute to position the helix across the bilayer. Instead, in all MAO B structures, the C-terminal α-helix is partly disordered (visible in the electron density only up to residue 501; Fig. 1a) and its far end contains a Lys-Arg motif that does not include a Tyr residue. Nevertheless, in MAO B structures, crystal packing is likely to produce conformational disorder in the C-terminus (Fig. 6a) and, indeed, molecular dynamics simulations predict the helix to span both membrane leaflets (Fowler et al. 2007).

The active site of MAOs

The Protein Data Bank contains 43 crystal structures of human MAO B, 1 of rat MAO A and 4 of human MAO A. The latter group includes two entries that were deposited by our group (both in complex with clorgyline, which had different crystalline forms) and two structures in complex with harmine determined by Tsukihara and coworkers (wild type and G110A mutant). The reproducibility and

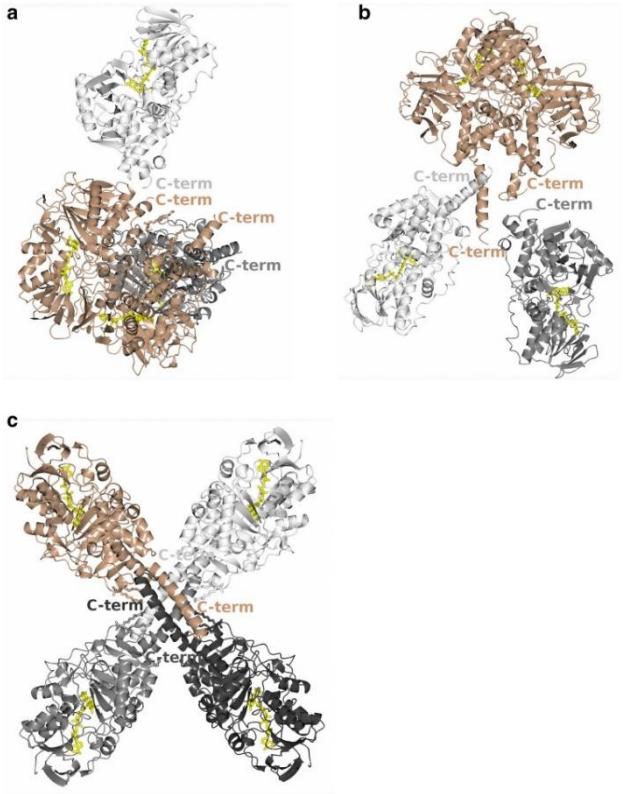

Fig. 6 Crystal packing in MAO structures highlighting the crystal contacts involving the C-terminal membrane-binding α-helix. Color code is as in Fig. 1 with the symmetry-related molecules in gray scale. FAD is in yellow, whereas the detergent molecules are colored according to the corresponding ribbon representation. **a** Human MAO B. **b** Rat MAO A. **c** Human MAO A (in complex with harmine; Son et al. 2008)

the good quality of human MAO B crystals allowed the structure of this isozyme in complex with a large number of different inhibitors to be obtained, as well as the use of site-directed mutagenesis to probe the role of active site residues in catalysis and ligand binding. Remarkably, both MAO A and MAO B could not be crystallized in their free form, i.e., without any inhibitor bound. In particular, in the case of MAO B, there is a clear correlation between the binding affinity of the inhibitor and the resolution of the X-ray data, suggesting that the inhibitors that best fit the enzyme active site cavity have a significant stabilizing effect on the protein fold. However, it is likely that the compact overall structure of MAOs is not perturbed by ligand binding, which, instead, determines only site-specific conformational changes of a few active site residues.

In a general perspective, the active site of MAOs consists of a hydrophobic cavity (whose volume is about 500 $Å^3$ and 700 $Å^3$ in MAO A and MAO B, respectively) that extends from the core of the globular body in front of the flavin to the protein surface (Fig. 1). The structure of the cavity is mainly determined by an entrance loop (residues 108–119 in MAO A and 99–110 in MAO B), which regulates ligand access to the active site, and a cavity-shaping loop formed by residues 209–218 in MAO A that correspond to 200–209 in MAO B (Fig. 7). Most of the residues lining the cavity are conserved between MAO A and MAO B, and differences arise from a few structural details, as described below. A

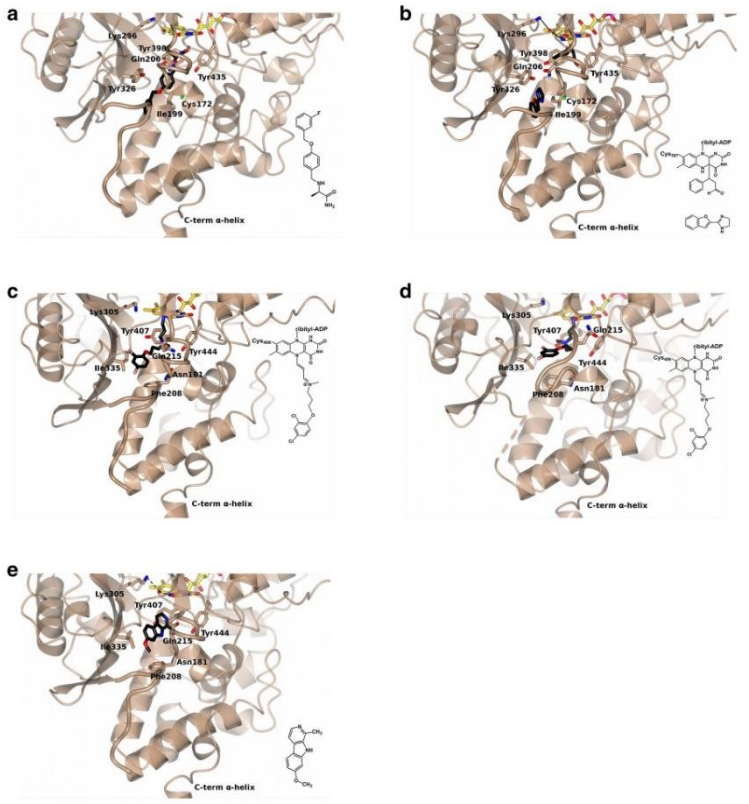

Fig. 7 Active site of MAO A and MAO B in complex with inhibitors, whose molecular structure is reported on the right side of each figure (for covalent inhibitors, the structure of the adduct formed with the flavin cofactor is shown). In the 3D figure on the left side, color code is as in Fig. 1 with inhibitors represented with carbon atoms in black (fluorine in cyan, chlorine is pink). For clarity, only the water molecule (red sphere) that is H-bonded (dashed lines) to the flavin N5 and to the active site Lys residue is shown, which could not be modelled in rat MAO A and human MAO A in complex with clorgyline because of low-resolution data. Moreover, the Cys-FAD covalent linkage that is found in both MAO A and MAO B is not shown in the 3D model. For each structure, a monomer is represented oriented by a rotation of approximately 90° around the vertical axis with respect to that in Fig. 1 (the ribbon diagram are semitransparent and foggy rendered to highlight the active site details; for the sake of clarity, the active site cavities shown in Fig. 1 were omitted here to avoid overlapping with inhibitors and protein residues). The entrance loop on the surface (residues 99–110 in MAO B and 108–119 in MAO A) and the cavity-shaping loop (residues 200–209 in MAO B and 209–218 in MAO A) are drawn as bold coils. **a** Human MAO B in complex with safinamide (PDB code 2v5z; Binda et al. 2007). **b** Human MAO B in complex with tranylcypromine (covalent adduct with the C4a atom of the flavin) and 2-BFI bound in the entrance cavity (PDB code 2xcg; Bonivento et al. 2010). **c** Rat MAO A in complex with clorgyline (PDB code 1o5w; Ma et al. 2004). **d** Human MAO A in complex with clorgyline (PDB code 2bxs; De Colibus et al.). The dashed line indicates a disordered conformation of the entrance loop. **e** Human MAO A in complex with harmine (PDB code 2z5x; Son et al. 2008)

common hallmark of MAOs, shared by other flavin-dependent amine oxidases (Forneris et al. 2009), is a Lys residue lying on the top of the flavin and H-bonded to a conserved water molecule (Fig. 7a, b, e) that most likely represents the oxygen-binding site during the FAD reoxidation step. Moreover, two aromatic residues stacking parallel to each other and perpendicular to the flavin ring (Tyr407/Tyr444 in MAO A and Tyr398/Tyr435 in MAO B) create an aromatic sandwich that stabilizes substrate binding (Fig. 7).

Human MAO B is characterized by a flat and elongated active site cavity (Fig. 1a) whose structure may vary depending on the size of the bound inhibitor (for a review, see Edmondson et al. 2009). From this comparative analysis, over many inhibitor classes (propargylamines, hydrazines, glitazones, etc.), it could be inferred that MAO B cavity has a quite rigid architecture that undergoes limited conformational changes. More precisely, it may switch from a single space when large inhibitors are bound (Figs. 1a, 7a) to a dipartite entity when smaller ligands occupy only the catalytic site in front of the flavin (Fig. 7b; Bonivento et al. 2010). The key residue in this structural plasticity is Ile199 that may exist in a closed conformation separating the catalytic site from the entrance cavity space. For example, this occurs in the MAO B structure solved in complex with both tranylcypromine, forming a covalent adduct with the flavin ring, and 2-(2-benzofuranyl)-2-imidazoline (2-BFI) that binds at the entrance of the active site (Fig. 7b; Bonivento et al. 2010). However, this double inhibition represents a peculiar case and, in general, the dipartite cavity was found when a single inhibitor was bound, provided that its size is small enough to occupy only the substrate-cavity space. Alternatively, Ile199 side chain can adopt a different rotamer conformation that is induced by large inhibitors occupying the entire cavity, as has been shown to be the case when the drug safinamide was used (Fig. 7a; Binda et al. 2007). Ile199 and Tyr326 (corresponding to Phe208 and Ile335 in MAO A; Fig. 7c–e) represent gating residues that mainly contribute to determine the shape of the cavity and the specific inhibitor/substrate-binding properties of human MAO B (Milczek et al. 2011). In addition, Cys172 is not conserved in human MAO A (replaced by Asn181): this residue was shown to adopt a double conformation and to interact with some inhibitor through an H-bond (Reis et al. 2018), although its role in the enzyme catalytic properties and substrate specificity was not explored.

The active site of MAO A, either human or rat, consists of a smaller and more spherical cavity that has a monopartite nature (Fig. 1b, c, d), although the paucity of available structures (essentially limited to two inhibitors, clorgyline and harmine) does not allow conformational changes in the active site of MAO A to be excluded. Indeed, it was reported that a tranylcypromine analog bearing a large-branched chain substituent on the aromatic ring can covalently inhibit MAO A but not MAO B (Binda et al. 2010), implying that, in certain conditions, MAO A may be endowed with an even more pronounced plasticity than the B isozyme leading to a wider and flexible cavity. This is consistent with some structural differences existing between the available MAO A structures. Human MAO A structure determined in complex with clorgyline features a disordered entrance loop and a conformation of the cavity-shaping loop (Fig. 7d) that is different from that observed in rat MAO A in complex with the same inhibitor (Fig. 7c), which, instead, resembles that found in the human MAO A–harmine complex (Fig. 7e) and in all the MAO B structures (Fig. 7a, b). In addition, the inhibitor clorgyline, although forming the same covalent adduct with the flavin cofactor, adopts a more folded conformation when bound to the human MAO A, which induces a change of side-chain rotamer of the active site Gln215. This residue corresponds to Gln206 in human MAO B, which also undergoes a conformational change in the tranylcypromine-inhibited enzyme most likely induced by the flavin C4a adduct formed specifically by this inhibitor (Fig. 7b).

Conclusions and future perspectives

MAOs discovery is approaching its centenary birthday, whereas the crystal structures of these enzymes are only in their adolescence, with the first one (human MAO B in complex with pargyline) elucidated in 2002. This temporal gap is due to the fact that MAOs are membrane proteins, localized on the outer envelope of mitochondria. They are classified as monotopic membrane proteins featuring a hydrophobic C-terminal α-helix that had been predicted to represent the anchor to the phospholipid bilayer, as was later confirmed by structural studies (Fig. 1). Although most of the protein is formed by a water-soluble globular domain that also includes the FAD-binding domain and the active site, both MAO A and MAO B are stably bound to the membrane and required detergent-based treatments to be extracted, purified, and crystallized. This feature is often neglected or not correlated with their central role in neurotransmitter metabolism and their reputation of validated drug targets. Indeed, MAOs are amine-metabolizing enzymes whose function is not directly related to the membrane environment and it may be argued that they could accomplish their job even (if not even more efficiently) dissociated from the membrane. The reason why MAOs are mitochondrial membrane proteins is still an open question (Tipton 2018). This issue should be also addressed considering another important aspect of MAO biology, i.e., the production of large amounts of hydrogen peroxide. On one hand, this byproduct is known to contribute to the overall cellular oxidative stress during ageing in both neuronal and cardiovascular tissues (Maggiorani et al. 2017), and on the other hand, hydrogen peroxide

is emerging as a molecular player in signaling mechanisms whose mis-regulation is supposed to lead to cancer development (Lin et al. 2017). Another interesting issue is the dimeric structure of MAOs when bound to the mitochondrial membrane. Since the active site is independent from the monomer–monomer interface and that, in vitro, these enzymes are active in their monomeric form, why do they feature this oligomeric organization? Is this functional for the interaction with other protein partners on or nearby the membrane? At the moment, these aspects are far from being understood and suggest that MAO story is not at the end.

Acknowledgements This work was supported by Fondazione Cariplo (Grant no. 2014 – 0672 to C.B.) and by the Italian Ministry of Education, University and Research (MIUR, "Dipartimenti di Eccellenza Program 2018–2022—Dept. of Biology and Biotechnology L. Spallanzani", University of Pavia).

Compliance with ethical standards

Conflict of interest The authors declare that they have no conflict of interest.

References

Bailey SD, Bucci L, Gosline E, Kline NS, Park IH, Rochlin D, Saunders JC, Vaisberg M (1959) Comparison of iproniazid with other amine oxidase inhibitors, including W-1544, JB-516, RO 4-1018, and RO 5-0700. Ann N Y Acad Sci 80:652–668

Binda C, Newton-Vinson P, Hubalek F, Edmondson DE, Mattevi A (2002) Structure of human monoamine oxidase B, a drug target for the treatment of neurological disorders. Nat Struct Biol 9(1):22–26. https://doi.org/10.1038/nsb732

Binda C, Wang J, Pisani L, Caccia C, Carotti A, Salvati P, Edmondson DE, Mattevi A (2007) Structures of human monoamine oxidase B complexes with selective noncovalent inhibitors: safinamide and coumarin analogs. J Med Chem 50(23):5848–5852. https://doi.org/10.1021/jm070677y

Binda C, Valente S, Romanenghi M, Pilotto S, Cirilli R, Karytinos A, Ciossani G, Botrugno OA, Forneris F, Tardugno M, Edmondson DE, Minucci S, Mattevi A, Mai A (2010) Biochemical, structural, and biological evaluation of tranylcypromine derivatives as inhibitors of histone demethylases LSD1 and LSD2. J Am Chem Soc 132(19):6827–6833. https://doi.org/10.1021/ja101557k

Binda C, Milczek EM, Bonivento D, Wang J, Mattevi A, Edmondson DE (2011) Lights and shadows on monoamine oxidase inhibition in neuroprotective pharmacological therapies. Curr Top Med Chem 11(22):2788–2796

Bonivento D, Milczek EM, McDonald GR, Binda C, Holt A, Edmondson DE, Mattevi A (2010) Potentiation of ligand binding through cooperative effects in monoamine oxidase B. J Biol Chem 285(47):36849–36856. https://doi.org/10.1074/jbc.M110.169482

Byrne B (2015) Pichia pastoris as an expression host for membrane protein structural biology. Curr Opin Struct Biol 32:9–17. https://doi.org/10.1016/j.sbi.2015.01.005

Caffrey M (2015) A comprehensive review of the lipid cubic phase or in meso method for crystallizing membrane and soluble proteins and complexes. Acta Crystallogr F Struct Biol Commun 71(Pt 1):3–18. https://doi.org/10.1107/S2053230X14026843

Cesura AM, Pletscher A (1992) The new generation of monoamine oxidase inhibitors. Prog Drug Res 38:171–297

Cherezov V, Rosenbaum DM, Hanson MA, Rasmussen SG, Thian FS, Kobilka TS, Choi HJ, Kuhn P, Weis WI, Kobilka BK, Stevens RC (2007) High-resolution crystal structure of an engineered human beta2-adrenergic G protein-coupled receptor. Science 318(5854):1258–1265. https://doi.org/10.1126/science.1150577

de Kroon AI, Dolis D, Mayer A, Lill R, de Kruijff B (1997) Phospholipid composition of highly purified mitochondrial outer membranes of rat liver and Neurospora crassa. Is cardiolipin present in the mitochondrial outer membrane? Biochim Biophys Acta 1325(1):108–116

De Colibus L, Li M, Binda C, Lustig A, Edmondson DE, Mattevi A (2005) Three-dimensional structure of human monoamine oxidase A (MAO A): relation to the structures of rat MAO A and human MAO B. Proc Natl Acad Sci USA 102(36):12684–12689. https://doi.org/10.1073/pnas.0505975102

Deisenhofer J, Michel H (1989) Nobel lecture. The photosynthetic reaction centre from the purple bacterium Rhodopseudomonas viridis. EMBO J 8(8):2149–2170

Edmondson DE, Binda C (2018) Monoamine Oxidases. Subcell Biochem 87:117–139. https://doi.org/10.1007/978-981-10-7757-9_5

Edmondson DE, Binda C, Wang J, Upadhyay AK, Mattevi A (2009) Molecular and mechanistic properties of the membrane-bound mitochondrial monoamine oxidases. Biochemistry 48(20):4220–4230. https://doi.org/10.1021/bi900413g

Forneris F, Battaglioli E, Mattevi A, Binda C (2009) New roles of flavoproteins in molecular cell biology: histone demethylase LSD1 and chromatin. FEBS J 276(16):4304–4312. https://doi.org/10.1111/j.1742-4658.2009.07142.x

Fowler PW, Balali-Mood K, Deol S, Coveney PV, Sansom MS (2007) Monotopic enzymes and lipid bilayers: a comparative study. Biochemistry 46(11):3108–3115. https://doi.org/10.1021/bi602455n

Hunte C, Michel H (2002) Crystallisation of membrane proteins mediated by antibody fragments. Curr Opin Struct Biol 12(4):503–508

Kuhlbrandt W (2014) Cryo-EM enters a new era. Elife 3:e03678. https://doi.org/10.7554/eLife.03678

Lees AJ, Shaw KM, Kohout LJ, Stern GM, Elsworth JD, Sandler M, Youdim MB (1977) Deprenyl in Parkinson's disease. Lancet 2(8042):791–795

Li M, Hubalek F, Newton-Vinson P, Edmondson DE (2002) High-level expression of human liver monoamine oxidase A in Pichia pastoris: comparison with the enzyme expressed in Saccharomyces cerevisiae. Protein Expr Purif 24(1):152–162. https://doi.org/10.1006/prep.2001.1546

Lin YC, Chang YT, Campbell M, Lin TP, Pan CC, Lee HC, Shih JC, Chang PC (2017) MAOA-a novel decision maker of apoptosis and autophagy in hormone refractory neuroendocrine prostate cancer cells. Sci Rep 7:46338. https://doi.org/10.1038/srep46338

Ma J, Yoshimura M, Yamashita E, Nakagawa A, Ito A, Tsukihara T (2004) Structure of rat monoamine oxidase A and its specific recognitions for substrates and inhibitors. J Mol Biol 338(1):103–114. https://doi.org/10.1016/j.jmb.2004.02.032

Maggiorani D, Manzella N, Edmondson DE, Mattevi A, Parini A, Binda C, Mialet-Perez J (2017) Monoamine oxidases, oxidative stress, and altered mitochondrial dynamics in cardiac ageing. Oxid Med Cell Longev 2017:3017947. https://doi.org/10.1155/2017/3017947

Magnani F, Serrano-Vega MJ, Shibata Y, Abdul-Hussein S, Lebon G, Miller-Gallacher J, Singhal A, Strege A, Thomas JA, Tate CG (2016) A mutagenesis and screening strategy to generate optimally thermostabilized membrane proteins for structural studies. Nat Protoc 11(8):1554–1571. https://doi.org/10.1038/nprot.2016.088

Manglik A, Kobilka BK, Steyaert J (2017) Nanobodies to study G protein-coupled receptor structure and function. Ann Rev Pharmacol

Toxicol 57:19–37. https://doi.org/10.1146/annurev-pharmtox-010716-104710
McNicholas S, Potterton E, Wilson KS, Noble ME (2011) Presenting your structures: the CCP4mg molecular-graphics software. Acta Crystallogr D Biol Crystallogr 67(Pt 4):386–394. https://doi.org/10.1107/S0907444911007281
Mialet-Perez J, Santin Y, Parini A (2018) Monoamine oxidase-A, serotonin and norepinephrine: synergistic players in cardiac physiology and pathology. J Neural Transm (Vienna). https://doi.org/10.1007/s00702-018-1908-y
Milczek EM, Binda C, Rovida S, Mattevi A, Edmondson DE (2011) The 'gating' residues Ile199 and Tyr326 in human monoamine oxidase B function in substrate and inhibitor recognition. FEBS J 278(24):4860–4869. https://doi.org/10.1111/j.1742-4658.2011.08386.x
Newton-Vinson P, Hubalek F, Edmondson DE (2000) High-level expression of human liver monoamine oxidase B in Pichia pastoris. Protein Expr Purif 20(2):334–345. https://doi.org/10.1006/prep.2000.1309
Pettersen EF, Goddard TD, Huang CC, Couch GS, Greenblatt DM, Meng EC, Ferrin TE (2004) UCSF Chimera—a visualization system for exploratory research and analysis. J Comput Chem 25(13):1605–1612. https://doi.org/10.1002/jcc.20084
Ramsay RR, Albreht A (2018) Kinetics, mechanism, and inhibition of monoamine oxidase. J Neural Transm (Vienna). https://doi.org/10.1007/s00702-018-1861-9
Rebrin I, Geha RM, Chen K, Shih JC (2001) Effects of carboxyl-terminal truncations on the activity and solubility of human monoamine oxidase B. J Biol Chem 276(31):29499–29506. https://doi.org/10.1074/jbc.M100431200
Reis J, Manzella N, Cagide F, Mialet-Perez J, Uriarte E, Parini A, Borges F, Binda C (2018) Tight-binding inhibition of human monoamine oxidase B by chromone analogs: A kinetic, crystallographic, and biological analysis. J Med Chem 61(9):4203–4212. https://doi.org/10.1021/acs.jmedchem.8b00357
Riederer P, Muller T (2017) Use of monoamine oxidase inhibitors in chronic neurodegeneration. Expert Opin Drug Metab Toxicol 13(2):233–240. https://doi.org/10.1080/17425255.2017.1273901
Shih JC (1991) Molecular basis of human MAO A and B. Neuropsychopharmacology 4(1):1–7
Son SY, Ma J, Kondou Y, Yoshimura M, Yamashita E, Tsukihara T (2008) Structure of human monoamine oxidase A at 2.2—a resolution: the control of opening the entry for substrates/inhibitors. Proc Natl Acad Sci USA 105(15):5739–5744. https://doi.org/10.1073/pnas.0710626105
Tatton W, Chalmers-Redman R, Tatton N (2003) Neuroprotection by deprenyl and other propargylamines: glyceraldehyde-3-phosphate dehydrogenase rather than monoamine oxidase B. J Neural Transm (Vienna) 110(5):509–515. https://doi.org/10.1007/s00702-002-0827-z
Tipton KF (2018) 90 years of monoamine oxidase: some progress and some confusion. J Neural Transm (Vienna). https://doi.org/10.1007/s00702-018-1881-5
Upadhyay AK, Edmondson DE (2009) Development of spin-labeled pargyline analogues as specific inhibitors of human monoamine oxidases A and B. Biochemistry 48(18):3928–3935. https://doi.org/10.1021/bi9002106
Weyler W, Hsu YP, Breakefield XO (1990) Biochemistry and genetics of monoamine oxidase. Pharmacol Ther 47(3):391–417
Youdim MB, Kupershmidt L, Amit T, Weinreb O (2014) Promises of novel multi-target neuroprotective and neurorestorative drugs for Parkinson's disease. Parkinsonism Relat Disord 20(Suppl 1):S132–S136. https://doi.org/10.1016/S1353-8020(13)70032-4
Zeller EA (1938) Über den enzymatischen Abbau von Histamin und Diaminen. 2. Mitteilung Helv Chim Acta 21 (1):880–890

1.2 MONOAMINE OXIDASE A AND CARDIAC SENESCENCE

As previously described in the Introduction Chapter, the oxidative de-amination of MAOs substrates involves the production of ammonia and hydrogen peroxide as secondary product of the reaction. The latter is physiologically important for governing life processes through redox signalling as it acts as second messenger in different pathways. However, when hydrogen peroxide levels go beyond a certain limit, they may represent a dangerous source of reactive species of oxygen (ROS) through the Fenton reaction triggering deleterious mechanisms for the cell, including mitochondrial damage and cell death. ROS are extremely reactive species that might irreversibly interact with biomolecules important for cell life. The over-expression of MAO-A in heart cells occurring during ageing is correlated to cardiac senescence in the elderly population and it represents one of the major sources of H_2O_2 in cardiomyoblasts. By a combination of enzymology and cell biology, we analysed the impact of MAO-A enzymatic activity and H_2O_2 production on the cardiomyocytes dysfunction and senescence. To do that, we exploited the structural features of the enzyme to develop different MAO-A mutants unable to produce hydrogen peroxide and use them as "molecular tools" probing MAOs role in the oxidative stress. In particular, we have selectively mutated the Lys305 of MAO-A that is directly involved with O_2 reactivity (Fig. 5). This work is reported in the article "Rational redesign of Monoamine Oxidase A into a Dehydrogenase to probe ROS in Cardiac Aging" published on the ACS Chemical Biology journal (attached at the end of this section).

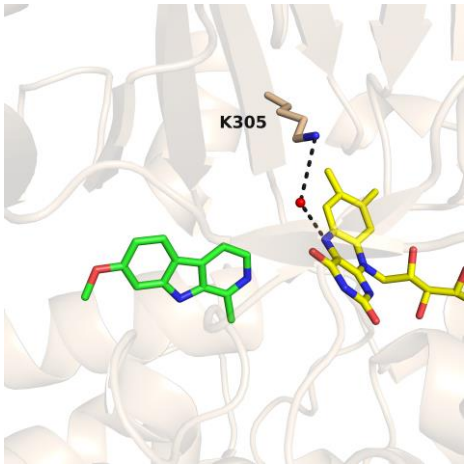

Figure 5. Crystal Structure of human MAO-A in complex with Harmine inhibitor (PDB code 2Z5X). A water molecule represented as red sphere is hydrogen bonded with K305 and the flavin N(5) ring. FAD and Harmine carbons are in yellow and green, respectively. The backbone trace is shown as wheat ribbon.

Lys305 is a highly conserved residue of flavoprotein amino oxidases superfamily. In several structures, this lysine forms a hydrogen bond with a water molecule that is hydrogen bonded in turn to the flavin N5 atom (Henderson Pozzi and Fitzpatrick 2010). This represents the putative binding site of the oxygen molecule involved in the FAD reoxidation. As shown in Fig. 5, Lys305 is lying on the top of the flavin, far from the active site cavity. Thus, mutation of this residue was not supposed to affect substrate recognition. The ratio behind was to selectively act on the FAD reoxidation half reaction without altering the binding of the amine substrate. Previous studies showed that mutation of this lysine residue abolishes the catalytic activity of this class of amine oxidases (Zhao, Bruckner et al. 2008, Henderson Pozzi and Fitzpatrick 2010), but the exact effects of this alteration were not analyzed in detail.

Different Lys305 MAO-A mutants were cloned, expressed and purified in our structural biology laboratory. To investigate the reactivity of these mutants and the production of hydrogen peroxide, the Horseradish Peroxide (HRP) Amplex Red coupled assay was used (Fig. 6). This coupled reaction exploits the hydrogen peroxide produced by MAOs which in turn triggers the HRP activity, whose product (Resorufin) can be spectrophotometrically detected at 515 nm (ε_{515} = 24000 M^{-1} cm^{-1}) (Vojinović, Azevedo et al. 2004).

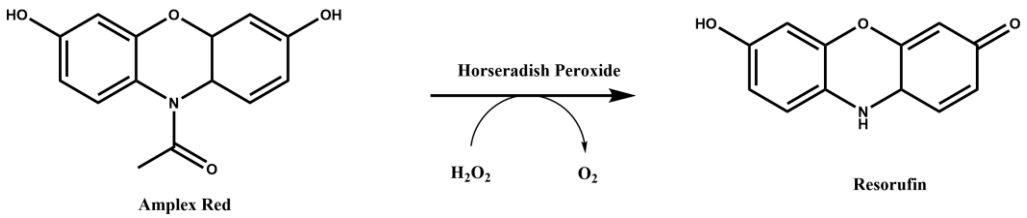

Figure 6. Reaction scheme of the Horseradish Peroxide.

We focused our attention on the methionine mutant K305M that was fully characterized through biochemical and cellular experiments in aerobic and anaerobic conditions. This variant was selected as methionine is structurally similar to lysine (including the length of the side chain), though it lacks the amino group H-bonded to the water molecule and,

possibly, the positive charge that favours oxygen binding (Chaiyen, Fraaije et al. 2012). Steady-state experiments in aerobic conditions on K305M variant showed that K_m (which indicates substrate binding affinity) was not affected by the mutation, but the enzyme activity (k_{cat}) was 200-fold lower compared to wild type, due to the lower reactivity with the oxygen. In collaboration with Prof. Maria Antonietta Vanoni (University of Milan), the FAD reactivity of K305M was also tested in anaerobiosis conditions removing any trace of molecular oxygen in the MAO-A solution. This isolated system allowed to measure UV-vis spectra of the enzyme during FAD reduction by substrate and coenzyme reoxidation by oxygen (or other electron acceptors). The time course of FAD reduction/oxidation was monitored at the maximum absorption at 456 nm (ε_{456} = 12000 M^{-1} cm^{-1}) and the results are reported in Fig. 7.

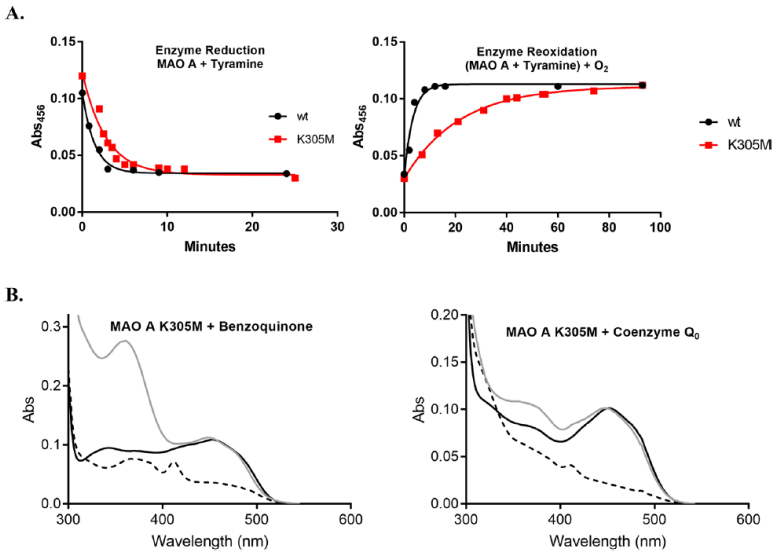

Figure 7. Spectrophotometric measurements of MAO-A wt and K305M mutant activity under anaerobiosis conditions. (adapted from Iacovino et al. 2020) (A) Flavin reduction was obtained by anaerobically addition of tyramine substrate; reoxidation by molecular oxygen was monitored for the K305M mutant (red) compared to the wild-type enzyme (black). (B) K305M flavin reoxidation by benzoquinone (left panel) and coenzyme Q_0. UV−vis spectra of the oxidized, photoreduced, and reoxidized K305M mutant are depicted as continuous black, dashed black, and gray lines, respectively (adapted from Iacovino et al. 2020).

In the presence of tyramine as substrate, enzyme reduction (Fig. 7A left panel) was fully achieved by both wild type and K305M mutant in a few minutes whereas a complete reoxidation of the coenzyme by oxygen was 10-fold slower for the mutant compared to the wild time (Fig. 7A right panel). These results highlighted that the mutant is able to bind and oxidize amines similarly to wild type but it is impaired in FAD reoxidation by oxygen.

We also tested the reactivity of K305M mutant with electron acceptors different from the molecular oxygen, specifically benzoquinone and Coenzyme Q_0. In this case, the FAD reduction was photoinduced to avoid multiple turnovers and also to avoid unspecific interactions of amine substrate (highly prone to a direct electron transfer) with these alternative electron acceptors. The profile of the photoreduced enzyme is consistent with a mixture of the anionic semiquinone and hydroquinone flavin forms that were previously observed for MAOs (Arslan and Edmondson 2010). It was already known that quinones, widely diffused in the mitochondrial environment, display binding affinity for MAO A (Ramsay, Dunford et al. 2007, Paudel, Seong et al. 2019). We found that in anaerobic conditions quinones are able to regenerate the FAD in its oxidized form, which is thus ready for another catalytic cycle. Given the interesting biochemical features of K305M, this mutant represented the main candidate to be tested in cellular assays to probe the effects of an enzymatically active MAO-A that does not produce hydrogen peroxide. K305M variant was over-expressed in cardiomyoblasts through adenoviral vectors and the enzyme activity was compared with MAO-A wild type. The cellular experiments were carried out by the group of Prof. Angelo Parini at INSERM Toulouse (France). Consistently with the results obtained on the purified enzyme, in cardiomyoblasts this mutant showed an enzymatic activity similar to MAO-A wild type (measured by radiolabelled serotonin assay), but lower production of ROS and reduced senescence markers.

These results highlighted a potentially new pharmacological role of MAOs, until now limited to neurological diseases. Indeed, a specific therapy targeting MAO-A in heart may be used to mitigate cardiac aging and heart failure in some frailty conditions of aged patients.

ACS chemical biology

pubs.acs.org/acschemicalbiology Letters

Rational Redesign of Monoamine Oxidase a into a Dehydrogenase to Probe ROS in Cardiac Aging

Luca Giacinto Iacovino, Nicola Manzella, Jessica Resta, Maria Antonietta Vanoni, Laura Rotilio, Leonardo Pisani, Dale Edward Edmondson, Angelo Parini, Andrea Mattevi, Jeanne Mialet-Perez, and Claudia Binda*

Cite This: https://dx.doi.org/10.1021/acschembio.0c00366 Read Online

ACCESS | Metrics & More | Article Recommendations | Supporting Information

ABSTRACT: Cardiac senescence is a typical chronic frailty condition in the elderly population, and cellular aging is often associated with oxidative stress. The mitochondrial-membrane flavoenzyme monoamine oxidase A (MAO A) catalyzes the oxidative deamination of neurotransmitters, and its expression increases in aged hearts. We produced recombinant human MAO A variants at Lys305 that play a key role in O_2 reactivity leading to H_2O_2 production. The K305Q variant is as active as the wild-type enzyme, whereas K305M and K305S have 200-fold and 100-fold lower k_{cat} values and similar K_m. Under anaerobic conditions, K305M MAO A was normally reduced by substrate, whereas reoxidation by O_2 was much slower but could be accomplished by quinone electron acceptors. When overexpressed in cardiomyoblasts by adenoviral vectors, the K305M variant showed enzymatic turnover similar to that of the wild-type but displayed decreased ROS levels and senescence markers. These results might translate into pharmacological treatments as MAO inhibitors may attenuate cardiomyocytes aging.

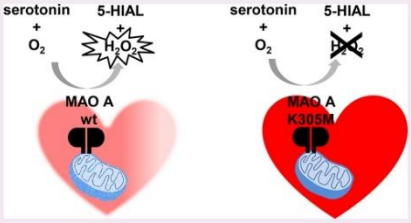

Oxidative stress is a pathophysiological condition resulting from an imbalance of cellular free radicals (reactive oxygen or nitrogen species, ROS or RNS, respectively) with respect to antioxidant defense systems.[1] This process is associated with a number of diseases such as cancer and neurodegenerative disorders, though the underlying molecular mechanisms are not fully understood. Many pathological or frailty states may lead to oxidative stress, but in certain circumstances ROS generated by cell oxidative metabolism may contribute themselves to triggering a disease. In this context, the role of H_2O_2 is dual because, while being physiologically involved in many signaling pathways, it represents a deleterious source of ROS through the Fenton or Haber−Weiss reaction when produced in excess.[2]

Mitochondrial respiration is the main source of superoxide anions and H_2O_2, but the membrane of these organelles contains also other enzymes that generate ROS. Monoamine oxidases A and B (MAO A and MAO B, respectively) are 60-kDa mammalian flavoproteins that feature a water-soluble globular main body anchored to the outer mitochondrial membrane through a C-terminal α-helix.[3] They belong to the FAD-dependent amine oxidase family of enzymes that catalyzes the oxidation of a carbon−nitrogen bond in various substrates with the concomitant reduction of the flavin coenzyme, which can be readily reoxidized by molecular oxygen leading to the generation of H_2O_2 (Figure 1).[4] MAOs are particularly abundant in mammalian cells where they play a key role in the metabolism of both endogenous and exogenous neuroactive aromatic amines. The function of MAOs has been thoroughly studied in the central nervous system where they represent established drug targets for Parkinson's disease and depression.[5] However, MAOs are widely expressed also in non-neuronal tissues, including the heart, in which they regulate the local concentrations of serotonin, noradrenaline, and dopamine. Interestingly, MAO A levels in the heart increase significantly with aging.[6] As a mimicry model of the elderly heart, the effects of cardiac overexpression and activation of MAO A in transgenic mice were studied by the authors of the present work, showing that an excess of H_2O_2 has multiple p53-mediated cell responses including mitochondrial damage and cell death.[7] More recently, they also demonstrated that a chronic MAO A-dependent increase of H_2O_2 in heart cell lines triggers lipid peroxidation, elevated p53/p21 levels, DNA

Received: May 10, 2020
Accepted: June 26, 2020
Published: June 26, 2020

https://dx.doi.org/10.1021/acschembio.0c00366
ACS Chem. Biol. XXXX, XXX, XXX−XXX

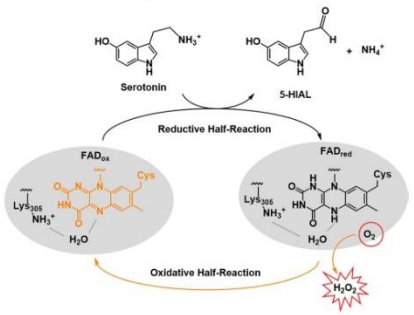

Figure 1. Scheme of amine substrate oxidation catalyzed by human MAO A (gray oval; the FAD coenzyme is covalently bound to a Cys residue). Oxidation of serotonin to 5-hydroxyindoleacetaldehyde (5-HIAL) is shown, with serotonin being the main MAO A substrate in heart metabolism. The two reductive and oxidative half reactions related to the flavin cofactor redox states are highlighted in black and yellow, respectively. In oxidases, the presence of a positive charge in proximity of the flavin isoalloxazine ring is believed to promote O_2 binding and activation followed by H_2O_2 generation.[1] In flavin-dependent amine oxidases, the conserved Lys305 lying on the top rim of the enzyme active site is H-bonded (dashed lines) to the flavin N5 atom through a bridging water molecule, which is believed to represent the O_2 binding site.

damage response, and other classical senescence markers.[8] This cascade of events is associated with mitochondrial dysfunction, decreased respiration, and inhibition of parkin-mediated mitophagy. These findings have important clinical implications because MAO A-dependent release of H_2O_2 may occur either under acute pathological conditions such as ischemia-reperfusion injury when MAO substrates are heavily released or chronically when MAO A expression increases during aging.

Although we supported evidence for the involvement of H_2O_2 in acute and chronic cardiac damage, it is still uncertain whether MAO A-dependent substrate regulation may also have an impact on cardiac dysfunction. In an effort to probe the molecular features of human MAO A in relation to H_2O_2 production, we produced recombinant enzyme variants at the Lys305 site lying close to the flavin cofactor. Lys305 is a conserved residue that is engaged with the flavin ring through a hydrogen bond mediated by a water molecule (Figure 1).[3] This site functions as a trap for molecular oxygen in flavin reoxidation following each MAO reductive half-reaction, which leads to H_2O_2 production.[9] Mutation of this lysine residue was shown to abolish the catalytic activity of this class of amine oxidases,[10,11] but the exact effects of this alteration were not studied in detail. In this work, we used Lys305 of human MAO A as a molecular tool to investigate the relevance of MAO A in age-related cardiovascular diseases based on the hypothesis that the increased enzyme-derived H_2O_2 levels may lead to oxidative stress. In particular, Lys305 mutants of human MAO A were tested through a combined enzymology/cell biology approach that involved activity assays on the purified proteins and overexpression of selected variants in the H9C2 cardiac cell line through an adenoviral vector. We show that the MAO A K305M mutant, which is seemingly inactive, is capable of oxidizing the amine substrate in the enzyme reductive half-reaction, while being impaired in enzymatic turnover due to lower reactivity with molecular oxygen. Nevertheless, its cellular enzymatic turnover can be restored by interaction with alternative electron acceptors without inducing the ROS-mediated senescence hallmarks of the wild-type enzyme.[8]

Four mutants of human MAO A (K305M, K305S, K305Q, K305R) were produced in *Pichia pastoris* as His-tagged recombinant proteins and purified as detergent preparations using protocols adapted from published procedures.[12] These variants were designed on the basis of the interaction of Lys305 with the water molecule mediating the H-bond bridge with the reactive N5 atom of the flavin (Figure 1). First, we tested the enzymatic activity of the variants compared to wild-type enzyme by the horseradish peroxidase (HRP)-coupled assay using kynuramine as a substrate. This is a widely used method to measure the activity of oxidases that generate H_2O_2 in stoichiometric amounts with the product (see Methods in the Supporting Information).[13] This assay is based on the enzyme's capability to bind and reduce molecular O_2 during flavin reoxidation. Under the conditions generally used to assay MAO activity (i.e., 0.07 μM enzyme, 1.67 mM kynuramine) only the K305Q variant of human MAO A was active, whereas the other mutations appeared to totally impair enzyme functionality. The same result was obtained when the enzyme concentration was increased 25-fold. Next, we used direct spectrophotometric assays that specifically monitor the product of amine oxidation.[14] One of these assays directly measures the absorbance of the kynuramine oxidation product at 316 nm (ε_{316} = 12 000 M^{-1} cm^{-1}). Another assay is based on the tertiary amine 1-methyl-4-(1-methyl-1*H*-pyrrol-2-yl)-1,2,3,6-tetrahydropyridine (MMTP) as a substrate, which can be efficiently oxidized by MAOs with kinetic parameters only slightly lower than those of primary amines. In this protocol, the product is detected spectrophotometrically at 420 nm with a sensitivity level equivalent to that of the HRP-coupled assay.[15] With both assays, the K305Q MAO A variant showed activity similar to that of the wild-type enzyme, whereas much lower (though detectable) activity was observed for K305M and K305S. The K305R variant was completely inactive under all conditions. We increased the enzyme concentration 25-fold to optimize the signal-to-noise ratio and measured the steady-state kinetic parameters exhibited by K305M, K305S, and K305Q MAO A mutants (Table 1). K305Q has k_{cat} values of the same order of magnitude as that measured for the wild-type enzyme. Instead, K305M and K305S are severely impaired in catalytic activity with k_{cat} values that are about 200-fold and 100-fold lower than wild-type, respectively, using both direct assays. These data suggest that replacing Lys305 with a hydrophobic side chain or with a small polar residue significantly affects MAO A catalytic efficiency, though retaining the capability to bind and oxidize the amine substrate. The longer polar side chain of Gln represents a good substitute of the conserved Lys, whereas the bulky and strongly basic Arg residue is definitely not tolerated by the enzymatic machinery. Interestingly, the K_m values are comparable for all active mutants, and only K305Q has a K_m value one order of magnitude lower than the wild-type using the MMTP assay. This observation suggests that, except for K305R, the mutations do not interfere with substrate binding within the MAO A active site.

MAOs can be irreversibly inactivated by inhibitors that form a covalent adduct with the enzyme FAD.[14] Three classes of

https://dx.doi.org/10.1021/acschembio.0c00366
ACS Chem. Biol. XXXX, XXX, XXX−XXX

Table 1. Steady-State Kinetic Parameters of MAO A Mutants Compared to Wild-Type Using MMTP and Kynuramine as Substrates

MAO A	k_{cat} (min^{-1})	K_m (mM)	k_{cat}/K_m (min^{-1} mM^{-1})
	MMTP direct assay (ε_{420} = 25000 M^{-1} cm^{-1})[a]		
wild-type	51.60 ± 1.70	0.18 ± 0.02	286.66
K305M	0.28 ± 0.01	0.36 ± 0.05	0.77
K305S	0.53 ± 0.03	0.20 ± 0.04	2.65
K305Q	21.4 ± 0.54	0.04 ± 0.005	528.50
K305R	not active	not active	not active
	kynuramine direct assay (ε_{316} = 12000 M^{-1} cm^{-1})[a]		
wild-type	120.20 ± 6.70	0.15 ± 0.01	801
K305M	0.67 ± 0.02	0.18 ± 0.02	3.72
K305S	0.98 ± 0.03	0.18 ± 0.03	5.44
K305Q	91.39 ± 2.81	0.16 ± 0.02	571.18
K305R	not active	not active	not active

[a]All details related to the experiments are reported in the Supporting Information. Briefly, all assays were performed at 25 °C in 50 mM HEPES/NaOH at pH 7.5 containing 0.25% reduced Triton X-100 (air saturated solution). Enzyme concentration was 0.07 μM for MAO A wt and 1.8 μM for MAO A mutants.

MAO covalent inhibitors are known that, though differing for the inactivation mechanism, all rely on the enzymatic functionality of the protein and the associated flavin cofactor. We exploited this property of MAOs to further test the Lys305 mutants. Within the propargylic class of molecules, clorgyline is a very well-known MAO A selective inhibitor that promptly forms an adduct with the flavin N5 atom that produces a sharp and intense peak at 415 nm in the UV−vis spectrum (Supporting Information Figure 1). Tranylcypromine and hydrazines are nonselective inhibitors of MAOs that behave as suicide substrates (i.e., implying a C−N bond oxidation) by reacting with either C4A or N5 atoms of the FAD cofactor, which can be detected spectrophotometrically as a bleached flavin peak. Though to different extents, both tranylcypromine and different hydrazine analogs are known to involve enzyme turnover (with molecular oxygen consumption) as part of the inactivation process; i.e., formation of the covalent adduct is preceded by unproductive cycles with a release of the oxidized inhibitor without formation of any bond with the flavin cofactor.[16] Instead, inhibition by propargylamine compounds is not strictly dependent on the redox catalytic cycle of MAOs, being nevertheless affected by a lower functionality of the protein (as for K305M and K305S mutants). UV−vis spectral

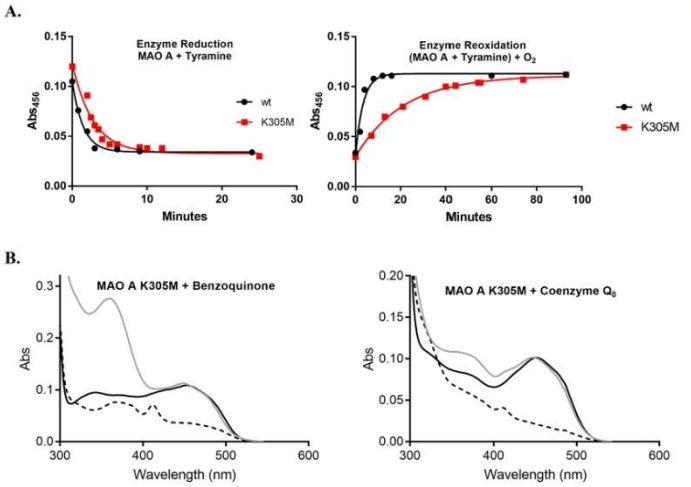

Figure 2. Spectrophotometric measurements of MAO A activity under anaerobiosis conditions. In all experiments, the cuvette contained 10 μM enzyme in 50 mM potassium phosphate at pH 7.8, 300 mM sodium chloride, 20% (w/v) glycerol, and 0.05% (w/v) Fos-Choline-12. (A) Flavin reduction was obtained by anaerobically adding 1 mM tyramine; reoxidation by molecular oxygen was monitored for the K305M mutant (red) compared to the wild-type enzyme (black). Enzyme reduction (left panel) was followed by measuring the absorbance at 456 nm corresponding to the peak of the oxidized flavin spectrum, which is bleached when flavin is reduced by the amine substrate. Enzyme reoxidation was monitored through the reappearance of the peak centered at 450 nm after exposure of the reaction mix to oxygen. Supporting Information Figure 2A and B show the overall UV−vis spectra of the oxidized and reduced enzyme for wild-type and K305M, respectively. (B) K305M flavin reoxidation by alternative electron acceptors: 200 μM benzoquinone (left) and 50 μM coenzyme Q_0 (right). UV−vis spectra of the oxidized (initial), photoreduced, and reoxidized K305M mutant are depicted as continuous black, dashed black, and gray lines, respectively. In this experiment, photochemical reduction of the enzyme was preferred to avoid multiple turnovers. In both panels, the profile of the photoreduced enzyme is consistent with a mixture of the anionic semiquinone and hydroquinone flavin forms that were previously observed for MAOs.[18] The peak at 350 nm in the left panel is due to benzoquinone absorbance.

https://dx.doi.org/10.1021/acschembio.0c00366
ACS Chem. Biol. XXXX, XXX, XXX−XXX

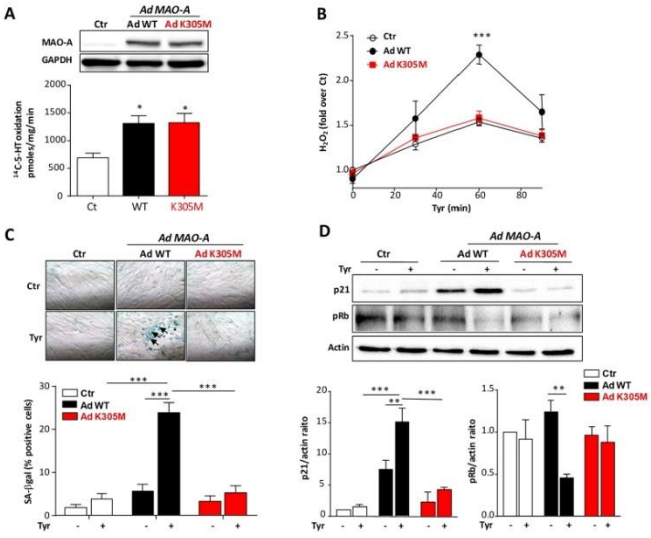

Figure 3. Cellular effects of wild-type and K305M mutant in H9C2 cells. Cells were transduced or not (Ctr) with adenovirus carrying either the wild-type (Ad WT) or mutant K305M (Ad K305M) MAO A. Assays were performed 72 h post-transduction. (A) MAO A expression was measured by immunoblot (upper panel, $n = 4$), and MAO A activity was determined by radioactive assay (lower panel, $n = 4$). (B) H_2O_2 was measured with Amplex Red assay in extracellular media at the times indicated after tyramine (500 μM) exposure ($n = 3$). (C) For SA-βgal activity ($n = 4$) and (D) immunoblots of p21 and phospho-Rb ($n = 3$), cells were preincubated 4 h with clorgyline before adenoviral transduction to block endogenous MAO A activity. After 72 h of tyramine treatment (500 μM), cells were monitored for senescence markers. SA-βgal activity was represented as % of blue cells (arrows). Data are expressed as means ± SEM. ***$p < 0.001$, **$p < 0.01$, *$p < 0.05$ vs indicated value.

measurements showed that the K305Q can be inactivated to the same extent as the wild-type enzyme by all inhibitors, whereas inactivation of both K305M and K305S is far less effective (Supporting Information Figure 1). Furthermore, these two mutants react less efficiently with those inhibitors that require enzyme turnover such as tranylcypromine and phenelzine. The only exception is represented by phenylhydrazine that takes about 20 min to inactivate all proteins, most likely due to the lower oxygen consumption required for the inactivation process.

The experiments described above showed that the K305M mutant is impaired in enzymatic activity, but it is not completely inactive (as for K305R). MAO A catalyzes a redox reaction in which the amine substrate is oxidized with the concomitant reduction of the FAD cofactor (reductive half reaction; Figure 1). The catalytic turnover is guaranteed by the prompt flavin reoxidation by molecular O_2 (oxidative half reaction).[4,17] To better dissect the role of Lys305 in H_2O_2 production by MAO A, we monitored the K305M enzyme reaction spectrophotometrically under anaerobiosis conditions, which were essential to keep the enzyme in the reduced state as the mutant is likely to retain some O_2 reactivity. This specific mutant (rather than K305S) was selected for these further studies because its side chain structurally mimics that of lysine, though returning an impaired turnover efficiency due to the lack of the positive charge that prevents an optimal interaction with the flavin through water as observed in wild-type MAO A. Incubation of the oxygen-free enzyme sample with a tyramine substrate led to full reduction of the flavin coenzyme, which could be stably reached with both wild-type and the K305M mutant in a few minutes (Figure 2A). When aerobic conditions were restored by exposing the system to air, the wild-type enzyme was promptly reoxidized, whereas in the case of K305M the reappearance of the oxidized flavin peak was only gradually obtained and required more than 1 h to reach completion. In agreement with the steady-state kinetic parameters (Table 1), these results indicate that K305M can bind and oxidize the amine substrate like the wild-type enzyme, while it is heavily impaired in oxidized flavin regeneration by molecular oxygen.

Next, we asked if the K305M mutant could be reoxidized by electron acceptors alternative to molecular oxygen. Although MAOs are "true" oxidases, their active site might bind organic molecules that accept electrons and, in the case of the K305M mutant, may work more efficiently than oxygen. Among these, quinones are electrophilic compounds normally found in mitochondria and other organelles where they serve as acceptors in cellular electron transport chains. It was reported that some quinones and other redox compounds display binding affinity for MAO A.[19,20] We tested benzoquinone and coenzyme Q_0 for their ability to reoxidize the K305M mutant under anaerobiosis conditions (Figure 2B). The former is the

https://dx.doi.org/10.1021/acschembio.0c00366
ACS Chem. Biol. XXXX, XXX, XXX−XXX

basic unit of quinones, the latter is the reactive part of the naturally occurring coenzyme Q_{10} that is highly hydrophobic and therefore very difficult to experimentally handle in acqueous solutions. For this experiment, K305M MAO A was anaerobically photoreduced rather than incubated with substrate to avoid any direct electron transfer from the substrate to the electron acceptor or multiple turnovers. The addition of either benzoquinone or coenzyme Q_0 readily led to the full reappearance of the peak at 456 nm, indicating that these molecules can reoxidize the enzyme-bound FAD coenzyme. The same experiment was carried out also with the wild-type enzyme using benzoquinone (Supporting Information Figure 3) obtaining similar results. Benzoquinone and coenzyme Q_0 were also tested for their ability to restore the normal enzyme turnover under aerobic conditions using the assays described above, but no significant change in enzymatic activity of K305M was observed. This may be due to the fact that the mutant is endowed with a, though limited, reactivity with oxygen and that the large amount of substrate may hamper the accessibility of the alternative electron acceptor. These results outlined the K305M MAO A mutant as an oxygen-inert tool to be tested in a cellular model of cardiomyocytes where the bioavailability of quinone-based electron acceptors may restore an efficient enzyme regeneration.

We thereby generated two adenoviral constructs in order to overexpress wild-type (Ad WT) and K305M (Ad K305M) human MAO A in cardiomyoblasts. As shown in Figure 3A, MAO A protein levels were similarly increased in cells transduced with Ad WT or Ad K305M, compared to control untransduced cells (Ctr). Interestingly, MAO A activity, measured as the quantity of products formed by ^{14}C-5-HT degradation, was equally increased in Ad WT and Ad K305M-transduced cells compared to Ctr. Thus, K305M appears to have turnover activity similarly to wild-type when expressed in cells, which raised the question whether the mutant uses O_2 or an alternative electron acceptor in cells. We directly measured the concentration of H_2O_2 generated during the oxidation of tyramine. As shown in Figure 3B, tyramine addition led to H_2O_2 production in Ctr cells with a maximum at 60 min, corresponding to endogenous MAO A activation. Most interestingly, Ad WT transduction potentiated H_2O_2 production upon tyramine administration, which was instead not observed for Ad K305M. This demonstrates that K305M mutant is able to degrade MAO substrate without production of H_2O_2. Thus, we took advantage of this unique property to establish the contribution of ROS in the senescent response induced by MAO A.[8] To better establish the specific effects of wild-type and K305M MAO A in cardiomyoblasts, we blocked endogenous MAO A with the irreversible inhibitor clorgyline before performing adenoviral transduction and treatment with tyramine (Supporting Information Figure 4A). In cells transduced with Ad WT, but not K305M, tyramine application for 30 min significantly increased ROS production compared to Ctr (Supporting Information Figure 4). We next evaluated the chronic effect of MAO A stimulation over 3 days with tyramine on aging markers by measuring senescence-associated-βgal (SA-βgal), a β-galactosidase activity detectable at pH 6.0 in senescent cells. Interestingly, SA-βgal activity was increased only in cells expressing Ad WT but not K305M. Similarly, the senescence marker p21 accumulated in Ad WT cells but not in Ad K305M cells, while the retinoblastoma protein (Rb) was dephosphorylated only in tyramine-activated Ad WT cells, preventing the progression of the cell cycle (Figure 3D). Altogether, our results show that substituting Lys305 with Met in MAO A impairs the production of H_2O_2, preventing oxidative stress and senescence induced by a chronic activation of MAO A.

In conclusion, our work provided an insightful investigation on the role of the conserved lysine residue of flavin-dependent amine oxidases in enzyme turnover and on the effects of H_2O_2 generated by human MAO A in cardiac cell aging. We demonstrated that in human MAO A, the K305M mutant retains the capability to bind and oxidize the amine substrate, while it is significantly impaired in reoxidation by molecular O_2. Using this mutant as a mimic of an oxygen-inert enzyme in the context of cardiomyocyte cells, we gave further support to the hypothesis that, in the heart, MAO A represents a noteworthy source of ROS promoting cell senescence. From this perspective, pharmacological treatments targeting MAO A, so far limited to neurological diseases, may be extended to prevent heart failure in some frailty conditions of aged patients. Moreover, since many reports indicate that MAO A promotes prostate and glioblastoma tumorigenesis and metastasis, this approach may also limit cancer growth.[21]

■ ASSOCIATED CONTENT

Supporting Information

The Supporting Information is available free of charge at https://pubs.acs.org/doi/10.1021/acschembio.0c00366.

Details of the experimental methods, supporting Table 1, supporting Figures 1−4 (PDF)

■ AUTHOR INFORMATION

Corresponding Author

Claudia Binda − *Department of Biology and Biotechnology, University of Pavia, Milan, Italy;* orcid.org/0000-0003-2038-9845; Phone: (+39)0382-985527; Email: claudia.binda@unipv.it

Authors

Luca Giacinto Iacovino − *Department of Biology and Biotechnology, University of Pavia, Milan, Italy*

Nicola Manzella − *Institute of Metabolic and Cardiovascular Diseases (I2MC), Institut National de la Santé et de la Recherche Médicale (INSERM), Université de Toulouse, Toulouse, France*

Jessica Resta − *Institute of Metabolic and Cardiovascular Diseases (I2MC), Institut National de la Santé et de la Recherche Médicale (INSERM), Université de Toulouse, Toulouse, France*

Maria Antonietta Vanoni − *Department of Biosciences, University of Milan, Milan, Italy;* orcid.org/0000-0001-7213-732X

Laura Rotilio − *Department of Biology and Biotechnology, University of Pavia, Milan, Italy*

Leonardo Pisani − *Department of Pharmacy-Drug Sciences, University of Bari Aldo Moro, Bari, Italy;* orcid.org/0000-0002-4198-3897

Dale Edward Edmondson − *Department of Biochemistry, Emory University, Atlanta, Georgia, United States;* orcid.org/0000-0002-1304-231X

Angelo Parini − *Institute of Metabolic and Cardiovascular Diseases (I2MC), Institut National de la Santé et de la*

https://dx.doi.org/10.1021/acschembio.0c00366
ACS Chem. Biol. XXXX, XXX, XXX−XXX

Recherche Médicale (INSERM), Université de Toulouse, Toulouse, France

Andrea Mattevi − *Department of Biology and Biotechnology, University of Pavia, Milan, Italy;* orcid.org/0000-0002-9523-7128

Jeanne Mialet-Perez − *Institute of Metabolic and Cardiovascular Diseases (I2MC), Institut National de la Santé et de la Recherche Médicale (INSERM), Université de Toulouse, Toulouse, France*

Complete contact information is available at: https://pubs.acs.org/10.1021/acschembio.0c00366

Funding

This work was supported by Fondazione Cariplo (grant no. 2014-0672 to C.B.), Italian Ministry of Education, University and Research (MIUR, "Dipartimenti di Eccellenza Program 2018−2022 - Dept. of Biology and Biotechnology L. Spallanzani," University of Pavia), Agence Nationale pour la Recherche referenced as SIGNALAGE "ANR-19-CE14−00384−01," Fondation pour la Recherche Médicale (équipe FRM2016, DEQ20160334892), Région Occitanie, Fédération Française de Cardiologie (FFC), Associazione Italiana per la Ricerca sul Cancro (AIRC; IG19808 to A.M.).

Notes

The authors declare no competing financial interest.

■ ACKNOWLEDGMENTS

We are grateful to Fondazione Cariplo, MIUR, Agence Nationale pour la Recherche, Fondation pour la Recherche Médicale, Région Occitanie, Fédération Française de Cardiologie, and AIRC for supporting the project. We thank S. Nenci for the initial cloning experiments of the K305M mutant and B. Couderc (INSERM CRCT Toulouse) for supervising adenovirus construction.

■ REFERENCES

(1) Sies, H., Berndt, C., and Jones, D. P. (2017) Oxidative Stress. *Annu. Rev. Biochem. 86*, 715−748.

(2) Sies, H. (2014) Role of metabolic H_2O_2 generation: redox signaling and oxidative stress. *J. Biol. Chem. 289*, 8735−8741.

(3) Iacovino, L. G., Magnani, F., and Binda, C. (2018) The structure of monoamine oxidases: past, present, and future. *J. Neural. Transm. (Vienna) 125*, 1567−1579.

(4) Romero, E., Gómez Castellanos, J. R., Gadda, G., Fraaije, M. W., and Mattevi, A. (2018) Same Substrate, Many Reactions: Oxygen Activation in Flavoenzymes. *Chem. Rev. 118*, 1742−1769.

(5) Youdim, M. B., Edmondson, D. E., and Tipton, K. F. (2006) The therapeutic potential of monoamine oxidase inhibitors. *Nat. Rev. Neurosci. 7*, 295−309.

(6) Maurel, A., Hernandez, C., Kunduzova, O., Bompart, G., Cambon, C., Parini, A., and Francés, B. (2003) Age-dependent increase in hydrogen peroxide production by cardiac monoamine oxidase A in rats. *Am. J. Physiol. Heart Circ. Physiol. 284*, H1460−1467.

(7) Villeneuve, C., Guilbeau-Frugier, C., Sicard, P., Lairez, O., Ordener, C., Duparc, T., De Paulis, D., Couderc, B., Spreux-Varoquaux, O., Tortosa, F., Garnier, A., Knauf, C., Valet, P., Borchi, E., Nediani, C., Gharib, A., Ovize, M., Delisle, M. B., Parini, A., and Mialet-Perez, J. (2013) p53-PGC-1α pathway mediates oxidative mitochondrial damage and cardiomyocyte necrosis induced by monoamine oxidase-A upregulation: role in chronic left ventricular dysfunction in mice. *Antioxid. Redox Signaling 18*, 5−18.

(8) Manzella, N., Santin, Y., Maggiorani, D., Martini, H., Douin-Echinard, V., Passos, J. F., Lezoualc'h, F., Binda, C., Parini, A., and Mialet-Perez, J. (2018) Monoamine oxidase-A is a novel driver of stress-induced premature senescence through inhibition of parkin-mediated mitophagy. *Aging Cell 17*, No. e12811.

(9) McDonald, C. A., Fagan, R. L., Collard, F., Monnier, V. M., and Palfey, B. A. (2011) Oxygen reactivity in flavoenzymes: context matters. *J. Am. Chem. Soc. 133*, 16809−16811.

(10) Henderson Pozzi, M., and Fitzpatrick, P. F. (2010) A lysine conserved in the monoamine oxidase family is involved in oxidation of the reduced flavin in mouse polyamine oxidase. *Arch. Biochem. Biophys. 498*, 83−88.

(11) Zhao, G., Bruckner, R. C., and Jorns, M. S. (2008) Identification of the oxygen activation site in monomeric sarcosine oxidase: role of Lys265 in catalysis. *Biochemistry 47*, 9124−9135.

(12) Li, M., Hubálek, F., Newton-Vinson, P., and Edmondson, D. E. (2002) High-level expression of human liver monoamine oxidase A in *Pichia pastoris*: comparison with the enzyme expressed in Saccharomyces cerevisiae. *Protein Expression Purif. 24*, 152−162.

(13) Veitch, N. C. (2004) Horseradish peroxidase: a modern view of a classic enzyme. *Phytochemistry 65*, 249−59.

(14) Ramsay, R. R., and Albreht, A. (2018) Kinetics, mechanism, and inhibition of monoamine oxidase. *J. Neural. Transm. (Vienna) 125*, 1659−1683.

(15) Bissel, P., Bigley, M. C., Castagnoli, K., and Castagnoli, N., Jr. (2002) Synthesis and biological evaluation of MAO-A selective 1,4-disubstituted-1,2,3,6-tetrahydropyridinyl substrates. *Bioorg. Med. Chem. 10*, 3031−3041.

(16) Binda, C., Wang, J., Li, M., Hubalek, F., Mattevi, A., and Edmondson, D. E. (2008) Structural and mechanistic studies of arylalkylhydrazine inhibition of human monoamine oxidases A and B. *Biochemistry 47*, 5616−5625.

(17) Chaiyen, P., Fraaije, M. W., and Mattevi, A. (2012) The enigmatic reaction of flavins with oxygen. *Trends Biochem. Sci. 37*, 373−380.

(18) Arslan, B. K., and Edmondson, D. E. (2010) Expression of zebrafish (*Danio rerio*) monoamine oxidase (MAO) in *Pichia pastoris*: purification and comparison with human MAO A and MAO B. *Protein Expression Purif. 70*, 290−297.

(19) Ramsay, R. R., Dunford, C., and Gillman, P. K. (2007) Methylene blue and serotonin toxicity: inhibition of monoamine oxidase A (MAO A) confirms a theoretical prediction. *Br. J. Pharmacol. 152*, 946−951.

(20) Paudel, P., Seong, S. H., Shrestha, S., Jung, H. A., and Choi, J. S. (2019) In Vitro and in Silico Human Monoamine Oxidase Inhibitory Potential of Anthraquinones, Naphthopyrones, and Naphthalenic Lactones from Cassia obtusifolia Linn Seeds. *ACS Omega. 4*, 16139−16152.

(21) Shih, J. C. (2018) Monoamine oxidase isoenzymes: genes, functions and targets for behavior and cancer therapy. *J. Neural Transm (Vienna) 125*, 1553−1566.

https://dx.doi.org/10.1021/acschembio.0c00366
ACS Chem. Biol. XXXX, XXX, XXX−XXX

Supporting Information

Rational re-design of Monoamine Oxidase A into a dehydrogenase to probe ROS in cardiac ageing

Luca Giacinto Iacovino[†], Nicola Manzella[§], Jessica Resta[§], Maria Antonietta Vanoni[¶], Laura Rotilio[†], Leonardo Pisani[#], Dale Edward Edmondson[¥], Angelo Parini[§], Andrea Mattevi[†], Jeanne Mialet-Perez[§], Claudia Binda[†,*]

[†]Department of Biology and Biotechnology, University of Pavia, Milan, Italy
[§]Institute of Metabolic and Cardiovascular Diseases (I2MC), Institut National de la Santé et de la Recherche Médicale (INSERM), Université de Toulouse, Toulouse, France
[¶]Department of Biosciences, University of Milan, Milan, Italy
[#]Department of Pharmacy-Drug Sciences, University of Bari Aldo Moro, Bari, Italy
[¥]Department of Biochemistry, Emory University, Atlanta, GA, USA

* Corresponding author: Claudia Binda
E-mail: claudia.binda@unipv.it. Phone: (+39)0382-985527
ORCID: 0000-0003-2038-9845

Index

Methods

Reagents. MMTP (1-methyl-4-(1-methyl-1H-pyrrol-2-yl)-1,2,3,6-tetrahydropyridine) oxalate salt was synthetized as previously described by Jian Yu and Castagnoli.[1] All other reagents were purchased from Sigma-Aldrich except for detergents that were from Anatrace.

MAO A mutants expression and purification. A DNA fragment encoding the full-length human MAO A was inserted into a pPIC 3.5 vector (Invitrogen) and used as template for site-specific mutagenesis. The primers are listed in Supporting Table 1 and correct incorporation of the mutation was checked by outsource sequencing (Eurofins Genomics). The mutant MAO A plasmids were linearized with MssI and transformation in *Pichia pastoris* was carried out by electroporation using KM71 strain (Invitrogen). The His^+ transformants were selected on minimal media plates without histidine, followed by random selection of eight colonies for small-scale expression analysis. The transformants yielding the highest level of protein expression were chosen for scale-up coltures. MAO A wild type and mutants were purified as previously described with few modifications of the published protocols.[2] Briefly, 30 g cells were resuspended in 100 ml of breaking buffer (50 mM sodium phosphate pH 7.2, 5 % (w/v) glycerol, 1 mM PSMF, 30 µM DTT, 1 mM EDTA) with an equal volume of silica-zirconia beads (0.5 mm in diameter) and then disrupted in a Beadbeater (Hamilton Beach Blender 908). The cell lysate was separated from beads through filtration with a layer of Miracloth (Calbiochem) followed by low speed centrifugation (1500 x g for 10 minutes at 4°C). The supernatant was centrifuged at high speed (70000 x g for 40 minutes at 4°C) in order to separate the membrane fraction. The pellet was resuspended to a final concentration of 15 mg/ml in 50 mM sodium phosphate pH 7.8, 300 mM sodium chloride, 20 mM imidazole, 20 % (w/v) glycerol, 1 mM PMSF, 30 µM DTT. The protein concentration was determined using the Biuret method.[3] Fos-Choline-12 was added to a concentration of 1 % (w/v) and the mixture was stirred at 4°C in the dark for 1 hour. After centrifugation (70000 x g for 30 minutes) the extract was loaded onto a 5 ml HisTrap column (GE-Healthcare) equilibrated with the buffer used for the resuspension. After washing with 10 column volumes of the buffer, the enzyme was eluted with 50 mM sodium phosphate buffer pH 7.8, 300 mM sodium chloride, 300 mM imidazole, 20 % glycerol (w/v), 1 mM PMSF, 30 µM DTT. The enzyme fractions were pooled according to the ratio of the absorbance at 280 nm and 456 nm, and concentrated with Amicon Ultra 30K centrifugal filters (Millipore). The excess of imidazole was removed with a 5 ml HiTrap Desalting column (GE Healthcare) equilibrated with 50 mM sodium phosphate buffer pH 7.8, 300 mM sodium chloride, 20 % (w/v) glycerol. The purity of the protein was determined by SDS-PAGE analysis and inspection of the UV-Vis spectrum. The final concentration of the pure protein was obtained spectrophotometrically with a NanoDrop ND-1408

1000 (Thermo Fisher Scientific Inc.) from the absorbance of the enzyme-bound FAD coenzyme at 456 nm (ε_{456} = 12000 M^{-1} cm^{-1}).

Steady-state kinetic analyses. The enzymatic activity of all MAO A constructs was tested by spectrophotometric measurements in the presence of different concentrations of kynuramine and MMTP as substrates using a Cary 100 UV/Vis spectrophotometer. In each assay the initial velocity value (v_0) was calculated from the absorbance changes at selected wavelengths and the known extinction coefficients. All experiments were performed at 25 °C in 50 mM Hepes/NaOH pH 7.5 containing 0.25 % (v/v) reduced Triton X-100. The rate of MMTP oxidation was monitored spectrophotometrically at 420 nm (ε_{420} = 25000 M^{-1} cm^{-1}),[4] whereas kynuramine consumption was detected at 316 nm (ε_{316} = 12000 M^{-1} cm^{-1}) in the direct assay[5] or at 515 nm when using the horseradish peroxidase (HRP) coupled assay that monitors the production of hydrogen peroxide.[6] In the direct assays the reaction was started by adding the enzyme at a final concentration of 0.07 µM for MAO A wt and 1.8 µM for MAO A mutants. In the HRP-coupled assay, the assay mixture contained 0.1 mM 4-aminoantipyrine, 1 mM 3,5-dichloro-2-hydroxybenzenesulfonic acid, 0.35 µM HRP and varying concentrations of kynuramine. The reaction was started by adding the enzyme at a final concentration of 0.07 µM for MAO A wt and 10 µM for mutants. Data were fit to the Michaelis-Menten equation $v_0 = v_{max}[S]/(K_m + [S])$ with GraphPad 5.0 software that provides the parameter values and the associated errors.

Covalent inhibition analyses. Irreversible inhibition of MAO A wt and mutants was tested by UV-Vis spectral measurement (Supporting Figure 1) using an Agilent 8453 UV/Vis diode-array spectrophotometer. The experiments were performed in presence of 10 µM of enzyme with 10-fold molar excess of irreversible inhibitor. The buffer used was 50 mM potassium phosphate pH 7.8, 300 mM sodium chloride, 20 % (w/v) glycerol, 0.05 % (w/v) Fos-Choline-12 in 150 µL final volume at 25°C. The reaction was monitored at different times until no further modification was detected. The final spectra and time-course of absorbance changes observed with each inhibitor were plotted using GraphPad 5.0 software.

Anaerobiosis experiments. All UV/Vis spectra analyses were performed using an Agilent HP 8453 spectrophotometer with a home-made quartz cuvette equipped with side-arms and connected with a vacuum/nitrogen apparatus.[7] Anaerobic solutions of 10 µM enzyme in 50 mM potassium phosphate pH 7.8, 300 mM sodium chloride, 20 % (w/v) glycerol, 0.05 % (w/v) Fos-Choline-12 were prepared in the tonometer 1 mL cuvette by repeating 50 cycles of evacuation and equilibration with oxygen-

free nitrogen. The buffer was the same as that used for aerobic experiments. Tyramine was used as substrate in 100-fold molar excess with respect to enzyme, made anaerobic separately in the side arm of the tonometer and anaerobically added to the enzyme solution to start the reaction. The re-oxidation of the enzyme was carried out by opening the cuvette and mixing the solution in order to promote the re-solubilization of oxygen. The time-course of FAD reduction/oxidation was monitored at the maximum of absorption at 456 nm (ε_{456} = 12000 M^{-1} cm^{-1}). In photoreduction experiments 10 μM enzyme was in the 1 ml quartz cuvette of the tonomenter mixed in the presence of 1 μM of deazaflavin and 10 mM EDTA[8] whereas the electron acceptors (either 200 μM p-benzoquinone or 50 μM coenzyme Q_0) were placed into the side arm of the anaerobic apparatus, and the system was made anaerobic as previously described. The anaerobic cuvette was placed in a water bath and illuminated with a projector lamp. After each period of irradiation (0.5 – 2 minutes) the absorbance spectrum was recorded until no spectral changes were observed. Once the flavin was stably reduced, the selected electron acceptor was added to the reduced enzyme to monitor the re-oxidation by acquiring spectra at different times.

Generation of adenoviral constructs. Adenovirus were generated using the RapaCMV adenoviral expression system (Cell Biolabs) according to manufacturer's instructions. Briefly, cDNAs of WT or K305M human MAO A were excised from PCR8 plasmid and inserted into the shuttle vector exploiting the *BamH*I and *Not*I restriction sites. Adenovirus were amplified in HEK293 cells and purified by cesium chloride gradient.

Cell culture and treatments. Rat H9c2 cardiomyoblasts obtained from the American Type Culture Collection (Rockville, MD, U.S.A.) were grown in Dulbecco's Modified Eagle Medium (DMEM, Thermo Fisher) containing 10% heat-inactivated fetal bovine serum (FBS) under 5% CO_2 at 37°C.

MAO A activity. Frozen pellets of H9C2 cells were homogenized in 50 mM sodium phosphate pH 7.5, supplemented with protease inhibitors and sonicated. Crude extracts (40 μg) were incubated at 37°C for 30 min, in the presence of 400 μM of [^{14}C]-serotonin. To define non specific activities, MAO A inhibitor clorgyline was used (0.1 μM). The reaction was stopped by the addition of 0.1 ml of HCl 4N at 4°C. The reaction product was extracted (efficiency 92%) with 1 mL of ethyl acetate/toluene (v/v), and the radioactivity contained in the organic phase was counted by liquid scintillation.

Western blot. H9C2 cells were lysed in 0.150 ml RIPA buffer (20 mM Tris-HCl pH 7.5, 150 mM NaCl, 1 mM EDTA, 1% (v/v) NP40, 0.1% (v/v) SDS, antiphosphates and antiproteases). Following centrifugation at 13,000 g for 5 min, the supernatant was collected and equal amount of proteins were subjected to SDS-PAGE electrophoresis and transferred to a nitrocellulose membrane (Trans-blot turbo transfer system, Bio-Rad). Primary antibody incubations were performed overnight with 1:1000 dilutions for anti-MAO A, anti-phospho-Rb (Cell Signaling) and anti-p21 (Santa Cruz Biotechnology) IgG followed by incubation with secondary antibodies for 1 h at room temperature (1:5000 dilutions). ECL (Life sciences) was used for detection and images were recorded with the BioRad ChemiDoc MP, Imaging System. Relative densities were quantified using Image-Lab 4.0 software (Bio-Rad).

ROS production. Extracellular H_2O_2 detection was evaluated with Amplex-Red probe (Invitrogen, Molecular Probes). Briefly, cells were seaded in 96-wells, treated with tyramine (500 µM) and the supernatant collected and mixed with a Amplex red assay solution for 30 min. Total cellular ROS were measured using the fluorescent probe DCFDA assay at a concentration of 5 µM (Thermo Fisher Scientific).

SA-βgal staining. SA-βGal activity was measured as previously described.[9] Briefly, cells were fixed with paraformaldehyde for 10 minutes, washed with PBS buffer (137 mM NaCl, 2.7 mM KCl, 8 mM Na_2HPO_4, and 2 mM KH_2PO_4), and stained with SA-β-Gal stain solution (1 mg/ml X-gal dissolved in DMSO, 40 mM citric acid/sodium phosphate buffer pH 6.0, 5 mM potassium ferrocyanide, 5 mM potassium ferricyanide, 150 mM NaCl, 2mM $MgCl_2$). After 16 hours, images were taken using a bright-fieldmicroscope.

Statistical analysis. Statistical analysis of significance was calculated using t-Student test, 1-way or 2-way ANOVA when appropriate using GraphPad Prism 6 (GraphPad Software, La Jolla, CA, USA). The results were shown as the means ± SEM. Values of p= 0.05, 0.01, and 0.001 were considered as statistically significant.

Supporting Table 1. Primers utilized for recombinant human MAO A mutagenesis

K305M	TCATTATGTGCATGATGTATTACAAG
K305S	AGCTGTCATTTCTTGCATGATGTATTACAAG
K305Q	GCTGTCATTCAATGCATGATGTATTACAAG
K305R	AGCTGTCATTCGCTGCATGATGTATTACAA

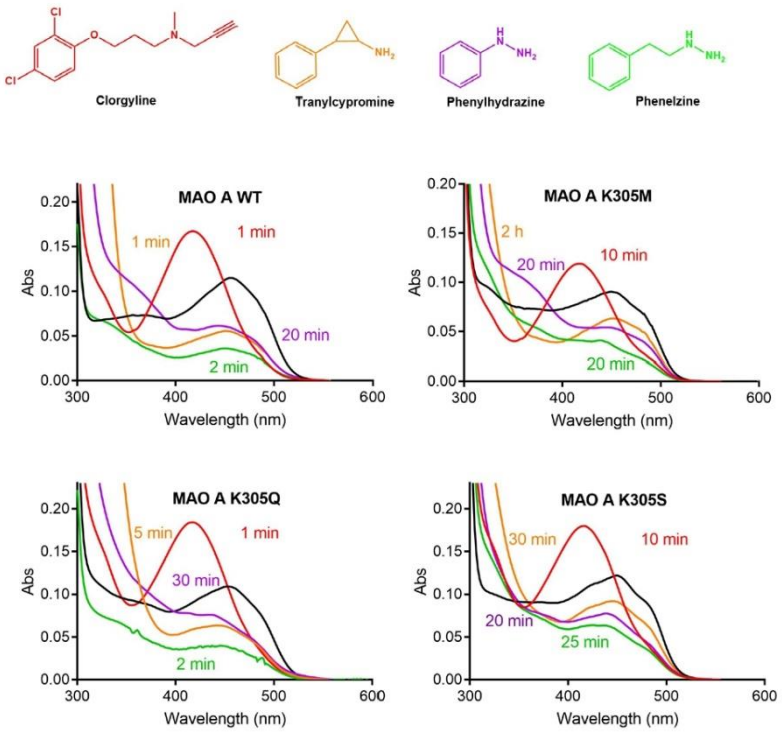

Supporting Figure 1. UV-Vis spectra of human MAO A (wild type enzyme and active mutants) during the time-dependent inactivation by covalent inhibitors. The absorption spectrum of the oxidized protein (prior to inhibitor additon) is in black, whereas the red, green, orange and purple traces indicate the enzyme inactivated by clorgyline, phenelzine, tranylcypromine and phenylhydrazine, respectively. Time required to reach the final spectrum is also specified (1 minute is the minimum recorded time after addition of the inhibitor to the enzyme solution, i.e. it may imply an even faster inactivation process). K305R MAO A does not react with any covalent inhibitor (data not shown).

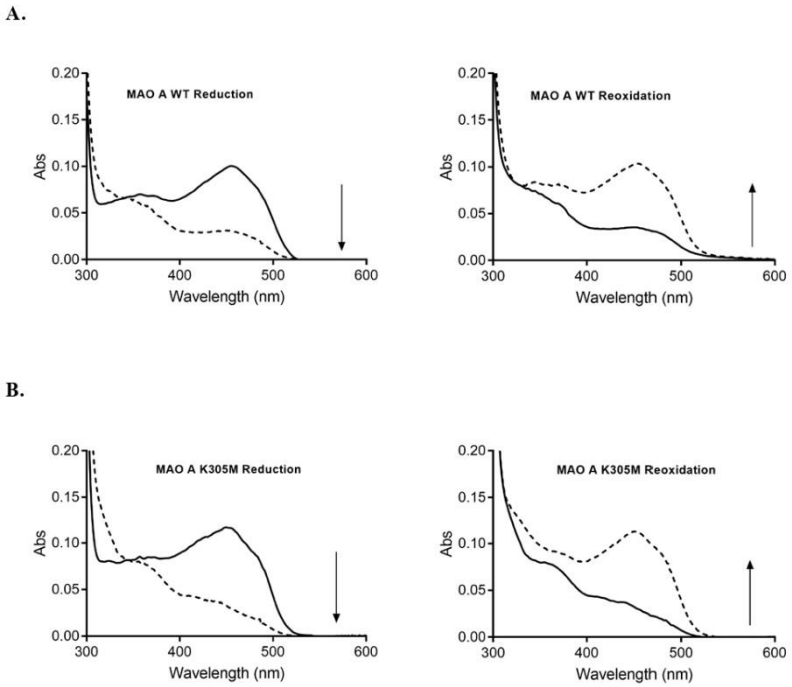

Supporting Figure 2. UV-vis spectra of wild type (A) and K305M (B) MAO A flavin reduction under anaerobiosis and reoxidation by molecular oxygen. In all panels the initial and final spectra are represented by continuous and dashed lines, respectively. The arrow indicates the bleaching of the flavin absorption peak centered at 456 nm in the reductive half-reaction and the reappearance of the peak during the oxidative half-reaction.

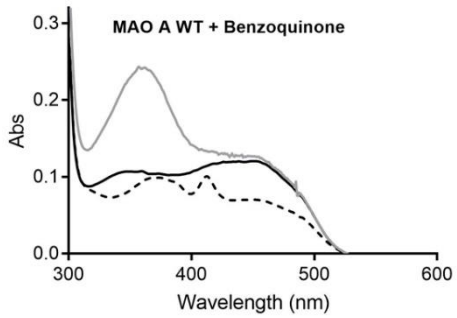

Supporting Figure 3. Spectrophotometric measurements of wild type MAO A flavin reoxidation by benzoquinone as alternative electron acceptor. UV-Vis spectra of the oxidized (initial), photoreduced and reoxidized MAO A are depicted as continuous black, dashed black and gray lines, respectively.

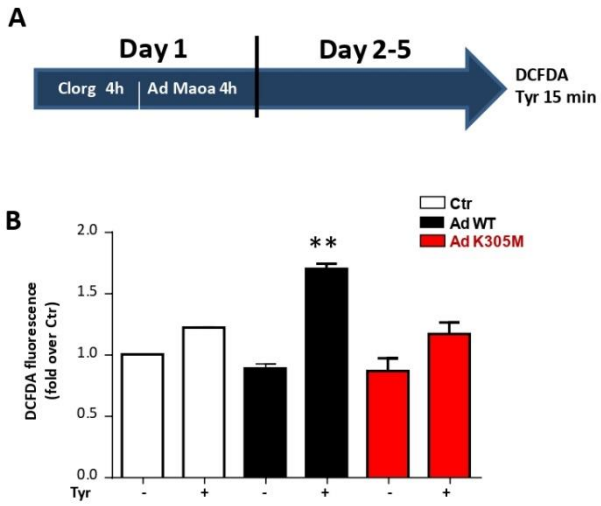

Supporting Figure 4. Total cellular ROS were measured with the DCFDA probe in H9C2 cells transduced with WT or K305M mutant. (A) Cells were preincubated for 4 h with clorgyline to block endogenous MAO A activity, before performing adenoviral transduction. (B) 72 h post-transduction, fluorescence of DCFDA was measured in the presence of 500 µM tyramine (Tyr in the figure) for 30 min. Data are expressed as means ± sem.

References

1. Yu, J., and Castagnoli, N. (1999) Synthesis and MAO-B Substrate Properties of 1-Methyl-4-heteroaryl-1,2,3,6-tetrahydropyridines. *Bioorganic & Medicinal Chemistry 7,* 231-239.

2. Li, M., Hubálek, F., Newton-Vinson, P., and Edmondson D. (2002) High-Level Expression of Human Liver Monoamine Oxidase A in Pichia pastoris: Comparison with the Enzyme Expressed in Saccharomyces cerevisiae. *Protein Expression and Purification. 24,* 152-162.

3. Layne, E. (1957) Spectrophotometric and turbidimetric methods for measuring proteins. *Methods in Enzymology 3*, 447-454.

4. Bissel, P., Bigley, M., Castagnoli, K., and Castagnoli, Jr. N. (2002) Synthesis and Biological Evaluation of MAO-A Selective 1,4-Disubstituted-1,2,3,6-tetrahydropyridinyl Substrates. *Bioorganic & Medicinal Chemistry 10,* 3031-3041.

5. Weissbach, H., Smith, T.E., Daly, J.W., Witkop, B., Udenfriend, S. (1960) A rapid spectrophotometric assay of mono-amine oxidase based on the rate of disappearance of kynuramine. *J. Biol. Chem. 235,* 1160-1163.

6. Vojinović, V., Azevedo A.M., Martins, V.C.B., Cabral, J., Gibson, T.D., and Fonseca, L.P. (2004) Assay of H_2O_2 by HRP catalysed co-oxidation of phenol-4-sulphonic acid and 4-aminoantipyrine: characterisation and optimisation. *Journal of Molecular Catalysis B: Enzymatic 28,* 129-135.

7. Williams, C.H. Jr., Arscott, L.D., Matthews, R.G., Thorpe, C., and Wilkinson, K.D. (1979) Methodology employed for anaerobic spectrophotometric titrations and for computer-assisted data analysis. *Methods Enzymol. 62,* 185-198.

8. Massey, V., and Hemmerich, P. (1978) Photoreduction of flavoproteins and other biological compounds catalyzed by deazaflavins. Biochemistry 17, 9-16.

9. Manzella, N., Santin, Y., Maggiorani, D., Martini, H., Douin-Echinard, V., Passos, J.F., Lezoualc'h, F., Binda, C., Parini, A., and Mialet-Perez, J. (2018) Monoamine oxidase-A is a novel driver of stress-induced premature senescence through inhibition of parkin-mediated mitophagy. *Aging Ce*ll 17, e12811.

1.3 STEREOSELECTIVE INHIBITION OF MAO-A AND MAO-B BY 1-PROPARGYL-4-STYRYLPIPERIDINE ANALOGUES

Monoamine Oxidase B inhibitors represent an established pharmaceutical treatment for neurological diseases such as Parkinson's disease. Given the high structural similarity among the two MAOs isoforms, a lot of effort has been made to develop new specific MAO-B inhibitors. To this aim, Prof. Stanislav Gobec and his team at the University of Lubijana synthetized and screened a wide library of irreversible inhibitors based on the scaffold of 1-propargyl-4-styrylpiperidines with different affinities between MAO-A and MAO-B. Compound 1 (Fig. 8A) was identified as a potent and selective MAO-B inhibitor (IC_{50} = 0.34 μM) with very low affinity for MAO-A (IC_{50} = 100 μM). These ligands incorporate a propargyl-amine function prone to generate an irreversible adduct with the N5 atom of the flavin ring (Fig. 8A) (Binda, Hubálek et al. 2004) which can be detected spectrophotometrically. After incubation with compound 1, the typical FAD absorbance spectrum characterized by a double peak at 370 nm and 456 nm is modified into a single peak at 415 nm (Fig. 8B). IC_{50} determination of the hit compound 1 and the respective analogues (as well as the measurement of K_i values performed during my PhD as described in the next pages) was carried out on both MAO-A and MAO-B using the HRP coupled assay (Fig. 6).

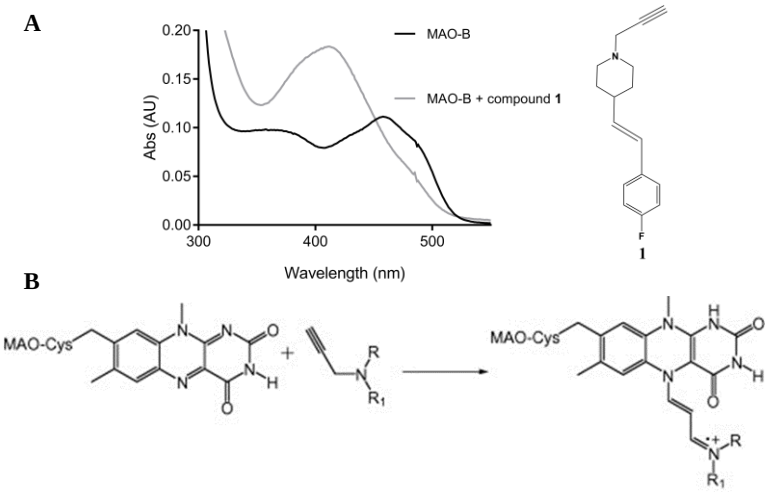

Figure 8. (A) Chemical structure of compound 1 and UV-vis spectra of MAO-B flavin before (black line) and after (grey line) incubation with compound 1. (adapted from Knez, Colettis, Iacovino et al. 2020) (B) General reaction scheme of propargyl-amines with FAD leading to the covalent adduct to the N(5) atom of the flavin ring.

The most important structure activity relationships (SAR) of the screening campaign performed by Prof. Gobec's group are summarized in Figure 9.

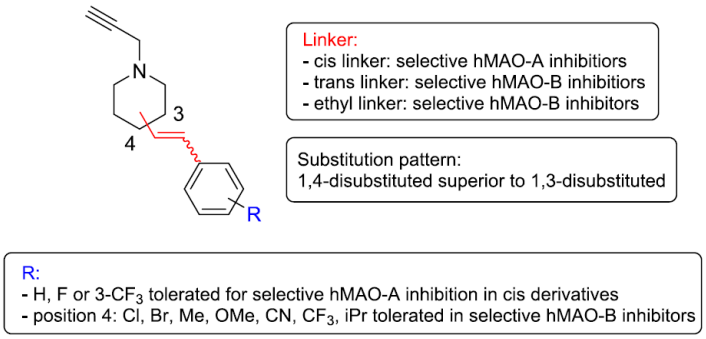

Figure 9. Structure activity relationships of the stilbene-like scaffold MAOs inhibitors (adapted from Knez, Colettis, Iacovino et al. 2020).

While the cis double bond isomers are potent MAO-A inhibitors, the trans analogues selectively target only MAO-B. This arises from the differences of active site size and shape, and the different amino acid residues involved for the ligand stabilization. In particular, 1,4 disubstituted piperidines with the double bond in trans conformation resulted 5-fold more potent than 1,3 disubstituted piperidines and MAO-B selective. Remarkably, the reduction of the trans double bond into the ethyl linker does not affect the selectivity of the target. The presence of either halogen atoms or small aliphatic chain on the phenyl ring position 4 increased further the MAO-B inhibition. On the other hand, the 1,4 disubstituted piperidines with the double bond in cis conformation are potent and selective MAO-A inhibitors. The presence of H, F or CF3 substituents on the phenyl ring in position 4 is tolerated for MAO-A selectivity.

In the framework of this project, our laboratory was involved to investigate in more detail the inhibition properties of the most promising compounds identified from this screening. We performed the structural and biochemical characterization of this new class of MAO inhibitors, which was published in the article "Stereoselective Activity of 1-Propargyl-4-styrylpiperidine-like Analogues That Can Discriminate between Monoamine Oxidase Isoforms A and B" in Journal of Medicinal Chemistry attached at the end of this section.

First, steady-state experiments in presence of benzylamine (MAO-B) and kynuramine (MAO-A). Compound 1 (Fig. 10A), 84 (Fig. 10B) and 97 (Fig. 10C) showed selectivity against MAO-B with inhibition constant (K_i) of 1.92 μM, 1.25 μM and 1.36 μM,

respectively. MAO-A inhibitors analysis was limited to the compound 69 with comparable activity to clorgyline (K_i = 0.23 μM), irreversible MAO-A selective inhibitor (De Colibus, Li et al. 2005) (Fig. 10D). To investigate the binding mode of these compounds, crystallization experiments were carried out with compounds 1, 84 and 97 according to previous protocols (Binda, Hubálek et al. 2004). The crystallographic analysis allowed to inspect in detail the SARs of stilbene-like scaffold MAO-B inhibitors and increase the inhibitor potency stabilizing protein-ligand interactions. As reported in Figure 10 A-C, the electron density map clearly shows that the compound 1, 84 and 97 are bound into the active site of the enzyme supporting the competitive inhibition mechanism provided by steady state experiments. Moreover, the electron density highlighted the covalent adduct with the N5 atom of the flavin ring. The trans double bond of compound 1 and 84 perfectly fits the flat and elongated cavity of MAO-B, whereas the ethyl linker in 97 determines a more folded conformation of the inhibitor, though orienting the compound similarly to the other inhibitors. The hydrophobic pocket designed by Ile316, Leu164, Phe103, Trp119, is able to host halogen atoms (compound 1, 84) and small aliphatic chains (compound 97) bound to the position 4 of the phenyl ring. The presence of these small hydrophobic substituents further increases the inhibition effect on MAO-B. The selective inhibition of these compounds was tested *ex-vivo* in mouse brain homogenates whereas the therapeutical potential of 1-propargyl-4-styrylpiperidines was evaluated with additional *in vivo* experiments in mice. The biological analysis was carried out by prof. Mariel Marder of the University of Buenos Aires and her team.

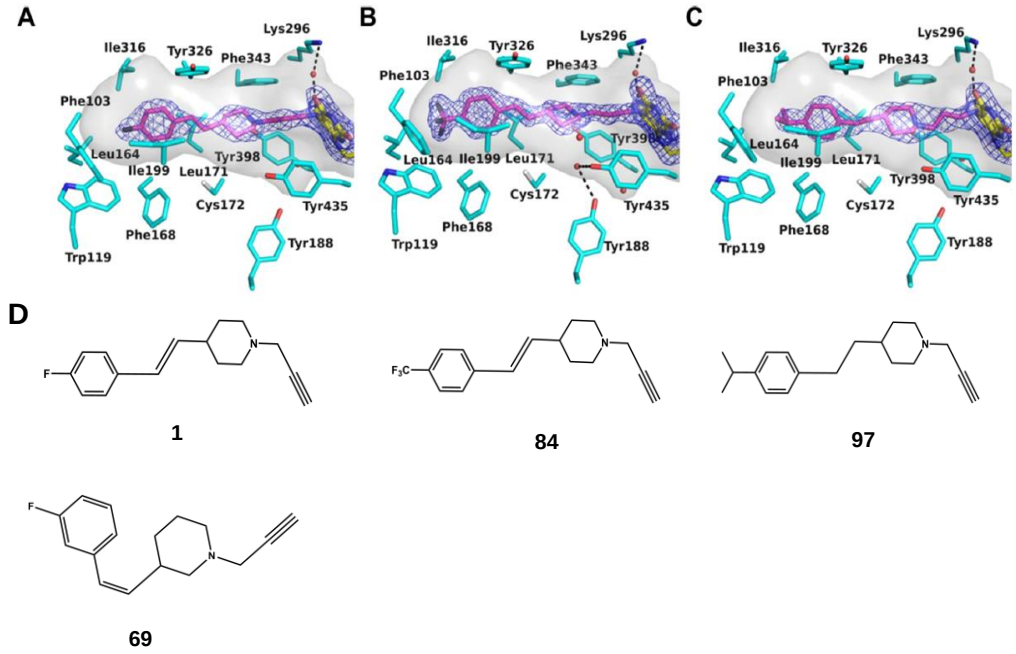

Figure 10. Crystal structures of the active site of hMAO-B-inhibitor complexes. The hMAO-B active site cavity is shown as a gray surface, whereas the protein residues are depicted in cyan. Water molecules are red spheres whereas hydrogen bonds are represented with dashed lines. The FAD cofactor is drawn as yellow sticks. The inhibitor molecule bound in the hMAO-B active site cavity is shown as sticks, with carbon, nitrogen, and fluorine in magenta, blue, and black, respectively. The refined 2Fo − Fc electron density map is shown in blue mesh for the inhibitor and the FAD molecules. (A) Active site of hMAO-B in complex with 1 (2.3 Å). (B) Active site of hMAOB in complex with 84 (1.7 Å). (C) Active site of hMAO-B in complex with 97 (2.3 Å). (D) Chemical structure of compound 1, 84, 97 and 69 (adapted from Knez, Colettis, Iacovino et al. 2020).

In summary, we gave the first characterization of these 1-propargyl-4-styrylpiperidines as potential scaffold in the design of pharmaceutical compounds that can be used to selectively target MAOs. Several examples of stereoselective activity with optical isomers are present in literature (Kasprzyk-Hordern 2010, Brooks, Guida et al. 2011). Remarkably, this studio represented a very peculiar case where it was possible to discriminate among two enzyme isoforms based on the cis/trans stereoselective activity of this series of inhibitors.

Journal of Medicinal Chemistry

pubs.acs.org/jmc Article

Stereoselective Activity of 1-Propargyl-4-styrylpiperidine-like Analogues That Can Discriminate between Monoamine Oxidase Isoforms A and B

Damijan Knez,[#] Natalia Colettis,[#] Luca G. Iacovino,[#] Matej Sova, Anja Pišlar, Janez Konc, Samo Lešnik, Josefina Higgs, Fabiola Kamecki, Irene Mangialavori, Ana Dolšak, Simon Žakelj, Jurij Trontelj, Janko Kos, Claudia Binda,* Mariel Marder,* and Stanislav Gobec*

Cite This: https://dx.doi.org/10.1021/acs.jmedchem.9b01886 Read Online

ACCESS | Metrics & More | Article Recommendations | Supporting Information

ABSTRACT: The resurgence of interest in monoamine oxidases (MAOs) has been fueled by recent correlations of this enzymatic activity with cardiovascular, neurological, and oncological disorders. This has promoted increased research into selective MAO-A and MAO-B inhibitors. Here, we shed light on how selective inhibition of MAO-A and MAO-B can be achieved by geometric isomers of *cis*- and *trans*-1-propargyl-4-styrylpiperidines. While the *cis* isomers are potent human MAO-A inhibitors, the *trans* analogues selectively target only the MAO-B isoform. The inhibition was studied by kinetic analysis, UV−vis spectrum measurements, and X-ray crystallography. The selective inhibition of the MAO-A and MAO-B isoforms was confirmed *ex vivo* in mouse brain homogenates, and additional *in vivo* studies in mice show the therapeutic potential of 1-propargyl-4-styrylpiperidines for central nervous system disorders. This study represents a unique case of stereoselective activity of *cis*/*trans* isomers that can discriminate between structurally related enzyme isoforms.

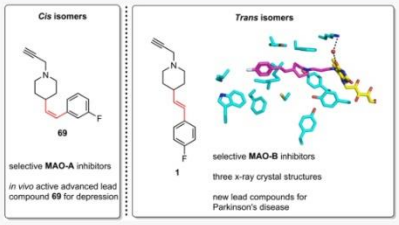

INTRODUCTION

Specific interaction patterns and molecular geometry are critical factors that influence ligand binding affinity and ligand selectivity toward a target.[1] Numerous examples of "chiral switching" in drug development have highlighted the effects of spatial geometry on not only pharmacodynamics but also pharmacokinetics and toxicology of drugs.[2,3] In addition to optical isomers, *cis* and *trans* isomers can have different pharmacological activities, as demonstrated by the well-known cases of cisplatin,[4] tamoxifen,[5] and combretastatin A4 (CA-4).[6] This last includes a stilbene motif in the *cis* conformation (Figure 1A), which efficiently binds to the colchicine binding site of tubulin and acts as a microtubule-destabilizing agent.[6] The binding of *trans*-combretastatin A4 (*trans*-CA-4, Figure 1A) to this site is thermodynamically less stable than that of *cis*-combretastatin A4 (*cis*-CA-4), and consequently the *trans* conformation does not prevent microtubule assembly.[6] However, examples of stereoselective activities of *cis*/*trans* isomers are rare in comparison with optical isomers.

Human monoamine oxidase A (hMAO-A) and human monoamine oxidase B (hMAO-B) are flavoenzymes that are encoded by separate genes on the X chromosome, and they share 70% sequence identity.[7] They are differentiated by their substrate specificities and inhibitor sensitivities. This arises from the differences in the active site size and shape, and the altered amino acid residues between these isoforms. The hMAO-A and hMAO-B active sites are hydrophobic cavities with volumes of about 550 Å^3 and 700 Å^3, respectively.[8] The active site of hMAO-B is flat and elongated, with a bipartite configuration, where Ile199 and Tyr326 are the gating residues that determine the shape of the cavity and the specificity of substrate/inhibitor binding.[9] hMAO-A has a monopartite and more spherical active site, with Ile335 and Phe208 as the gating residues. MAOs catalyze the oxidative deamination of primary and some secondary amines, and they are responsible for neurotransmitter metabolism in peripheral tissues and in the central nervous system.[10] This reaction produces an imino intermediate, which is spontaneously hydrolyzed to the corresponding aldehyde, with ammonia and hydrogen peroxide as side-products.[11] Reduced levels of neurotransmitters, increased activity and levels of MAOs, and the production of

Received: November 14, 2019
Published: January 9, 2020

https://dx.doi.org/10.1021/acs.jmedchem.9b01886
J. Med. Chem. XXXX, XXX, XXX−XXX

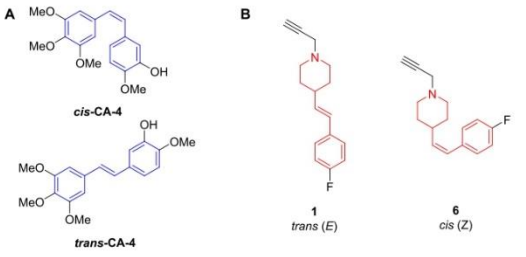

C

Compound	IC_{50} (hMAO-A)[a] [μM]	IC_{50} (hMAO-B)[a] [μM]	Selectivity Ratio[b]
1 (*trans*)	> 100	0.3422 ±0.0224	>292
6 (*cis*)	0.7261 ±0.0269	6.2215 ±0.7268	0.12

Figure 1. Stilbene derivatives and MAO inhibitory potencies. Chemical structures of *cis*/*trans*-combretastatin A4 (CA-4) (A) and hit inhibitor **1** (B) and *cis* isomer **6** (B). The stilbene core is blue, and the stilbene-like moiety of inhibitor **1** is red. (C) [a]IC_{50} values are mean ± SEM values (n = 2, 3). [b]Selectivity ratio is defined as IC_{50}(hMAO-A)/IC_{50}(hMAO-B).

Scheme 1. Resynthesis of Hit Inhibitor 1[a]

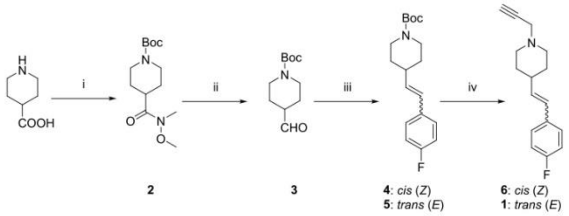

[a]Reagents and conditions: (i) 1) Boc_2O, 1.0 M NaOH, 1,4-dioxane, 0 °C, rt, 1 h (91%); 2) *N*,*O*-dimethyhydroxylamine hydrochloride, Et_3N, TBTU, CH_2Cl_2, 0 °C to rt, overnight (76%); (ii) $LiAlH_4$, anh THF, 0 °C, 1 h (crude product, 83%); (iii) (4-fluorobenzyl)triphenylphosphonium bromide, sodium bis(trimethylsilyl)amide (NaHMDS, 2 N in THF), anh THF, Ar(g), rt, overnight (52%); (iv) (1) 4.0 M HCl in 1,4-dioxane, 80 °C, 2 h (100%); (2) propargyl bromide (80% solution in toluene), Cs_2CO_3, DMF, Ar(g), 0 °C, rt, overnight (yield, **1**, 26%; **6**, 72%).

toxic metabolites are linked with various neurological,[12,13] psychological,[14] and cardiovascular disorders[15] and cancers.[16]

MAO-A inhibitors have been widely used for several decades in the therapy of depression and affective disorders.[17] On the other hand, selective MAO-B inhibitors are used as monotherapies in the early stages of Parkinson's disease and as add-on therapy to levodopa in advanced forms of Parkinson's disease.[18] MAO-A and MAO-B are recognized as validated targets. In terms of their contribution to increased cellular oxidative stress,[19] novel inhibitors are emerging as important disease-modifying therapeutic agents in such devastating neurodegenerative diseases as Alzheimer's disease and a number of others.[20]

To the best of our knowledge, *cis*/*trans* isomerisms of double bonds have never been used to achieve stereoselective inhibition of MAO isoforms. Here, we demonstrate a unique case study whereby configuration of the double bond in stilbene-like derivatives can define the selectivity for either MAO-A or MAO-B. We identify 1-propargyl-4-((*E*)-styryl)-piperidines as potent, selective, and irreversible hMAO-B inhibitors. *Cis* analogues with small substituents on the phenyl ring selectively inhibit hMAO-A. These inhibitors were evaluated for their MAO inhibitory activities and pharmacological properties.

RESULTS

Identification, Design, Synthesis, and Selectivity Profile of Potent and Selective hMAO-A and hMAO-B Inhibitors. Compound **1** (Figure 1B) contains a stilbene-like motif, and it was identified as a hit inhibitor in an in-house library screening campaign. Indeed, compound **1** is a potent selective hMAO-B inhibitor, with no significant inhibition of hMAO-A at 100 μM (Figure 1C).

This hit inhibitor was resynthesised using an efficient and straightforward synthesis (Scheme 1) that started from readily available isonipecotic acid, which was transformed into Weinreb's amide **2** and subsequently reduced to obtain aldehyde **3**. The aldehyde then underwent the Wittig reaction with phosphonium ylide to yield a mixture of *cis* (**4**) and *trans* (**5**) Boc-protected piperidines, which were separated using

https://dx.doi.org/10.1021/acs.jmedchem.9b01886
J. Med. Chem. XXXX, XXX, XXX−XXX

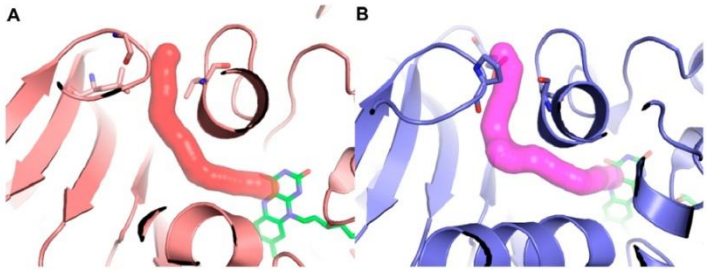

Figure 2. Active sites of hMAO-A (PDB code 2Z5X) and hMAO-B (PDB code 6FVZ). (A) MAO-A; FAD cofactor (green sticks); active site (red surface) spans from FAD to the entrance; bottleneck residues Leu97, Gly110, and Val210 at the entrance (salmon sticks). (B) MAO-B; FAD cofactor (green sticks); active site (violet surface) spans from FAD to the entrance; bottleneck residues Glu84, Pro102, and Ser200 at the entrance (purple sticks).

column chromatography. Following acidolysis, the corresponding secondary amine was reacted with propargyl bromide to obtain hit compound **1** and the *cis* isomer **6**. Compound **6** showed preferential inhibition of hMAO-A over hMAO-B (Figure 1C).

The selectivity profile was explained through analysis of the binding cavity using the Caver tool.[21] Human (h)MAO-A (Figure 2A) has a wide cavity at the active site near the FAD cofactor (r = 2.1 Å), which is lined with Tyr407, Phe352, and Gly215. In the direction toward the entrance, the cavity widens ($r \simeq$ 2.5 Å) and remains wide to Val210, Gln215, and Ile335, and then it narrows to Val210, Cys323, and Ile335 (r = 1.9 Å) and remains narrow to the entrance, which is also the narrowest part of the active site (r = 1.9 Å) and is composed of Leu97, Gly110, and Val210. In hMAO-B (Figure 2B), the entrance is even wider in the active site near the FAD cofactor (r = 2.3 Å), with Gln206, Tyr398, and Tyr435, but then narrows in the direction of the entrance (r = 1.9 Å) at Leu171 and Ile199 and then widens again (r = 2.5 Å) to Ile199, Ile316, and Tyr326. The narrowest part is at the entrance (r = 1.6 Å), and it is composed of Glu84, Pro102, and Ser200. The hMAO-A active site entrance is thus significantly wider (r = 1.9 Å) than the hMAO-B active site entrance (r = 1.6 Å). Both entrances are also the bottlenecks, which indicates that the active site of hMAO-B might be more difficult to reach by wider ligands.

The active site of hMAO-B is also significantly more curved than the active site of hMAO-A, with a bend of 90°, while in hMAO-A, the cavity bends at an angle of ∼60° (compare Figure 2A,B). The narrow entrance of hMAO-B and the higher curvature might prevent the relatively wider *cis* isomer **6** from entering the hMAO-B binding site. Indeed, **6** has a maximum width of 4.1 Å when measured as the height of the triangle composed of the fluorine atom, one of the sp^2 carbons, and the carbon bonded to the nitrogen, while the maximum width of the *trans* isomer **1** is only 2.5 Å when measured as the distance between two opposing carbon atoms in the piperidine ring. The *cis* isomer thus appears to inhibit hMAO-A but not hMAO-B because it is too wide to enter the narrower hMAO-B entrance. Its maximum width is only slightly greater than the 3.8 Å diameter of the hMAO-A entrance, while it is significantly greater than the 3.2 Å diameter of the hMAO-B entrance, which suggests that the hMAO-B entrance would need to undergo more substantial conformational changes to accommodate the *cis* isomer **6**. The active site loop in hMAO-A contains Gly (i.e., Gly110), which is replaced by Pro102 in hMAO-B. This produces much higher rigidity in comparison to hMAO-A, where the active site loop is more flexible. This lack of flexibility of hMAO-B adds to the restricted access of the *cis* isomer to the hMAO-B active site. The *cis* isomer **6** inactivity against hMAO-B thus appears to be caused by steric hindrance in the active site, compound **6** being unable to fit into the elongated and rigid cavity (Figure 2).

However, the selectivity of the *trans* isomer **1** is not explained only by the analysis of its access to the active site, as *trans* isomer **1** can bind to both hMAO-A and hMAO-B. To simulate the transport process of the inhibitor from the active site to the surface of the protein, these two isomers were undocked from hMAO-A and hMAO-B using the CaverDock software.[22] Starting from the docked conformations of both ligands at the active sites, the energetically most favorable trajectories of the ligands to the protein surfaces were investigated (Figure 3). In hMAO-A, *cis* isomer **6** is oriented with the propargyl group facing the FAD cofactor, with a binding energy of −8.3 kcal/mol (Figure 3A, movie file jm9b01886_si_002.mp4 in Supporting Information). As *cis* isomer **6** moves toward the entrance, its energy peaks at 0.4 kcal/mol and then falls to −3.8 kcal/mol at the entrance (Figure 3B). *Trans* isomer **1** in the correct orientation has a binding energy of −6.2 kcal/mol (Figure 3C), which is higher than for **6**. As the *trans* isomer is undocked, its binding energy peaks at −3.4 kcal/mol and then falls to −4.1 kcal/mol at the entrance (Figure 3D). Further, the *trans* ligand in the "wrong" orientation in the active site (i.e., with the fluorophenyl group facing the FAD cofactor) has a much lower energy of −10.1 kcal/mol (Figure 3D; lower-bounds energy curve). However, in this orientation, the *trans* ligand cannot form the covalent bond with FAD. Thus, in agreement with the experimental findings, the computational undocking simulation of hMAO-A showed that *cis* isomer **6** has lower binding energy at the active site than *trans* isomer **1**, which indicates that the *cis* isomer is more likely to bind to hMAO-A than the *trans* isomer. In addition, the *trans* isomer might preferentially access the active site in an orientation that does not allow formation of the covalent bond, as can be seen by the lower binding energy of the "wrong" conformation compared to the energy of the

https://dx.doi.org/10.1021/acs.jmedchem.9b01886
J. Med. Chem. XXXX, XXX, XXX−XXX

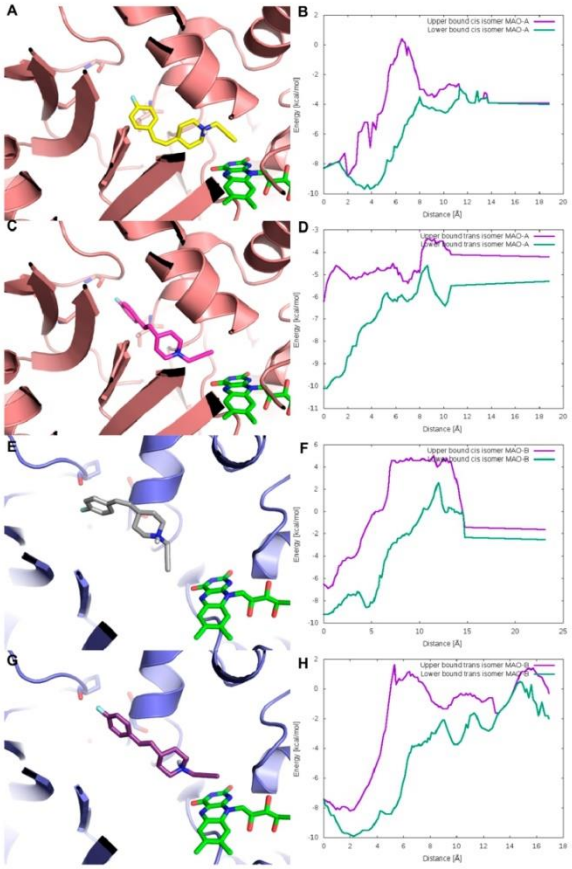

Figure 3. Undocking of *trans* (**1**) and *cis* (**6**) isomers in hMAO-A and hMAO-B. (A) Docked **6** in hMAO-A: *cis* isomer (yellow sticks) with propargyl group facing the FAD cofactor (green sticks), with binding energy of −8.3 kcal/mol; bottleneck residues at the active site entrance at the back (salmon sticks). (B) Energy profile for undocking of **6** from active site of hMAO-A in the correct conformation (propargyl facing FAD). (C) Docked **1** in hMAO-A: *trans* isomer (violet sticks) with propargyl group facing the FAD cofactor (green sticks), with binding energy of −6.2 kcal/mol; bottleneck residues at active site entrance at the back (salmon sticks). (D) Energy profile for undocking of **1** from active site of hMAO-A. (E) Docked **6** in hMAO-B: *cis* isomer (gray sticks) with propargyl group facing FAD cofactor (green sticks), with binding energy of −6.5 kcal/mol; bottleneck residues at entrance at the back (violet sticks). (F) Energy profile for undocking of **6** from active site of hMAO-B. (G) Docked **1** in hMAO-B: *trans* isomer (purple sticks) with propargyl group facing FAD cofactor (green sticks), with binding energy of −7.4 kcal/mol; bottleneck residues at entrance at the back (violet sticks). (H) Energy profile for undocking of **1** from active site of hMAO-B.

correctly oriented *trans* isomer. This noncovalent only binding of the *trans* isomer might lead to the worse performance observed experimentally of this inhibitor with hMAO-A.

In hMAO-B, the docked *cis* ligand **6** in the correct orientation in the active site has energy of −6.5 kcal/mol (Figure 3E; movie file jm9b01886_si_003.mp4 in Supporting Information). No energy peaks were observed along the active site for this isomer, whereby the energy reaches a plateau of 4.6 kcal/mol near the active site entrance (Figure 3F). *Trans* isomer **1** in the correct orientation has the energy of −7.4 kcal/

https://dx.doi.org/10.1021/acs.jmedchem.9b01886
J. Med. Chem. XXXX, XXX, XXX−XXX

Scheme 2. Synthesis of Inhibitors 19−26[a]

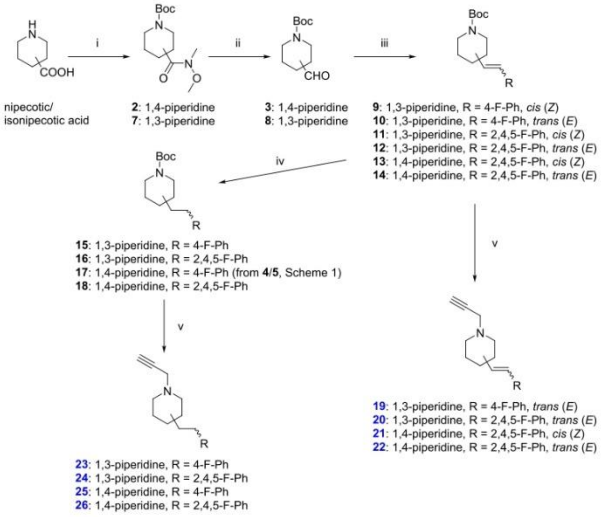

[a]Reagents and conditions: (i) 1) Boc_2O, 1.0 M NaOH, 1,4-dioxane, 0 °C, rt, 1−3 h (86−91%); (2) *N*,*O*-dimethyhydroxylamine hydrochloride, Et_3N, TBTU, CH_2Cl_2, 0 °C to rt, overnight (76−82%); (ii) $LiAlH_4$, anh THF, 0 °C, 1−2 h (crude products, 79−83%); (iii) corresponding Wittig salts ((4-fluorobenzyl)triphenylphosphonium bromide or (2,4,5-trifluorobenzyl)triphenylphosphonium bromide), NaHMDS (2 N in THF), anh THF, Ar(g), rt, overnight (overall yield for both isomers combined, 47−56%); (iv) corresponding mixture of *cis* and *trans* isomer (**9**−**14**), H_2(g), Pd/C, EtOH, rt, overnight (97−100%); (v) (1) 4.0 M HCl in 1,4-dioxane, 80 °C, 2 h (100%); (2) propargyl bromide (80% solution in toluene), Cs_2CO_3, DMF, Ar(g), 0 °C, rt, overnight (26−85%).

mol (Figure 3G; movie file jm9b01886_si_003.mp4 in Supporting Information), which is lower than the energy of the *cis* isomer, and then this falls further to −8.2 kcal/mol at the lowest point on the way out of the entrance (Figure 3H). The energy barrier to reach the active site is lower for the *trans* isomer than it is for the *cis* isomer, with the highest peak of 1.5 kcal/mol near the entrance, which is lower than the 4.6 kcal/mol energy barrier for the *cis* isomer. This lower energy barrier of the *trans* isomer at the entrance might be explained by the smaller maximum width of the *trans* isomer compared to the *cis* isomer, as discussed above. We also note that the docked *trans* inhibitor position in the active site has a root-mean-square deviation of 2.1 Å, compared to the cocrystal structure of inhibitor **1** in hMAO-B reported in the present study (PDB code 6RKB). This indicates that the docking successfully predicted the positioning of this inhibitor in the active site. In agreement with the experimental findings, the lower binding energies at the active site for the *trans* isomer and the lower energy barrier to reach the active site for the *trans* isomer indicate that the binding of *trans* isomer **1** to hMAO-B is favored compared to the binding of *cis* isomer **6**.

The distinct activity of this geometric isomer pair prompted us to study the structure−activity relationships (SARs) through the construction of a focused library of substituted piperidines (**19**−**26**; Scheme 2, Table 1) to probe the effect of piperidine disubstitution pattern on the inhibitory potency. 1,4-Disubstituted piperidines were the most tolerated and showed the highest selectivity for both hMAO-A and hMAO-B, and thus several analogues with various substituents on the phenyl ring were synthesized (Scheme 3, compounds **67**−**107**).

Structure−Activity Relationships and Stability of Compounds. Hit inhibitor **1** and the synthesized analogues **6**, **19**−**26**, and **67**−**107** were evaluated for their inhibition of both hMAO-A and hMAO-B using a horseradish peroxidase (HRP)−Amplex Red coupled assay (Table 1). The most important findings regarding the SARs are summarized in Figure 4. Scanning the 1,3- and 1,4-disubstitution patterns of piperidine derivatives with the *trans* configuration of the double bond revealed at least 5-fold superior inhibition of hMAO-B for the 1,4-disubstitution (e.g., **19** IC_{50} = 1470 nM vs **1** IC_{50} = 342 nM). Interestingly, reduction of the double bond retained this selective hMAO-B inhibition (IC_{50} of 243 nM and 370 nM for hit compound **1** and analogue **25**, respectively. Broadening the series of 1,4-disubsituted piperidines showcased selective inhibition of hMAO-A by *cis* analogues with small substituents on the phenyl ring (e.g., fluorine). The most potent was **69**, a 3-fluorophenyl derivative, with an IC_{50} of 68.4 nM and almost a 3-log unit selectivity over hMAO-B. On the other hand, the *trans* derivatives preferentially inhibited hMAO-B, with a general trend of improved inhibitory potencies with increasing hydrophobicity/size of the sub-

https://dx.doi.org/10.1021/acs.jmedchem.9b01886
J. Med. Chem. XXXX, XXX, XXX−XXX

Table 1. Inhibitory Potencies and Structures of Hit Compound 1 and All of the Synthesized Inhibitors and Positive Controls[a]

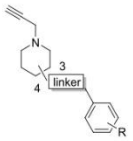

	structure			IC_{50} ± SEM [nM] or % RA ± SD at 100 μM		
compd	Pdp[b]	linker	R	hMAO-A	hMAO-B	selectivity ratio[c]
1	1,4	*trans*-vinyl	4-F	60.2 ± 1.6%	**342.2 ± 22.4**	>292
6	1,4	*cis*-vinyl	4-F	**726.1 ± 26.9**	**6221.5 ± 726.8**	0.12
25	1,4	*ethyl*	4-F	76.9 ± 2.2%	**370.1 ± 37.3**	>270
21	1,4	*cis*-vinyl	2,4,5-F	**5243.7 ± 323.4**	66.5 ± 3.9%	<0.05
22	1,4	*trans*-vinyl	2,4,5-F	81.2 ± 3.1%	**436.2 ± 11.7**	>229
26	1,4	ethyl	2,4,5-F	65.6 ± 4.4%	**216.4 ± 14.2**	>462
19	1,3	*trans*-vinyl	4-F	91.0 ± 3.1%	**1469.5 ± 233.2**	>68
23	1,3	ethyl	4-F	93.1 ± 3.2%	**7411.6 ± 1190.0**	>13
20	1,3	*trans*-vinyl	2,4,5-F	102.5 ± 5.2%	**2195.6 ± 228.3**	>46
24	1,3	ethyl	2,4,5-F	86.0 ± 5.2%	**11229.4 ± 974.7**	>9
67	1,4	*cis*-vinyl	H	**168.8 ± 8.5**	79.1 ± 4.0%	<0.002
68	1,4	*trans*-vinyl	H	**32960.7 ± 3476.5**	**3540.2 ± 611.8**	9
93	1,4	ethyl	H	**75779.6 ± 7566.0**[d]	**4603.4 ± 371.1**	16
69	1,4	*cis*-vinyl	3-F	**68.4 ± 4.3**	**48912.0 ± 2525.4**	0.001
70	1,4	*trans*-vinyl	3-F	**6906.8 ± 860.2**	**5048.7 ± 1224.6**	1.4
94	1,4	ethyl	3-F	**19927.3 ± 1608.5**	**3363.5 ± 310.5**	6
71	1,4	*cis*-vinyl	2-F	**3013.7 ± 207.3**	65.5 ± 0.3%	<0.03
72	1,4	*trans*-vinyl	2-F	**27293.2 ± 1758.4**	**11830.4 ± 766.5**	2
95	1,4	ethyl	2-F	**5927.3 ± 223.8**	**14159.5 ± 708.9**	0.4
73	1,4	*cis*-vinyl	2-Cl-4-F	**46121.5 ± 10141.6**	**53000.5 ± 2662.5**	0.9
74	1,4	*trans*-vinyl	2-Cl-4-F	**66028.4 ± 8419.0**	**417.6 ± 46.9**	158
75	1,4	*cis*-vinyl	4-Me	62.2 ± 4.4%	**19162.8 ± 5139.7**	>5
76	1,4	*trans*-vinyl	4-Me	57.3 ± 2.9%	**147.0 ± 13.8**	>680
96	1,4	ethyl	4-Me	68.1 ± 1.6%	**159.0 ± 13.3**	>630
77	1,4	*cis*-vinyl	4-*i*Pr	83.2 ± 0.5%	**1883.9 ± 278.6**	>53
78	1,4	*trans*-vinyl	4-*i*Pr	**73638.2 ± 11010.1**[d]	**44.4 ± 8.2**	1658
97	1,4	ethyl	4-*i*Pr	**162399.3 ± 9715.9**[d]	**7.0 ± 2.2**	23200
79	1,4	*cis*-vinyl	4-Cl	**118844.3 ± 26412.7**[d]	**11745.1 ± 555.9**	10
80	1,4	*trans*-vinyl	4-Cl	71.7 ± 0.2%	**50.4 ± 4.7**	>1984
98	1,4	ethyl	4-Cl	67.7 ± 0.0%	**38.1 ± 6.8**	>2625
81	1,4	*trans*-vinyl	4-Br	54.5 ± 1.2%	**21.2 ± 4.2**	>4717
82	1,4	*trans*-vinyl	4-OMe	56.1 ± 1.6%	**68.1 ± 11.1**	>1468
99	1,4	ethyl	4-OMe	62.2 ± 1.9%	**67.0 ± 11.4**	>1493
83	1,4	*cis*-vinyl	4-CF_3	80.1 ± 4.5%	**1506.6 ± 216.3**	>66
84	1,4	*trans*-vinyl	4-CF_3	64.9 ± 0.5%	**18.6 ± 3.3**	>5376
100	1,4	ethyl	4-CF_3	62.3 ± 0.7%	**10.9 ± 3.0**	>9174
85	1,4	*cis*-vinyl	3-CF_3	**858.0 ± 29.2**	**9352.5 ± 1512.9**	0.09
86	1,4	*trans*-vinyl	3-CF_3	64.8 ± 4.0%	**549.7 ± 127.5**	>182
101	1,4	ethyl	3-CF_3	71.6 ± 2.2%	**501.8 ± 107.1**	>199
87	1,4	*cis*-vinyl	4-CN	68.1 ± 2.7%	**1745.3 ± 315.4**	>57
88	1,4	*trans*-vinyl	4-CN	**129064.0 ± 8079.7**[d]	**57.0 ± 7.1**	2264
102	1,4	ethyl	4-CN	**21478.3 ± 6280.3**	**56.6 ± 8.7**	379
89	1,4	*cis*-vinyl	4-SO_2Me	70.6 ± 5.8%	**8444.7 ± 627.1**	>12
90	1,4	*trans*-vinyl	4-SO_2Me	68.7 ± 0.2%	**32.7 ± 2.5**	>3058
91	1,4	*cis*-vinyl	4-cyclopropyl	**7398.7 ± 661.8**	**2640.1 ± 342.8**	3
92	1,4	*trans*-vinyl	4-cyclopropyl	**20564.5 ± 2315.8**	**43.7 ± 6.4**	471
103	1,4	ethyl	4-propyl	**80305.3 ± 9033.0**	**36.1 ± 4.1**	2225
104	1,4	*cis*-vinyl	4-$CONH_2$	89.5 ± 0.6%	**51019.0 ± 6046.5**	2
105	1,4	*trans*-vinyl	4-$CONH_2$	64.8 ± 1.1%	**1737.0 ± 691.0**	58
106	1,4	ethyl	4-$CONH_2$	75.1 ± 2.2%	**5554.5 ± 1778.9**	>18
107	1,4	ethyl	4-OH	67.7 ± 0.5%	**7440.7 ± 1291.3**	>13

https://dx.doi.org/10.1021/acs.jmedchem.9b01886
J. Med. Chem. XXXX, XXX, XXX−XXX

Table 1. continued

compd	structure: Pdp[b]	structure: linker	structure: R	IC_{50} ± SEM [nM] or % RA ± SD at 100 μM: hMAO-A	IC_{50} ± SEM [nM] or % RA ± SD at 100 μM: hMAO-B	selectivity ratio[c]
pargyline				**3967.9 ± 275.1**	**195.5 ± 19.1**	20
L-deprenyl				**62663.8 ± 4113.6**	**12.1 ± 4.2**	5179
rasagiline				**29520 ± 8597**	**36.0 ± 4.1**	820
clorgiline				**3.4 ± 0.3**	**13568.4 ± 1157.3**	0.0003

[a]Data are mean values ± SEM: IC_{50} (in boldface), $n = 2, 3$; residual activity (RA), $n = 2$. [b]Pdn: piperidine disubstitution pattern. [c]Selectivity ratio is defined as IC_{50}(hMAO-A)/IC_{50}(hMAO-B). [d]Estimated IC_{50} values from the RAs below 100 μM. Compounds showed precipitation in the assay buffer at concentrations above 100 μM.

Scheme 3. Synthesis of Inhibitors 67−107[a]

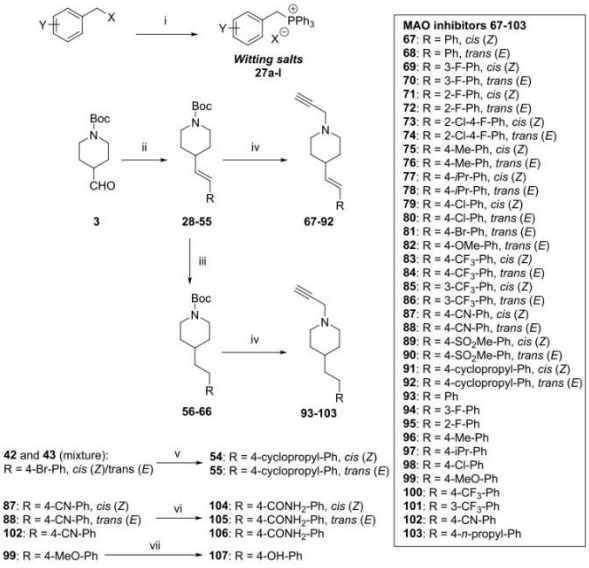

[a]Reagents and conditions: (i) benzyl halide, PPh_3, MeCN, 85 °C, overnight (80−97%); (ii) corresponding Wittig salts (**27a−l**), NaHMDS (2 N in THF)/KHMDS (0.5 M in toluene), anh THF, Ar(g), rt, overnight (overall yield, 30−66%); (iii) mixture of *cis* and *trans* isomers (**28−55**), H_2(g), Pd/C, EtOH, rt, overnight (83−100%); (iv) (1) 4.0 M HCl in 1,4-dioxane (or HCl in EtOH), 80 °C, 2 h (100%); (2) propargyl bromide (80% in toluene), K_2CO_3, MeCN, Ar(g), 0 °C, rt, overnight (6−89%); (v) cyclopropylboronic acid, K_3PO_4, tricyclohexylphosphine (20% in toluene), $Pd(OAc)_2$, toluene, water, Ar(g), 100 °C, 3 h (78%); (vi) KOH, *t*BuOH, 90 °C, 12−24 h (42−63%); (vii) BBr_3 (1 M in CH_2Cl_2), toluene, Ar(g), − 20 °C, 1 h, rt, 1 h (57%).

stituents on phenyl ring position 4 (−H < −F < −Cl < −Br and −H < −Me < −*i*Pr ∼ −cyclopropyl). Double-digit nanomolar inhibition of hMAO-B was also obtained for **82**, **84**, **88**, and **90** with −OMe, $-CF_3$, −CN, $-SO_2Me$ substituents, respectively, on position 4 of the phenyl ring. Compounds with an ethyl moiety that connected the rings showed comparable selective inhibition of hMAO-B as their *trans* congeners. All the *N*-propargylpiperidine derivatives inhibited corresponding isoenzyme in an irreversible manner as demonstrated by the 100-fold dilution assay.

For additional experiments, compounds **1**, **6**, **67**, **69**, **84**, **97**, and **100** were used in the form of hydrochloride salts to avoid possible solubility issues. The thermodynamic solubility of the compounds in PBS (pH 7.4) was at least 17.6 g/250 mL, 10.5 g/250 mL, 8.6 g/250 mL, 12.5 g/250 mL, 14.5 g/250 mL, and 16.3 g/250 mL for **6**, **67**, **69**, **84**, **97**, and **100**, respectively, which is good solubility according to biopharmaceutical classification for any realistically expected dose of investigated compounds.

Possible chemical instability and photoisomerization of *E*/*Z* isomers were also addressed as these are known liabilities of

https://dx.doi.org/10.1021/acs.jmedchem.9b01886
J. Med. Chem. XXXX, XXX, XXX−XXX

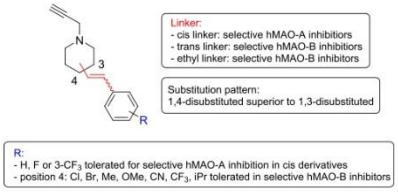

Figure 4. Crucial observations regarding SARs of the stilbene-like MAO inhibitors.

stilbene derivatives.[23] Proton NMRs of **69** (*cis* derivative), **84** (*trans* derivative), and **100** (ethyl analogue) in the form of hydrochloride salts were recorded in D_2O (Figures S1−S3). Inspection of the spectra confirmed that these compounds are relatively stable after more than 1 year of storage at room temperature (protected from sunlight) as only smaller amounts of impurities were detected for **84** (in the aromatic area), whereas compounds **69** and **100** showed no signs of chemical instability. The samples dissolved in the NMR tubes were then left on the benchtop exposed to natural daylight for 7 days, which could induce photoisomerization. No spectral changes were observed in comparison to spectra of freshly prepared samples. Altogether, these studies imply reasonable stability of the compounds.

Kinetic Evaluation. The exploration of SARs allowed the identification of a few compounds for more in-depth kinetic analysis with the purified enzyme samples, which allowed their inhibition mechanism to be better defined. On the basis of their inhibitory potencies and molecular features, compounds **1**, **84**, and **97** were selected for hMAO-B, whereas for hMAO-A the analysis was restricted to **69**. The inhibitors were tested using UV−vis spectrum measurements (Figure 5) and steady-state enzymatic assays (Table 2). The propargyl unit is known to react covalently with the *N*5 atom of the flavin cofactor by rapidly forming a stable covalent adduct that produces a typical modification of the spectrum; this is seen as bleaching of the peak at 450 nm and appearance of a stronger peak at 415 nm.[24] All of these selected compounds were tested by adding them in 10-fold excess to the protein solution in the spectrophotometer cuvette and measuring the spectra over time until no further modification was detected. All of the irreversible inhibitors produced a clear change in the enzyme spectra (Figure 5), similar to other classic acetylenic inhibitors, like L-deprenyl and clorgyline.[24] However, there were differences in the times required to complete the reactions for the adduct formation, i.e., to reach the final spectrum with no further modification. While **69** fully inactivated hMAO-A almost instantaneously (Figure 5A), similar to clorgyline, the hMAO-B selective compounds were slower. In particular, **84** initiated the reaction with the flavin within 1 min, showing an intermediate spectrum profile that evolved into the final 415 nm peak in 30 min (Figure 5B). Instead, **1** and **97** did not show any spectral modifications in the first few minutes and required half an hour to obtain an intermediate profile and more than 2 h to complete the reaction (Figure 5C and Figure 5D, respectively).

Full kinetic analysis was then undertaken for hMAO-A and hMAO-B inhibition by the selected compounds, using purified enzyme samples and the spectrophotometric version of the assay coupled to HRP that was used for IC_{50} determination, as described above. As enzyme inhibition by propargyl-based

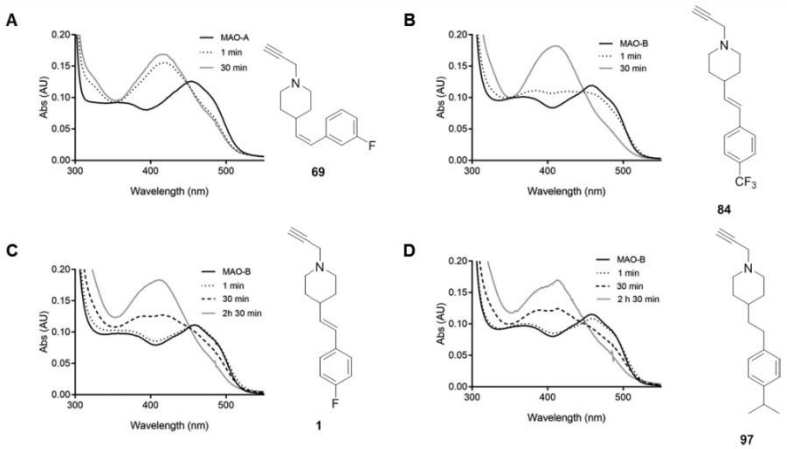

Figure 5. UV−vis absorption spectra of the hMAO enzymes after FAD cofactor modification by irreversible covalent inhibitors. The oxidized enzyme (10 μM) before inhibitor addition (100 μM) is shown as the continuous black line, whereas the gray profile indicates the final spectrum (i.e., no further changes were observed), which was reached at different times depending on the inhibitor. The intermediate spectra are shown as either dotted or dashed lines. (A) hMAO-A and **69**; (B) hMAO-B and **84**; (C) hMAO-B and **1**; (D) hMAO-B and **97**.

https://dx.doi.org/10.1021/acs.jmedchem.9b01886
J. Med. Chem. XXXX, XXX, XXX−XXX

Table 2. Kinetic Parameters for the Reversible and Irreversible Inhibition of the hMAOs by the Selected 4-Styrylpiperidine Inhibitors

		reversible inhibition	irreversible inhibition		
MAO	inhibitor	K_i (μM)	K_I (μM)	k_{inact} (min^{-1})	k_{inact}/K_I (min^{-1} μM^{-1})
hMAO-A	**69**	0.23 ± 0.02	1.01 ± 0.76	1.25 ± 0.25	1.24
	clorgyline[a]	0.040 ± 0.004[b]	0.22 ± 0.08[b]	0.12 ± 0.05[b]	0.55[b]
hMAO-B	**1**	1.92 ± 0.32	1.38 ± 0.29	0.66 ± 0.04	0.48
	84	1.25 ± 0.23	17.25 ± 4.38	2.03 ± 0.38	0.12
	97	1.36 ± 0.31	6.55 ± 1.62	1.04 ± 0.12	0.16
	L-deprenyl[a]	0.97 ± 0.11	5.68 ± 0.78	2.56 ± 0.24	0.45

[a]Kinetic parameters were compared to clorgyline and L-deprenyl in the cases of hMAO-A and hMAO-B selective inhibitors, respectively. [b]Data from Esteban et al. (2014).[25]

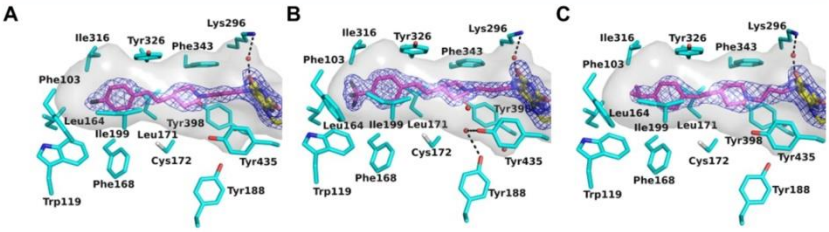

Figure 6. Crystal structures of the active site of hMAO-B-inhibitor complexes. The hMAO-B active site cavity is shown as a gray semitransparent surface, which is lined by the protein residues (represented in cyan). Water molecules are red spheres, and hydrogen bonds are dashed lines. The FAD cofactor is in yellow stick representation. The inhibitor molecule bound in the hMAO-B active site cavity is shown as sticks, with carbon, nitrogen, and fluorine in magenta, blue, and black, respectively. The refined $2F_o - F_c$ electron density map contoured at 1.2σ is shown in blue for the inhibitor and the FAD molecules. (A) Active site of hMAO-B in complex with **1** (2.3 Å resolution; PDB code 6RKB). (B) Active site of hMAO-B in complex with **84** (1.7 Å resolution; PDB code 6RKP). (C) Active site of hMAO-B in complex with **97** (2.3 Å resolution; PDB code 6RLE).

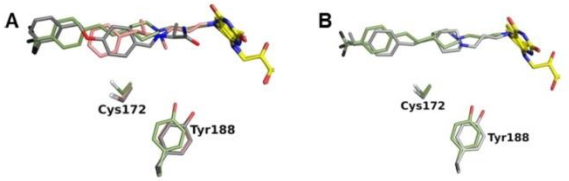

Figure 7. Structural superposition to highlight differences and common features in the binding modes of the hMAO-B inhibitors. The protein, inhibitor, and cofactor atoms are represented as sticks (color code as in Figure 6 except for the carbon atoms of protein and inhibitor molecules, which are depicted accordingly to distinguish the different structures). For clarity, only Cys172 and Tyr188 of the protein active site residues are shown, which undergo some conformational changes. (A) Superposition of structures in complex with **84** (green), safinamide (gray) and L-deprenyl (pink). (B) Superposition of structures in complex with **84** (green) and **97** (light gray).

inhibitors involves a first step in which the ligand is accommodated into the protein active site to be correctly oriented for flavin adduct formation, competitive inhibition can be measured under steady-state conditions using kynuramine and benzylamine as substrates for hMAO-A and hMAO-B, respectively. Thus, both the reversible and irreversible inhibition parameters were determined (Table 2). Compound **69** is a potent hMAO-A inhibitor with a reversible K_i of 0.23 μM, which is 5-fold higher than that reported for clorgyline. This difference is in line with the irreversible constant K_I, and it is balanced by the irreversible inactivation velocity that is 10-fold higher that for clorgyline. Overall, **69** is a very potent hMAO-A inhibitor with comparable activity to clorgyline. Similar to L-deprenyl, in the case of hMAO-B selective ligands, the reversible K_i values are all in the micromolar range. The irreversible constant K_I for covalent hMAO-B inhibitors is in general 5-fold the reversible K_i; however, the k_{inact}/K_I indicated comparable inhibitory potencies of the hMAO-B inhibitors to L-deprenyl.

Structure of hMAO-B in Complex with Inhibitors. Structural studies were performed by cocrystallization of hMAO-B with the inhibitors selected for the kinetic analyses, using previously published procedures.[26] Structures for inhibitors **1**, **84**, and **97** were solved at resolution ranging

https://dx.doi.org/10.1021/acs.jmedchem.9b01886
J. Med. Chem. XXXX, XXX, XXX−XXX

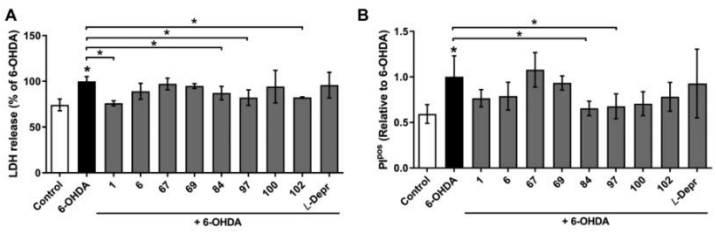

Figure 8. Effects of inhibitors on 6-OHDA-induced cell death in SH-SY5Y cells. (A, B) SH-SY5Y cells were pretreated with the compounds (5 μM) for 30 min (as indicated) and then treated with 6-OHDA (100 μM). After 24 h, LDH assays (A) and PI staining (B) were performed. Data are mean values ± standard deviation ($n \geq 2$; each in duplicate): *, $p < 0.05$ (one-way ANOVA, with Bonferroni correction, followed by *t*-tests).

from 2.3 to1.7 Å (Figure 6). The crystallographic statistics are reported in Table S1. Crystallographic studies on hMAO-B in complex with **1**, **84**, and **97** showed that these inhibitor molecules are certain to be bound to the enzyme active site (Figure 6). Ligand binding does not cause any major conformational changes to the overall protein dimeric structure (Figure S4). As for all of the inhibitors, the structure of the active site is identical in the two monomers present in the asymmetric unit that forms the protein dimer, and here we will refer to chain A of each structure in the following discussion. The electron density map clearly showed that all of these inhibitors form a covalent adduct with the flavin (Figure 6).

All of these inhibitors bind to the hMAO-B active site in a similar fashion, from the covalent adduct with the flavin to the 4-substituted phenyl ring at the other end of the molecule (Figure 6). They adopt an extended conformation, as they occupy both the substrate and the cavity spaces (Ile199 in the open conformation). The 4-substituted phenyl ring is constrained by the flat hydrophobic shape of the hMAO-B cavity in a position perpendicular to the flavin plane, as for other well-known inhibitors, such as L-deprenyl and safinamide (Figure 7A). The site occupied by the halogen substituent on the aromatic ring of **1** is also conserved, which is a common feature of many hMAO-B inhibitors.[27] The more polar substituents that have lower inhibitory activities (e.g., **82**, **105**) would be much less favored in their binding to this highly hydrophobic site. The enzyme active site architecture does not undergo any conformational change with respect to that of other hMAO-B structures except for minor modifications to the side chains of Cys172 and Tyr188 (Figure 7A). This is due to the position adopted by the piperidine ring that represents the hallmark of this series of inhibitors. Despite the flat shape of the hMAO-B cavity, the nonplanar conformation of the piperidine and its pyramidal nitrogen that is involved in the covalent adduct constrain the piperidine ring to bind perpendicular to the plane of the cavity (Figure 6). Instead, with other inhibitors such as L-deprenyl and safinamide, there is an aromatic ring that binds coplanar with the cavity plane and with any substituted aromatic at the other end of the molecule, if present (Figure 7A). Therefore, the position of the piperidine in the upper part of the cavity allows Cys172 and Tyr188 to move slightly upward. In the structure of the complex with **97**, the conformation of the Cys172 and Tyr188 is conserved to some extent with respect to the previous structures. This is due to the linker that is devoid of the double bond, and the consequent tetrahedral conformation of its carbon atoms results in a more contracted conformation of the inhibitor molecule with respect to **84** (Figure 7B) and **1**. As a result, the piperidine collapses toward the bottom of the cavity, and the covalent linkage is forced to adopt a slightly different conformation with respect to the other propargyl inhibitors (Figure 7).

Cell-Based Assays. Following the chemical-space exploration and kinetic and structural evaluations, several of these structurally diverse hMAO-A and hMAO-B inhibitors were also tested *in vitro* in cell models. First, their cytotoxicity profiles were defined using the SH-SY5Y human neuroblastoma cell line. By use of the MTS assay, no significant cytotoxic effects were seen for 24 h treatments of these cells with the compounds **1**, **6**, **67**, **69**, **84**, **97**, **100**, and **102** at concentrations of 5 μM and 10 μM (Figure S5). Indeed, at 50 μM, the cell viabilities remained >80% for almost all of the compounds, which is roughly 3 log units higher than the concentrations needed to achieve 50% *in vitro* inhibition of either of the two MAO isoforms.

The experimental *in vitro* cell model with the neurotoxin 6-hydroxydopamine (6-OHDA) is commonly used to study neurodegenerative processes, as it induces toxicity that mimics the biochemistry and neuropathology of Parkinson's disease.[28] To determine the possibility that MAO inhibitors can abrogate 6-OHDA-induced toxicity, we examined lactate dehydrogenase (LDH) release and propidium iodide (PI) staining in the SH-SY5Y cells after 30 min pretreatment with the compounds at the noncytotoxic concentration of 5 μM, followed by 6-OHDA treatment for 24 h (Figure 8). The active treatment with 6-OHDA significantly increased LDH release (135% vs control), while pretreatment with compounds **1**, **84**, **97**, and **102** protected against this increased LDH release (76%, 87%, 82%, 82% vs 6-OHDA, respectively), thus indicating improved cell viability. In the confirmation using flow cytometry, the proportion of PI-positive cells increased after the active 24 h treatment with 6-OHDA and was significantly reduced following the pretreatments with the hMAO-B inhibitors **84** and **97** (0.65 and 0.68, respectively), compared to the 6-OHDA-treated cells. Altogether, this indicates that the selective hMAO-B inhibitors **84** and **97** reduced the 6-OHDA-induced cytotoxicity and increased the viability of these SH-SY5Y neuronal-like cells.

***In Vivo* MAO Inhibition in Mouse Brain Homogenates and *in Vitro* Permeability.** The inhibition of the MAOs in mouse brain homogenates was also investigated both *in vitro* and *ex vivo* (Table 3). Here, the more potent of the inhibitors

https://dx.doi.org/10.1021/acs.jmedchem.9b01886
J. Med. Chem. XXXX, XXX, XXX−XXX

Table 3. *In Vitro* and *ex Vivo* Mouse Brain Homogenate Residual Activities of 69 and 100 at 60 mg/kg ip on MAO-A and MAO-B According to Substrate[a]

	residual activity (%)					
	MAO-A substrate 5-HT (0.25 mM)		MAO-A/B substrate *p*-tyramine (0.5 mM)		MAO-B substrate benzylamine (0.5 mM)	
compd	*in vitro*[b]	*ex vivo*[c]	*in vitro*[b]	*ex vivo*[c]	*in vitro*[b]	*ex vivo*[c]
69	−1.3 ± 0.1	1.6 ± 0.02	31.3 ± 0.2	14.2 ± 0.2	nd	nd
100	nd	nd	59.4 ± 0.2	77.2 ± 0.2	−7.7 ± 0.2	24.3 ± 0.5

[a]Data are mean values ± SD (n = 1, in triplicate). nd, not determined. [b]*In vitro*: 50 μM compounds (final concentrations) versus 0.9% saline with mouse brain homogenate from nontreated mice. [c]*Ex vivo*: brain homogenates from mice treated (n = 3, per group) with 60 mg/kg ip compounds or 0.9% saline 30 min before brain homogenate preparation.

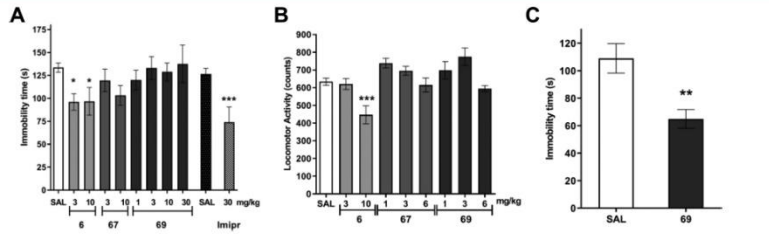

Figure 9. *In vivo* evaluation in mice of antidepressant-like activity of the selective MAO-A inhibitors **6**, **67**, and **69**. (A) Effects of acute ip treatment with **6** (3, 10 mg/kg, n = 13, 9), **67** (3, 10 mg/kg, n = 6, 10), and **69** (1, 3, 10, 30 mg/kg, n = 8, 7, 8, 6) and imipramine (30 mg/kg, n = 8) in the tail suspension test. Data are mean values ± SEM of immobility time in comparison to control mice (SAL, n = 23): *, $p < 0.05$; ***, $p < 0.001$ (one-way ANOVA, followed by Dunnett's tests). (B) Effects of acute ip treatment with **6** (3, 10 mg/kg, n = 8, 8), **67** (1, 3, 6 mg/kg; n = 5, 5, 5), and **69** (1, 3, 6 mg/kg, n = 10, 5, 5) on locomotor activity of the mice. Data are mean values ± SEM of spontaneous locomotor activity counts recorded in 5 min sessions: ***, $p < 0.001$ (one-way ANOVA, followed by Dunnett's tests). (C) Effects of 10-day chronic ip treatment with **69** (0.3 mg/kg, daily; n = 10) in the tail suspension test. Data are mean values ± SEM of the immobility time, compared to control mice (n = 8): **, $p < 0.01$ (unpaired t-test).

against hMAO-A (i.e., **69**) and hMAO-B (i.e., **100**) were tested based on their IC_{50} values and structural features. Brain homogenates from male Swiss mice were first characterized in terms of their MAOs activity and substrate specificity (Table S2, Figure S6).

Compound **69** completely abolished MAO-A activity *in vitro* at 50 μM when 5-HT was used as the selective MAO-A substrate. Compound **100** at 50 μM inhibited mice MAO-B when benzylamine was used as the selective MAO-B substrate (Table 3). When the dual hMAO-A/B substrate *p*-tyramine was used, the inhibition was lower (i.e., higher residual activities; RAs). The same profile of inhibition was established *ex vivo* for brain homogenates from mice treated with these compounds, which were injected intraperitoneally (ip) 30 min before preparation of the brain homogenates. Again, more potent inhibition was seen in these brain homogenates when the isoenzyme-selective substrates were used. Selective MAO-A inhibitor **69** was the most active compound when administered at 60 mg/kg ip (RA, 1.6% ± 0.02%), while 60 mg/kg ip **100** resulted in similar MAO-B inhibition (RA, 24.3% ± 0.5%). Compounds **69** and **100** showed dose-dependent inhibition of these corresponding MAO isoforms (ED_{50} of 0.43 ± 0.26 mg/kg and 1.38 ± 0.87 mg/kg, respectively).

MAO inhibitors are in clinical use for treatment of psychiatric and neurological disorders, where they are used in chronic, low-dose regimes.[29] These MAO-A and MAO-B activities in *ex vivo* mouse brain homogenates were therefore studied after chronic 10-day administration to the mice of **69** and **100** at the low dose of 0.3 mg/kg ip. This chronic administration of selective MAO-A inhibitor **69** significantly reduced MAO-A activity compared to 0.9% saline ip in the control mice. After the single administration of **69** at 0.3 mg/kg ip, the *ex vivo* MAO-A RA was reduced to 67.8% ± 31.2% (i.e., compared to 0.9% saline), whereas the 10-day treatment resulted in MAO-A RA of 9.5% ± 23.4%. Similar to **69**, one single ip injection of **100** at 0.3 mg/kg showed MAO-B RA of 83.4% ± 19.2%, while chronic 10-day treatment resulted in RA of 28.3% ± 13.8%, which demonstrated accumulation of inhibition over time.

The *ex vivo* inhibitory activity of inhibitors **69** and **100** was also demonstrated in the mouse brain homogenates prepared 90 min after acute oral administration to the mice, via oral gavage at 30 mg/kg. Inhibitors **69** and **100** showed RAs of 45.3% ± 14.6% (vs 0.9% saline-treated mice) and 30.5% ± 10.4% (vs 0.9% saline treated mice), respectively. This prompted us to also study gut permeability of these representative inhibitors (i.e., **69**, **84**, and **100**) *in vitro* on rat intestine. The apparent bidirectional permeability coefficient for the rat intestine *in vitro* was determined for **69**. This was 108 ± 13 nm/s (as mean ± SEM) in the absorptive direction and 354 ± 99 nm/s in the eliminatory direction. For comparison, the apparent permeability coefficients of the internal low- and high-permeability standards furosemide and metoprolol in the absorptive direction were 64 ± 11 nm/s and 140 ± 18 nm/s, respectively.

https://dx.doi.org/10.1021/acs.jmedchem.9b01886
J. Med. Chem. XXXX, XXX, XXX−XXX

Behavioral Studies with the Selective MAO-A and MAO-B Inhibitors. MAO-A inhibitors are currently used in the therapy of treatment-resistant major depressive disorder and some specific types of depression.[30] Symptoms of depression correlate highly with those of anxiety.[31] These have been shown to be associated with 5-HT_{1A} receptors,[32] which are presynaptic and postsynaptic G-protein-coupled receptors that are involved in neuromodulation. 5-HT_{1A} receptor agonists, such as buspirone, show efficacy for the relief of anxiety and depression.[32] The binding affinities (K_i values) for this 5-HT_{1A} receptor subtype were thus determined for these MAO inhibitors to potentially further explain their behavioral effects. These ranged from low micromolar to submicromolar K_i values (Table S3). Following treatments with the selective irreversible MAO-A inhibitors **6**, **67**, and **69**, the Swiss mice were subjected to the different behavioral tasks to determine whether these compounds have any antidepressant-like activity, any activity in an anxiety model and whether they affect locomotor activity.[33]

The antidepressant-like activity was screened with the widely used tail suspension test. At 30 min before the behavioral assays, the mice were treated with **6**, **67**, and **69** at 3 mg/kg and 10 mg/kg ip, with **69** also at 1 mg/kg and 30 mg/kg ip, or were injected with 0.9% saline as control. Imipramine (30 mg/kg ip) was used as the reference drug. Compounds **67** and **69** did not decrease the immobility time, whereas selective MAO-A inhibitor **6** and imipramine significantly reduced it, which demonstrated the antidepressant-like effects of these compounds under acute treatment (Figure 9A).

The performance of mice in the "elevated plus maze test" was used here as a rodent model of anxiety, which was carried out 30 min after the ip treatments with **6**, **67**, and **69** (Table S4). Compound **6** at the dose of 10 mg/kg ip induced a significant decrease compared to mice injected with 0.9% saline, for both the number of total arm entries (9.7 ± 2.9 vs 22.0 ± 1.5; $p < 0.001$) and the proportion of time spent in the center of the apparatus (13.4 ± 2.3 vs 43.5 ± 2.8; $p < 0.001$), and also an increase in the proportion of open-arm entries (2.0-fold; $p < 0.001$). Meanwhile, **69** at 3 mg/kg ip produced a significant increase in the proportion of open-arm entries (2.0-fold; $p < 0.001$) and in the time spent in those entries (2.1-fold; $p < 0.001$), similar to diazepam (reference drug) at 1 mg/kg ip (2.1-fold, 2.4-fold, respectively; $p < 0.001$ for both).

The locomotor activity of the mice was also determined, as it can affect the data obtained in these behavioral assays. It was shown that **6** at 10 mg/kg ip significantly decreased spontaneous locomotor activity (Figure 9B), which is correlated with the decrease in the total arm entries in the elevated plus maze test. This indicates that the effects of **6** after acute 10 mg/kg ip treatment are not associated with antidepressant-like or anxiolytic effects but rather with a decrease in the locomotion of the mice. On the other hand, the increased open arm parameters in the elevated plus maze for **69** (3 mg/kg ip) appear to be correlated with an anxiolytic-like effect, which would be mediated through the 5-HT_{1A} receptor, as locomotion was not altered at this dose of **69**. Importantly, chronic 10-day treatment with **69** at a low dose (i.e., 0.3 mg/kg ip, daily) significantly decreased the immobility time in the treated group (Figure 9C). No significant effects were seen for this chronic low dose of **69** in the elevated plus maze and locomotor activity tests (Table S5). This confirmed the antidepressant-like effects of **69** when administered chronically, which were not seen for the acute treatment regime.

Behavioral studies of the selective hMAO-B inhibitors were performed with compound **100** (irreversible MAO-B inhibitor). Although *trans* derivative **84** also showed potent irreversible MAO-B inhibition (IC_{50} = 18.6 ± 3.3 nM; equipotent to **100**), it was not studied here *in vivo* due to its poor permeability in the rat gut (see above) and its low binding potential for the 5-HT_{1A} receptor (Table S3).

The hole–board test is commonly used to study stress-related changes in exploratory behavior of animals.[34] This was combined here with the locomotor activity test. At acute ip doses of ≥10 mg/kg of **100** in the mice, the hole–board test parameters and locomotor activities were reduced (Table S6, Figure S7A–C). Due to the locomotor impairment at high doses, compound **100** was further studied in the haloperidol-induced catalepsy test at lower doses (see Supplementary Results and Discussion). Compound **100** was also tested in the same battery of behavioral tests after 10 days of low-dose ip treatment (0.3 mg/kg, daily), where it did not affect the locomotor activity of the mice (Figure S7D) or the parameters of the hole–board test (Figure S8). During these 10-day treatments (i.e., **69**, **100** at 0.3 mg/kg ip, daily), the body mass of the mice was also monitored (Figure S9). No significant differences were seen for the proportions of body mass variations versus the control mice (0.9% saline treated). Also, all of these mice survived these 10-day treatments without any apparent signs of changes in behavior, which supports the general safety of these compounds.

■ DISCUSSION AND CONCLUSIONS

Biological receptors differ greatly in shape, polarity, and conformational dynamics.[1] However, it is a challenging task to obtain selectivity between structurally related targets such as isoenzymes, which requires different ligand-design approaches. MAO-A and MAO-B are two closely related isoenzymes where numerous selective inhibitors have been described in the literature, with some now used in the clinical setting for treatment of neurological disorders.[35]

Selective hMAO-B inhibitor **6** was identified in a screening campaign, and chemistry-driven exploration of the chemical space revealed that the *trans* isomers selectively inhibit hMAO-B over hMAO-A. On the other hand, *cis* isomers were identified as selective hMAO-A inhibitors. The inhibitory potencies in the SARs exploration phase are generally expressed as IC_{50} values (Table 1), although these derivatives are irreversible. The IC_{50} values are thus dependent on the assay conditions and particularly on the preincubation period.[36] Despite these limitations, the measured IC_{50} values still allow relatively simple, yet not the most precise, comparisons between such compounds in a series.[11] The inhibitory activity against hMAO-B was increased by introducing bulkier and more lipophilic substituents onto position 4 of the phenyl ring, as previously reported in the literature.[37] A similar trend was also observed for the turnover of variously substituted substrates of the benzylamine and phenethylamine classes,[38] where the binding affinity improved with increasing hydrophobicity of the substituent.

Further examination of the binding kinetics for the selected compounds here using purified enzyme samples confirmed the variable nature of these IC_{50} values. The overall higher affinity inferred from the IC_{50} values (Table 1) compared to K_i (Table 2) is related to the covalent nature of these inhibitors, which fully inactivate the enzyme during the preincubation step in the absence of substrate (not included in competitive steady-state

https://dx.doi.org/10.1021/acs.jmedchem.9b01886
J. Med. Chem. XXXX, XXX, XXX−XXX

experiments used to determine IC_{50}). For the same reason, the variability of the IC_{50} values among the different inhibitors that was not seen for K_i has to be interpreted in light of the time-dependent inactivation process that showed different kinetics depending on the inhibitor (Table 2). For example, **84** showed an IC_{50} that is 0.05-fold that of **1** and a similar reversible K_i, while its inactivation rate was 4-fold that of **1**, which results in a k_{inact}/K_I ratio that is comparable between these two inhibitors. Similar observations can be reasoned for the other covalent analogues and for L-deprenyl.

Crystallographic studies confirmed the covalent adduct formation with flavin for the inhibitors investigated here. A similar binding mode for all of these inhibitors was seen, with only minor modifications of the active site arrangements in comparison to other hMAO-B structures reported in the literature. These changes were most prominent with the *trans* inhibitors **1** and **84**, which imposed a slight upward shift of Cys172 and Tyr188. This is related to the conformation adopted by the piperidine ring, which represents the hallmark of this class of inhibitors, as a novel element with respect to previous propargyl inhibitors (i.e., where the nitrogen atom is within a linear molecular structure rather than part of a ring).

The inhibitor series studied here were not cytotoxic to SH-SY5Y cells up to treatments of 50 μM. Remarkably, only the selective hMAO-B inhibitors decreased the LDH release induced by the neurotoxin 6-OHDA. The reduced proportion of PI-positive SH-SY5Y cells was also confirmed for the two MAO-B-selective ligands during 6-OHDA-induced toxicity. This indicated their neuroprotective nature, which might also be attributed, among others possibilities, to their selective MAO-B inhibition. Following ip and peroral administration, these compounds inhibited MAO-A and MAO-B activities *ex vivo* in the mouse brain homogenates. The extent of their inhibition varied depending on the inhibitor selectivity and the substrate used. Selective MAO-A inhibitor **69** completely inhibited MAO-A *ex vivo* when the MAO-A substrate 5-HT was used (RA, 1.6%), while its inhibition was lower when using *p*-tyramine (RA, 14.2%), which is a dual MAO-A/B substrate. The difference is even more evident for the MAO-B inhibitors, with decreased inhibition when switching from the MAO-B substrate benzylamine to dual substrate *p*-tyramine. Both MAO-A and MAO-B can metabolize *p*-tyramine; however, only one of them was inhibited by the selective inhibitor, which explained the impaired inhibition. This additionally confirmed the *in vitro* selectivity of these inhibitors not only on the isolated human enzymes but also in complex matrices, such as mouse brain homogenates. The MAO inhibition in these mouse brain homogenates after peroral single-dose administration also indicated the oral bioavailability of these analogues. The *in vitro* permeability of **69** studied for rat intestine was between that of the low-permeability and high-permeability standards, and as such, **69** should be classified with an intermediate/moderate permeability, with the possibility of interference by the intestinal efflux mechanisms, as seen by the higher apparent permeability coefficient determined for the eliminatory direction. The permeabilities of **84** and **100** were not determinable *in vitro* due to their high tissue binding. These findings do not correlate directly with the *ex vivo* effects; however, the *ex vivo* effects show that both **69** and **100** reached the brain tissue and inhibited the MAO activity after their oral administration.

Under the acute treatment regime in these mice, the selective MAO-A inhibitor **69** did not affect the immobility time of the mice in the tail suspension test. The observed anxiolytic-like activity with acute treatment with **69**, which can be attributed to 5-HT_{1A} binding, prompted us to also study **69** in a 10-day treatment regime. The antidepressant-like effects of **69** in this setup, together with no significant toxic effects, confirmed the therapeutic potential for this class of selective hMAO-A inhibitors. On the other hand, the selective MAO-B inhibitor **100** did not produce the expected results for haloperidol-induced catalepsy, in terms of what would be expected for a MAO-B inhibitor.[39] Nonetheless, the general safety of these compounds has been established in the chronic low-dose treatment regime.

In summary, we have generated the first example of selective hMAO-A and hMAO-B inhibitors where this selectivity is conferred by the configurational *cis*/*trans* isomerism of a double bond. *Cis* isomers with fluorine or unsubstituted benzene ring selectively inhibit hMAO-A. On the other hand, *trans* derivatives and their corresponding reduced ethyl analogues with small lipophilic substituents on benzene ring selectively inhibit hMAO-B. In addition, we provide the first in depth, and we believe critical, kinetic and structural characterization of these 1-propargyl-4-styrylpiperidines as potential fragments in the design of pharmaceuticals that can be used to target the MAOs.

■ EXPERIMENTAL SECTION

Chemistry. General Information. The reagents and solvents used were obtained from commercial sources (i.e., Acros Organics, Sigma-Aldrich, TCI Europe, Merck, Carlo Erba, Apollo Scientific) and were used as provided. Anhydrous THF was prepared by distillation over sodium and benzophenone under Ar(g). Analytical thin-layer chromatography was performed on silica gel aluminum sheets (60 F254, 0.20 mm; Merck). Flash column chromatography was performed on silica gel 60 (particle size 0.040−0.063 mm, Merck). ^{1}H NMR and ^{13}C spectra were recorded at 400 and 100 MHz, respectively, on a Bruker Avance III NMR spectrometer (Bruker, MA, USA) at 295 K. The chemical shifts (δ) are reported in ppm and are referenced to the deuterated solvent used. HRMS measurements were performed (Autospec Q Micromass MS; Fisons, VG Analytical, Manchester, U.K.) at the Jozef Stefan Institute, Ljubljana, Slovenia, and on a LC−MS/MS system (Q Executive Plus; Thermo Scientific, MA, USA). MS measurements were performed on an Expression CMS mass spectrometer (Advion, NY, USA). Infrared spectra were obtained on a Thermo Nicolet FT-IR spectrometer using the ATR technique. Analytical reversed-phase HPLC analyses were performed on a modular system (1100LC; Agilent Technologies, CA, USA, and Thermo Scientific Dionex UltiMate 3000; Thermo Fisher Scientific Inc., MA, USA). Method: C18 column (Eclipse Plus; 5 μm, 4.6 mm × 150 mm; Agilent), T = 25 °C; sample 0.2 mg/mL in MeCN; flow rate = 1.0 mL/min; detector λ = 220 nm; mobile phase A (0.1% TFA [v/v] in water), mobile phase B (MeCN). Gradient (for mobile phase B): 0−12 min, 10−90%; 12−14 min, 90%; 14−15 min, 90−10%. Purities of the tested compounds were established to be ≥95%, as determined by HPLC. All compounds described in Table 1 were checked by SwissADME[40] for the presence of PAINS substructures,[41] and no PAINS substructures were identified.

General Synthetic Chemistry Experimental Protocols. General Procedure A: Synthesis of Wittig Reagents. Appropriate benzyl halide (25.0 mmol, 1.0 equiv) was dissolved in MeCN (25−50 mL), and triphenylphosphine (6.56 g, 25.0 mmol, 1.0 equiv) was added at room temperature. The reaction mixture was stirred at 85 °C for 16−24 h. The solvent was evaporated, and CH_2Cl_2 (10 mL) and Et_2O (50 mL) were added to the residue. The precipitated solid was filtered off, washed with Et_2O (20 mL), and dried overnight at room temperature. The crude product was used in the following reaction step without further purification.

https://dx.doi.org/10.1021/acs.jmedchem.9b01886
J. Med. Chem. XXXX, XXX, XXX−XXX

General Procedure B: Wittig Reaction. Appropriate Witting reagent synthesized according to general procedure A (1.1 equiv) was dissolved in anhydrous THF (30 mL) under argon atmosphere. NaHMDS (2 N in THF, 1.2 equiv) or KHMDS (0.5 M in toluene, 1.1 equiv) was added to the resulting suspension at room temperature. The orange-red colored reaction mixture was then stirred for 30 min under argon, followed by a dropwise addition of *N*-Boc protected 3- or 4- formylpiperidine (1.0 equiv) solution in anhydrous THF (10 mL). The reaction mixture was stirred at room temperature overnight (16−24 h) and then quenched by adding saturated aqueous $NaHCO_3$ solution (10−15 mL). The solvent was evaporated, and the white residue was resuspended in EtOAc (50 mL) and saturated aqueous $NaHCO_3$ solution (50 mL) and transferred into a separating funnel. The phases were separated, and the aqueous phase was additionally extracted with EtOAc (2 × 50 mL). Combined organic phases were washed with saturated brine (100 mL), dried over Na_2SO_4, and evaporated. The crude product was purified by flash column chromatography to yield (in a majority of cases) both pure *cis* and *trans* isomers.

General Procedure C: Reduction of the Double Bond. Alkene derivative (Wittig reaction product-mixture of *cis* and *trans* isomer, 1.0 equiv) was dissolved in EtOH (50 mL) and purged under a stream of argon for 10 min. Catalytic amount of Pd/C (10% load on carbon, 10−20% [w/w] calculated to the starting material) was added, and the resulting suspension mixture was stirred under H_2(g) atmosphere at room temperature for 16−24 h. The catalyst was removed by filtration through Celite and evaporated to obtain crude product. The product was used without further purification unless stated otherwise.

General Procedure D: Boc Protection Removal (HCl Method). To the solution of Boc-protected derivative (1.0 equiv) in 1,4-dioxane or EtOH (30 mL), concentrated HCl (10.0 equiv) was added at room temperature. The reaction mixture was stirred at 80 °C for 2 h. The solvent was evaporated under reduced pressure, and the crude product was used in the next step without further purification.

General Procedure E: Alkylation of Piperidine. Piperidine intermediate (in the form of the salt with HCl) was dissolved in MeCN (20−30 mL) or DMF (5−10 mL) at 0 °C under an argon atmosphere. K_2CO_3 or Cs_2CO_3 (3.0 equiv) was added, followed by dropwise addition of propargyl bromide (80% solution in toluene, 1.2 equiv). The resulting suspension was stirred at room temperature (unless specified otherwise) for 16−72 h. The solvent was evaporated, the residue dissolved in a mixture of CH_2Cl_2 (50 mL) and saturated aqueous $NaHCO_3$ solution (50 mL) and transferred into a separating funnel. The organic phase was further washed with saturated brine solution (50 mL), dried over Na_2SO_4, and evaporated. The crude product was purified by flash column chromatography.

General Procedure F: Hydrolysis of Nitrile. The starting nitrile (1.0 equiv) was dissolved in *tert*-butanol (20−50 mL), followed by the addition of powdered KOH (3.0 equiv). The resulting suspension was stirred at 90 °C for 12−24 h, and then the solvent was evaporated. The residue was dissolved in a mixture of CH_2Cl_2 (50 mL) and saturated aqueous $NaHCO_3$ (50 mL) and transferred into a separating funnel. The water layer was additionally extracted with CH_2Cl_2 (50 mL). The combined organic layers were washed with saturated brine (50 mL), dried over Na_2SO_4, and evaporated. The crude product was purified by flash column chromatography.

Synthesis of Intermediates and Inhibitors. (*E*)-4-(4-Fluorostyryl)-1-(prop-2-yn-1-yl)piperidine (1). Synthesized from **5** (0.157 g, 0.514 mmol, 1.0 equiv) via general procedures D and E. Column chromatography, EtOAc/n-hex = 1/1 (v/v). Yield: 26% (33 mg); yellow oil. ^{1}H NMR (400 MHz, $CDCl_3$): δ 1.57 (dt, J = 12.3, 3.4 Hz, 1H), 1.60 (dt, J = 12.0, 3.7 Hz, 1H), 1.77−1.83 (m, 2H), 2.08−2.18 (m, 1H), 2.27 (t, J = 2.4 Hz, 1H), 2.30 (dd, J = 11.7, 2.0 Hz, 2H), 2.95 (td, J = 11.1, 2.8 Hz, 2H), 3.34 (d, J = 2.4 Hz, 2H), 6.07 (dd, J = 16.0, 7.0 Hz, 1H), 6.34 (d, J = 16.0 Hz, 1H), 6.95−7.00 (m, 2H), 7.28−7.33 (m, 2H). ^{13}C NMR (100 MHz, $CDCl_3$): δ 31.89, 38.71, 47.20, 52.19, 73.26, 78.73, 115.31 (d, $J_{C,F}$ = 21.4 Hz), 127.14, 127.41 (d, $J_{C,F}$ = 7.7 Hz), 133.70 (d, $J_{C,F}$ = 3.3 Hz), 134.49, 161.94 (d, $J_{C,F}$ = 245.9 Hz). HRMS (ESI+): m/z calcd for $C_{16}H_{19}FN$ $[M + H]^+$ 244.1502; found 244.1508. IR (ATR): 3287, 2925, 2804, 1599, 1507, 1425, 1314, 1222, 1124, 966, 855, 669, 631 cm^{-1}. HPLC purity, 96.2% (t_R = 9.11 min).

***tert*-Butyl 4-(Methoxy(methyl)carbamoyl)piperidine-1-carboxylate (2).** Piperidine-4-carboxylic acid (15.00 g, 116.1 mmol, 1.0 equiv) was dissolved in a mixture of 1,4-dioxane (75 mL) and 1 M NaOH (116.1 mL, 116.1 mmol, 1.0 equiv) and cooled to 0 °C. A solution of Boc_2O (30.41 g, 139.3 mmol, 1.2 equiv) in 1,4-dioxane (100 mL) was added dropwise over 30 min. The resulting suspension was stirred at room temperature for 1 h. The organic solvent was evaporated, and the aqueous residue was transferred into a separating funnel and extracted with Et_2O (2 × 100 mL). The aqueous layer was acidified with 2 M HCl to pH 2−3. The precipitated solid was filtered under suction, washed with cold water (100 mL), and dried at 50 °C overnight to obtain 1-(*tert*-butoxycarbonyl)piperidine-4-carboxylic acid. Yield: 91% (24.22 g); white crystals, mp 158−160 °C. ^{1}H NMR (400 MHz, $CDCl_3$): δ 1.46 (s, 9H), 1.62−1.69 (m, 2H), 1.88−1.94 (m, 2H), 2.48 (tt, J = 10.9, 3.9 Hz, 1H), 2.82−2.89 (m, 2H), 4.03 (td, J = 13.6, 3.7 Hz, 2H), 9.13 (bs, 1H).

1-(*tert*-Butoxycarbonyl)piperidine-4-carboxylic acid (10.00 g, 43.61 mmol, 1.0 equiv) was suspended in CH_2Cl_2 (150 mL) and cooled to 0 °C. Then Et_3N (15.11 mL, 109.03 mmol, 2.5 equiv) was added, followed by TBTU (14.70 g, 45.78 mmol, 1.05 equiv). After stirring for 30 min at 0 °C, *N*,*O*-dimethylhydroxylamine hydrochloride (5.10 g, 52.32 mmol, 1.2 equiv) was added, and the mixture was stirred overnight at room temperature. The resulting solution was transferred into a separating funnel and washed with saturated aqueous $NaHCO_3$ solution (2 × 100 mL), 1 M HCl (100 mL), saturated brine solution (100 mL), dried over Na_2SO_4, and evaporated. Column chromatography, EtOAc/n-hex = 1/2 (v/v). Yield: 76% (9.03 g); white crystals, mp 68−72 °C. ^{1}H NMR (400 MHz, $CDCl_3$): δ 1.45 (s, 9H), 1.61−1.74 (m, 4H), 2.72−2.83 (m, 3H), 3.17 (s, 3H), 3.70 (s, 3H), 4.17 (td, J = 13.4, 2.9 Hz, 2H).

***tert*-Butyl 4-Formylpiperidine-1-carboxylate (3).** *tert*-Butyl 4-(methoxy(methyl)carbamoyl)piperidine-1-carboxylate **2** (9.03 g, 33.16 mmol, 1.0 equiv) was dissolved in anhydrous THF (75 mL) and cooled to 0 °C. After stirring 10 min under an argon atmosphere, $LiAlH_4$ (1.89 g, 49.73 mmol, 1.5 equiv) was added. The mixture was stirred at 0 °C for 2 h and afterward quenched by adding saturated aqueous $NaHCO_3$ solution (30 mL). The suspension formed was transferred into a separating funnel and extracted with EtOAc (3 × 100 mL). Combined organic phases were washed with saturated aqueous $NaHCO_3$ solution (100 mL), 1 M HCl (100 mL), saturated brine solution (100 mL), dried over Na_2SO_4, and evaporated. The crude product was used without further purification. Yield: 83% (5.87 g); pale yellow oil.

***tert*-Butyl 4-(4-Fluorostyryl)piperidine-1-carboxylate [Isomers (*Z*)-4 and (*E*)-5].** Synthesized from aldehyde **3** (2.0 g, 9.38 mmol, 1.0 equiv), (4-fluorobenzyl)triphenylphosphonium bromide (4.66 g, 10.3 mmol, 1.1 equiv) and NaHMDS (2 N in THF, 5.63 mL, 11.26 mmol, 1.2 equiv) via general procedure B. Column chromatography, petroleum ether/Et_2O = 10/1 (v/v). Overall yield of reaction: 52% (mass of both *Z* and *E* isomers, 1.5 g); isolated pure *Z* isomer, 55 mg; isolated pure *E* isomer, 155 mg; mixture of *E*/*Z* isomers, 1.29 g.

4: R_f = 0.82 (EtOAc/n-hex = 1/2, v/v); white crystals, mp 80−82 °C. ^{1}H NMR (400 MHz, $CDCl_3$): δ 1.34 (dt, J = 12.4, 4.6 Hz, 1H), 1.37 (dt, J = 12.7, 4.7 Hz, 1H), 1.45 (s, 9H), 1.59−1.66 (m, 2H), 2.58−2.66 (m, 1H), 2.72 (t, J = 11.7 Hz, 2H), 4.08 (d, J = 12.5 Hz, 2H), 5.44 (dd, J = 11.6, 10.1 Hz, 1H), 6.34 (d, J = 11.6 Hz, 1H), 6.99−7.05 (m, 2H), 7.16−7.21 (m, 2H). HRMS (ESI+): m/z calcd for $C_{18}H_{24}FNO_2Na$ $[M + Na]^+$ 328.1689; found 328.1688.

5: R_f = 0.79 (EtOAc/n-hex = 1/2, v/v); yellow oil. ^{1}H NMR (400 MHz, $CDCl_3$): δ 1.30−1.42 (m, 2H), 1.46 (s, 9H), 1.51−1.57 (m, 1H), 1.71−1.77 (m, 2H), 2.77 (dt, J = 13.2, 2.7 Hz, 2H), 4.13 (d, J = 13.0 Hz, 2H), 6.05 (dd, J = 15.9, 6.9 Hz, 1H), 6.34 (d, J = 16.2 Hz, 1H), 6.95−7.01 (m, 2H), 7.27−7.32 (m, 2H). HRMS (ESI+): m/z calcd for $C_{18}H_{24}FNO_2Na$ $[M + Na]^+$ 328.1689; found 328.1686.

(*Z*)-4-(4-Fluorostyryl)-1-(prop-2-yn-1-yl)piperidine (6). Synthesized from **4** (57 mg, 0.187 mmol, 1.0 equiv) via general procedures D and E. Column chromatography, EtOAc/n-hex = 1/1

https://dx.doi.org/10.1021/acs.jmedchem.9b01886
J. Med. Chem. XXXX, XXX, XXX−XXX

(v/v). Yield: 72% (33 mg); white crystals, mp 45−46 °C. ^{1}H NMR (400 MHz, $CDCl_3$): δ 1.51−1.61 (m, 2H), 1.69−1.76 (m, 2H), 2.21−2.28 (m, 3H), 2.45−2.55 (m, 1H), 2.90 (dt, J = 9.0, 2.7 Hz, 2H), 3.32 (d, J = 2.4 Hz, 2H), 5.48 (dd, J = 11.5, 10.1 Hz, 1H), 6.33 (d, J = 11.6 Hz, 1H), 6.99−7.05 (m, 2H), 7.17−7.21 (m, 2H). ^{13}C NMR (100 MHz, $CDCl_3$): δ 32.16, 34.31, 47.22, 51.85, 73.21, 78.77, 115.12 (d, $J_{C,F}$ = 21.3 Hz), 127.07, 130.00 (d, $J_{C,F}$ = 7.9 Hz), 133.58 (d, $J_{C,F}$ = 3.3 Hz), 137.05, 161.52 (d, $J_{C,F}$ = 246.1 Hz). HRMS (ESI+): m/z calcd for $C_{16}H_{19}FN$ $[M + H]^+$ 244.1502; found 244.1503. IR (ATR): 3299, 2930, 1601, 1508, 1446, 1225, 1157, 972, 845, 657 cm^{-1}. HPLC purity, 99.5% (t_R = 9.03 min).

(±)-*tert*-Butyl 3-(Methoxy(methyl)carbamoyl)piperidine-1-carboxylate (7). Synthesis of (±)-1-(*tert*-butoxycarbonyl)-piperidine-3-carboxylic acid was carried out following the procedure described for the synthesis of compound **2**, starting from (±)-piperidine-3-carboxylic acid (7.75 g, 60.0 mmol, 1.0 equiv). Yield: 86% (11.83 g); white crystals, mp 164−165 °C. ^{1}H NMR (400 MHz, $CDCl_3$): δ 1.43−1.53 (m, 1H), 1.45 (s, 9H), 1.59−1.75 (m, 2H), 2.03−2.09 (m, 1H), 2.48 (tt, J = 10.2, 4.0 Hz, 1H), 2.82−2.89 (m, 1H), 3.03 (dd, J = 12.7, 10.6 Hz, 1H), 3.88 (td, J = 13.3, 4.0 Hz, 1H), 4.08−4.15 (m, 1H), 8.67 (bs, 1H).

(±)1-(*Tert*-butoxycarbonyl)piperidine-3-carboxylic acid (10.00 g, 43.61 mmol, 1.0 equiv) was transformed to Weinreb amide **7** following the procedure described for compound **2**. Yield: 82% (9.74 g); white crystals, mp 89−91 °C. ^{1}H NMR (400 MHz, $CDCl_3$): δ 1.41−1.52 (m, 1H), 1.44 (s, 9H), 1.58−1.73 (m, 2H), 1.87−1.94 (m, 1H), 2.68 (tt, J = 12.8, 2.9 Hz, 1H), 2.72−2.82 (m, 1H), 2.86 (t, J = 11.7 Hz, 1H), 3.17 (s, 3H), 3.72 (s, 3H), 4.05−4.15 (m, 2H).

(±)-*tert*-Butyl 3-Formylpiperidine-1-carboxylate (8). Synthesis of aldehyde **8** was carried out following the procedure described for compound **3**, starting from amide **7** (9.74 g, 35.76 mmol, 1.0 equiv). Yield: 79% (6.03 g); pale yellow oil.

(±)-*tert*-Butyl 3-(4-Fluorostyryl)piperidine-1-carboxylate [Isomers (*Z*)-9 and (*E*)-10]. Synthesized from **8** (1.02 g, 4.78 mmol, 1.0 equiv), (4-fluorobenzyl)triphenylphosphonium bromide (2.59 g, 5.74 mmol, 1.2 equiv), and NaHMDS (2 N in THF, 2.87 mL, 5.74 mmol, 1.2 equiv) via general procedure B. Column chromatography, petroleum ether/Et_2O = 10/1 (v/v) yielding pure *trans* isomer **10** (<8% *cis* isomer **9** was present in the mixture as estimated from ^{1}H NMR). Overall yield of reaction (mixture of *E*/*Z* isomers): 56% (0.817 g).

10: R_f = 0.38 (Et_2O/petroleum ether = 1/10, v/v); yellow oil. ^{1}H NMR (400 MHz, $CDCl_3$, *E* isomer): δ 1.31−1.41 (m, 1H), 1.47 (s, 9H), 1.68−1.73 (m, 1H), 1.90−1.94 (m, 1H), 2.26−2.34 (m, 1H), 2.60−2.71 (m, 1H), 2.78 (dd, J = 13.2, 11.5 Hz, 2H), 3.97 (d, J = 13.1 Hz, 2H), 5.99 (dd, J = 16.0, 7.0 Hz, 1H), 6.40 (d, J = 16.0 Hz, 1H), 6.95−7.02 (m, 2H), 7.27−7.32 (m, 2H). HRMS (ESI+): m/z calcd for $C_{18}H_{24}FNO_2Na$ $[M + Na]^+$ 328.1689; found 328.1682.

(±)-*tert*-Butyl 3-(2,4,5-Trifluorostyryl)piperidine-1-carboxylate [Isomers (*Z*)-11 and (*E*)-12]. Synthesized from **8** (0.79 g, 3.71 mmol, 1.0 equiv), (2,4,5-trifluorobenzyl)triphenylphosphonium bromide (2.23 g, 4.58 mmol, 1.2 equiv), and NaHMDS (2 N in THF, 2.29 mL, 4.58 mmol, 1.2 equiv) via general procedure B. Column chromatography, petroleum ether/Et_2O = 10/1 (v/v) to obtain a mixture of *cis*/*trans* isomers (ratio ∼40/60, estimated from ^{1}H NMR). Overall yield of reaction: 47% (mass of both *Z* and *E* isomers, 0.595 g).

11 and **12** (mixture of both isomers): R_f = 0.34 (petroleum ether/Et_2O = 10/1, v/v); yellow oil. ^{1}H NMR (400 MHz, $CDCl_3$): δ 1.30−1.40 (m, 3.4H), 1.45 (1.46) (s + s, 15.3H), 1.62−1.73 (m, 1.7H), 1.88−1.94 (m, 0.7H), 2.30−2.38 (m, 0.7H), 2.43−2.53 (m, 1H), 2.62−2.84 (m, 3.4H), 3.92−4.08 (m, 3.4H), 5.58 (dd, J = 11.5, 10.4 Hz, 0.7H), 6.07 (dd, J = 16.2, 7.1 Hz, 1H), 6.32 (d, J = 11.5 Hz, 0.7H), 6.49 (d, J = 16.3 Hz, 1H), 6.85−6.96 (m, 1.7H), 7.11 (ddd, J = 10.6, 8.8, 6.9 Hz, 1H), 7.21 (ddd, J = 11.2, 8.7, 7.0 Hz, 0.7H). HRMS (ESI+): m/z calcd for $C_{18}H_{22}F_3NO_2Na$ $[M + Na]^+$ 364.1500; found 364.1491.

***tert*-Butyl 4-(2,4,5-Trifluorostyryl)piperidine-1-carboxylate [Isomers (*Z*)-13 and (*E*)-14].** Synthesized from aldehyde **3** (0.575 g, 2.70 mmol, 1.0 equiv), (2,4,5-trifluorobenzyl)triphenylphosphonium bromide (1.59 g, 3.25 mmol, 1.2 equiv) and NaHMDS (2 N solution in THF, 1.63 mL, 3.25 mmol, 1.2 equiv) via general procedure B. Column chromatography, petroleum ether/Et_2O = 10/1 (v/v). Overall yield of reaction: 52% (mass of both *Z* and *E* isomers, 0.48 g); isolated pure *Z* isomer, 165 mg; isolated pure *E* isomer, 135 mg; mixture of *E*/*Z* isomers, 180 mg.

13: R_f = 0.80 (EtOAc/n-hex = 1/2, v/v); yellow crystals, mp 86−87 °C. ^{1}H NMR (400 MHz, $CDCl_3$): δ 1.30−1.40 (m, 2H), 1.46 (s, 9H), 1.58−1.64 (m, 2H), 2.37−2.48 (m, 1H), 2.70 (dt, J = 13.4, 2.7 Hz, 2H), 4.08 (td, J = 13.4, 2.7 Hz, 2H), 5.55 (dd, J = 11.4, 10.3 Hz, 1H), 6.17 (d, J = 11.6 Hz, 1H), 6.93 (ddd, J = 10.1, 9.2, 6.7 Hz, 1H), 7.01 (ddd, J = 10.6, 8.7, 6.9 Hz, 1H). HRMS (ESI+): m/z calcd for $C_{18}H_{22}F_3NO_2Na$ $[M + Na]^+$ 364.1500; found 364.1503.

14: R_f = 0.78 (EtOAc/n-hex = 1/2, v/v); pale yellow crystals, mp 60−63 °C. ^{1}H NMR (400 MHz, $CDCl_3$): δ 1.36 (dt, J = 12.4, 4.2 Hz, 1H), 1.39 (dt, J = 12.3, 4.3 Hz, 1H), 1.47 (s, 9H), 1.71−1.79 (m, 2H), 2.25−2.36 (m, 1H), 2.78 (t, J = 12.0 Hz, 2H), 4.14 (bs, 2H), 6.13 (dd, J = 16.1, 6.9 Hz, 1H), 6.44 (d, J = 16.1 Hz, 1H), 6.88 (dt, J = 9.9, 6.6 Hz, 1H), 7.01 (ddd, J = 11.1, 8.8, 7.0 Hz, 1H). HRMS (ESI+): m/z calcd for $C_{18}H_{22}F_3NO_2Na$ $[M + Na]^+$ 364.1500; found 364.1497.

(±)-*tert*-Butyl 3-(4-Fluorophenethyl)piperidine-1-carboxylate (15). Synthesized from a mixture of **9** and **10** (0.55 g, 1.80 mmol, 1.0 equiv) via general procedure C. Yield: quantitative (0.55 g); yellow oil. ^{1}H NMR (400 MHz, $CDCl_3$): δ 1.08−1.13 (m, 1H), 1.35−1.56 (m, 3H), 1.45 (s, 9H), 1.59−1.66 (m, 1H), 1.80−1.87 (m, 1H), 2.41−2.56 (m, 1H), 2.61 (t, J = 12.2 Hz, 2H), 2.79 (dt, J = 12.2, 2.5 Hz, 2H), 3.89 (td, J = 13.1, 3.9 Hz, 1H), 4.04 (bs, 1H), 6.92−6.98 (m, 2H), 7.09−7.14 (m, 2H). HRMS (ESI+): m/z calcd for $C_{18}H_{26}FNO_2Na$ $[M + Na]^+$ 330.1845; found 330.1842.

(±)-*tert*-Butyl 3-(2,4,5-Trifluorophenethyl)piperidine-1-carboxylate (16). Synthesized from a mixture of **11** and **12** (0.30 g, 0.88 mmol, 1.0 equiv) via general procedure C. Yield: 97% (0.29 g); yellow oil. ^{1}H NMR (400 MHz, $CDCl_3$): δ 1.09−1.18 (m, 1H), 1.37−1.55 (m, 4H), 1.47 (s, 9H), 1.62−1.69 (m, 1H), 1.83−1.90 (m, 1H), 2.55 (dd, J = 13.0, 9.3 Hz, 1H), 2.62 (t, J = 7.6 Hz, 2H), 2.82 (ddd, J = 13.2, 11.2, 3.2 Hz, 1H), 3.89 (td, J = 13.2, 4.1 Hz, 1H), 3.97 (d, J = 12.6 Hz, 1H), 6.88 (ddd, J = 10.1, 9.3, 6.7 Hz, 1H), 7.00 (ddd, J = 10.6, 8.7, 6.9 Hz, 1H). HRMS (ESI+): m/z calcd for $C_{18}H_{24}F_3NO_2Na$ $[M + Na]^+$ 366.1657; found 366.1653.

***tert*-Butyl 4-(4-Fluorophenethyl)piperidine-1-carboxylate (17).** Synthesized from a mixture of **4** and **5** (0.152 g, 0.50 mmol, 1.0 equiv) via general procedure C. Yield: quantitative (0.155 g); yellow oil. ^{1}H NMR (400 MHz, $CDCl_3$): δ 1.11 (dt, J = 12.4, 4.2 Hz, 1H), 1.14 (dt, J = 12.5, 4.2 Hz, 1H), 1.35−1.44 (m, 1H), 1.45 (s, 9H), 1.51−1.56 (m, 2H), 1.60−1.62 (m, 1H), 1.65−1.72 (m, 2H), 2.57−2.62 (m, 1H), 2.66 (t, J = 11.5 Hz, 2H), 4.07 (bs, 2H), 6.93−6.99 (m, 2H), 7.09−7.14 (m, 2H). HRMS (ESI+): m/z calcd for $C_{18}H_{26}FNO_2Na$ $[M + Na]^+$ 330.1845; found 330.1848.

***tert*-Butyl 4-(2,4,5-Trifluorophenethyl)piperidine-1-carboxylate (18).** Synthesized from a mixture of **13** and **14** (0.152 g, 0.45 mmol, 1.0 equiv) via general procedure C. Yield: quantitative (0.155 g); yellow oil. ^{1}H NMR (400 MHz, $CDCl_3$): δ 1.11 (dt, J = 12.4, 4.3 Hz, 1H), 1.14 (dt, J = 12.7, 4.2 Hz, 1H), 1.35−1.44 (m, 1H), 1.45 (s, 9H), 1.49−1.54 (m, 2H), 1.66−1.73 (m, 2H), 2.59 (t, J = 8.0 Hz, 2H), 2.66 (dt, J = 13.2, 2.5 Hz, 2H), 4.09 (d, J = 13.2 Hz, 2H), 6.87 (ddd, J = 10.0, 9.4, 6.7 Hz, 1H), 6.97 (ddd, J = 10.6, 8.8, 7.1 Hz, 1H). HRMS (ESI+): m/z calcd for $C_{18}H_{24}F_3NO_2Na$ $[M + Na]^+$ 366.1657; found 366.1652.

(±)-(*E*)-3-(4-Fluorostyryl)-1-(prop-2-yn-1-yl)piperidine (19). Synthesized from a mixture of **9** and **10** (0.190 g, 2.11 mmol, 1.0 equiv) via general procedures D and E. Column chromatography, EtOAc/n-hex = 1/1 (v/v) yielding pure *trans* isomer **19**. Yield: 45% (68 mg); yellow oil. ^{1}H NMR (400 MHz, $CDCl_3$): δ 1.17 (dt, J = 12.3, 4.1 Hz, 1H), 1.61−1.72 (m, 1H), 1.74−1.80 (m, 1H), 1.81−1.87 (m, 1H), 2.09 (t, J = 10.8 Hz, 1H), 2.19 (dt, J = 11.4, 3.0 Hz, 1H), 2.25 (t, J = 2.4 Hz, 1H), 2.41−2.50 (m, 1H), 2.82−2.87 (m, 1H), 2.89−2.93 (m, 1H), 3.34 (d, J = 2.5 Hz, 2H), 6.04 (dd, J = 16.0, 7.2 Hz, 1H), 6.38 (d, J = 16.0 Hz, 1H), 6.95−7.01 (m, 2H), 7.28−7.33 (m, 2H). ^{13}C NMR (100 MHz, $CDCl_3$): δ 24.64, 29.94, 39.41,

https://dx.doi.org/10.1021/acs.jmedchem.9b01886
J. Med. Chem. XXXX, XXX, XXX−XXX

47.18, 52.23, 57.76, 73.97, 77.87, 115.34 (d, $J_{C,F}$ = 21.7 Hz), 127.47 (d, $J_{C,F}$ = 8.0 Hz), 128.41, 131.95, 133.50 (d, $J_{C,F}$ = 3.3 Hz), 162.03 (d, $J_{C,F}$ = 246.0 Hz). HRMS (ESI+): *m/z* calcd for $C_{16}H_{19}FN$ $[M + H]^+$ 244.1502; found 244.1509. IR (ATR): 3433, 3196, 2934, 2544, 2124, 1507, 1225, 1159, 1012, 858, 750, 647 cm^{-1}. HPLC purity, 99.4% (t_R = 9.10 min).

(±)-(*E*)-1-(Prop-2-yn-1-yl)-3-(2,4,5-trifluorostyryl)piperidine (20). Synthesized from a mixture of **11** and **12** (0.219 g, 0.64 mmol, 1.0 equiv) via general procedures D and E. Column chromatography, EtOAc/n-hex = 1/1 (v/v) to obtain pure *trans* isomer **20**. Yield: 34% (61 mg); yellow oil. ^1H NMR (400 MHz, $CDCl_3$): δ 1.21 (ddd, *J* = 15.8, 12.1, 4.1 Hz, 1H), 1.63−1.87 (m, 3H), 2.13 (t, *J* = 10.7 Hz, 1H), 2.24 (dt, *J* = 11.2, 2.6 Hz, 1H), 2.27 (t, *J* = 2.4 Hz, 1H), 2.47−2.56 (m, 1H), 2.84−2.87 (m, 1H), 2.90−2.94 (m, 1H), 3.36 (d, *J* = 2.4 Hz, 2H), 6.12 (dd, *J* = 16.1, 7.2 Hz, 1H), 6.46 (d, *J* = 16.2 Hz, 1H), 6.88 (dt, *J* = 9.9, 6.7 Hz, 1H), 7.22 (ddd, *J* = 11.1, 8.8, 7.0 Hz, 1H). ^{13}C NMR (100 MHz, $CDCl_3$): δ 24.77, 29.89, 39.90, 47.28, 52.32, 57.64, 73.44, 78.51, 105.56 (dd, $J_{C,F}$ = 28.4, 21.0 Hz), 114.14 (dd, $J_{C,F}$ = 19.8, 5.1 Hz), 120.01−120.02 (m), 121.74−121.93 (m), 136.12−136.16 (m), 146.93 (ddd, $J_{C,F}$ = 243.9, 13.2, 3.6 Hz), 148.83 (ddd, $J_{C,F}$ = 251.2, 14.8, 12.4 Hz), 154.78 (ddd, $J_{C,F}$ = 248.0, 9.0, 2.1 Hz). IR (ATR): 3304, 2932, 2798, 1621, 1512, 1427, 1336, 1154, 1106, 969, 879, 850, 665 cm^{-1}. HRMS (ESI+): *m/z* calcd for $C_{16}H_{17}F_3N$ $[M + H]^+$ 280.1313; found 280.1316. HPLC purity, 99.1% (t_R = 9.57 min).

(*Z*)-1-(Prop-2-yn-1-yl)-4-(2,4,5-trifluorostyryl)piperidine (21). Synthesized from **13** (165 mg, 0.483 mmol, 1.0 equiv) via general procedures D and E. Column chromatography, EtOAc/n-hex = 1/1 (v/v). Yield: 68% (92 mg); white crystals, mp 72−74 °C. ^1H NMR (400 MHz, $CDCl_3$): δ 1.55 (dt, *J* = 12.5, 3.8 Hz, 1H), 1.58 (dt, *J* = 11.7, 3.8 Hz, 1H), 1.66−1.71 (m, 2H), 2.20−2.35 (m, 3H), 2.25 (t, *J* = 2.5 Hz, 1H) 2.90 (dt, *J* = 11.6, 2.8 Hz, 2H), 3.32 (d, *J* = 2.4 Hz, 2H), 5.64 (dd, *J* = 11.3, 10.4 Hz, 1H), 6.23 (d, *J* = 11.6 Hz, 1H), 6.92 (ddd, *J* = 10.0, 9.3, 6.7 Hz, 1H), 7.01 (ddd, *J* = 10.6, 8.8, 6.9 Hz, 1H). ^{13}C NMR (100 MHz, $CDCl_3$): δ 31.77, 34.96, 47.19, 51.71, 73.33, 78.62, 105.51 (dd, $J_{C,F}$ = 28.7, 20.7 Hz), 117.62 (dd, $J_{C,F}$ = 19.4, 4.6 Hz), 119.00, 121.36 (ddd, $J_{C,F}$ = 17.7, 5.8, 4.4 Hz), 140.20, 146.36 (ddd, $J_{C,F}$ = 243.7, 12.6, 3.6 Hz), 148.88 (ddd, $J_{C,F}$ = 248.8, 14.4, 12.6 Hz); 154.97 (ddd, $J_{C,F}$ = 246.8, 9.0, 2.7 Hz). HRMS (ESI+): *m/z* calcd for $C_{16}H_{17}F_3N$ $[M + H]^+$ 280.1313; found 280.1317. IR (ATR): 3293, 2905, 2824, 1618, 1503, 1423, 1310, 1192, 1151, 1133, 972, 882, 779, 679, 653 cm^{-1}. HPLC purity, 100% (t_R = 9.47 min).

(*E*)-1-(Prop-2-yn-1-yl)-4-(2,4,5-trifluorostyryl)piperidine (22). Synthesized from **14** (0.135 g, 0.395 mmol, 1.0 equiv) via general procedures D and E. Column chromatography, EtOAc/n-hex = 1/1 (v/v). Yield: 74% (82 mg); yellow oil. ^1H NMR (400 MHz, $CDCl_3$): δ 1.56 (dt, *J* = 12.4, 3.4 Hz, 1H), 1.59 (dt, *J* = 12.0, 3.7 Hz, 1H), 1.78−1.84 (m, 2H), 2.11−2.20 (m, 1H), 2.26 (t, *J* = 2.4 Hz, 1H), 2.30 (dt, *J* = 11.7, 2.3 Hz, 2H), 2.95 (dt, *J* = 11.6, 2.8 Hz, 2H), 3.34 (d, *J* = 2.4 Hz, 2H), 6.13 (dd, *J* = 16.1, 7.0 Hz, 1H), 6.43 (d, *J* = 16.1 Hz, 1H), 6.87 (dt, *J* = 9.9, 6.7 Hz, 1H), 7.23 (ddd, *J* = 11.1, 8.8, 7.0 Hz, 1H). ^{13}C NMR (100 MHz, $CDCl_3$): δ 31.69, 39.02, 47.17, 52.07, 73.23, 78.73, 105.51 (dd, $J_{C,F}$ = 28.5, 20.9 Hz), 114.06 (dd, $J_{C,F}$ = 19.6, 5.2 Hz), 118.96−119.03 (m), 121.95 (ddd, $J_{C,F}$ = 14.8, 5.8, 4.4 Hz), 138.10−138.17 (m), 146.93 (ddd, $J_{C,F}$ = 243.5, 12.9, 3.4 Hz), 148.76 (ddd, $J_{C,F}$ = 251.1, 14.9, 12.6 Hz); 154.73 (ddd, $J_{C,F}$ = 247.4, 9.1, 2.3 Hz). HRMS (ESI+): *m/z* calcd for $C_{16}H_{17}F_3N$ $[M + H]^+$ 280.1313; found 280.1318. IR (ATR): 3305, 3180, 2931, 2804, 2513, 1619, 1510, 1426, 1335, 1150, 1107, 970, 878, 706, 630 cm^{-1}. HPLC purity, 100% (t_R = 9.57 min).

(±)-3-(4-Fluorophenethyl)-1-(prop-2-yn-1-yl)piperidine (23). Synthesized from **15** (0.193 g, 0.628 mmol, 1.0 equiv) via general procedures D and E. Column chromatography, EtOAc/n-hex = 1/1 (v/v). Yield: 33% (51 mg); yellow oil. ^1H NMR (400 MHz, $CDCl_3$): δ 0.85−0.95 (m, 1H), 1.46−1.54 (m, 2H), 1.55−1.65 (m, 2H), 1.66−1.74 (m, 1H), 1.75−1.82 (m, 1H), 1.88 (t, *J* = 10.6 Hz, 1H), 2.14 (dt, *J* = 11.4, 3.0 Hz, 1H), 2.24 (t, *J* = 2.4 Hz, 1H), 2.60 (t, *J* = 7.9 Hz, 2H), 2.79−2.83 (m, 1H), 2.84−2.89 (m, 1H), 3.30 (d, *J* = 2.4 Hz, 2H), 6.91−6.97 (m, 2H), 7.09−7.14 (m, 2H). ^{13}C NMR (100 MHz, $CDCl_3$): δ 25.03, 30.25, 32.26, 35.55, 36.44, 47.29, 52.72, 58.53, 73.49, 78.45, 115.00 (d, $J_{C,F}$ = 21.0 Hz), 129.54 (d, $J_{C,F}$ = 7.9 Hz), 138.00 (d, $J_{C,F}$ = 3.2 Hz), 161.13 (d, $J_{C,F}$ = 243.3 Hz). HRMS (ESI+): *m/z* calcd for $C_{16}H_{21}FN$ $[M + H]^+$ 246.1658; found 246.1652. IR (ATR): 3302, 2929, 2853, 2797, 1601, 1509, 1452, 1222, 1157, 1106, 828, 661 cm^{-1}. HPLC purity, 98.5% (t_R = 9.16 min).

(±)-3-(2,4,5-Trifluorophenethyl)-1-(prop-2-yn-1-yl)-piperidine (24). Synthesized from **16** (0.181 g, 0.527 mmol, 1.0 equiv) via general procedures D and E. Column chromatography, EtOAc/n-hex = 1/2 (v/v). Yield: 26% (39 mg); yellow oil. ^1H NMR (400 MHz, $CDCl_3$): δ 0.88−0.98 (m, 1H), 1.45−1.56 (m, 2H), 1.58−1.77 (m, 3H), 1.78−1.85 (m, 1H), 1.91−2.00 (m, 1H), 2.17−2.25 (m, 1H), 2.26−2.29 (m, 1H), 2.54−2.66 (m, 2H), 2.88 (t, *J* = 12.6 Hz, 2H), 3.35 (d, *J* = 2.5 Hz, 2H), 6.86 (ddd, *J* = 10.0, 9.5, 6.7 Hz, 1H), 6.98 (ddd, *J* = 10.6, 8.8, 6.9 Hz, 1H). ^{13}C NMR (100 MHz, $CDCl_3$): δ 25.08, 25.67, 30.21, 34.61, 35.62, 47.33, 52.76, 58.46, 73.28, 78.69, 105.20 (dd, $J_{C,F}$ = 28.6, 20.6 Hz), 117.71 (dd, $J_{C,F}$ = 18.7, 6.2 Hz), 125.50 (td, $J_{C,F}$ = 18.1, 4.4 Hz), 146.57 (ddd, $J_{C,F}$ = 243.7, 12.4, 3.7 Hz), 148.14 (ddd, $J_{C,F}$ = 248.6, 14.3, 12.5 Hz), 155.73 (ddd, $J_{C,F}$ = 243.8, 9.2, 2.7 Hz). HRMS (ESI+): *m/z* calcd for $C_{16}H_{19}F_3N$ $[M + H]^+$ 282.1470; found 282.1464. IR (ATR): 3306, 2931, 2798, 1515, 1422, 1331, 1209, 1150, 1100, 843, 659 cm^{-1}. HPLC purity, 100% (t_R = 9.57 min).

4-(4-Fluorophenethyl)-1-(prop-2-yn-1-yl)piperidine (25). Synthesized from **17** (0.130 g, 0.423 mmol, 1.0 equiv) via general procedures D and E. Column chromatography, EtOAc/n-hex = 1/1 (v/v). Yield: 85% (88 mg); colorless oil. ^1H NMR (400 MHz, $CDCl_3$): δ 1.21−1.40 (m, 3H), 1.52−1.57 (m, 2H), 1.73−1.79 (m, 2H), 2.19−2.24 (m, 2H), 2.25 (t, *J* = 2.4 Hz, 1H), 2.57−2.61 (m, 2H), 2.89−2.93 (m, 2H), 3.33 (d, *J* = 2.4 Hz, 2H), 6.92−6.98 (m, 2H), 7.09−7.14 (m, 2H). ^{13}C NMR (100 MHz, $CDCl_3$): δ 32.07, 32.21, 34.61, 38.35, 47.16, 52.48, 73.09, 78.90, 114.99 (d, $J_{C,F}$ = 21.1 Hz), 129.54 (d, $J_{C,F}$ = 7.9 Hz), 138.16 (d, $J_{C,F}$ = 3.1 Hz), 161.11 (d, $J_{C,F}$ = 243.2 Hz). HRMS (ESI+): *m/z* calcd for $C_{16}H_{21}FN$ $[M + H]^+$ 246.1658; found 246.1657. IR (ATR): 3300, 2923, 1601, 1508, 1453, 1218, 1156, 824, 642 cm^{-1}. HPLC purity, 97.5% (t_R = 9.15 min).

1-(Prop-2-yn-1-yl)-4-(2,4,5-trifluorophenethyl)piperidine (26). Synthesized from **18** (0.175 g, 0.509 mmol, 1.0 equiv) via general procedures D and E. Column chromatography, EtOAc/n-hex = 1/1 (v/v). Yield: 32% (45 mg); yellow oil. ^1H NMR (400 MHz, $CDCl_3$): δ 1.22−1.39 (m, 3H), 1.49−1.55 (m, 2H), 1.72−1.79 (m, 2H), 2.17−2.23 (m, 2H), 2.23−2.25 (m, 1H), 2.59 (t, *J* = 7.8 Hz, 2H), 2.88−2.93 (m, 2H), 3.30−3.32 (m, 2H), 6.86 (ddd, *J* = 10.0, 9.5, 6.7 Hz, 1H), 6.97 (ddd, *J* = 10.7, 8.8, 6.5 Hz, 1H). ^{13}C NMR (100 MHz, $CDCl_3$): δ 25.56, 31.94, 34.68, 36.55, 47.13, 52.40, 73.16, 78.81, 105.18 (dd, $J_{C,F}$ = 28.7, 20.6 Hz), 117.66 (dd, $J_{C,F}$ = 19.1, 6.5 Hz), 125.50−125.82 (m), 146.57 (ddd, $J_{C,F}$ = 243.6, 12.6, 3.2 Hz), 148.09 (ddd, $J_{C,F}$ = 249.2, 13.4, 11.5 Hz); 155.72 (ddd, $J_{C,F}$ = 243.4, 9.3, 2.7 Hz). HRMS (ESI+): *m/z* calcd for $C_{16}H_{19}F_3N$ $[M + H]^+$ 282.1470; found 282.1471. IR (ATR): 3306, 2920, 2803, 1517, 1423, 1334, 1210, 1151, 1108, 876, 660 cm^{-1}. HPLC purity, 100% (t_R = 9.63 min).

Wittig Salts (27a−l). Synthesized according to general procedure A. The product was used in next reaction step without purification.

***tert*-Butyl 4-Styrylpiperidine-1-carboxylate [Isomers (*Z*)-28 and (*E*)-29].** Synthesized from aldehyde **3** (2.00 g, 9.38 mmol, 1.0 equiv), benzyltriphenylphosphonium chloride (4.01 g, 10.32 mmol, 1.1 equiv), and NaHMDS (2 N in THF, 5.63 mL, 11.26 mmol, 1.2 equiv) via general procedure B. Column chromatography, petroleum ether/Et_2O = 9/1 (v/v). Overall yield of reaction: 66% (mass of both *Z* and *E* isomers, 1.78 g); isolated pure *Z* isomer, 95 mg; isolated pure *E* isomer, 285 mg; mixture of *E*/*Z* isomers, 1.4 g.

28: R_f = 0.31 (petroleum ether/Et_2O = 9/1, v/v); colorless oil. ^1H NMR (400 MHz, $CDCl_3$): δ 1.36 (ddd, *J* = 17.1, 13.9, 5.3 Hz, 2H), 1.46 (s, 9H), 1.65−1.68 (m, 2H), 2.68−2.76 (m, 3H), 4.08 (bs, 2H), 5.45 (dd, *J* = 11.7, 10.0 Hz, 1H), 6.39 (d, *J* = 11.7 Hz, 1H), 7.21−7.25 (m, 3H), 7.31−7.35 (m, 2H). MS (ESI+): *m/z* $[M + Na]^+$ 310.18; found 310.17.

29: R_f = 0.28 (petroleum ether/Et_2O = 9/1, v/v); colorless oil. ^1H NMR (400 MHz, $CDCl_3$): δ 1.36 (ddd, *J* = 16.6, 12.6, 4.5 Hz, 2H), 1.47 (s, 9H), 1.73−1.76 (m, 2H), 2.22−2.31 (m, 1H), 2.77 (t, *J* =

https://dx.doi.org/10.1021/acs.jmedchem.9b01886
J. Med. Chem. XXXX, XXX, XXX−XXX

11.5 Hz, 2H), 4.12 (bs, 2H), 6.13 (dd, J = 17.0, 6.9 Hz, 1H), 6.38 (d, J = 16.0 Hz, 1H), 7.17−7.21 (m, 1H), 7.27−7.35 (m, 4H). MS (ESI+): m/z $[M + Na]^+$ 310.18; found 310.12.

***tert*-Butyl 4-(3-Fluorostyryl)piperidine-1-carboxylate [Isomers (*Z*)-30 and (*E*)-31].** Synthesized from aldehyde **3** (2.00 g, 9.38 mmol, 1.0 equiv), **27a** (4.20 g, 10.32 mmol, 1.1 equiv), and NaHMDS (2 N in THF, 5.63 mL, 11.26 mmol, 1.2 equiv) via general procedure B. Column chromatography, petroleum ether/Et_2O = 10/1 (v/v). Overall yield of reaction: 56% (mass of both *Z* and *E* isomers, 1.60 g); isolated pure *Z* isomer, 120 mg; isolated pure *E* isomer, 355 mg; mixture of *E*/*Z* isomers, 1.125 g.

30: R_f = 0.70 (EtOAc/n-hex = 1/2, v/v); pale yellow oil. ^{1}H NMR (400 MHz, $CDCl_3$): δ 1.35 (dt, J = 12.4, 3.9 Hz, 1H), 1.38 (dt, J = 12.2, 3.7 Hz, 1H), 1.46 (s, 9H), 1.60−1.69 (m, 2H), 2.62−2.77 (m, 3H), 4.09 (bs, 2H), 5.50 (dd, J = 11.6, 10.2 Hz, 1H), 6.35 (d, J = 11.6 Hz, 1H), 6.91−6.97 (m, 2H), 6.99−7.01 (m, 1H), 7.27−7.32 (m, 1H). MS (ESI+): m/z $[M + Na]^+$ 328.17; found 328.42.

31: R_f = 0.67 (EtOAc/n-hex = 1/2, v/v); white crystals, mp 45−46 °C. ^{1}H NMR (400 MHz, $CDCl_3$): δ 1.31−1.44 (m, 2H), 1.47 (s, 9H), 1.71−1.78 (m, 2H), 2.23−2.33 (m, 1H), 2.78 (t, J = 12.2 Hz, 2H), 4.13 (bs, 2H), 6.15 (dd, J = 16.0, 6.8 Hz, 1H), 6.35 (d, J = 16.0 Hz, 1H), 6.89 (ddt, J = 8.4, 2.6, 0.9 Hz, 1H), 7.02−7.06 (m, 1H), 7.07−7.11 (m, 1H), 7.25 (td, J = 8.0, 5.8 Hz, 1H). MS (ESI+): m/z $[M + Na]^+$ 328.17; found 328.40.

***tert*-Butyl 4-(2-Fluorostyryl)piperidine-1-carboxylate [Isomers (*Z*)-32 and (*E*)-33].** Synthesized from aldehyde **3** (1.50 g, 7.04 mmol, 1.0 equiv), **27b** (3.49 g, 7.74 mmol, 1.1 equiv), and NaHMDS (2 N in THF, 4.22 mL, 8.45 mmol, 1.2 equiv) via general procedure B. Column chromatography, petroleum ether/Et_2O = 10/1 (v/v). Overall yield of reaction: 58% (mass of both *Z* and *E* isomers, 1.25 g); isolated pure *Z* isomer, 252 mg; isolated pure *E* isomer, 194 mg; mixture of *E*/*Z* isomers, 0.804 g.

32: R_f = 0.16 (petroleum ether/Et_2O = 10/1, v/v); colorless oil. ^{1}H NMR (400 MHz, $CDCl_3$): δ 1.27−1.40 (m, 2H), 1.43 (s, 9H), 1.56−1.62 (m, 2H), 2.44−2.54 (m, 1H), 2.61−2.70 (m, 2H), 4.09 (bs, 2H), 5.53 (dd, J = 11.6, 10.2 Hz, 1H), 6.33 (d, J = 11.6 Hz, 1H), 6.96 (ddd, J = 10.8, 8.2, 1.3 Hz, 1H), 7.00−7.10 (m, 2H), 7.17−7.22 (m, 1H). MS (ESI+): m/z $[M + Na]^+$ 328.17; found 328.42.

33: R_f = 0.14 (petroleum ether/Et_2O = 10/1, v/v); colorless oil. ^{1}H NMR (400 MHz, $CDCl_3$): δ 1.36 (dt, J = 12.3, 4.2 Hz, 1H), 1.39 (dt, J = 12.3, 4.2 Hz, 1H), 1.46 (s, 9H), 1.70−1.77 (m, 2H), 2.23−2.33 (m, 1H), 2.76 (t, J = 11.0 Hz, 2H), 4.12 (bs, 2H), 6.20 (dd, J = 16.1, 7.0 Hz, 1H), 6.53 (d, J = 16.1 Hz, 1H), 6.99 (ddd, J = 10.8, 8.1, 1.2 Hz, 1H), 7.05 (dt, J = 7.6, 1.2 Hz, 1H), 7.12−7.18 (m, 1H), 7.41 (dt, J = 7.7, 1.8 Hz, 1H). MS (ESI+): m/z $[M + Na]^+$ 328.17; found 328.42.

***tert*-Butyl 4-(2-Chloro-4-fluorostyryl)piperidine-1-carboxylate [Isomers (*Z*)-34 and (*E*)-35].** Synthesized from aldehyde **3** (1.50 g, 7.03 mmol, 1.0 equiv), **27c** (3.76 g, 7.74 mmol, 1.1 equiv) and NaHMDS (2 N in THF, 4.22 mL, 8.44 mmol, 1.2 equiv) via general procedure B. Column chromatography, petroleum ether/Et_2O = 10/1 (v/v). Overall yield of reaction: 52% (mass of both *Z* and *E* isomers, 1.24 g); isolated pure *Z* isomer, 114 mg; isolated pure *E* isomer, 285 mg; mixture of *E*/*Z* isomers, 0.841 g.

34: R_f = 0.73 (EtOAc/n-hex = 1/2, v/v); colorless oil. ^{1}H NMR (400 MHz, $CDCl_3$): δ 1.27 (dt, J = 12.9, 4.4 Hz, 1H), 1.30 (dt, J = 12.3, 4.0 Hz, 1H), 1.39 (s, 9H), 1.50−1.58 (m, 2H), 2.60−2.40 (m, 1H), 2.60 (t, J = 11.4 Hz, 2H), 4.01 (bs, 2H), 5.51 (dd, J = 11.4, 10.2 Hz, 1H), 6.29 (d, J = 11.5 Hz, 1H), 6.89 (dt, J = 8.5, 3.0 Hz, 1H), 7.06 (dd, J = 8.5, 2.6 Hz, 1H), 7.13 (dd, J = 8.6, 6.2 Hz, 1H). MS (ESI+): m/z $[M + K]^+$ 378.10; found 378.66.

35: R_f = 0.68 (EtOAc/n-hex = 1/2, v/v); white crystals, mp 90−92 °C. ^{1}H NMR (400 MHz, $CDCl_3$): δ 1.36 (dt, J = 12.4, 4.1 Hz, 1H), 1.39 (dt, J = 12.3, 4.2 Hz, 1H), 1.46 (s, 9H), 1.72−1.79 (m, 2H), 2.27−2.36 (m, 1H), 2.77 (t, J = 11.4 Hz, 2H), 4.13 (bs, 2H), 6.04 (dd, J = 15.9, 6.9 Hz, 1H), 6.67 (d, J = 15.9 Hz, 1H), 6.92 (dt, J = 8.4, 2.6 Hz, 1H), 7.07 (dd, J = 8.5, 2.6 Hz, 1H), 7.44 (dd, J = 8.8, 6.1 Hz, 1H). MS (ESI+): m/z $[M + Na]^+$ 362.13; found 362.40.

***tert*-Butyl 4-(4-Methylstyryl)piperidine-1-carboxylate [Isomers (*Z*)-36 and (*E*)-37].** Synthesized from aldehyde **3** (1.49 g, 7.00 mmol, 1.0 equiv), **27d** (3.13 g, 7.00 mmol, 1.0 equiv), and KHMDS (0.5 M in toluene, 15.40 mL, 7.70 mmol, 1.1 equiv) via general procedure B. Column chromatography, EtOAc/n-hex = 1/5 (v/v). Overall yield of reaction: 45% (mass of both *Z* and *E* isomers, 0.94 g); isolated pure *Z* isomer, 159 mg; isolated pure *E* isomer, 155 mg; mixture of *E*/*Z* isomers, 0.626 g.

36: R_f = 0.75 (EtOAc/n-hex = 1/5, v/v); colorless oil. ^{1}H NMR (400 MHz, $CDCl_3$): δ 1.29−1.41 (m, 2H), 1.46 (s, 9H), 1.64−1.70 (m, 2H), 2.35 (s, 3H), 2.66−2.77 (m, 3H), 4.08 (bs, 2H), 5.41 (dd, J = 11.6, 10.0 Hz, 1H), 6.36 (d, J = 11.5 Hz, 1H), 7.12−7.17 (m, 4H). MS (ESI+): m/z $[M + Na]^+$ 324.19; found 324.63.

37: R_f = 0.72 (EtOAc/n-hex = 1/5, v/v); colorless oil. ^{1}H NMR (400 MHz, $CDCl_3$): δ 1.36 (dt, J = 12.2, 4.2 Hz, 1H), 1.39 (dt, J = 12.4, 4.3 Hz, 1H), 1.47 (s, 9H), 1.71−1.78 (m, 2H), 2.22−2.31 (m, 1H), 2.32 (s, 3H), 2.77 (t, J = 12,6 Hz, 2H), 4.12 (bs, 2H), 6.09 (dd, J = 16.0, 6.9 Hz, 1H), 6.35 (d, J = 15.8 Hz, 1H), 7.09−7.12 (m, 2H), 7.22−7.25 (m, 2H). MS (ESI+): m/z $[M + H]^+$ 302.21; found 302.60.

***tert*-Butyl 4-(4-Isopropylstyryl)piperidine-1-carboxylate [Isomers (*Z*)-38 and (*E*)-39].** Synthesized from aldehyde **3** (1.30 g, 6.10 mmol, 1.0 equiv), **27e** (3.19 g, 6.71 mmol, 1.1 equiv), and NaHMDS (2 N in THF, 3.66 mL, 7.32 mmol, 1.2 equiv) via general procedure B. Column chromatography, petroleum ether/Et_2O = 9/1 (v/v). Overall yield of reaction: 65% (mass of both *Z* and *E* isomers, 1.78 g); isolated pure *Z* isomer, 194 mg; isolated pure *E* isomer, 235 mg; mixture of *E*/*Z* isomers, 1.351 g.

38: R_f = 0.31 (petroleum ether/Et_2O = 10/1, v/v); colorless oil. ^{1}H NMR (400 MHz, $CDCl_3$): δ 1.28 (d, J = 7.0 Hz, 6H), 1.36 (dd, J = 11.9, 3.3 Hz, 1H), 1.39 (dd, J = 11.8, 3.0 Hz, 1H), 1.49 (s, 9H), 1.68−1.75 (m, 2H), 2.72−2.81 (m, 3H), 2.92 (sept, J = 6.9 Hz, 1H), 4.11 (bs, 2H), 5.42 (dd, J = 11.7, 10.0 Hz, 1H), 6.36 (d, J = 11.7 Hz, 1H), 7.18−7.23 (m, 4H). MS (ESI+): m/z $[M + Na]^+$ 352.22; found 352.00.

39: R_f = 0.24 (petroleum ether/Et_2O = 10/1, v/v); colorless oil. ^{1}H NMR (400 MHz, $CDCl_3$): δ 1.25 (d, J = 7.0 Hz, 6H), 1.37 (dd, J = 12.8, 4.1 Hz, 1H), 1.40 (dd, J = 12.1, 3.9 Hz, 1H), 1.49 (s, 9H), 1.71−1.79 (m, 2H), 2.22−2.30 (m, 1H), 2.78 (t, J = 11.4 Hz, 2H), 2.89 (sept, J = 7.0 Hz, 1H), 4.14 (bs, 2H), 6.11 (dd, J = 16.0, 6.9 Hz, 1H), 6.38 (d, J = 15.9 Hz, 1H), 7.16−7.18 (m, 2H), 7.28−7.30 (m, 2H). MS (ESI+): m/z $[M + Na]^+$ 352.22; found 352.01.

***tert*-Butyl 4-(4-Chlorostyryl)piperidine-1-carboxylate [Isomers (*Z*)-40 and (*E*)-41].** Synthesized from aldehyde **3** (2.00 g, 9.38 mmol, 1.0 equiv), **27f** (4.37 g, 10.32 mmol, 1.1 equiv), and NaHMDS (2 N in THF, 5.63 mL, 11.26 mmol, 1.2 equiv) via general procedure B. Column chromatography, petroleum ether/Et_2O = 10/1 (v/v). Overall yield of reaction: 63% (mass of both *Z* and *E* isomers, 1.78 g); isolated pure *Z* isomer, 202 mg; isolated pure *E* isomer, 221 mg; mixture of *E*/*Z* isomers, 1.357 g.

40: R_f = 0.15 (petroleum ether/Et_2O = 10/1, v/v); white crystals, mp 69−70 °C. ^{1}H NMR (400 MHz, $CDCl_3$): δ 1.38 (ddd, J = 17.4, 13.3, 4.7 Hz, 2H), 1.46 (s, 9H), 1.61−1.67 (m, 2H), 2.58−2.76 (m, 3H), 4.08 (bs, 2H), 5.47 (dd, J = 11.6, 10.1 Hz, 1H), 6.36 (d, J = 11.7 Hz, 1H), 7.14−7.17 (m, 2H), 7.28−7.32 (m, 2H). MS (ESI+): m/z $[M + Na]^+$ 344.14; found 344.54.

41: R_f = 0.10 (petroleum ether/Et_2O = 10/1, v/v); white crystals, mp 60−62 °C. ^{1}H NMR (400 MHz, $CDCl_3$): δ 1.35 (dd, J = 12.4, 4.1 Hz, 1H), 1.38 (dd, J = 12.2, 4.1 Hz, 1H), 1.46 (s, 9H), 1.71−1.77 (m, 2H), 2.22−2.31 (m, 1H), 2.77 (t, J = 11.5 Hz, 2H), 4.14 (bs, 2H), 6.11 (dd, J = 16.0, 6.9 Hz, 1H), 6.32 (dd, J = 16.0, 1.2 Hz, 1H), 7.52 (s, 4H). MS (ESI+): m/z $[M + Na]^+$ 344.14; found 344.48.

***tert*-Butyl 4-(4-Bromostyryl)piperidine-1-carboxylate [Isomers (*Z*)-42 and (*E*)-43].** Synthesized from aldehyde **3** (2.00 g, 9.38 mmol, 1.0 equiv), **27g** (5.28 g, 10.31 mmol, 1.1 equiv), and NaHMDS (2 N in THF, 5.63 mL, 11.26 mmol, 1.2 equiv) via general procedure B. Column chromatography, EtOAc/n-hex = 1/2 (v/v). Overall yield of reaction: 48% (mass of both *Z* and *E* isomers, 1.66 g); pure *Z* isomer was not isolated; isolated pure *E* isomer, 325 mg; mixture of *E*/*Z* isomers, 1.335 g.

43: R_f = 0.40 (EtOAc/n-hex = 1/2, v/v); white crystals, mp 65−67 °C. ^{1}H NMR (400 MHz, $CDCl_3$): δ 1.36 (dt, J = 12.4, 4.2 Hz, 1H),

https://dx.doi.org/10.1021/acs.jmedchem.9b01886
J. Med. Chem. XXXX, XXX, XXX−XXX

1.39 (dt, J = 12.4, 4.5 Hz, 1H), 1.47 (s, 9H), 1.71−1.78 (m, 2H), 2.22−2.32 (m, 1H), 2.74−2.81 (m, 2H), 4.12 (bs, 2H), 6.13 (dd, J = 16.0, 6.8 Hz, 1H), 6.32 (d, J = 16.0 Hz, 1H), 7.19−7.22 (m, 2H), 7.39−7.43 (m, 2H).

***tert*-Butyl 4-(4-Methoxystyryl)piperidine-1-carboxylate [Isomers (*Z*)-44 and (*E*)-45].** Synthesized from aldehyde **3** (1.87 g, 8.77 mmol, 1.0 equiv), **27h** (4.04 g, 9.65 mmol, 1.1 equiv), and NaHMDS (2 N in THF, 5.26 mL, 10.52 mmol, 1.2 equiv) via general procedure B. Column chromatography, EtOAc/n-hex = 1/9 (v/v) yielding a mixture of *cis*/*trans* isomers (ratio 20/80, estimated from ^{1}H NMR). Overall yield of reaction: 40% (mass of both *Z* and *E* isomers, 1.12 g); pure *Z* and *E* isomers were not isolated.

44 and **45** (mixture of both isomers): R_f = 0.13 (EtOAc/n-hex = 1/9, v/v); colorless oil. ^{1}H NMR (400 MHz, $CDCl_3$): δ 1.31−1.41 (m, 2.6H), 1.46−1.47 (m, 11.5H), 1.63−1.75 (m, 2.6H), 2.20−2.29 (m, 1H), 2.69−2.82 (m, 2.6H), 3.78 (s, 3H), 3.78 (s, 0.7H), 4.12 (bs, 2.6H), 5.36 (dd, J = 11.6, 10.0 Hz, 0.2H), 5.99 (dd, J = 16.0, 6.9 Hz, 1H), 6.30−6.34 (m, 1.2H), 6.81−6.85 (m, 2H), 6.85−6.89 (m, 0.5H), 7.16−7.19 (m, 0.5H), 7.24−7.29 (m, 2H). MS (ESI+): m/z $[M + Na]^+$ 340.19; found 340.04.

***tert*-Butyl 4-(4-(Trifluoromethyl)styryl)piperidine-1-carboxylate [Isomers (*Z*)-46 and (*E*)-47].** Synthesized from aldehyde **3** (2.00 g, 9.38 mmol, 1.0 equiv), **27i** (5.56 g, 10.32 mmol, 1.1 equiv), and NaHMDS (2 N in THF, 5.63 mL, 11.26 mmol, 1.2 equiv) via general procedure B. Column chromatography, petroleum ether/Et_2O = 9/1 (v/v). Overall yield of reaction: 66% (mass of both *Z* and *E* isomers, 2.18 g); isolated pure *Z* isomer, 85 mg; isolated pure *E* isomer, 780 mg; mixture of *E*/*Z* isomers, 1.305 g.

46: R_f = 0.23 (petroleum ether/Et_2O = 9/1, v/v); colorless oil. ^{1}H NMR (400 MHz, $CDCl_3$): δ 1.32−1.42 (m, 2H), 1.45 (s, 9H), 1.62−1.67 (m, 2H), 2.59−2.68 (m, 1H), 2.71 (t, J = 12.8 Hz, 2H), 4.09 (bs, 2H), 5.56 (dd, J = 11.7, 10.2 Hz, 1H), 6.36 (d, J = 11.7 Hz, 1H), 7.32 (d, J = 8.5 Hz, 2H), 7.58 (d, J = 8.1 Hz, 2H).

47: R_f = 0.18 (petroleum ether/Et_2O = 9/1, v/v); white crystals, mp 46−48 °C. ^{1}H NMR (400 MHz, $CDCl_3$): δ 1.35 (dd, J = 12.2, 4.1 Hz, 1H), 1.39 (dd, J = 12.5, 4.1 Hz, 1H), 1.46 (s, 9H), 1.71−1.77 (m, 2H), 2.24−2.33 (m, 1H), 2.76 (t, J = 11.4 Hz, 2H), 4.14 (bs, 2H), 6.22 (dd, J = 16.0, 6.8 Hz, 1H), 6.38 (d, J = 16.1 Hz, 1H), 7.40 (d, J = 8.4 Hz, 2H), 7.51 (d, J = 8.2 Hz, 2H).

***tert*-Butyl 4-(3-(Trifluoromethyl)styryl)piperidine-1-carboxylate [Isomers (*Z*)-48 and (*E*)-49].** Synthesized from aldehyde **3** (1.49 g, 7.00 mmol, 1.0 equiv), **27j** (3.51 g, 7.00 mmol, 1.0 equiv), and KHMDS (0.5 M in toluene, 15.40 mL, 7.70 mmol, 1.1 equiv) via general procedure B. Column chromatography, petroleum ether/Et_2O = 8/1, (v/v). Overall yield of reaction: 62% (mass of both *Z* and *E* isomers, 1.53 g); isolated pure *Z* isomer, 51 mg; isolated pure *E* isomer, 404 mg; mixture of *E*/*Z* isomers, 1.075 g.

48: R_f = 0.20 (petroleum ether/Et_2O = 8/1, v/v), colorless oil. ^{1}H NMR (400 MHz, $CDCl_3$): δ: 1.35 (dt, J = 12.6, 4.0 Hz, 1H), 1.36−1.43 (m, 1H), 1.45 (s, 9H), 1.61−1.68 (m, 2H), 2.56−2.66 (m, 1H), 2.71 (t, J = 11.2 Hz, 2H), 4.08 (bs, 2H), 5.55 (dd, J = 11.6, 10.2 Hz, 1H), 6.40 (d, J = 11.6 Hz, 1H), 7.38−7.50 (m, 4H). MS (ESI+): m/z $[M + Na]^+$ 378.17; found 378.76.

49: R_f = 0.15 (petroleum ether/Et_2O = 8/1, v/v); colorless oil. ^{1}H NMR (400 MHz, $CDCl_3$): δ 1.37 (dt, J = 12.4, 4.3 Hz, 1H), 1.40 (dt, J = 12.2, 4.1 Hz, 1H), 1.47 (s, 9H), 1.73−1.80 (m, 2H), 2.26−2.36 (m, 1H), 2.78 (t, J = 12.0 Hz, 2H), 4.14 (bs, 2H), 6.22 (dd, J = 16.0, 6.9 Hz, 1H), 6.41 (d, J = 16.0 Hz, 1H), 7.38−7.46 (m, 2H), 7.48−7.51 (m, 1H), 7.57−7.59 (m, 1H). MS (ESI+): m/z $[M + Na]^+$ 378.17; found 378.69.

***tert*-Butyl 4-(4-Cyanostyryl)piperidine-1-carboxylate [Isomers (*Z*)-50 and (*E*)-51].** Synthesized from aldehyde **3** (2.35 g, 11.02 mmol, 1.0 equiv), **27k** (5.56 g, 12.12 mmol, 1.1 equiv), and NaHMDS (2 N in THF, 6.61 mL, 13.22 mmol, 1.2 equiv) via general procedure B. Column chromatography, petroleum ether/Et_2O = 3/1 (v/v). Overall yield of reaction: 39% (mass of both *Z* and *E* isomers, 1.35 g); isolated pure *Z* isomer, 370 mg; isolated pure *E* isomer, 320 mg; mixture of *E*/*Z* isomers, 0.66 g.

50: R_f = 0.20 (petroleum ether/Et_2O = 3/1, v/v); white crystals, mp 65−68 °C. ^{1}H NMR (400 MHz, $CDCl_3$): δ 1.31−1.40 (m, 2H), 1.43 (s, 9H), 1.57−1.64 (m, 2H), 2.54−2.64 (m, 1H), 2.70 (t, J = 11.7 Hz, 2H), 4.05 (bs, 2H), 5.58 (dd, J = 11.7, 10.2 Hz, 1H), 6.36 (d, J = 11.8 Hz, 1H), 7.28−7.31 (m, 2H), 7.58−7.61 (m, 2H). MS (ESI+): m/z $[M + Na]^+$ 335.17; found 335.31.

51: R_f = 0.14 (petroleum ether/Et_2O = 3/1, v/v); white crystals, mp 88−90 °C. ^{1}H NMR (400 MHz, $CDCl_3$): δ 1.30−1.40 (m, 2H), 1.43 (s, 9H), 1.70−1.75 (m, 2H), 2.25−2.34 (m, 1H), 2.75 (t, J = 10.7 Hz, 2H), 4.11 (bs, 2H), 6.26 (dd, J = 16.0, 6.6 Hz, 1H), 6.36 (d, J = 16.0 Hz, 1H), 7.37−7.39 (m, 2H), 7.52−7.55 (m, 2H). MS (ESI+): m/z $[M - H]^-$ 311.17; found 311.37.

***tert*-Butyl 4-(4-(Methylsulfonyl)styryl)piperidine-1-carboxylate [Isomers (*Z*)-52 and (*E*)-53].** Synthesized from aldehyde **3** (0.94 g, 4.10 mmol, 1.0 equiv), **27l** (1.94 g, 4.50 mmol, 1.1 equiv), and NaHMDS (2 N in THF, 2.45 mL, 4.90 mmol, 1.2 equiv) via general procedure B. Column chromatography, EtOAc/n-hex = 1/2 (v/v). Overall yield of reaction: 30% (mass of both *Z* and *E* isomers, 0.46 g); isolated pure *Z* isomer, 180 mg; isolated pure *E* isomer, 260 mg; mixture of *E*/*Z* isomers, 0.02 g.

52: R_f = 0.27 (EtOAc/n-hex = 1/2, v/v); colorless oil. ^{1}H NMR (400 MHz, $CDCl_3$): δ 1.34−1.45 (m, 2H), 1.47 (s, 9H), 1.62−1.69 (m, 2H), 2.58−2.68 (m, 1H), 2.72 (t, J = 12.0 Hz, 2H), 3.08 (s, 3H), 4.11 (bs, 2H), 5.62 (dd, J = 11.6, 10.4 Hz, 1H), 6.44 (d, J = 11.6 Hz, 1H), 7.40−7.43 (m, 2H), 7.90−7.93 (m, 2H). MS (ESI+): m/z $[M + Na]^+$ 388.16; found 387.91.

53: R_f = 0.22 (EtOAc/n-hex = 1/2, v/v); white crystals, mp 93−97 °C. ^{1}H NMR (400 MHz, $CDCl_3$): δ 1.38 (dt, J = 12.4, 4.1 Hz, 1H), 1.41 (dd, J = 12.4, 4.0 Hz, 1H), 1.47 (s, 9H), 1.75−1.83 (m, 2H), 2.30−2.39 (m, 1H), 2.79 (t, J = 10.7 Hz, 2H), 3.05 (s, 3H), 4.15 (bs, 2H), 6.33 (dd, J = 16.0, 6.7 Hz, 1H), 6.45 (d, J = 16.0 Hz, 1H), 7.50−7.53 (m, 2H), 7.85−7.88 (m, 2H). MS (ESI+): m/z $[M + Na]^+$ 388.16; found 387.91.

***tert*-Butyl 4-(4-Cyclopropylstyryl)piperidine-1-carboxylate [Isomers (*Z*)-54 and (*E*)-55].** To the solution of **42** and **43** (0.733 g, 2.0 mmol, 1.0 equiv), cyclopropylboronic acid (0.224 g, 2.60 mmol, 1.3 equiv), K_3PO_4 (1.48 g, 7.00 mmol, 3.5 equiv) and tricyclohexylphosphine (20% solution in toluene, 0.316 mL, 0.20 mmol, 0.1 equiv) in toluene (10 mL) and water (0.4 mL), $Pd(OAc)_2$ (23 mg, 0.1 mmol, 0.05 equiv) was added under an argon atmosphere. The reaction mixture was stirred at 100 °C for 3 h and then allowed to cool down to room temperature. Water (20 mL) was added to the mixture, which was then transferred into a separating funnel, and extracted with EtOAc (2 × 50 mL). Combined organic layers were washed with saturated brine (20 mL), dried over Na_2SO_4, and evaporated. Column chromatography, petroleum ether/Et_2O = 10/1 (v/v). Overall yield of reaction: 78% (mass of both *Z* and *E* isomers, 0.511 g); isolated pure *Z* isomer, 85 mg; isolated pure *E* isomer, 210 mg; mixture of *E*/*Z* isomers, 0.216 g.

54: R_f = 0.29 (petroleum ether/Et_2O = 10/1, v/v); colorless oil. ^{1}H NMR (400 MHz, $CDCl_3$): δ 0.68−0.73 (m, 2H), 0.94−1.00 (m, 2H), 1.30−1.41 (m, 2H), 1.47 (s, 9H), 1.63−1.70 (m, 2H), 1.86−1.93 (m, 1H), 2.67−2.79 (m, 3H), 4.09 (bs, 2H), 5.40 (dd, J = 11.6, 10.0 Hz, 1H), 6.35 (d, J = 11.6 Hz, 1H), 7.03−7.06 (m, 2H), 7.12−7.16 (m, 2H).

55: R_f = 0.22 (petroleum ether/Et_2O = 10/1, v/v); colorless oil. ^{1}H NMR (400 MHz, $CDCl_3$): δ 0.66−0.70 (m, 2H), 0.92−0.97 (m, 2H), 1.36 (dt, J = 12.7, 4.4 Hz, 1H), 1.39 (dt, J = 12.3, 4.1 Hz, 1H), 1.48 (s, 9H), 1.70−1.78 (m, 2H), 1.83−1.90 (m, 1H), 2.21−2.31 (m, 1H), 2.78 (t, J = 11.6 Hz, 2H), 4.13 (bs, 2H), 6.08 (dd, J = 16.0, 6.9 Hz, 1H), 6.34 (d, J = 16.0 Hz, 1H), 6.98−7.02 (m, 2H), 7.22−7.25 (m, 2H).

***tert*-Butyl 4-Phenethylpiperidine-1-carboxylate (56).** Synthesized from a mixture of **28** and **29** (1.139 g, 4.84 mmol, 1.0 equiv) via general procedure C. Yield: quantitative (1.39 g); colorless oil. ^{1}H NMR (400 MHz, $CDCl_3$): δ 1.21 (ddd, J = 16.5, 12.5, 4.3 Hz, 2H), 1.35−1.43 (m, 1H), 1.45 (s, 9H), 1.53−1.59 (m, 2H), 1.68−1.71 (m, 2H), 2.60−2.69 (m, 4H), 4.07 (bs, 2H), 7.15−7.19 (m, 3H), 7.24−7.29 (m, 2H). MS (ESI+): m/z $[M + Na]^+$ 312.19; found 311.91.

***tert*-Butyl 4-(3-Fluorophenethyl)piperidine-1-carboxylate (57).** Synthesized from a mixture of **30** and **31** (0.452 g, 1.48 mmol, 1.0 equiv) via general procedure C. Yield: 95% (0.432 g); pale

https://dx.doi.org/10.1021/acs.jmedchem.9b01886
J. Med. Chem. XXXX, XXX, XXX−XXX

yellow oil. ^{1}H NMR (400 MHz, $CDCl_3$): δ 1.11 (dt, J = 12.3, 4.1 Hz, 1H), 1.14 (dt, J = 12.5, 4.2 Hz, 1H), 1.35−1.44 (m, 1H), 1.45 (s, 9H), 1.50−1.59 (m, 2H), 1.65−1.72 (m, 2H), 2.59−2.72 (m, 4H), 4.08 (bs, 2H), 6.84−6.89 (m, 2H), 6.91−6.95 (m, 1H), 7.22 (ddd, J = 8.9, 7.6, 6.1 Hz, 1H). MS (ESI+): m/z $[M + Na]^+$ 330.18; found 330.42.

***tert*-Butyl 4-(2-Fluorophenethyl)piperidine-1-carboxylate (58).** Synthesized from a mixture of **32** and **33** (0.252 g, 0.83 mmol, 1.0 equiv) via general procedure C. Yield: 95% (0.242 g); pale yellow oil. ^{1}H NMR (400 MHz, $CDCl_3$): δ 1.12 (dt, J = 12.4, 4.1 Hz, 1H), 1.15 (dt, J = 12.4, 4.2 Hz, 1H), 1.37−1.44 (m, 1H), 1.46 (s, 9H), 1.52−1.59 (m, 2H), 1.69−1.76 (m, 2H), 2.58−2.72 (m, 4H), 4.08 (bs, 2H), 6.97−7.02 (m, 1H), 7.03−7.04 (m, 1H), 7.13−7.19 (m, 2H). MS (ESI+): m/z $[M + Na]^+$ 330.18; found 330.41.

***tert*-Butyl 4-(4-Methylphenethyl)piperidine-1-carboxylate (59).** Synthesized from a mixture of **36** and **37** (0.28 g, 0.93 mmol, 1.0 equiv) via general procedure C. Yield: quantitative; yellow oil. ^{1}H NMR (400 MHz, $CDCl_3$): δ 1.11 (dt, J = 12.3, 4.1 Hz, 1H), 1.14 (dt, J = 12.4, 4.1 Hz, 1H), 1.36−1.44 (m, 1H), 1.45 (s, 9H), 1.51−1.57 (m, 2H), 1.65−1.73 (m, 2H), 2.32 (s, 3H), 2.56−2.61 (m, 2H), 2.63−2.70 (m, 2H), 4.07 (bs, 2H), 7.04−7.10 (m, 4H). MS (ESI+): m/z $[M + Na]^+$ 326.21; found 326.73.

***tert*-Butyl 4-(4-Isopropylphenethyl)piperidine-1-carboxylate (60).** Synthesized from a mixture of **38** and **39** (0.870 g, 2.64 mmol, 1.0 equiv) via general procedure C. Yield: 83% (0.727 g); colorless oil. ^{1}H NMR (400 MHz, $CDCl_3$): δ 1.16 (ddd, J = 16.9, 12.9, 5.5 Hz, 2H), 1.27 (d, J = 7.0 Hz, 6H), 1.40−1.47 (m, 1H), 1.49 (s, 9H), 1.54−1.61 (m, 2H), 1.70−1.76 (m, 2H), 2.61−2.64 (m, 2H), 2.70 (t, J = 11.5 Hz, 2H), 2.91 (sept. J = 6.9 Hz, 1H), 4.10 (bs, 2H), 7.11−7.13 (m, 2H), 7.16−7.18 (m, 2H). MS (ESI+): m/z $[M + Na]^+$ 354.24; found 354.05.

***tert*-Butyl 4-(4-Chlorophenethyl)piperidine-1-carboxylate (61).** Synthesized from a mixture of **40** and **41** (0.850 g, 2.64 mmol, 1.0 equiv) via general procedure C. Column chromatography, petroleum ether/Et_2O = 3/1 (v/v). Yield: 86% (0.736 g); colorless oil. ^{1}H NMR (400 MHz, $CDCl_3$): δ 1.08 (dd, J = 12.3, 4.2 Hz, 1H), 1.11 (dd, J = 12.8, 3.9 Hz, 1H), 1.33−1.40 (m, 1H), 1.44 (s, 9H), 1.48−1.53 (m, 2H), 1.63−1.68 (m, 2H), 2.55−2.59 (m, 2H), 2.64 (t, J = 11.6 Hz, 2H), 4.07 (bs, 2H), 7.05−7.08 (m, 2H), 7.18−7.22 (m, 2H). MS (ESI+): m/z $[M + Na]^+$ 346.15; found 346.55.

***tert*-Butyl 4-(4-Methoxyphenethyl)piperidine-1-carboxylate (62).** Synthesized from a mixture of **44** and **45** (0.250 g, 0.79 mmol, 1.0 equiv) via general procedure C. Yield: 86% (0.245 g); colorless oil. ^{1}H NMR (400 MHz, $CDCl_3$): δ 1.12 (ddd, J = 16.3, 12.5, 4.3 Hz, 2H), 1.35−1.43 (m, 1H), 1.45 (s, 9H), 1.50−1.56 (m, 2H), 1.64−1.71 (m, 2H), 2.55−2.59 (m, 2H), 2.66 (t, J = 11.8 Hz, 2H), 3.79 (s, 3H), 4.07 (bs, 2H), 6.81−6.84 (m, 2H), 7.07−7.10 (m, 2H). MS (ESI+): m/z $[M + Na]^+$ 342.20; found 342.59.

***tert*-Butyl 4-(4-(Trifluoromethyl)phenethyl)piperidine-1-carboxylate (63).** Synthesized from a mixture of **46** and **47** (0.24 g, 0.68 mmol, 1.0 equiv) via general procedure C. Yield: quantitative; yellow oil. ^{1}H NMR (400 MHz, $CDCl_3$): δ 1.12 (dt, J = 12.4, 4.2 Hz, 1H), 1.15 (dt, J = 12.3, 4.3 Hz, 1H), 1.36−1.44 (m, 1H), 1.45 (s, 9H), 1.53−1.61 (m, 2H), 1.65−1.73 (m, 2H), 2.60−2.70 (m, 4H), 4.08 (bs, 2H), 7.25−7.28 (m, 2H), 7.50−7.53 (m, 2H).

***tert*-Butyl 4-(3-(Trifluoromethyl)phenethyl)piperidine-1-carboxylate (64).** Synthesized from a mixture of **48** and **49** (0.27 g, 0.76 mmol, 1.0 equiv) via general procedure C. Yield: quantitative; colorless oil. ^{1}H NMR (400 MHz, $CDCl_3$): δ 1.13 (dt, J = 12.2, 4.2 Hz, 1H), 1.16 (dt, J = 12.4, 4.2 Hz, 1H), 1.37−1.45 (m, 1H), 1.46 (s, 9H), 1.55−1.61 (m, 2H), 1.67−1.74 (m, 2H), 2.63−2.72 (m, 4H), 4.09 (bs, 2H), 7.34−7.45 (m, 4H). MS (ESI+): m/z $[M + Na]^+$ 380.18; found 380.77.

***tert*-Butyl 4-(4-Cyanophenethyl)piperidine-1-carboxylate (65).** Synthesized from a mixture of **50** and **51** (0.658 g, 2.11 mmol, 1.0 equiv) via general procedure C. Column chromatography, petroleum ether/Et_2O = 3/1 (v/v). Yield: 95% (0.632 g); colorless oil. ^{1}H NMR (400 MHz, $CDCl_3$): δ 1.09 (dd, J = 12.4, 4.2 Hz, 1H), 1.12 (dd, J = 12.5, 4.3 Hz, 1H), 1.34−1.40 (m, 1H), 1.42 (s, 9H), 1.51−1.58 (m, 2H), 1.63−1.68 (m, 2H), 2.61−2.68 (m, 4H), 4.06 (bs, 2H), 7.23−7.25 (m, 2H), 7.51−7.54 (m, 2H). MS (ESI+): m/z $[M + Na]^+$ 337.19; found 337.07.

***tert*-Butyl 4-(4-Propylphenethyl)piperidine-1-carboxylate (66).** Synthesized from a mixture of **54** and **55** (0.216 g, 0.660 mmol, 1.0 equiv) via general procedure C. The reaction conditions applied resulted in cyclopropyl ring opening to yield the titled compound. Yield: 92% (0.200 g); colorless oil. ^{1}H NMR (400 MHz, $CDCl_3$): δ 0.95 (t, J = 7.3 Hz, 3H), 1.07−1.17 (m, 2H), 1.37−1.45 (m, 1H), 1.45 (s, 9H), 1.52−1.67 (m, 6H), 2.53−2.61 (m, 4H), 2.67 (t, J = 13.0 Hz, 2H), 4.07 (bs, 2H), 7.06−7.11 (m, 4H). ^{13}C NMR (100 MHz, $CDCl_3$): δ 13.89, 24.63, 28.47, 32.11, 32.48, 35.53, 37.64, 38.41, 43.98, 79.17, 128.10, 128.40, 139.65, 140.03, 154.89. HRMS (ESI+): m/z calcd for $C_{21}H_{33}O_2NNa$ $[M + Na]^+$ 354.2404; found 354.2401.

***(Z)*-1-(Prop-2-yn-1-yl)-4-styrylpiperidine (67).** Synthesized from **28** (0.100 g, 0.348 mmol, 1.0 equiv) via general procedures D and E. Column chromatography, EtOAc/n-hex = 1/1 (v/v). Yield: 82% (64 mg); white crystals, mp 42−43 °C. ^{1}H NMR (400 MHz, $CDCl_3$): δ 1.50−1.60 (m, 2H), 1.74 (bd, J = 16.0 Hz, 2H), 2.19−2.26 (m, 3H), 2.52−2.62 (m, 1H), 2.86−2.90 (m, 2H), 3.29 (d, J = 2.4 Hz, 2H), 5.49 (dd, J = 11.4, 10.3 Hz, 1H), 6.38 (d, J = 11.7 Hz, 1H), 7.21−7.25 (m, 3H), 7.31−7.35 (m, 2H). ^{13}C NMR (100 MHz, $CDCl_3$): δ 32.29, 34.38, 47.23, 51.87, 72.93, 79.03, 126.55, 128.03, 128.18, 128.45, 137.19, 137.57. HRMS (ESI+): m/z calcd for $C_{16}H_{20}N$ $[M + H]^+$ 226.1596; found 226.1598. IR (ATR): 3210, 2988, 2945, 2917, 2800, 1498, 1446, 1425, 1330, 1311, 1127, 1103, 1073, 969, 904, 799, 775, 727, 696, 670, 560 cm^{-1}. HPLC purity, 99.9% (t_R = 8.86 min).

***(E)*-1-(Prop-2-yn-1-yl)-4-styrylpiperidine (68).** Synthesized from **29** (0.196 g, 0.682 mmol, 1.0 equiv) via general procedures D and E. Column chromatography, EtOAc/n-hex = 1/1 (v/v). Yield: 89% (137 mg); white crystals, mp 44−46 °C. ^{1}H NMR (400 MHz, $CDCl_3$): δ 1.56 (dd, J = 11.9, 3.9 Hz, 1H), 1.59 (dd, J = 11.9, 3.9 Hz, 1H), 1.79−1.84 (m, 2H), 2.09−2.19 (m, 1H), 2.25−2.31 (m, 3H), 2.94 (td, J = 11.1, 2.4 Hz, 2H), 3.33 (d, J = 2.5 Hz, 2H), 6.18 (dd, J = 16.0, 7.0 Hz, 1H), 6.39 (d, J = 16.5 Hz, 1H), 7.18−7.22 (m, 1H), 7.26−7.32 (m, 2H), 7.34−7.37 (m, 2H). ^{13}C NMR (100 MHz, $CDCl_3$): δ 31.91, 38.71, 47.13, 52.13, 72.91, 78.98, 125.87, 126.85, 128.10, 128.35, 134.76, 137.47. HRMS (ESI+): m/z calcd for $C_{16}H_{20}N$ $[M + H]^+$ 226.1596; found 226.1594. IR (ATR): 3264, 2929, 2909, 2805, 1446, 1429, 1315, 1223, 1135, 1106, 976, 962, 897, 744, 686, 670, 619, 519 cm^{-1}. HPLC purity, 99.2% (t_R = 8.90 min).

***(Z)*-4-(3-Fluorostyryl)-1-(prop-2-yn-1-yl)piperidine (69).** Synthesized from **30** (110 mg, 0.360 mmol, 1.0 equiv) via general procedures D and E. Column chromatography, EtOAc/n-hex = 1/2 (v/v). Yield: 12% (11 mg); yellow crystals, mp 51−53 °C. ^{1}H NMR (400 MHz, $CDCl_3$): δ 1.49−1.60 (m, 2H), 1.69−1.76 (m, 2H), 2.23 (dt, J = 11.7, 2.5 Hz, 2H), 2.24 (t, J = 2.4 Hz, 1H), 2.48−2.58 (m, 1H), 2.86−2.91 (m, 2H), 3.30 (d, J = 2.4 Hz, 2H), 5.53 (dd, J = 11.6, 10.2 Hz, 1H), 6.33 (d, J = 11.7 Hz, 1H), 6.90−6.95 (m, 2H), 6.99−7.01 (m, 1H), 7.26−7.31 (m, 1H). ^{13}C NMR (100 MHz, $CDCl_3$): δ 32.16, 34.45, 47.23, 51.81, 73.02, 78.96, 113.44 (d, $J_{C,F}$ = 21.2 Hz), 115.17 (d, $J_{C,F}$ = 21.3 Hz), 124.22 (d, $J_{C,F}$ = 2.8 Hz), 127.01 (d, $J_{C,F}$ = 2.1 Hz), 129.62 (d, $J_{C,F}$ = 8.6 Hz), 138.29, 139.76 (d, $J_{C,F}$ = 7.9 Hz), 162.66 (d, $J_{C,F}$ = 245.2 Hz). HRMS (ESI+): m/z calcd for $C_{16}H_{19}FN$ $[M + H]^+$ 244.1502; found 244.1504. IR (ATR): 3304, 2924, 2851, 2805, 2755, 1611, 1580, 1513, 1487, 1465, 1444, 1386, 1364, 1335, 1311, 1272, 1247, 1231, 1138, 1124, 1105, 1073, 1018, 973, 937, 923, 878, 792, 764, 752, 694, 667, 634 cm^{-1}. HPLC purity, 97.9% (t_R = 9.10 min).

***(E)*-4-(3-Fluorostyryl)-1-(prop-2-yn-1-yl)piperidine (70).** Synthesized from **31** (0.300 g, 0.982 mmol, 1.0 equiv) via general procedures D and E. Column chromatography, EtOAc/n-hex = 1/2 (v/v). Yield: 38% (91 mg); pale yellow oil. ^{1}H NMR (400 MHz, $CDCl_3$): δ 1.57 (dt, J = 12.0, 3.9 Hz, 1H), 1.60 (dt, J = 11.9, 3.9 Hz, 1H), 1.78−1.84 (m, 2H), 2.10−2.19 (m, 1H), 2.27 (t, J = 2.5 Hz, 1H), 2.31 (dt, J = 11.7, 2.5 Hz, 2H), 2.93−2.98 (m, 2H), 3.35 (d, J = 2.5 Hz, 2H), 6.17 (dd, J = 16.0, 6.9 Hz, 1H), 6.34 (d, J = 16.0 Hz, 1H), 6.88 (ddt, J = 8.4, 2.6, 0.9 Hz, 1H), 7.02−7.06 (m, 1H), 7.07−7.11 (m, 1H), 7.21−7.27 (m, 1H). ^{13}C NMR (100 MHz, $CDCl_3$): δ

https://dx.doi.org/10.1021/acs.jmedchem.9b01886
J. Med. Chem. XXXX, XXX, XXX−XXX

31.71, 38.64, 47.15, 52.10, 73.32, 78.62, 112.39 (d, $J_{C,F}$ = 22.0 Hz), 113.73 (d, $J_{C,F}$ = 21.3 Hz), 121.87 (d, $J_{C,F}$ = 2.9 Hz), 127.33 (d, $J_{C,F}$ = 2.9 Hz), 129.84 (d, $J_{C,F}$ = 8.7 Hz), 136.10, 139.94 (d, $J_{C,F}$ = 7.3 Hz), 163.06 (d, $J_{C,F}$ = 244.9 Hz). HRMS (ESI+): *m/z* calcd for $C_{16}H_{19}FN$ $[M + H]^+$ 244.1502; found 244.1504. IR (ATR): 3303, 2931, 2808, 2751, 1651, 1611, 1583, 491, 1466, 1445, 1385, 1364, 1336, 1312, 1267, 1245, 1140, 1106, 1074, 962, 939, 897, 873, 829, 809, 777, 684, 631, 590 cm^{-1}. HPLC purity, 99.6% (t_R = 9.15 min).

(*Z*)-4-(2-Fluorostyryl)-1-(prop-2-yn-1-yl)piperidine (71). Synthesized **32** (225 mg, 0.737 mmol, 1.0 equiv) via general procedures D and E. Column chromatography, EtOAc/n-hex = 1/2 (v/v). Yield: 5% (9 mg); colorless oil. ^1H NMR (400 MHz, $CDCl_3$): δ 1.49−1.59 (m, 2H), 1.68−1.75 (m, 2H), 2.16−2.23 (m, 2H), 2.23 (t, *J* = 2.4 Hz, 1H), 2.33−2.43 (m, 1H), 2.85−2.90 (m, 2H), 3.30 (d, *J* = 2.4 Hz, 2H), 5.62 (dd, *J* = 11.6, 10.2 Hz, 1H), 6.37 (d, *J* = 11.4 Hz, 1H), 7.03−7.08 (m, 1H), 7.09−7.13 (m, 1H), 7.21−7.26 (m, 2H). ^{13}C NMR (100 MHz, $CDCl_3$): δ 32.11, 34.98, 47.28, 51.89, 72.94, 79.08, 115.43 (d, $J_{C,F}$ = 22.3 Hz), 120.66 (d, $J_{C,F}$ = 3.0 Hz), 123.66 (d, $J_{C,F}$ = 3.6 Hz), 125.22 (d, $J_{C,F}$ = 15.0 Hz), 128.45 (d, $J_{C,F}$ = 8.2 Hz), 130.28 (d, $J_{C,F}$ = 3.7 Hz), 139.25, 160.03 (d, $J_{C,F}$ = 246.6 Hz). HRMS (ESI+): *m/z* calcd for $C_{16}H_{19}FN$ $[M + H]^+$ 244.1502; found 244.1505. IR (ATR): 3300, 2918, 2802, 2754, 1485, 1451, 1334, 1310, 1272, 1232, 1134, 1095, 972, 835, 780, 758, 634 cm^{-1}. HPLC purity, 97.1% (t_R = 9.04 min).

(*E*)-4-(2-Fluorostyryl)-1-(prop-2-yn-1-yl)piperidine (72). Synthesized from **33** (0.180 g, 0.589 mmol, 1.0 equiv) via general procedures D and E. Column chromatography, EtOAc/n-hex = 1/2 (v/v). Yield: 58% (83 mg); pale yellow oil. ^1H NMR (400 MHz, $CDCl_3$): δ 1.56 (dt, *J* = 12.0, 3.9 Hz, 1H), 1.59 (dt, *J* = 12.0, 3.9 Hz, 1H), 1.79−1.85 (m, 2H), 2.12−2.20 (m, 1H), 2.25 (t, *J* = 2.4 Hz, 1H), 2.28 (dt, *J* = 11.7, 2.5 Hz, 2H), 2.91−2.96 (m, 2H), 3.33 (d, *J* = 2.4 Hz, 2H), 6.23 (dd, *J* = 16.1, 7.1 Hz, 1H), 6.55 (d, *J* = 16.1 Hz, 1H), 7.00 (ddd, *J* = 10.8, 8.1, 1.2 Hz, 1H), 7.07 (dt, *J* = 7.4, 1.0 Hz, 1H), 7.14−7.19 (m, 1H), 7.44 (dt, *J* = 7.7, 1.7 Hz, 1H). ^{13}C NMR (100 MHz, $CDCl_3$): δ 31.93, 39.22, 47.24, 52.21, 72.97, 79.06, 115.58 (d, $J_{C,F}$ = 22.3 Hz), 120.59 (d, $J_{C,F}$ = 3.8 Hz), 123.95 (d, $J_{C,F}$ = 3.6 Hz), 125.32 (d, $J_{C,F}$ = 12.3 Hz), 126.88 (d, $J_{C,F}$ = 12.3 Hz), 128.14 (d, $J_{C,F}$ = 8.5 Hz), 137.41 (d, $J_{C,F}$ = 4.2 Hz), 159.94 (d, $J_{C,F}$ = 248.4 Hz). HRMS (ESI+): *m/z* calcd for $C_{16}H_{19}FN$ $[M + H]^+$ 244.1502; found 244.1500. IR (ATR): 3183, 2947, 2921, 2802, 2756, 1576, 1485, 1455, 1445, 1389, 1371, 1360, 1331, 1301, 1277, 1263, 1230, 1213, 1194, 1183, 1141, 1108, 1091, 1031, 1020, 983, 968, 946, 842, 811, 777, 754, 713 cm^{-1}. HPLC purity, 99.5% (t_R = 9.09 min).

(*Z*)-4-(2-Chloro-4-fluorostyryl)-1-(prop-2-yn-1-yl)piperidine (73). Synthesized from **34** (110 mg, 0.324 mmol, 1.0 equiv) via general procedures D and E. Column chromatography, EtOAc/n-hex = 1/2 (v/v). Yield: 6% (5 mg); white-yellow crystals, mp 51−53 °C. ^1H NMR (400 MHz, $CDCl_3$): δ 1.48−1.58 (m, 2H), 1.64−1.69 (m, 2H), 2.13−2.30 (m, 3H), 2.23 (t, *J* = 2.4 Hz, 1H), 2.83−2.88 (m, 2H), 3.28 (d, *J* = 2.4 Hz, 2H), 5.61 (dd, *J* = 10.8, 10.4 Hz, 1H), 6.35 (d, *J* = 11.5 Hz, 1H), 6.96 (dt, *J* = 8.4, 2.4 Hz, 1H), 7.14 (dd, *J* = 8.4, 2.4 Hz, 1H), 7.19 (dd, *J* = 8.2, 6.4 Hz, 1H). ^{13}C NMR (100 MHz, $CDCl_3$): δ 32.09, 34.57, 47.23, 51.78, 72.99, 78.97, 113.64 (d, $J_{C,F}$ = 20.7 Hz), 116.70 (d, $J_{C,F}$ = 24.8 Hz), 124.51, 130.93 (d, $J_{C,F}$ = 8.3 Hz), 132.06 (d, $J_{C,F}$ = 3.7 Hz), 134.16 (d, $J_{C,F}$ = 10.2 Hz), 138.65, 161.35 (d, $J_{C,F}$ = 248.6 Hz). HRMS (ESI+): *m/z* calcd for $C_{16}H_{18}FClN$ $[M + H]^+$ 278.1112; found 244.1105. IR (ATR): 3166, 3010, 2932, 2789, 2758, 1601, 1574, 1485, 1467, 1445, 1403, 1390, 1367, 1331, 1307, 1295, 1271, 1257, 1230, 1221, 1210, 1169, 1142, 1121, 1109, 1064, 1041, 1016, 1006, 973, 951, 901, 875, 863, 821, 790, 768, 747, 704, 687, 643, 615, 583, 547 cm^{-1}. HPLC purity, 99.7% (t_R = 9.85 min).

(*E*)-4-(2-Chloro-4-fluorostyryl)-1-(prop-2-yn-1-yl)piperidine (74). Synthesized from **35** (0.263 g, 0.774 mmol, 1.0 equiv) via general procedures D and E. Column chromatography, EtOAc/n-hex = 1/2 (v/v). Yield: 58% (125 mg); pale yellow oil. ^1H NMR (400 MHz, $CDCl_3$): δ 1.56 (dt, *J* = 12.0, 3.9 Hz, 1H), 1.59 (dt, *J* = 11.9, 3.9 Hz, 1H), 1.77−1.85 (m, 2H), 2.12−2.23 (m, 1H), 2.25 (t, *J* = 2.4 Hz, 1H), 2.28 (dt, *J* = 11.7, 2.5 Hz, 2H), 2.91−2.96 (m, 2H), 3.32 (d, *J* = 2.4 Hz, 2H), 6.07 (dd, *J* = 15.9, 7.1 Hz, 1H), 6.68 (d, *J* = 15.9 Hz, 1H), 6.90−6.95 (m, 1H), 7.08 (dd, *J* = 8.5, 2.6 Hz, 1H), 7.47 (dt, *J* = 8.8, 6.1 Hz, 1H). ^{13}C NMR (100 MHz, $CDCl_3$): δ 31.88, 38.93, 47.18, 52.10, 72.95, 78.98, 114.11 (d, $J_{C,F}$ = 21.3 Hz), 116.56 (d, $J_{C,F}$ = 24.7 Hz), 123.61 (d, $J_{C,F}$ = 1.1 Hz), 127.48 (d, $J_{C,F}$ = 8.8 Hz), 131.97 (d, $J_{C,F}$ = 3.7 Hz), 133.00 (d, $J_{C,F}$ = 10.2 Hz), 137.51 (d, $J_{C,F}$ = 1.7 Hz), 161.32 (d, $J_{C,F}$ = 249.4 Hz). HRMS (ESI+): *m/z* calcd for $C_{16}H_{18}FClN$ $[M + H]^+$ 278.1112; found 278.1120. IR (ATR): 3303, 2933, 2803, 2753, 1650, 1600, 1574, 1466, 1445, 1396, 1364, 1336, 1312, 1269, 1258, 1237, 1183, 1137, 1122, 1040, 966, 904, 858, 805, 776, 760, 686, 627, 579 cm^{-1}. HPLC purity, 100% (t_R = 9.86 min).

(*Z*)-4-(4-Methylstyryl)-1-(prop-2-yn-1-yl)piperidine (75). Synthesized from **36** (0.07 g, 0.23 mmol, 1.0 equiv) via general procedures D and E. Column chromatography, EtOAc/n-hex = 1/2 (v/v). Yield: 49% (27 mg); yellow crystals, mp 85−86 °C. ^1H NMR (400 MHz, $CDCl_3$): δ 1.49−1.57 (m, 2H), 1.72−1.76 (m, 2H), 2.20−2.26 (m, 3H), 2.35 (s, 3H), 2.52−2.62 (m, 1H), 2.86−2.91 (m, 2H), 3.30 (d, *J* = 2.4 Hz, 2H), 5.45 (dd, *J* = 11.6, 10.0 Hz, 1H), 6.35 (d, *J* = 11.6 Hz, 1H), 7.15 (s, 4H). ^{13}C NMR (100 MHz, $CDCl_3$): δ 21.16, 32.36, 34.45, 47.29, 51.96, 72.94, 79.10, 127.94, 128.43, 128.94, 134.74, 136.33, 136.62. HRMS (ESI+): *m/z* calcd for $C_{17}H_{22}N$ $[M + H]^+$ 240.1752; found 240.1756. IR (ATR): 3210, 2934, 2858, 2798, 2756, 1466, 1450, 1432, 1335, 1272, 1143, 1109, 1067, 972, 946, 836, 824, 810, 785, 738, 687, 560 cm^{-1}. HPLC purity, 100% (t_R = 9.62 min).

(*E*)-4-(4-Methylstyryl)-1-(prop-2-yn-1-yl)piperidine (76). Synthesized from **37** (0.42 g, 1.39 mmol, 1.0 equiv) via general procedures D and E. Column chromatography, EtOAc/n-hex = 1/3 (v/v). Yield: 36% (121 mg); orange crystals, mp 65−67 °C. ^1H NMR (400 MHz, $CDCl_3$): δ 1.62−1.72 (m, 2H), 1.89−1.95 (m, 2H), 2.18−2.28 (m, 1H), 2.34−2.41 (m, 3H), 2.43 (s, 3H), 3.01−3.06 (m, 2H), 3.43 (d, *J* = 2.5 Hz, 2H), 6.22 (dd, *J* = 16.0, 7.0 Hz, 1H), 6.46 (d, *J* = 15.9 Hz, 1H), 7.21 (d, *J* = 7.9 Hz, 2H), 7.36 (d, *J* = 8.3 Hz, 2H). ^{13}C NMR (100 MHz, $CDCl_3$): δ 21.09, 32.04, 38.77, 47.21, 52.25, 72.92, 79.07, 125.83, 127.98, 129.13, 133.84, 134.78, 136.62. HRMS (ESI+): *m/z* calcd for $C_{17}H_{22}N$ $[M + H]^+$ 240.1752; found 240.1756. IR (ATR): 3209, 2933, 2858, 2800, 2756, 1513, 1450, 1427, 1335, 1311, 1271, 1134, 1109, 1067, 1019, 972, 910, 824, 795, 785, 739, 685, 642, 561, 518 cm^{-1}. HPLC purity, 97.7% (t_R = 9.65 min).

(*Z*)-4-(4-Isopropylstyryl)-1-(prop-2-yn-1-yl)piperidine (77). Synthesized from **38** (0.180 g, 0.546 mmol, 1.0 equiv) via general procedures D and E. Column chromatography, EtOAc/n-hex = 1/2 (v/v). Yield: 79% (115 mg); colorless oil. ^1H NMR (400 MHz, $CDCl_3$): δ 1.27 (d, *J* = 6.9 Hz, 6H), 1.50−1.60 (m, 2H), 1.74−1.78 (m, 2H), 2.21−2.28 (m, 2H), 2.24 (t, *J* = 2.4 Hz, 1H), 2.56−2.66 (m, 1H), 2.87−2.95 (m, 3H), 3.31 (d, *J* = 2.5 Hz, 2H), 5.45 (dd, *J* = 11.7, 10.0 Hz, 1H), 6.35 (d, *J* = 11.7 Hz, 1H), 7.17−7.23 (m, 4H). ^{13}C NMR (100 MHz, $CDCl_3$): δ 23.95, 32.36, 33.77, 34.44, 47.28, 51.95, 72.93, 79.10, 126.29, 127.90, 128.49, 135.09, 136.56, 147.27. HRMS (ESI+): *m/z* calcd for $C_{19}H_{26}N$ $[M + H]^+$ 268.2065; found 268.2061. IR (ATR): 3295, 2958, 2937, 2801, 1508, 1335, 1311, 1136, 973, 849, 676 cm^{-1}. HPLC purity, 99.1% (t_R = 10.83 min).

(*E*)-4-(4-Isopropylstyryl)-1-(prop-2-yn-1-yl)piperidine (78). Synthesized from **39** (0.207 g, 0.628 mmol, 1.0 equiv) via general procedures D and E. Column chromatography, EtOAc/n-hex = 1/1 (v/v). Yield: 45% (76 mg); pale yellow crystals, mp 60−64 °C. ^1H NMR (400 MHz, $CDCl_3$): δ 1.24 (d, *J* = 6.9 Hz, 6H), 1.52−1.61 (m, 2H), 1.78−1.83 (m, 2H), 2.05−2.20 (m, 1H), 2.24−2.31 (m, 2H), 2.26 (t, *J* = 2.5 Hz, 1H), 2.83−2.95 (m, 3H), 3.32 (d, *J* = 2.5 Hz, 2H), 6.13 (dd, *J* = 16.0, 7.0 Hz, 1H), 6.37 (d, *J* = 16.6 Hz, 1H), 7.15−7.17 (m, 2H), 7.28−7.30 (m, 2H). ^{13}C NMR (100 MHz, $CDCl_3$): δ 23.93, 32.05, 33.76, 38.76, 47.23, 52.25, 72.90, 79.08, 125.89, 126.549, 127.96, 134.01, 135.21, 147.73. HRMS (ESI+): *m/z* calcd for $C_{19}H_{26}N$ $[M + H]^+$ 268.2065; found 268.2062. IR (ATR): 3299, 2959, 2936, 2908, 2802, 1514, 1457, 1425, 1384, 1310, 1131, 1103, 1053, 977, 899, 855, 812, 762, 685, 654, 639, 553 cm^{-1}. HPLC purity, 98.5% (t_R = 10.89 min).

(*Z*)-4-(4-Chlorostyryl)-1-(prop-2-yn-1-yl)piperidine (79). Synthesized from **40** (0.150 g, 0.466 mmol, 1.0 equiv) via general procedures D and E. Column chromatography, EtOAc/n-hex = 1/2

https://dx.doi.org/10.1021/acs.jmedchem.9b01886
J. Med. Chem. XXXX, XXX, XXX−XXX

(v/v). Yield: 67% (81 mg); white crystals, mp 97–99 °C. ^{1}H NMR (400 MHz, $CDCl_3$): δ 1.49–1.59 (m, 2H), 1.68–1.74 (m, 2H), 2.18–2.25 (m, 2H), 2.23 (t, J = 2.5 Hz, 1H), 2.44–2.54 (m, 1H), 2.85–2.90 (m, 2H), 3.30 (d, J = 2.5 Hz, 2H), 5.51 (dd, J = 11.6, 10.1 Hz, 1H), 6.32 (d, J = 11.7 Hz, 1H), 7.14–7.17 (m, 2H), 7.28–7.31 (m, 2H). ^{13}C NMR (100 MHz, $CDCl_3$): δ 32.20, 34.45, 47.24, 51.83, 73.01, 78.97, 126.92, 128.37, 129.74, 132.30, 135.99, 137.88. HRMS (ESI+): m/z calcd for $C_{16}H_{19}ClN$ $[M + H]^+$ 260.1206; found 260.1201. IR (ATR): 3198, 2936, 2800, 2757, 1487, 1452, 1335, 1272, 1144, 1120, 1090, 1068, 971, 836, 797, 756, 716, 695, 586, 557 cm^{-1}. HPLC purity, 98.6% (t_R = 9.78 min).

(*E*)-4-(4-Chlorostyryl)-1-(prop-2-yn-1-yl)piperidine (80). Synthesized from **41** (0.165 g, 0.513 mmol, 1.0 equiv) via general procedures D and E. Column chromatography, EtOAc/n-hex = 1/2 (v/v). Yield: 45% (87 mg); white crystals, mp 83–85 °C. ^{1}H NMR (400 MHz, $CDCl_3$): δ 1.49–1.59 (m, 2H), 1.76–1.82 (m, 2H), 2.06–2.16 (m, 1H), 2.23–2.29 (m, 2H), 2.25 (t, J = 2.4 Hz, 1H), 2.92 (td, J = 11.1, 2.4 Hz, 2H), 3.31 (d, J = 2.5 Hz, 2H), 6.13 (dd, J = 16.0, 7.0 Hz, 1H), 6.31 (dd, J = 16.0, 1.1 Hz, 1H), 7.22–7.27 (m, 4H). ^{13}C NMR (100 MHz, $CDCl_3$): δ 31.89, 38.77, 47.18, 52.15, 72.95, 79.00, 127.00, 127.13, 128.51, 132.39, 135.55, 136.04. HRMS (ESI+): m/z calcd for $C_{16}H_{19}ClN$ $[M + H]^+$ 260.1206; found 260.1207. IR (ATR): 3154, 2931, 2916, 2797, 1489, 1441, 1422, 1329, 1313, 1135, 1089, 1010, 971, 907, 850, 801, 722, 594, 519 cm^{-1}. HPLC purity, 99.6% (t_R = 9.81 min).

(*E*)-4-(4-Bromostyryl)-1-(prop-2-yn-1-yl)piperidine (81). Synthesized from **43** (0.36 g, 0.98 mmol, 1.0 equiv) via general procedures D and E. Column chromatography, EtOAc/n-hex = 1/2 (v/v). Yield: 34% (102 mg); white crystals, mp 103–106 °C. ^{1}H NMR (400 MHz, $CDCl_3$): δ 1.50–1.60 (m, 2H), 1.77–1.83 (m, 2H), 2.08–2.17 (m, 1H), 2.24–2.30 (m, 3H), 2.91–2.95 (m, 2H), 3.32 (d, J = 2.2 Hz, 2H), 6.15 (dd, J = 16.0, 6.9 Hz, 1H), 6.31 (d, J = 16.2 Hz, 1H), 7.19–7.22 (m, 2H), 7.39–7.42 (m, 2H). ^{13}C NMR (100 MHz, $CDCl_3$): δ 31.93, 38.85, 47.25, 52.22, 72.96, 79.06, 120.59, 127.15, 127.56, 131.53, 135.78, 136.59. HRMS (ESI+): m/z calcd for $C_{16}H_{19}NBr$ $[M + H]^+$ 304.0701; found 304.0706. IR (ATR): 3150, 2929, 2850, 2798, 2745, 1485, 1466, 1423, 1328, 1310, 1135, 1117, 1098, 1069, 1007, 970, 906, 848, 822, 798, 754, 715, 579, 516 cm^{-1}. HPLC purity, 100% (t_R = 10.00 min).

(*E*)-4-(4-Methoxystyryl)-1-(prop-2-yn-1-yl)piperidine (82). Synthesized from a mixture of **44** and **45** (0.810 g, 2.552 mmol, 1.0 equiv) via general procedures D and E. Column chromatography EtOAc/n-hex = 1/1 (v/v), yielding only *trans* isomer **82**. Yield: 32% (192 mg); white crystals, mp 59–61 °C. ^{1}H NMR (400 MHz, $CDCl_3$): δ 1.50–1.60 (m, 2H), 1.76–1.82 (m, 2H), 2.06–2.15 (m, 1H), 2.23–2.30 (m, 2H), 2.25 (t, J = 2.4 Hz, 1H), 2.90–2.95 (m, 2H), 3.32 (d, J = 2.4 Hz, 2H), 3.79 (s, 3H), 6.02 (dd, J = 15.9, 7.0 Hz, 1H), 6.32 (d, J = 15.9 Hz, 1H), 6.81–6.85 (m, 2H), 7.26–7.30 (m, 2H). ^{13}C NMR (100 MHz, $CDCl_3$): δ 32.13, 38.77, 47.23, 52.28, 55.23, 72.90, 79.11, 113.85, 127.02, 127.49, 130.39, 132.77, 158.69. HRMS (ESI+): m/z calcd for $C_{17}H_{22}NO$ $[M + H]^+$ 256.1701; found 256.1706. IR (ATR): 3270, 2940, 2907, 2825, 1604, 1509, 1467, 1313, 1241, 1176, 1128, 1029, 968, 959, 906, 854, 831, 801, 769, 719, 645, 622, 529 cm^{-1}. HPLC purity, 97.7% (t_R = 8.92 min).

(*Z*)-1-(Prop-2-yn-1-yl)-4-(4-(trifluoromethyl)styryl)-piperidine (83). Synthesized from **46** (0.075 g, 0.211 mmol, 1.0 equiv) via general procedures D and E. Column chromatography, EtOAc/n-hex = 2/1 (v/v). Yield: 81% (45 mg); pale yellow oil. ^{1}H NMR (400 MHz, $CDCl_3$): δ 1.51–1.61 (m, 2H), 1.70–1.74 (m, 2H), 2.19–2.25 (m, 2H), 2.24 (t, J = 2.5 Hz, 1H), 2.45–2.55 (m, 1H), 2.87–2.91 (m, 2H), 3.30 (d, J = 2.5 Hz, 2H), 5.60 (dd, J = 11.7, 10.2 Hz, 1H), 6.39 (d, J = 11.7 Hz, 1H), 7.33 (d, J = 8.6 Hz, 2H), 7.59 (d, J = 8.2 Hz, 2H). ^{13}C NMR (100 MHz, $CDCl_3$): δ 32.18, 34.55, 47.24, 51.78, 73.05, 78.92, 124.19 (q, $J_{C,F}$ = 271.8 Hz), 125.17 (q, $J_{C,F}$ = 3.9 Hz), 126.89, 128.58 (t, $J_{C,F}$ = 32.3 Hz), 128.67, 139.22, 141.18 (q, $J_{C,F}$ = 1.4 Hz). HRMS (ESI+): m/z calcd for $C_{17}H_{19}F_3N$ $[M + H]^+$ 294.1470; found 294.1469. IR (ATR): 3305, 2933, 2805, 1615, 1331, 1167, 1129, 1068, 1017, 973, 851, 634, 603 cm^{-1}. HPLC purity, 100% (t_R = 10.21 min).

(*E*)-1-(Prop-2-yn-1-yl)-4-(4-(trifluoromethyl)styryl)-piperidine (84). Synthesized from **47** (0.580 g, 1.632 mmol, 1.0 equiv) via general procedures D and E. Column chromatography, EtOAc/n-hex = 2/1 (v/v). Yield: 85% (376 mg); white crystals, mp 72–74 °C. ^{1}H NMR (400 MHz, $CDCl_3$): δ 1.52–1.62 (m, 2H), 1.80–1.85 (m, 2H), 2.12–2.20 (m, 1H), 2.26 (t, J = 2.4 Hz, 1H), 2.25–2.32 (m, 2H), 2.92–2.96 (m, 2H), 3.33 (d, J = 2.5 Hz, 2H), 6.27 (dd, J = 16.0, 6.9 Hz, 1H), 6.41 (d, J = 16.0 Hz, 1H), 7.43 (d, J = 8.4 Hz, 2H), 7.54 (d, J = 8.2 Hz, 2H). ^{13}C NMR (100 MHz, $CDCl_3$): δ 31.78, 38.84, 47.17, 52.11, 72.97, 78.95, 124.20 (q, $J_{C,F}$ = 271.8 Hz), 125.34 (q, $J_{C,F}$ = 3.9 Hz), 126.07, 127.02, 128.69 (q, $J_{C,F}$ = 32.4 Hz), 137.62, 141.07 (q, $J_{C,F}$ = 1.4 Hz). HRMS (ESI+): m/z calcd for $C_{17}H_{19}F_3N$ $[M + H]^+$ 294.1470; found 294.1464. IR (ATR): 3157, 2933, 2917, 2806, 1613, 1312, 1160, 1109, 1066, 1055, 972, 866, 831, 736, 600, 579, 517 cm^{-1}. HPLC purity, 99.9% (t_R = 10.19 min).

(*Z*)-1-(Prop-2-yn-1-yl)-4-(3-(trifluoromethyl)styryl)-piperidine (85). Synthesized from **48** (0.05 g, 0.14 mmol, 1.0 equiv) via general procedures D and E. Column chromatography, EtOAc/n-hex = 1/3 (v/v). Yield: 27% (11 mg); yellow oil. ^{1}H NMR (400 MHz, $CDCl_3$): δ 1.59–1.77 (m, 2H), 1.75 (dd, J = 12.8, 2.2 Hz, 2H), 2.26–2.32 (m, 3H), 2.44–2.54 (m, 1H), 2.92–2.98 (m, 2H), 3.35 (d, J = 2.4 Hz, 2H), 5.60 (dd, J = 11.6, 10.2 Hz, 1H), 5.41 (d, J = 11.7 Hz, 1H), 7.39–7.51 (m, 4H). ^{13}C NMR (100 MHz, $CDCl_3$): δ 31.83, 34.35, 47.10, 51.69, 73.79, 78.08, 123.37 (q, $J_{C,F}$ = 3.8 Hz), 124.10 (q, $J_{C,F}$ = 272.3 Hz), 125.21 (q, $J_{C,F}$ = 3.7 Hz), 127.08, 128.72, 130.64 (q, $J_{C,F}$ = 32.2 Hz), 131.60, 138.20, 138.45. HRMS (ESI+): m/z calcd for $C_{17}H_{19}NF_3$ $[M + H]^+$ 294.1470; found 294.1466. IR (ATR): 3306, 2933, 2850, 2804, 2757, 1688, 1444, 1327, 1162, 1122, 1092, 1072, 972, 905, 807, 703, 696, 656, 628 cm^{-1}. HPLC purity, 95.9% (t_R = 10.13 min).

(*E*)-1-(Prop-2-yn-1-yl)-4-(3-(trifluoromethyl)styryl)-piperidine (86). Synthesized from **49** (0.19 g, 0.53 mmol, 1.0 equiv) via general procedures D and E. Column chromatography, EtOAc/n-hex = 1/3 (v/v). Yield: 70% (109 mg); green oil. ^{1}H NMR (400 MHz, $CDCl_3$): δ 1.52–1.62 (m, 2H), 1.78–1.84 (m, 2H), 2.11–2.20 (m, 1H), 2.26 (t, J = 2.4 Hz, 1H), 2.29 (dt, J = 11.8, 2.3 Hz, 2H), 2.91–2.97 (m, 2H), 3.33 (d, J = 2.4 Hz, 2H), 6.24 (dd, J = 16.0, 6.9 Hz, 1H), 6.41 (d, J = 16.0 Hz, 1H), 7.38–7.45 (m, 2H), 7.51 (d, J = 7.5 Hz, 1H), 7.58 (s, 1H). ^{13}C NMR (100 MHz, $CDCl_3$): δ 31.87, 38.86, 47.24, 52.18, 73.01, 79.02, 122.64 (q, $J_{C,F}$ = 3.9 Hz), 123.50 (q, $J_{C,F}$ = 3.9 Hz), 124.16 (q, $J_{C,F}$ = 272.3 Hz), 127.03, 128.88, 129.18, 130.85 (q, $J_{C,F}$ = 32.1 Hz), 136.91, 138.39. HRMS (ESI+): m/z calcd for $C_{17}H_{19}NF_3$ $[M + H]^+$ 294.1470; found 294.1465. IR (ATR): 3306, 2934, 2849, 2804, 2755, 1444, 1329, 1201, 1162, 1120, 1094, 1071, 965, 900, 792, 696, 662, 628 cm^{-1}. HPLC purity, 99.8% (t_R = 10.16 min).

(*Z*)-4-(2-(1-(Prop-2-yn-1-yl)piperidin-4-yl)vinyl)benzonitrile (87). Synthesized from **50** (0.350 g, 1.120 mmol, 1.0 equiv) via general procedures D and E. Column chromatography, EtOAc/CH_2Cl_2 = 3/7 (v/v). Yield: 50% (125 mg); white crystals, mp 118–121 °C. ^{1}H NMR (400 MHz, $CDCl_3$): δ 1.51–1.61 (m, 2H), 1.68–1.74 (m, 2H), 2.19–2.25 (m, 2H), 2.24 (t, J = 2.4 Hz, 1H), 2.42–2.50 (m, 1H), 2.86–2.91 (m, 2H), 3.30 (d, J = 2.5 Hz, 2H), 5.64 (dd, J = 11.7, 10.2 Hz, 1H), 6.37 (d, J = 11.8 Hz, 1H), 7.30–7.33 (m, 2H), 7.61–7.63 (m, 2H). ^{13}C NMR (100 MHz, $CDCl_3$): δ 32.01, 34.61, 47.15, 51.64, 73.05, 78.81, 110.05, 118.88, 126.58, 129.00, 132.02, 140.13, 142.21. HRMS (ESI+): m/z calcd for $C_{17}H_{19}N_2$ $[M + H]^+$ 251.1548; found 251.1550. IR (ATR): 3199, 2930, 2812, 2793, 2771, 2225, 1602, 1500, 1451, 1396, 1337, 1274, 1226, 1143, 1110, 970, 850,729, 697, 569, 528 cm^{-1}. HPLC purity, 98.3% (t_R = 8.39 min).

(*E*)-4-(2-(1-(Prop-2-yn-1-yl)piperidin-4-yl)vinyl)benzonitrile (88). Synthesized from (**51** (0.300 g, 0.960 mmol, 1.0 equiv) via general procedures D and E. Column chromatography, CH_2Cl_2/MeOH = 50/1 (v/v). Yield: 54% (130 mg); white crystals, mp 59–62 °C. ^{1}H NMR (400 MHz, $CDCl_3$): δ 1.47–1.58 (m, 2H), 1.74–1.80 (m, 2H), 2.09–2.18 (m, 1H), 2.21–2.27 (m, 2H), 2.23 (t, J = 2.4 Hz, 1H), 2.87–2.92 (m, 2H), 3.28 (d, J = 2.5 Hz, 2H), 6.27 (dd, J = 16.0, 6.5 Hz, 1H), 6.35 (d, J = 16.1 Hz, 1H), 7.36–7.39 (m, 2H), 7.51–7.54 (m, 2H). ^{13}C NMR (100 MHz, $CDCl_3$): δ 31.58, 38.79, 47.06, 51.95, 72.96, 78.83, 109.93, 118.93, 126.35, 126.77, 132.16, 138.94,

https://dx.doi.org/10.1021/acs.jmedchem.9b01886
J. Med. Chem. XXXX, XXX, XXX−XXX

141.99. HRMS (ESI+): m/z calcd for $C_{17}H_{19}N_2$ $[M + H]^+$ 251.1548; found 251.1549. IR (ATR): 3284, 2941, 2916, 2802, 2224, 1646, 1602, 1503, 1423, 1382, 1338, 1315, 1223, 1138, 1104, 984, 970, 900, 855, 831, 762, 692, 630, 551 cm^{-1}. HPLC purity, 99.3% (t_R = 8.34 min).

(*Z*)-4-(4-(Methylsulfonyl)styryl)-1-(prop-2-yn-1-yl)-piperidine (89). Synthesized from **52** (0.126 g, 0.346 mmol, 1.0 equiv) via general procedures D and E. Column chromatography, EtOAc/n-hex = 2/1 (v/v). Yield: 76% (80 mg); white crystals, mp 71−74 °C. ^1H NMR (400 MHz, $CDCl_3$): δ 1.49−1.60 (m, 2H), 1.67−1.73 (m, 2H), 2.20 (dt, J = 11.7, 2.5 Hz, 2H), 2.23 (t, J = 2.4 Hz, 1H), 2.41−2.51 (m, 1H), 2.86 (td, J = 8.9, 2.7 Hz, 2H), 3.05 (s, 3H), 3.28 (d, J = 2.5 Hz, 2H), 5.64 (dd, J = 11.7, 10.3 Hz, 1H), 6.39 (d, J = 11.7 Hz, 1H), 7.37−7.40 (m, 2H), 7.86−7.90 (m, 2H). ^{13}C NMR (100 MHz, $CDCl_3$): δ 32.03, 34.60, 44.46, 47.16, 51.64, 73.08, 78.82, 126.42, 127.32, 129.17, 138.28, 140.29, 143.22. HRMS (ESI+): m/z calcd for $C_{17}H_{22}NO_2S$ $[M + H]^+$ 304.1371; found 304.1370. IR (ATR): 3273, 2937, 2799, 2757, 1640, 1593, 1463, 1415, 1296, 1141, 1078, 955, 848, 774, 723, 679, 615, 593, 525 cm^{-1}. HPLC purity, 98.3% (t_R = 4.60 min).

(*E*)-4-(4-(Methylsulfonyl)styryl)-1-(prop-2-yn-1-yl)piperidine (90). Synthesized from **53** (0.205 g, 0.56 mmol, 1.0 equiv) via general procedures D and E. Column chromatography, EtOAc/n-hex = 2/1 (v/v). Yield: 85% (145 mg); white crystals, mp 101−105 °C. ^1H NMR (400 MHz, $CDCl_3$): δ 1.52−1.62 (m, 2H), 1.80−1.85 (m, 2H), 2.14−2.23 (m, 1H), 2.25−2.32 (m, 3H), 2.92−2.97 (m, 2H), 3.04 (s, 3H), 3.33 (d, J = 2.2 Hz, 2H), 6.34 (dd, J = 16.0, 6.6 Hz, 1H), 6.43 (d, J = 16.1 Hz, 1H), 7.51 (d, J = 8.1 Hz, 2H), 7.85 (d, J = 8.0 Hz, 2H). ^{13}C NMR (100 MHz, $CDCl_3$): δ 31.73, 38.98, 44.60, 47.22, 52.11, 73.05, 78.94, 126.66, 126.74, 127.68, 138.37, 139.35, 143.16. HRMS (ESI+): m/z calcd for $C_{17}H_{22}NO_2S$ $[M + H]^+$ 304.1371; found 304.1372. IR (ATR): 3282, 2927, 2797, 2750, 1647, 1595, 1466, 1404, 1303, 1146, 1091, 960, 858, 767, 705, 684, 649, 595, 544, 526 cm^{-1}. HPLC purity, 95.1% (t_R = 5.06 min).

(*Z*)-4-(4-Cyclopropylstyryl)-1-(prop-2-yn-1-yl)piperidine (91). Synthesized from **54** (0.080 g, 0.244 mmol, 1.0 equiv) via general procedures D and E. Column chromatography, EtOAc/n-hex = 1/2 (v/v). Yield: 20% (16 mg); colorless oil. ^1H NMR (400 MHz, $CDCl_3$): δ 0.68−0.72 (m, 2H), 0.94−0.99 (m, 2H), 1.49−1.59 (m, 2H), 1.71−1.77 (m, 2H), 1.86−1.92 (m, 1H), 2.20−2.26 (m, 3H), 2.52−2.62 (m, 1H), 2.86−2.91 (m, 2H), 3.30 (d, J = 2.5 Hz, 2H), 5.43 (dd, J = 11.6, 10.0 Hz, 1H), 6.33 (d, J = 11.6 Hz, 1H), 7.02−7.06 (m, 2H), 7.12−7.16 (m, 2H). ^{13}C NMR (100 MHz, $CDCl_3$): δ 9.31, 15.16, 32.35, 34.45, 47.28, 51.95, 72.96, 79.08, 125.44, 127.88, 128.47, 134.75, 136.53, 142.48. HRMS (ESI+): m/z calcd for $C_{19}H_{24}N$ $[M + H]^+$ 266.1909; found 266.1905. IR (ATR): 3355, 2973, 2916, 2849, 1739, 1654, 1468, 1373, 1239, 1086, 1045, 879, 719 cm^{-1}. HPLC purity, 95.9% (t_R = 10.27 min).

(*E*)-4-(4-Cyclopropylstyryl)-1-(prop-2-yn-1-yl)piperidine (92). Synthesized from **55** (0.200 g, 0.611 mmol, 1.0 equiv) via general procedures D and E. Column chromatography, EtOAc/n-hex = 1/2 (v/v). Yield: 40% (65 mg); pale yellow crystals, mp 66−68 °C. ^1H NMR (400 MHz, $CDCl_3$): δ 0.66−0.70 (m, 2H), 0.92−0.97 (m, 2H), 1.50−1.61 (dt, 2H), 1.77−1.83 (m, 2H), 1.85−1.90 (m, 1H), 2.07−2.17 (m, 1H), 2.26 (t, J = 2.4 Hz, 1H), 2.27 (dt, J = 11.7, 2.5 Hz, 2H), 2.90−2.95 (m, 2H), 3.32 (d, J = 2.4 Hz, 2H), 6.10 (dd, J = 15.9, 7.0 Hz, 1H), 6.34 (d, J = 15.9 Hz, 1H), 6.98−7.01 (m, 2H), 7.23−7.26 (m, 2H). ^{13}C NMR (100 MHz, $CDCl_3$): δ 9.17, 15.12, 32.04, 38.75, 47.20, 52.23, 72.91, 79.06, 125.66, 125.84, 127.90, 133.77, 134.82, 142.79. HRMS (ESI+): m/z calcd for $C_{19}H_{24}N$ $[M + H]^+$ 266.1909; found 266.1908. IR (ATR): 3007, 2932, 2919, 2854, 2805, 2748, 1607, 1514, 1424, 1385, 1312, 1135, 1103, 1041, 1022, 972, 891, 851, 804, 684, 665, 644, 630, 546 cm^{-1}. HPLC purity, 98.1% (t_R = 10.27 min).

4-Phenethyl-1-(prop-2-yn-1-yl)piperidine (93). Synthesized from **56** (1.040 g, 3.593 mmol, 1.0 equiv) via general procedures D and E. Column chromatographym EtOAc/n-hex = 1/2 (v/v). Yield: 56% (202 mg); yellow oil. ^1H NMR (400 MHz, $CDCl_3$): δ 1.24−1.39 (m, 3H), 1.56−1.62 (m, 2H), 1.75−1.81 (m, 2H), 2.15−2.22 (m, 2H), 2.24 (t, J = 2.5 Hz, 1H), 2.62−2.66 (m, 2H), 2.87−2.92 (m, 2H), 3.30 (d, J = 2.5 Hz, 2H), 7.16−7.21 (m, 3H), 7.26−7.31 (m, 2H). ^{13}C NMR (100 MHz, $CDCl_3$): δ 32.05, 32.89, 34.58, 38.15, 47.03, 52.34, 72.74, 79.02, 125.44, 128.10 (4 × C), 142.43. HRMS (ESI+): m/z calcd for $C_{16}H_{22}N$ $[M + H]^+$ 228.1752; found 228.1755. IR (ATR): 3297, 2935, 2908, 2801, 1496, 1337, 1313, 750, 700, 641 cm^{-1}. HPLC purity, 99.9% (t_R = 8.86 min).

4-(3-Fluorophenethyl)-1-(prop-2-yn-1-yl)piperidine (94). Synthesized from **57** (0.320 g, 1.04 mmol, 1.0 equiv) via general procedures D and E. Column chromatography EtOAc/n-hex = 1/2 (v/v). Yield: 18% (46 mg); yellow oil. ^1H NMR (400 MHz, $CDCl_3$): δ 1.21−1.37 (m, 3H), 1.52−1.58 (m, 2H), 1.73−1.78 (m, 2H), 2.14−2.20 (m, 2H), 2.23 (t, J = 2.4 Hz, 1H), 2.59−2.63 (m, 2H), 2.86−2.91 (m, 2H), 3.29 (d, J = 2.4 Hz, 2H), 6.83−6.89 (m, 2H), 6.92−6.95 (m, 1H), 7.18−7.24 (m, 1H). ^{13}C NMR (100 MHz, $CDCl_3$): δ 32.10, 32.76, 32.78 34.64, 37.90, 47.14, 52.45, 72.93, 79.04, 112.46 (d, $J_{C,F}$ = 21.9 Hz), 115.04 (d, $J_{C,F}$ = 20.5 Hz), 123.90 (d, $J_{C,F}$ = 2.2 Hz), 129.60 (d, $J_{C,F}$ = 8.7 Hz), 145.18 (d, $J_{C,F}$ = 7.2 Hz), 162.83 (d, $J_{C,F}$ = 245.0 Hz). HRMS (ESI+): m/z calcd for $C_{16}H_{21}FN$ $[M + H]^+$ 246.1658; found 246.1659. IR (ATR): 3305, 2919, 2849, 2803, 2755, 1616, 1588, 1488, 1466, 1446, 1387, 1367, 1337, 1312, 1251, 1183, 1139, 1125, 1105, 1085, 1021, 995, 976, 959, 934, 888, 866, 782, 741, 719, 691, 629 cm^{-1}. HPLC purity, 97.6% (t_R = 9.26 min).

4-(2-Fluorophenethyl)-1-(prop-2-yn-1-yl)piperidine (95). Synthesized from **58** (0.220 g, 0.716 mmol, 1.0 equiv) via general procedures D and E. Column chromatography, EtOAc/n-hex = 1/2 (v/v). Yield: 8% (14 mg); yellow oil. ^1H NMR (400 MHz, $CDCl_3$): δ 1.25−1.37 (m, 3H), 1.53−1.58 (m, 2H), 1.77−1.80 (m, 2H), 2.15−2.20 (m, 2H), 2.23 (t, J = 2.4 Hz, 1H), 2.63−2.67 (m, 2H), 2.87−2.90 (m, 2H), 3.30 (d, J = 2.4 Hz, 2H), 6.97−7.02 (m, 1H), 7.03−7.07 (m, 1H), 7.13−7.20 (m, 2H). ^{13}C NMR (100 MHz, $CDCl_3$): δ 26.17, 32.12, 34.85, 36.88, 47.20, 52.53, 72.89, 79.15, 115.15 (d, $J_{C,F}$ = 22.5 Hz), 123.88 (d, $J_{C,F}$ = 3.4 Hz), 127.32 (d, $J_{C,F}$ = 8.0 Hz), 129.41 (d, $J_{C,F}$ = 16.1 Hz), 130.41 (d, $J_{C,F}$ = 5.3 Hz), 161.08 (d, $J_{C,F}$ = 244.5 Hz). HRMS (ESI+): m/z calcd for $C_{16}H_{21}FN$ $[M + H]^+$ 246.1658; found 246.1657. IR (ATR): 3383, 2975, 2931, 1691, 1638, 1492, 1453, 1423, 1366, 1324, 1277, 1228, 1161, 1127, 1086, 1033, 966, 863, 804, 757 cm^{-1}. HPLC purity, 95.1% (t_R = 9.20 min).

4-(4-Methylphenethyl)-1-(prop-2-yn-1-yl)piperidine (96). Synthesized from **59** (0.28 g, 0.92 mmol, 1.0 equiv) via general procedures D and E. Column chromatography, EtOAc/n-hex = 1/3 (v/v). Yield: 36% (79 mg); yellow oil. ^1H NMR (400 MHz, $CDCl_3$): δ 1.21−1.36 (m, 3H), 1.52−1.57 (m, 2H), 1.75−1.78 (m, 2H), 2.14−2.20 (m, 2H), 2.23 (t, J = 2.4 Hz, 1H), 2.31 (s, 3H), 2.56−2.60 (m, 2H), 2.86−2.89 (m, 2H), 3.29 (d, J = 2.4 Hz, 2H), 7.05−7.10 (m, 4H). ^{13}C NMR (100 MHz, $CDCl_3$): δ 20.97, 32.21, 32.57, 34.68, 38.43, 47.21, 52.55, 72.83, 79.05, 128.17, 128.97, 135.05, 139.58. HRMS (ESI+): m/z calcd for $C_{17}H_{24}N$ $[M + H]^+$ 242.1909; found 242.1904. IR (ATR): 3183, 2932, 2917, 2847, 2798, 2752, 1515, 1451, 1333, 1293, 1270, 1144, 1103, 1080, 974, 850, 800, 784, 739, 559, 506 cm^{-1}. HPLC purity, 97.4% (t_R = 9.75 min).

4-(4-Isopropylphenethyl)-1-(prop-2-yn-1-yl)piperidine (97). Synthesized from **60** (0.290 g, 0.875 mmol, 1.0 equiv) via general procedures D and E. Column chromatography, EtOAc/n-hex = 1/2 (v/v). Yield: 55% (112 mg); yellow oil. ^1H NMR (400 MHz, $CDCl_3$): δ 1.28 (d, J = 7.0 Hz, 6H), 1.32−1.39 (m, 3H), 1.58−1.63 (m, 2H), 1.79−1.84 (m, 2H), 2.19−2.25 (m, 2H), 2.26 (t, J = 2.4 Hz, 1H), 2.62−2.66 (m, 2H), 2.88−2.95 (m, 3H), 3.33 (d, J = 2.5 Hz, 2H), 7.13−7.16 (m, 2H), 7.17−7.20 (m, 2H). ^{13}C NMR (100 MHz, $CDCl_3$): δ 24.02, 32.18, 32.56, 33.59, 34.76, 38.34, 47.16, 52.50, 72.78, 79.17, 126.24, 128.10, 139.90, 146.03. HRMS (ESI+): m/z calcd for $C_{19}H_{28}N$ $[M + H]^+$ 270.2222; found 270.2226. IR (ATR): 3282, 2958, 2933, 2908, 2801, 2753, 1512, 1128, 1105, 976, 817, 677, 654, 641 cm^{-1}. HPLC purity, 99.8% (t_R = 10.99 min).

4-(4-Chlorophenethyl)-1-(prop-2-yn-1-yl)piperidine (98). Synthesized from **61** (0.195 g, 0.602 mmol, 1.0 equiv) via general procedures D and E. Column chromatography, EtOAc/n-hex = 1/2 (v/v). Yield: 62% (85 mg); white crystals, mp 37−39 °C. ^1H NMR (400 MHz, $CDCl_3$): δ 1.18−1.34 (m, 3H), 1.49−1.55 (m, 2H), 1.70−1.76 (m, 2H), 2.12−2.18 (m, 2H), 2.22 (t, J = 2.5 Hz, 1H), 2.55−2.59 (m, 2H), 2.84−2.89 (m, 2H), 3.27 (d, J = 2.5 Hz, 2H),

https://dx.doi.org/10.1021/acs.jmedchem.9b01886
J. Med. Chem. XXXX, XXX, XXX−XXX

7.06−7.10 (m, 2H), 7.20−7.24 (m, 2H). ^{13}C NMR (100 MHz, $CDCl_3$): δ 32.11, 32.32, 34.60, 38.09, 47.13, 52.42, 72.82, 79.10, 128.28, 129.55, 131.21, 140.97. HRMS (ESI+): m/z calcd for $C_{16}H_{21}ClN$ $[M + H]^+$ 262.1363; found 262.1362. IR (ATR): 3219, 2931, 2919, 2863, 2801, 2758, 1492, 1451, 1407, 1335, 1282, 1261, 1138, 1121, 1109, 1084, 1015, 992, 974, 826, 797, 729, 688, 631, 539 cm^{-1}. HPLC purity, 100% (t_R = 9.90 min).

4-(4-Methoxyphenethyl)-1-(prop-2-yn-1-yl)piperidine (99). Synthesized from **62** (0.230 g, 0.720 mmol, 1.0 equiv) via general procedures D and E. Column chromatography, EtOAc/n-hex = 1/1 (v/v). Yield: 57% (103 mg); white crystals, mp 31−32 °C. ^{1}H NMR (400 MHz, $CDCl_3$): δ 1.22−1.36 (m, 3H), 1.50−1.56 (m, 2H), 1.73−1.77 (m, 2H), 2.13−2.19 (m, 2H), 2.23 (t, J = 2.5 Hz, 1H), 2.54−2.58 (m, 2H), 2.85−2.90 (m, 2H), 3.28 (d, J = 2.5 Hz, 2H), 3.77 (s, 3H), 6.80−6.84 (m, 2H), 7.07−7.10 (m, 2H). ^{13}C NMR (100 MHz, $CDCl_3$): δ 32.01, 32.14, 34.57, 38.46, 47.13, 52.46, 55.10, 72.77, 79.15, 113.60, 129.04, 134.60, 157.51. HRMS (ESI+): m/z calcd for $C_{17}H_{24}NO$ $[M + H]^+$ 258.1858; found 258.1857. IR (ATR): 3273, 2926, 2908, 2850, 2806, 1609, 1510, 1314, 1250, 1238, 1175, 1101, 1031, 975, 898, 832, 812, 702, 640, 577, 523 cm^{-1}. HPLC purity, 100% (t_R = 8.95 min).

1-(Prop-2-yn-1-yl)-4-(4-(trifluoromethyl)phenethyl)-piperidine (100). Synthesized from **63** (0.23 g, 0.64 mmol, 1.0 equiv) via general procedures D and E. Column chromatography, EtOAc/n-hex = 1/2 (v/v). Yield: 7% (14 mg); brown crystals, mp 31−33 °C. ^{1}H NMR (400 MHz, $CDCl_3$): δ 1.23−1.37 (m, 3H), 1.54−1.60 (m, 2H), 1.74−1.78 (m, 2H), 2.14−2.20 (m, 2H), 2.23 (t, J = 2.4 Hz, 1H), 2.65−2.70 (m, 2H), 2.86−2.90 (m, 2H), 3.29 (d, J = 2.4 Hz, 2H), 7.26−7.28 (m, 2H), 7.51−7.53 (m, 2H). ^{13}C NMR (100 MHz, $CDCl_3$): δ 32.14, 32.91, 34.71, 37.97, 47.17, 52.45, 72.89, 79.11, 124.34 (q, $J_{C,F}$ = 270.0 Hz), 125.20 (q, $J_{C,F}$ = 7.9 Hz), 128.02 (q, $J_{C,F}$ = 32.3 Hz) 128.57, 146.77. HRMS (ESI+): m/z calcd for $C_{17}H_{21}F_3N$ $[M + H]^+$ 296.1626; found 296.1625. IR (ATR): 3153, 2932, 2852, 2798, 1615, 1429, 1318, 1157, 1116, 1093, 1065, 1017, 978, 910, 854, 831, 735, 682, 637, 598, 552, 511 cm^{-1}. HPLC purity, 100% (t_R = 10.29 min).

1-(Prop-2-yn-1-yl)-4-(3-(trifluoromethyl)phenethyl)-piperidine (101). Synthesized from **64** (0.27 g, 0.76 mmol, 1.0 equiv) via general procedures D and E. Column chromatography, EtOAc/n-hex = 1/3 (v/v). Yield: 29% (65 mg); yellow-orange oil. ^{1}H NMR (400 MHz, $CDCl_3$): δ 1.22−1.37 (m, 3H), 1.54−1.59 (m, 2H), 1.72−1.78 (m, 2H), 2.14−2.19 (m, 2H), 2.22 (t, J = 2.4 Hz, 1H), 2.64−2.69 (m, 2H), 2.86−2.90 (m, 2H), 3.28 (d, J = 2.46 Hz, 2H), 7.32−7.43 (m, 4H). ^{13}C NMR (100 MHz, $CDCl_3$): δ 32.10, 32.88, 34.82, 38.03, 47.13, 52.43, 72.86, 79.07, 122.51 (q, $J_{C,F}$ = 3.8 Hz), 124.21 (q, $J_{C,F}$ = 272.2 Hz), 124.88 (q, $J_{C,F}$ = 3.7 Hz), 128.63, 130.51 (q, $J_{C,F}$ = 31.8 Hz), 131.64, 143.48. HRMS (ESI+): m/z calcd for $C_{17}H_{21}NF_3$ $[M + H]^+$ 296.1626; found 296.1629. IR (ATR): 3308, 2923, 2849, 2804, 2757, 1449, 1329, 1199, 1161, 1121, 1072, 976, 900, 879, 800, 735, 702, 660, 631 cm^{-1}. HPLC purity, 98.7% (t_R = 10.25 min).

4-(2-(1-(Prop-2-yn-1-yl)piperidin-4-yl)ethyl)benzonitrile (102). Synthesized from **65** (0.075 g, 0.239 mmol, 1.0 equiv) via general procedures D and E. Column chromatography, EtOAc/n-hex = 1/1 (v/v). Yield: 59% (106 mg); white crystals, mp 40−42 °C. ^{1}H NMR (400 MHz, $CDCl_3$): δ 1.20−1.36 (m, 3H), 1.53−1.58 (m, 2H), 1.72−1.77 (m, 2H), 2.13−2.19 (m, 2H), 2.22 (t, J = 2.4 Hz, 1H), 2.65−2.69 (m, 2H), 2.85−2.90 (m, 2H), 3.28 (d, J = 2.5 Hz, 2H), 7.25−7.28 (m, 2H), 7.54−7.57 (m, 2H). ^{13}C NMR (100 MHz, $CDCl_3$): δ 31.99, 33.13, 34.62, 37.60, 47.03, 52.28, 72.82, 78.97, 109.39, 118.96, 128.96, 132.01, 148.23. HRMS (ESI+): m/z calcd for $C_{17}H_{21}N_2$ $[M + H]^+$ 253.1705; found 253.1706. IR (ATR): 3270, 2925, 2795, 2224, 1606, 1424, 1326, 1310, 1180, 1137, 1105, 977, 901, 852, 836, 821, 766, 682, 573, 545 cm^{-1}. HPLC purity, 96.0% (t_R = 8.42 min).

1-(Prop-2-yn-1-yl)-4-(4-propylphenethyl)piperidine (103). Synthesized from **66** (0.185 g, 0.561 mmol, 1.0 equiv) via general procedures D and E. Column chromatography, EtOAc/n-hex = 1/2 (v/v). Yield: 45% (68 mg); pale yellow oil. ^{1}H NMR (400 MHz, $CDCl_3$): δ 0.95 (t, J = 7.4 Hz, 3H), 1.25−1.37 (m, 3H), 1.53−1.59 (m, 2H), 1.60−1.68 (m, 2H), 1.76−1.80 (m, 2H), 2.15−2.21 (m, 2H), 2.23 (t, J = 2.4 Hz, 1H), 2.53−2.62 (m, 4H), 2.87−2.91 (m, 2H), 3.30 (d, J = 2.4 Hz, 2H), 7.07−7.11 (m, 4H). ^{13}C NMR (100 MHz, $CDCl_3$): δ 13.86, 24.60, 32.20, 32.60, 34.75, 37.61, 38.37, 47.19, 52.53, 72.80, 79.20, 128.07, 128.32, 139.80 139.88. HRMS (ESI+): m/z calcd for $C_{19}H_{28}N$ $[M + H]^+$ 270.2216; found 270.2215. IR (ATR): 3008, 2925, 2852, 2801, 2753, 1513, 1454, 1337, 1312, 1117, 1106, 1021, 976, 897, 806, 787, 679, 645, 623, 503 cm^{-1}. HPLC purity, 97.1% (t_R = 11.12 min).

(*Z*)-4-(2-(1-(Prop-2-yn-1-yl)piperidin-4-yl)vinyl)benzamide (104). Synthesized from **87** (0.065 g, 0.260 mmol, 1.0 equiv) via general procedure F. Column chromatography, CH_2Cl_2/MeOH = 20/1 (v/v). Yield: 46% (32 mg); white crystals, mp 127−130 °C. ^{1}H NMR (400 MHz, $CDCl_3$): δ 1.49−1.59 (m, 2H), 1.68−1.74 (m, 2H), 2.20 (td, J = 11.7, 2.6 Hz, 2H), 2.23 (t, J = 2.4 Hz, 1H), 2.46−2.57 (m, 1H), 2.87 (dt, J = 11.0, 2.4 Hz, 2H), 3.28 (d, J = 2.5 Hz, 2H), 5.57 (dd, J = 11.7, 10.1 Hz, 1H), 6.27 (bs, 2H), 6.39 (d, J = 11.7 Hz, 1H), 7.27−7.30 (m, 2H), 7.77−7.80 (m, 2H). ^{13}C NMR (100 MHz, $CDCl_3$): δ 32.12, 34.58, 47.19, 51.77, 73.07, 78.89, 127.17, 127.34, 128.61, 131.35, 139.00, 141.40, 169.32. HRMS (ESI+): m/z calcd for $C_{17}H_{21}N_2O$ $[M + H]^+$ 269.1654; found 269.1652. IR (ATR): 3331, 3307, 3285, 3204, 2928, 2806, 1658, 1604, 1550, 1418, 1386, 1309, 1259, 1131, 1122, 1104, 969, 856, 794, 765, 736, 659, 636, 509 cm^{-1}. HPLC purity, 98.2% (t_R = 6.34 min).

(*E*)-4-(2-(1-(Prop-2-yn-1-yl)piperidin-4-yl)vinyl)benzamide (105). Synthesized from **88** (0.080 g, 0.320 mmol, 1.0 equiv) via general procedure F. Column chromatography, CH_2Cl_2/MeOH = 20/1 (v/v). Yield: 63% (54 mg); white crystals, mp 181−184 °C. ^{1}H NMR (400 MHz, DMSO-d_6): δ 1.42 (dq, J = 12.7, 3.9 Hz, 2H), 1.72−1.75 (m, 2H), 2.06−2.12 (m, 1H), 2.17 (td, J = 11.5, 2.2 Hz, 2H), 2.79−2.83 (m, 2H), 3.14 (t, J = 2.4 Hz, 1H), 3.26 (d, J = 2.4 Hz, 2H), 6.36−6.46 (m, 2H), 7.30 (bs, 1H), 7.45−7.47 (m, 2H), 7.80−7.82 (m, 2H), 7.93 (bs, 1H). ^{13}C NMR (100 MHz, DMSO-d_6): δ 31.34, 38.32, 46.38, 51.42, 75.53, 79.53, 125.53, 126.96, 127.75, 132.40, 137.04, 139.99, 167.43. HRMS (ESI+): m/z calcd for $C_{17}H_{21}N_2O$ $[M + H]^+$ 269.1654; found 269.1656. IR (ATR): 3401, 3281, 3147, 2937, 2913, 2805, 1645, 1614, 1564, 1442, 1415, 1393, 1313, 1289, 1221, 1136, 1101, 976, 870, 829, 800, 767, 682, 647, 635, 599, 544 cm^{-1}. HPLC purity, 99.4% (t_R = 6.20 min).

4-(2-(1-(Prop-2-yn-1-yl)piperidin-4-yl)ethyl)benzamide (106). Synthesized from **102** (0.075 g, 0.297 mmol, 1.0 equiv) via general procedure F. Column chromatography, CH_2Cl_2/MeOH = 9/1 (v/v). Yield: 42% (34 mg); white crystals, mp 155−158 °C. ^{1}H NMR (400 MHz, MeOD): δ 1.28−1.36 (m, 3H), 1.58−1.63 (m, 2H), 1.80−1.83 (m, 2H), 2.21 (t, J = 11.3 Hz, 2H), 2.69 (t, J = 2.5 Hz, 1H), 2.70−2.74 (m, 2H), 2.94−2.99 (m, 2H), 3.29 (d, J = 2.5 Hz, 2H), 7.30−7.32 (m, 2H), 7.79−7.82 (m, 2H), resonances for NH_2 missing (exchange with MeOD). ^{13}C NMR (100 MHz, MeOD): δ 32.74, 33.88, 35.92, 39.11, 47.65, 53.55, 75.10, 79.19, 128.82, 129.50, 132.39, 148.40, 172.38. HRMS (ESI+): m/z calcd for $C_{17}H_{23}N_2O$ $[M + H]^+$ 269.1810; found 269.1816. IR (ATR): 3178, 2932, 2919, 2847, 2798, 2752, 2543, 2373, 1610, 1563, 1421, 1404, 1333, 1270, 1186, 1144, 1103, 1019, 973, 915, 859, 767, 755, 709, 594 cm^{-1}. HPLC purity, 99.6% (t_R = 6.29 min).

4-(2-(1-(Prop-2-yn-1-yl)piperidin-4-yl)ethyl)phenol (107). The methoxy substituted compound **99** (50 mg, 0.194 mmol, 1.0 equiv) was dissolved in anhydrous toluene (6 mL) under argon and cooled to −20 °C. BBr_3 (1 M in CH_2Cl_2, 582 μL, 0.582 mmol, 3.0 equiv) was added dropwise and the reaction mixture was stirred for another hour at −20 °C. The mixture was allowed to warm up to room temperature (1 h). Saturated aqueous $NaHCO_3$ (10 mL) was added, and the resulting emulsion was stirred vigorously for 15 min before EtOAc (30 mL) was added. The phases were separated, and the organic layer was washed with saturated brine (50 mL), dried over Na_2SO_4, and evaporated. Column chromatography, CH_2Cl_2/MeOH = 20/1 (v/v). Yield: 57% (27 mg); white crystals, mp 104−106 °C. ^{1}H NMR (400 MHz, $CDCl_3$): δ 1.23−1.39 (m, 3H), 1.48−1.54 (m, 2H), 1.73−1.79 (m, 2H), 2.21−2.27 (m, 2H), 2.25 (t, J = 2.4 Hz, 1H), 2.51−2.55 (m, 2H), 2.90−2.94 (m, 2H), 3.32 (d, J = 2.5 Hz, 2H), 6.71−6.73 (m, 2H), 6.99−7.02 (m, 2H), resonance for OH

https://dx.doi.org/10.1021/acs.jmedchem.9b01886
J. Med. Chem. XXXX, XXX, XXX−XXX

missing (exchange with water in solvent). ^{13}C NMR (100 MHz, $CDCl_3$): δ 31.89, 32.09, 34.56, 38.41, 47.07, 52.42, 73.33, 78.68, 115.28, 129.27, 134.34, 153.91. HRMS (ESI+): m/z calcd for $C_{16}H_{22}NO$ $[M + H]^+$ 244.1701; found 244.1697. IR (ATR): 3278, 2909, 2853, 2815, 2598, 1614, 1593, 1515, 1464, 1392, 1337, 1269, 1249, 1170, 1116, 974, 819, 785, 692, 636, 563, 516, 501 cm^{-1}. HPLC purity, 96.1% (t_R = 7.17 min).

Preparation of Hydrochloride Salts. Compounds **1**, **6**, **67**, **69**, **84**, **97**, and **100** were transformed into corresponding hydrochloride salts following the described procedure. Compound in the form of a free base (0.2−2.5 g, 1.0 equiv) was dissolved in MeOH (5−20 mL). Then a 2 M solution of HCl in Et_2O (2.0 equiv) was added at room temperature under vigorous stirring with magnetic stirrer. The precipitate formed was filtered off, washed with Et_2O (50−100 mL), and dried at reduced pressure to obtain hydrochloride salts. These salts were used for the crystallization, permeability, *ex vivo* and *in vivo* experiments.

Biology. Protein Production, Enzymatic Assays, and X-ray Crystallography. All of the reagents were purchased from Sigma-Aldrich unless specified otherwise. The effects of the compounds on hMAO-A and hMAO-B were first investigated by determining the IC_{50} values using a previously described fluorimetric assay.[42] The inhibitory activities of the compounds were determined according to their effects on the generation of hydrogen peroxide (H_2O_2) as a side-product of hMAO activity. For details on protein production, enzymatic assays, and X-ray crystallography, see Supporting Information.

Cell Culture and Treatments. The human neuroblastoma SH-SY5Y cell line was purchased from American Type Culture Collection (CRL-2266; VA, USA). These cells were cultured in Advanced Dulbecco's modified Eagle's medium (Gibco, Thermo Fisher Scientific, MA, USA) supplemented with 10% fetal bovine serum (Gibco), 2 mM L-glutamine, 50 U/mL penicillin, and 50 μg/mL streptomycin (Sigma, MO, USA) in a humidified atmosphere of 95% air and 5% CO_2 at 37 °C and grown to 80% confluence. Prior to cell treatments, the complete medium was replaced with serum-depleted medium. Compounds were prepared as stock solutions of 20 mM in DMSO and were used at concentrations of 5−50 μM. For the cytotoxic stimuli, the 10 mM 6-OHDA (Sigma, MO, USA) stock was prepared in phosphate buffered saline, pH 7.4, with 0.01% ascorbic acid. For the detailed experimental procedures see Supporting Information.

Animals. Adult male Swiss mice (weight, 25−30 g) and adult male Wistar rats (weight, 200−300 g) were obtained from the Central Animal House of the School of Pharmacy and Biochemistry, University of Buenos Aires, Buenos Aires, Argentina. For behavioral assays, the mice were housed in groups of five in a controlled environment (20−23 °C), with free access to food and water, and maintained on a 12 h/12 h day/night cycle, with light on at 07:00 h. The housing, handling, and experimental procedures for both the mice and rats complied with the recommendations set out by the National Institutes of Health Guide for Care and Use of Laboratory Animals (NIH Publication No. 8023, revised 1996) and the Institutional Committees for the Care and Use of Laboratory Animals of the Faculty of Pharmacy and Biochemistry, University of Buenos Aires, Argentina (Code 31682/2014). All efforts were taken to minimize animal suffering. The number of animals used was the minimum number consistent with obtaining significant data. The mice were randomly assigned to the treatment groups and were used only once. The pharmacological tests were evaluated by experimenters who were not aware of the treatments administered and were performed between 10:00 h and 14:00 h.

Administrations and Procedures. The test compounds (used as their hydrochloride salts) were dissolved in 0.9% saline. Haloperidol, diazepam, and imipramine were diluted by sequential additions of DMSO, an aqueous solution of 0.25% Tween 80, and 0.9% saline to their final concentrations of 5%, 20%, and 75%, respectively. In each session, a control group of mice received only vehicle, in parallel with the mice that received the drug treatments. The volumes of the ip injections and oral gavage (po) administrations were 0.10−0.20 mL/30 g body weight and 0.30 mL/30 g body weight, respectively. The protein concentrations in the mouse brain homogenates were determined using the method of Bradford, with bovine serum albumin as the standard.

For the acute behavioral assays, all of the compounds were tested 30 min after ip administrations. For the chronical treatments, the mice were injected ip with 0.3 mg/kg **69**, **100** or 0.9% saline (control group) once a day between 09:00 and 10:00 h over 10 consecutive days. On days 1, 3, 5, 7, and 9, these mice were weighted. On day 8, at 30 min after the relevant ip treatment, the mice were submitted to the plus maze (for **69**) or the hole−board tests (for **100**), and their locomotor activity was recorded immediately afterward. On day 10, at 30 min after the relevant ip treatment, the mice were submitted to the tail suspension test (for **69**) or the haloperidol-induced catalepsy assay (for **100**) (Figures S10 and S11). For all of these behavioral assays, the arena/apparatus was cleaned with 60% ethanol between each trial with each mouse. Behavioral assays are described in detail in Supporting Information.

Mouse Brain Homogenate Preparation. The mice were killed humanely by decapitation at 30 min after drug or 0.9% saline treatment (for acute ip injections), at 60 min after drug or 0.9% saline treatment (for acute oral gavage), or on day 10 at 90 min after the last drug or 0.9% saline ip treatment after the tail suspension test (for the mice chronically treated with **69**) or after haloperidol-induced catalepsy test (for the mice chronically treated with **100**). Also, three mice that were chronically treated with **100** or 0.9% saline ip but without the haloperidol injection were also tested to determine any haloperidol effects in the *ex vivo* MAO-B activity assay (Figures S10 and S11). After removal of the olfactory bulb, the whole mouse brains were washed several times in ice-cold 50 mM potassium phosphate buffer (pH 7.4, 0.05% [v/v] Triton X-114). Then, each brain was independently homogenized using a blender homogenizer (PRO Scientific Inc., CT, USA) at 30 000 rpm for 1 min, in 1.5 mL of 100 mM potassium phosphate buffer (pH 7.4, 0.1% [v/v] Triton X-114) at 4 °C (in ice). The homogenate was then centrifuged at 3000g for 20 min at 4 °C. The supernatant was stored at −20 °C until the following day for the MAO inhibition assays.

***Ex Vivo* MAO Inhibition Assay.** The *ex vivo* effects of **69** on MAO-A and **100** on MAO-B enzymatic activities (ip or oral administration, 30 min before decapitation) in the mouse brain homogenates were investigated using a previously described fluorimetric assay, with minor modifications.[42] For details see Supporting Information.

■ ASSOCIATED CONTENT

Supporting Information

The Supporting Information is available free of charge at https://pubs.acs.org/doi/10.1021/acs.jmedchem.9b01886.

Supplementary figures, supplementary tables, supplementary results and discussion, supplementary methods, HPLC traces for representative final compounds, and ^{1}H and ^{13}C NMR spectra for final compounds (PDF)

Movie for undocking experiment, MAO-A (MP4)

Movie for undocking experiment, MAO-B (MP4)

Molecular formula strings and activity data (CSV)

Model of undocking in Figure 3 (PDB)

Model of undocking in Figure 3 (PDB)

Model of undocking in Figure 3 (PDB)

Model of undocking in Figure 3 (PDB)

Accession Codes

The coordinates and structure factors have been deposited in the PDB under accession codes 6RKB (compound **1**), 6RKP (compound **84**), and 6RLE (compound **97**). Authors will release the atomic coordinates and experimental data upon article publication.

https://dx.doi.org/10.1021/acs.jmedchem.9b01886
J. Med. Chem. XXXX, XXX, XXX−XXX

AUTHOR INFORMATION

Corresponding Authors

Claudia Binda − *Department of Biology and Biotechnology, University of Pavia, Pavia 27100, Italy*; orcid.org/0000-0003-2038-9845; Email: claudia.binda@unipv.it

Mariel Marder − *Universidad de Buenos Aires, Consejo Nacional de Investigaciones Científicas y Técnicas, and Instituto de Química y Fisicoquímica Biológicas, Facultad de Farmacia y Bioquímica, Universidad de Buenos Aires, Buenos Aires C1113AAD, Argentina*; Email: mmarder@qb.ffyb.uba.ar

Stanislav Gobec − *Faculty of Pharmacy, University of Ljubljana, Ljubljana 1000, Slovenia*; orcid.org/0000-0002-9678-3083; Email: stanislav.gobec@ffa.uni-lj.si

Authors

Damijan Knez − *Faculty of Pharmacy, University of Ljubljana, Ljubljana 1000, Slovenia*

Natalia Colettis − *Universidad de Buenos Aires, Consejo Nacional de Investigaciones Científicas y Técnicas, and Instituto de Química y Fisicoquímica Biológicas, Facultad de Farmacia y Bioquímica, Universidad de Buenos Aires, Buenos Aires C1113AAD, Argentina*

Luca G. Iacovino − *Department of Biology and Biotechnology, University of Pavia, Pavia 27100, Italy*

Matej Sova − *Faculty of Pharmacy, University of Ljubljana, Ljubljana 1000, Slovenia*

Anja Pišlar − *Faculty of Pharmacy, University of Ljubljana, Ljubljana 1000, Slovenia*

Janez Konc − *National Institute of Chemistry, Ljubljana 1000, Slovenia*

Samo Lešnik − *National Institute of Chemistry, Ljubljana 1000, Slovenia*

Josefina Higgs − *Universidad de Buenos Aires, Consejo Nacional de Investigaciones Científicas y Técnicas, and Instituto de Química y Fisicoquímica Biológicas, Facultad de Farmacia y Bioquímica, Universidad de Buenos Aires, Buenos Aires C1113AAD, Argentina*

Fabiola Kamecki − *Universidad de Buenos Aires, Consejo Nacional de Investigaciones Científicas y Técnicas, and Instituto de Química y Fisicoquímica Biológicas, Facultad de Farmacia y Bioquímica, Universidad de Buenos Aires, Buenos Aires C1113AAD, Argentina*

Irene Mangialavori − *Universidad de Buenos Aires, Consejo Nacional de Investigaciones Científicas y Técnicas, and Instituto de Química y Fisicoquímica Biológicas, Facultad de Farmacia y Bioquímica, Universidad de Buenos Aires, Buenos Aires C1113AAD, Argentina*

Ana Dolšak − *Faculty of Pharmacy, University of Ljubljana, Ljubljana 1000, Slovenia*

Simon Žakelj − *Faculty of Pharmacy, University of Ljubljana, Ljubljana 1000, Slovenia*

Jurij Trontelj − *Faculty of Pharmacy, University of Ljubljana, Ljubljana 1000, Slovenia*

Janko Kos − *Faculty of Pharmacy, University of Ljubljana, Ljubljana 1000, Slovenia*

Complete contact information is available at: https://pubs.acs.org/10.1021/acs.jmedchem.9b01886

Author Contributions

#D.K., N.C., and L.G.I. contributed equally to this work. D.K. designed the inhibitors, performed the chemistry and *in vitro* MAO inhibition, participated in the inhibition kinetic studies, crystallographic studies, and *ex vivo* and *in vivo* evaluations, and oversaw the full study. N.C. performed the *ex vivo* and *in vivo* assays and contributed to the statistical analysis of the data. L.G.I. performed the inhibition kinetic studies and UV−vis measurements and refined and analyzed the crystallographic data. M.S. performed the chemistry. A.P. performed the cytotoxicity and neuroprotection assays with the SH-SY5Y cells. J.K. and S.L. performed the molecular modeling. J.H. performed the *in vitro* binding experiments and participated in the *in vivo* assays. F.K. performed the *ex vivo* assays and participated in the *in vitro* binding experiments. I.M. participated in the *ex vivo* assays and contributed to the statistical analysis of the data. A.D. performed the chemistry. S.Ž. performed the *in vitro* permeability assays and contributed to the LC−MS analysis. J.T. performed the LC−MS analysis. J.K. oversaw the cytotoxicity and neuroprotection assays with the SH-SY5Y cells. C.B. supervised the inhibition kinetic studies, UV−vis measurements, and crystallography analysis. M.M. designed and performed the *in vivo* experiments. S.G. designed and oversaw the project and contributed to the editing of the manuscript. All of the authors contributed to the design, analysis, and discussion of the research and the writing of the manuscript.

Notes

The authors declare no competing financial interest.

ACKNOWLEDGMENTS

This work was supported by ARRS (Grants P1-0208, L1-8157, BI-AR/15-17-003, P4-0127, L7-8269), Fondazione Cariplo (Grant 2014-0672), MIUR "Dipartimenti di Eccellenza" Programme (2018−2022), and European Community Seventh Framework Programme (FP7/2007−2013) under BioStruct-X (Grants 7551 and 10205) and CALIPSOplus (Horizon 2020 EC access program). Financial support is acknowledged from CONICET (PIP No. 112 201501 00410), UBA (UBACyT No. 20020100100415 and 20020150100012BA), ANPCyT (PICT No. 2011-0328), and MINCYT. We thank ESRF (Grenoble) and SLS (Villigen) for use of synchrotrons. We also thank Chris Berrie for critical reading of the manuscript.

ABBREVIATIONS USED

DMSO, dimethylsulfoxide; FAD, flavin adenine dinucleotide; hMAO-A/B, human monoamine oxidases A and B; KHMDS, potassium bis(trimethylsilyl)amide; NaHMDS, sodium bis(trimethylsilyl)amide; n-hex, *n*-hexane; LDH, lactate dehydrogenase; MAO, monoamine oxidase; PI, propidium iodide; SAR, structure−activity relationship; TBTU, 2-(1*H*-benzotriazole-1-yl)-1,1,3,3-tetramethylaminium tetrafluoroborate; THF, tetrahydrofuran

REFERENCES

(1) Persch, E.; Dumele, O.; Diederich, F. Molecular Recognition in Chemical and Biological Systems. *Angew. Chem., Int. Ed.* **2015**, *54* (11), 3290−3327.

(2) Kasprzyk-Hordern, B. Pharmacologically Active Compounds in the Environment and Their Chirality. *Chem. Soc. Rev.* **2010**, *39* (11), 4466−4503.

(3) Brooks, W. H.; Guida, W. C.; Daniel, K. G. The Significance of Chirality in Drug Design and Development. *Curr. Top. Med. Chem.* **2011**, *11* (7), 760−770.

(4) Nafisi, S.; Norouzi, Z. A Comparative Study on the Interaction of *Cis*- and *Trans*-Platin with DNA and RNA. *DNA Cell Biol.* **2009**, *28* (9), 469−477.

https://dx.doi.org/10.1021/acs.jmedchem.9b01886
J. Med. Chem. XXXX, XXX, XXX−XXX

(5) Robertson, D. W.; Katzenellenbogen, J. A.; Long, D. J.; Rorke, E. A.; Katzenellenbogen, B. S. Tamoxifen Antiestrogens. A Comparison of the Activity, Pharmacokinetics, and Metabolic Activation of the *Cis* and *Trans* Isomers of Tamoxifen. *J. Steroid Biochem.* **1982**, *16* (1), 1−13.
(6) Gaspari, R.; Prota, A. E.; Bargsten, K.; Cavalli, A.; Steinmetz, M. O. Structural Basis of *Cis*- and *Trans*-Combretastatin Binding to Tubulin. *Chem-US* **2017**, *2* (1), 102−113.
(7) Bach, A. W.; Lan, N. C.; Johnson, D. L.; Abell, C. W.; Bembenek, M. E.; Kwan, S. W.; Seeburg, P. H.; Shih, J. C. Cdna Cloning of Human Liver Monoamine Oxidase A and B: Molecular Basis of Differences in Enzymatic Properties. *Proc. Natl. Acad. Sci. U. S. A.* **1988**, *85* (13), 4934−4938.
(8) De Colibus, L.; Li, M.; Binda, C.; Lustig, A.; Edmondson, D. E.; Mattevi, A. Three-Dimensional Structure of Human Monoamine Oxidase A (Mao A): Relation to the Structures of Rat MAO A and Human MAO B. *Proc. Natl. Acad. Sci. U. S. A.* **2005**, *102* (36), 12684−12689.
(9) Milczek, E. M.; Binda, C.; Rovida, S.; Mattevi, A.; Edmondson, D. E. The 'Gating' Residues Ile199 and Tyr326 in Human Monoamine Oxidase B Function in Substrate and Inhibitor Recognition. *FEBS J.* **2011**, *278* (24), 4860−4869.
(10) Ramsay, R. R. Molecular Aspects of Monoamine Oxidase B. *Prog. Neuro-Psychopharmacol. Biol. Psychiatry* **2016**, *69*, 81−89.
(11) Ramsay, R. R.; Albreht, A. Kinetics, Mechanism, and Inhibition of Monoamine Oxidase. *J. Neural Transm. (Vienna)* **2018**, *125* (11), 1659−1683.
(12) Kim, D.; Baik, S. H.; Kang, S.; Cho, S. W.; Bae, J.; Cha, M. Y.; Sailor, M. J.; Mook-Jung, I.; Ahn, K. H. Close Correlation of Monoamine Oxidase Activity with Progress of Alzheimer's Disease in Mice, Observed by in Vivo Two-Photon Imaging. *ACS Cent. Sci.* **2016**, *2* (12), 967−975.
(13) Schedin-Weiss, S.; Inoue, M.; Hromadkova, L.; Teranishi, Y.; Yamamoto, N. G.; Wiehager, B.; Bogdanovic, N.; Winblad, B.; Sandebring-Matton, A.; Frykman, S.; Tjernberg, L. O. Monoamine Oxidase B is Elevated in Alzheimer Disease Neurons, is Associated with γ-Secretase and Regulates Neuronal Amyloid β-Peptide Levels. *Alzheimer's Res. Ther.* **2017**, *9* (1), 57.
(14) Chiuccariello, L.; Houle, S.; Miler, L.; Cooke, R. G.; Rusjan, P. M.; Rajkowska, G.; Levitan, R. D.; Kish, S. J.; Kolla, N. J.; Ou, X.; Wilson, A. A.; Meyer, J. H. Elevated Monoamine Oxidase A Binding During Major Depressive Episodes is Associated with Greater Severity and Reversed Neurovegetative Symptoms. *Neuropsychopharmacology* **2014**, *39* (4), 973−980.
(15) Deshwal, S.; Di Sante, M.; Di Lisa, F.; Kaludercic, N. Emerging Role of Monoamine Oxidase as a Therapeutic Target for Cardiovascular Disease. *Curr. Opin. Pharmacol.* **2017**, *33*, 64−69.
(16) Shih, J. C. Monoamine Oxidase Isoenzymes: Genes, Functions and Targets for Behavior and Cancer Therapy. *J. Neural Transm. (Vienna)* **2018**, *125* (11), 1553−1566.
(17) Thase, M. E. The Role of Monoamine Oxidase Inhibitors in Depression Treatment Guidelines. *J. Clin. Psychiatry* **2012**, *73* (Suppl. 1), 10−16.
(18) Dezsi, L.; Vecsei, L. Monoamine Oxidase B Inhibitors in Parkinson's Disease. *CNS Neurol. Disord.: Drug Targets* **2017**, *16* (4), 425−439.
(19) Youdim, M. B. H. Monoamine Oxidase Inhibitors, and Iron Chelators in Depressive Illness and Neurodegenerative Diseases. *J. Neural. Transm. (Vienna)* **2018**, *125* (11), 1719−1733.
(20) Youdim, M. B.; Edmondson, D.; Tipton, K. F. The Therapeutic Potential of Monoamine Oxidase Inhibitors. *Nat. Rev. Neurosci.* **2006**, *7* (4), 295−309.
(21) Petrek, M.; Otyepka, M.; Banas, P.; Kosinova, P.; Koca, J.; Damborsky, J. Caver: A New Tool to Explore Routes from Protein Clefts, Pockets and Cavities. *BMC Bioinf.* **2006**, *7*, 316.
(22) Filipovič, J.; Vávra, O.; Plhák, J.; Bednář, D.; Marques, S. M.; Brezovský, J.; Matyska, L.; Damborský, J. CaverDock: A Novel Method for the Fast Analysis of Ligand Transport. *arXiv* **2018**, 1809.03453.
(23) Waldeck, D. H. Photoisomerization Dynamics of Stilbenes. *Chem. Rev.* **1991**, *91* (3), 415−436.
(24) Albreht, A.; Vovk, I.; Mavri, J.; Marco-Contelles, J.; Ramsay, R. R. Evidence for a Cyanine Link between Propargylamine Drugs and Monoamine Oxidase Clarifies the Inactivation Mechanism. *Front. Chem.* **2018**, *6*, 169.
(25) Esteban, G.; Allan, J.; Samadi, A.; Mattevi, A.; Unzeta, M.; Marco-Contelles, J.; Binda, C.; Ramsay, R. R. Kinetic and Structural Analysis of the Irreversible Inhibition of Human Monoamine Oxidases by ASS234, a Multi-Target Compound Designed for Use in Alzheimer's Disease. *Biochim. Biophys. Acta, Proteins Proteomics* **2014**, *1844* (6), 1104−1110.
(26) Binda, C.; Hubalek, F.; Li, M.; Herzig, Y.; Sterling, J.; Edmondson, D. E.; Mattevi, A. Crystal Structures of Monoamine Oxidase B in Complex with Four Inhibitors of the *N*-Propargylaminoindan Class. *J. Med. Chem.* **2004**, *47* (7), 1767−1774.
(27) Reis, J.; Manzella, N.; Cagide, F.; Mialet-Perez, J.; Uriarte, E.; Parini, A.; Borges, F.; Binda, C. Tight-Binding Inhibition of Human Monoamine Oxidase B by Chromone Analogs: A Kinetic, Crystallographic, and Biological Analysis. *J. Med. Chem.* **2018**, *61* (9), 4203−4212.
(28) Lopes, F. M.; Schroder, R.; da Frota Junior, M. L.; Zanotto-Filho, A.; Muller, C. B.; Pires, A. S.; Meurer, R. T.; Colpo, G. D.; Gelain, D. P.; Kapczinski, F.; Moreira, J. C. F.; da Cruz Fernandes, M.; Klamt, F. Comparison between Proliferative and Neuron-Like SH-SY5Y Cells as an in Vitro Model for Parkinson Disease Studies. *Brain Res.* **2010**, *1337*, 85−94.
(29) Finberg, J. P.; Rabey, J. M. Inhibitors of MAO-A and MAO-B in Psychiatry and Neurology. *Front. Pharmacol.* **2016**, *7*, 340.
(30) Shulman, K. I.; Herrmann, N.; Walker, S. E. Current Place of Monoamine Oxidase Inhibitors in the Treatment of Depression. *CNS Drugs* **2013**, *27* (10), 789−797.
(31) Kircanski, K.; LeMoult, J.; Ordaz, S.; Gotlib, I. H. Investigating the Nature of Co-Occurring Depression and Anxiety: Comparing Diagnostic and Dimensional Research Approaches. *J. Affective Disord.* **2017**, *216*, 123−135.
(32) Akimova, E.; Lanzenberger, R.; Kasper, S. The Serotonin-1A Receptor in Anxiety Disorders. *Biol. Psychiatry* **2009**, *66* (7), 627−635.
(33) Fernandez, S. P.; Wasowski, C.; Loscalzo, L. M.; Granger, R. E.; Johnston, G. A.; Paladini, A. C.; Marder, M. Central Nervous System Depressant Action of Flavonoid Glycosides. *Eur. J. Pharmacol.* **2006**, *539* (3), 168−176.
(34) Bali, A.; Jaggi, A. S. Preclinical Experimental Stress Studies: Protocols, Assessment and Comparison. *Eur. J. Pharmacol.* **2015**, *746*, 282−292.
(35) Tripathi, A. C.; Upadhyay, S.; Paliwal, S.; Saraf, S. K. Privileged Scaffolds as MAO Inhibitors: Retrospect and Prospects. *Eur. J. Med. Chem.* **2018**, *145*, 445−497.
(36) Holt, A. On the Practical Aspects of Characterising Monoamine Oxidase Inhibition in Vitro. *J. Neural. Transm. (Vienna)* **2018**, *125* (11), 1685−1705.
(37) Pettersson, F.; Svensson, P.; Waters, S.; Waters, N.; Sonesson, C. Synthesis and Evaluation of a Set of Para-Substituted 4-Phenylpiperidines and 4-Phenylpiperazines as Monoamine Oxidase (MAO) Inhibitors. *J. Med. Chem.* **2012**, *55* (7), 3242−3249.
(38) Heuson, E.; Storgaard, M.; Huynh, T. H.; Charmantray, F.; Gefflaut, T.; Bunch, L. Profiling Substrate Specificity of Two Series of Phenethylamine Analogs at Monoamine Oxidase A and B. *Org. Biomol. Chem.* **2014**, *12* (43), 8689−8695.
(39) Kumar, S.; Ali, J.; Baboota, S. Design Expert(®) Supported Optimization and Predictive Analysis of Selegiline Nanoemulsion *Via* the Olfactory Region with Enhanced Behavioural Performance in Parkinson's Disease. *Nanotechnology* **2016**, *27* (43), 435101.
(40) Daina, A.; Michielin, O.; Zoete, V. SwissADME: A Free Web Tool to Evaluate Pharmacokinetics, Drug-Likeness and Medicinal Chemistry Friendliness of Small Molecules. *Sci. Rep.* **2017**, *7*, 42717.
(41) Baell, J. B.; Holloway, G. A. New Substructure Filters for Removal of Pan Assay Interference Compounds (PAINS) from

https://dx.doi.org/10.1021/acs.jmedchem.9b01886
J. Med. Chem. XXXX, XXX, XXX−XXX

Screening Libraries and for Their Exclusion in Bioassays. *J. Med. Chem.* **2010**, *53* (7), 2719−2740.
(42) Zhou, M.; Panchuk-Voloshina, N. A One-Step Fluorometric Method for the Continuous Measurement of Monoamine Oxidase Activity. *Anal. Biochem.* **1997**, *253* (2), 169−174.

https://dx.doi.org/10.1021/acs.jmedchem.9b01886
J. Med. Chem. XXXX, XXX, XXX−XXX

1.4 MONOAMINE OXIDASE-B AND DIPHENYLENE IODONIUM

Diphenylene iodonium (DPI) is an antioxidant and reactive oxygen species (ROS) scavenger compound with very interesting biochemical features, widely used as flavoenzyme inhibitor in cellular studies (Holland and Sherratt 1972, Mandriota, Pyke et al. 2000, Paudel, Lewis et al. 2019) (Figure 11).

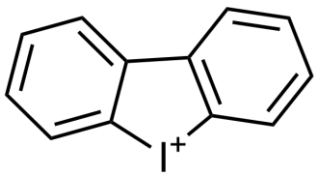

Figure 11. Chemical structure of DPI.

DPI is endowed with a pan-flavoenzyme inhibitory activity, several biochemical studies elucidated the irreversible radical mechanism by which DPI binds the reduced form of the FAD leading to a covalent adduct with the flavin ring (Chakraborty and Massey 2002, Lu, Risbood et al. 2017). Due to this high reactivity, DPI has also been described as inhibitor of several heme-containing enzymes such as NADPH oxidases (NOXs) (Ogrunc, Di Micco et al. 2014, Ju, Ying et al. 2017, Paudel, Lewis et al. 2019) and cytochrome P-450 reductase (Chakraborty and Massey 2002), irreversibly reacting with the reduced form of the heme group. Considering the main relevance of this compound in ROS-biology and the functional similarity of MAOs and NOXs in different ROS systems, we probed the reactivity of DPI with both MAO-A and MAO-B through biochemical and crystallographic experiments. This work is reported in the article "Diphenylene Iodonium Is a Noncovalent MAO Inhibitor: A Biochemical and Structural Analysis" published in ChemMedChem journal and attached at the end of this section.

Monitoring the FAD UV-vis spectra of the DPI-bound MAO-A and MAO-B unequivocally clarified that this compound represented a non-covalent inhibitor of MAOs as in anaerobic conditions no evidence of covalent adducts were shown in the FAD spectra. Moreover, steady-state experiments showed that MAO-A and MAO-B were inhibited by DPI without evident selectivity with K_i values of 1.7 and 0.3 μM, respectively. To this aim, we used 1-methyl-4-(1-methyl-1H-pyrrol-2-yl)-1,2,3,6-tetrahydropyridine (MMTP) whose oxidation can be monitored spectrophotometrically (ε_{420}= 24000 $M^{-1}cm^{-1}$) (Yu and

Castagnoli 1999). The reaction pathway of the MMTP oxidation proceeds via MAO catalysed α-carbon oxidation of the MMTP amino group, followed by autoxidation of the intermediate **1** and subsequent solvent deprotonation yielding the MMTP oxidized (Fig. 12) that is detected spectrophotometrically.

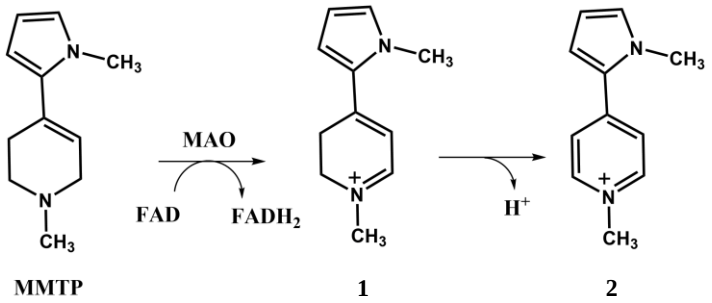

Figure 12. MMTP substrate oxidative reaction catalyzed by MAO.

MMTP is an analogue of the 1-methyl-4-phenyl-1,2,3,6-tetrahydropyridine (MPTP), a compound that causes permanent symptoms of Parkinson's disease in humans and animal models destroying dopaminergic neurons in the substantia nigra of the brain (Chiba, Trevor et al. 1984, Heikkila, Hess et al. 1984, Langston, Irwin et al. 1984). In this studio, we used MMTP as unspecific substrate for both MAOs monitoring the enzyme reaction in the presence of the DPI inhibitor. The advantage of this direct assay is to avoid non-specific interference of the inhibitor with other enzymes compared to the more widely used HRP coupled assay, where the hydrogen peroxide produced by MAOs is exploited (Reis, Massari et al. 2020). To complete our analysis, we also performed X-ray crystallographic studies of DPI in complex with MAO-B (1.8 Å). High-resolution crystal structure showed that DPI is bound into the MAO-B active site in front of FAD with no evidence of a covalent adduct with the flavin ring (Fig. 13). As a classic reversible and competitive MAO-B inhibitor, DPI is oriented perpendicularly to FAD within the "aromatic cage" Tyr398 and Tyr435, without perturbing the well-known position of the residues involved in substrate recognition. DPI is mainly stabilized by hydrophobic interactions (Van der Vaals bonds and π-π stacking) with the residues shaping the active site. Strikingly, the electron density highlights that one of the two carbon-iodine bond is missing, potentially caused by radiation damage accumulated during the X-ray data collection (Garman and Weik 2019).

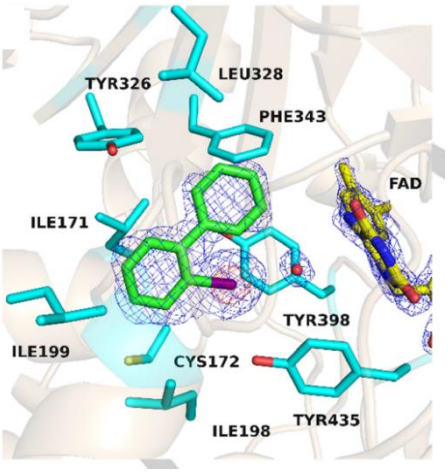

Figure 13. DPI binding to the active site of MAO B (protein residues shown in cyan). The weighted 2Fo-Fc electron density for FAD and DPI is shown in blue mesh representation. The iodine atom of DPI can be unambiguously located by its strong electron density peak visible also at the contour level of 20 σ (red). The iodine of DPI is localized between Tyr398 and Tyr435 (adapted from Iacovino, Reis et al. 2020).

This study showed that DPI inhibition mechanism clearly diverges between NOXs (and other flavoenzymes) and MAOs. In the first case, DPI inhibition proceeds through an uncompetitive mechanism in which the reduced state of FAD is necessary, whereas in MAOs DPI competes with substrate in the active site without any direct covalent binding to the FAD. These findings suggests that whenever DPI is used as a modulator of ROS signalling with NOXs or other flavo/heme systems susceptible to its activity, it should also be taken in consideration that it represents a good MAO inhibitor.

ChemMedChem | Communications
doi.org/10.1002/cmdc.202000264

Special Collection

Diphenylene Iodonium Is a Noncovalent MAO Inhibitor: A Biochemical and Structural Analysis

Luca G. Iacovino+,[a] Joana Reis+,[a] Antonello Mai,[b] Claudia Binda,[a] and Andrea Mattevi*[a]

Diphenylene iodonium (DPI) is known for its inhibitory activities against many flavin- and heme-dependent enzymes, and is often used as an NADPH oxidase inhibitor. We probed the efficacy of DPI on two well-known drug targets, the human monoamine oxidases MAO A and B. UV-visible spectrophotometry and steady-state kinetics experiments demonstrate that DPI acts as a competitive and reversible MAO inhibitor with K_i values of 1.7 and 0.3 μM for MAO A and MAO B, respectively. Elucidation of the crystal structure of human MAO B bound to the inhibitor revealed that DPI binds deeply in the active-site cavity to establish multiple hydrophobic interactions with the surrounding side chains and the flavin. These data prove that DPI is a genuine MAO inhibitor and that the inhibition mechanism does not involve a reaction with the reduced flavin. This binding and inhibitory activity against the MAOs, two major reactive oxygen species (ROS)-producing enzymes, will have to be carefully considered when interpreting experiments that rely on DPI for target validation and chemical biology studies on ROS functions.

Diphenylene iodonium (DPI, Scheme 1) is a widely used antioxidant capable of inhibiting several flavoenzymes and heme-containing proteins.[1] Similar to other iodonium compounds, DPI is a reactive molecule often employed in chemical synthesis.[2] It can undergo radical reactions and its antioxidative activity is thought to partly arise from its reactive oxygen species (ROS)-scavenging properties. In the fields of biochemistry and pharmacology, DPI is mostly known as a pan-flavoenzyme inhibitor that reacts with the reduced flavin to generate a covalent adduct.[1d,g] DPI is indeed one of the most widely employed flavoenzyme inhibitors, used in cell studies and cell-free assays as negative control to assess enzymatic activities.[3] In addition, there is extensive literature showing

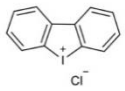

Scheme 1. Chemical structure of DPI.

that DPI binds and reacts with the reduced heme of several heme-containing enzymes.[1b] In particular, DPI is very often used as a NADPH oxidase inhibitor (NOXs; see, e.g., refs. [3a,4]) and has also been described as an inhibitor of cytochrome P-450 reductase,[1d] xanthine oxidase,[5] nitric-oxide synthase[6] and NADH-ubiquinone oxidoreductase.[7] Overall, DPI is remarkably effective against many redox and ROS-generating enzymes but it suffers from an inherent lack of selectivity causing pleiotropic effects. It is therefore not surprising that DPI can be cytotoxic.[8]

A comprehensive understanding of the pharmacological and biochemical activities of DPI remains a very relevant issue in ROS biology in light of the wide usage of this compound as a probe for ROS-dependent processes. With regard to flavoenzyme inhibition by DPI, monoamine oxidases (MAOs) stand out as they are among the most extensively studied oxidative flavoenzymes in humans.[9] This notion is especially pertinent considering the functional proximity of MAOs and NOXs in several ROS systems and redox-signaling axes.[10] The two MAO isoforms, A and B, are present in most mammals and are central players in the neurotransmitter metabolism of both the central nervous system and peripheral tissues.[11,12] MAO inhibitors have well-established therapeutic efficacies in several known neurodegenerative diseases due to their diverse functions in neuron survival.[13]

Here, we unequivocally demonstrate that DPI is a competitive and noncovalent inhibitor of MAOs, revealing its specific binding to the enzyme active site in contact with the flavin without formation of any covalent adduct with the prosthetic group. This finding has far-reaching implications for all studies that employ DPI to probe ROS biochemistry and pharmacology.

First, we measured the UV-visible spectra of human recombinant MAOs upon incubation with DPI to detect any perturbation of the absorbance profile which may result from either covalent or noncovalent interaction of the inhibitor with flavin adenine dinucleotide (FAD). We observed that upon addition of DPI to MAO A, the characteristic peak at 456 nm of the oxidized protein-bound prosthetic group was blue-shifted to a shorter wavelength of 444 nm. Moreover, the spectrum of the DPI-incubated enzyme exhibited a pronounced shoulder around 470 nm (green curve, Figure 1A). Changes in the optical

[a] L. G. Iacovino,+ Dr. J. Reis,+ Prof. C. Binda, Prof. A. Mattevi
Department of Biology and Biotechnology "Lazzaro Spallanzani"
University of Pavia, Via Ferrata 9
27100, Pavia (Italy)
E-mail: andrea.mattevi@unipv.it
[b] Prof. A. Mai
Department of Drug Chemistry and Technologies
Sapienza University of Rome
P.le A. Moro 5, 00185 Rome (Italy)

[+] These authors contributed equally to this work.

Supporting information for this article is available on the WWW under https://doi.org/10.1002/cmdc.202000264

This article belongs to the Special Collection "NMMC 2019: DCF-SCI 40th Anniversary"

ChemMedChem | Communications
doi.org/10.1002/cmdc.202000264
Chemistry Europe
European Chemical Societies Publishing

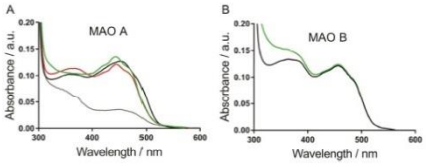

Figure 1. UV-visible spectra of the DPI-bound human MAO A and MAO B. In both panels, the black curve shows the spectrum of the resting oxidized enzyme (10 μM), and the green line indicates the spectrum after addition of 1 mM DPI (100-fold molar excess). A) The characteristic 456 nm peak of oxidized MAO A is blue-shifted to 444 nm by the binding of DPI. Addition of dithionite (1 mM) causes reduction of the enzyme as evidenced by the bleaching of the spectrum (gray). Upon dithionite consumption, the enzyme slowly (overnight) re-oxidizes with the concomitant re-appearance of the spectrum of the DPI-incubated oxidized enzyme (red). B) The spectral properties of human MAO B are not significantly affected by DPI binding.

properties of the flavin can be caused by ligand binding in close proximity to the flavin, for instance leading to charge-transfer complexes or other electronic effects.[14] Therefore, this initial experiment immediately suggested that DPI does indeed bind to the active site of MAO A. As DPI was reported to form covalent adducts with the reduced form of flavoenzymes, we performed a second spectroscopic experiment whereby dithionite was used to fully reduce the protein in the presence of DPI (gray curve, Figure 1A). We observed that upon overnight consumption of dithionite, which reacts with air, the enzyme became slowly re-oxidized. Critical insight was gained from the observation that the spectrum of the re-oxidized MAO A was indistinguishable from the spectrum of the original DPI-incubated oxidized protein (compare the green and red curves in Figure 1A). These findings ruled out the formation of a stable covalent adduct between the inhibitor and the reduced flavin. DPI rather exhibited the properties of a noncovalent active-site ligand. The same experiment was performed with MAO B, which, however, did not exhibit any detectable spectral perturbation upon DPI addition. This could reflect either a different interaction between the flavin and the inhibitor or a weaker binding of DPI to MAO B compared to MAO A (Figure 1B).

To clarify the magnitude and mechanism of MAO inhibition by DPI, we next performed steady-state kinetics on both human MAOs. To this end, we used 1-methyl-4-(1-methyl-1*H*-pyrrol-2-yl)-1,2,3,6-tetrahydropyridine (MMTP) whose oxidation can be conveniently monitored spectrophotometrically (ε_{420} = 25000 $M^{-1}cm^{-1}$).[15] This assay was especially advantageous for DPI evaluation because it avoids issues that can arise from the interference of the inhibitor with other enzymes (e.g., the horseradish peroxidase often used in enzyme-coupled assays) and/or the hydrogen peroxide generated by the reaction.[1a] The Michaelis-Menten kinetic parameters determined with the MMTP assay were in agreement with those obtained with other known methods for MAO activity assessment and consistent with previous literature (Table 1).[13,16]

Table 1. Steady-state kinetics of MAO A and MAO B inhibition by DPI.[a]

	K_i [μM]	k_{cat} [min^{-1}]	K_M [mM]	k_{cat}/K_M [$min^{-1}mM^{-1}$]
MAO A	1.72 ± 0.16	33.04 ± 0.43	0.064 ± 0.01	516.25
MAO B	0.31 ± 0.05	57.17 ± 1.48	0.094 ± 0.01	608.19

[a] The inhibition data are shown in Figure 2. MMTP was used as substrate in the assays. Biochemical data are reported as the mean (±SD) for 2 or more replicates.

Figure 2 shows the measurements of the initial rates of MMTP oxidation by MAO A and MAO B in the presence of varying DPI concentrations. The non-linear regression analysis gave the best fitting to the equation corresponding to competitive inhibition with K_i values of 1.7 and 0.3 μM for MAO A and MAO B, respectively. These observations highlighted a clear difference from the uncompetitive inhibition profile of DPI featured by NOXs and other flavoenzymes, in which the reduced state of FAD is necessary for binding.[1a,b,d,g] In fact, this result was clearly suggestive of a classical competitive mechanism of inhibition where DPI out-competes the substrate by binding to the oxidised protein.

To complete the analysis of the MAO inhibition by DPI, we carried out further investigations using X-ray crystallography, taking advantage of the well-diffracting crystals of human MAO B. The three-dimensional structure of the enzyme in complex with DPI was solved at a 1.8 Å resolution as detailed in Table 1S in the Supporting Information. Thanks to the good quality of the electron density, the binding of the inhibitor could be revealed and analyzed in detail. In particular, the electron-rich iodine atom featured a very strong density, making its positioning in the active site perfectly clear (Figure 3A). DPI was found to bind close to the flavin moiety with no evidence for the presence of a covalent adduct with the prosthetic group. We also observed that the electron density is not consistent with a tricycle ring structure because one of the two carbon-iodine bonds of the iodonium was evidently missing. Such a bond disruption is likely to be caused by the radiation damage accumulated during X-ray data as often observed for redox-reactive compounds (Figure 3A). [17]

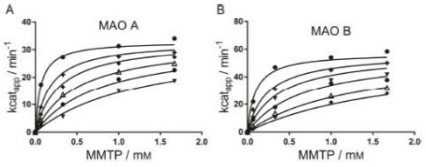

Figure 2. Steady-state kinetics of human MAO A and MAO B and inhibition by DPI. MAO A and MAO B activities were measured by monitoring the consumption of the MMTP substrate (ε_{420} = 25000 $M^{-1}cm^{-1}$) at different inhibitor concentrations (0, 3, 6, 12, 20 and 33 μM for MAO A and 0, 0.5, 1, 2, 4 and 6 μM for MAO B).

ChemMedChem | Communications doi.org/10.1002/cmdc.202000264 | Chemistry Europe European Chemical Societies Publishing

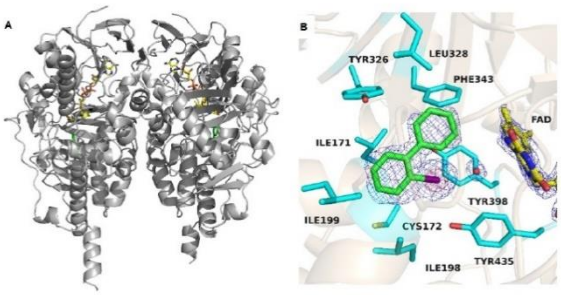

Figure 3. Crystal structure of human MAO B in complex with DPI. A) Ribbon diagram (gray) of the overall dimer of human MAO B bound to DPI (stick representation with carbon and iodine atoms in green and purple, respectively). FAD is also shown with carbon, nitrogen, oxygen and phosphorous atoms in yellow, blue, red and dark purple, respectively. B) DPI binding to the active site of MAO B (protein residues shown in cyan). The weighted unbiased $2F_o-F_c$ electron densities for FAD and DPI are shown in blue chicken-wire representation (contoured at 1.5 σ). The iodine atom of DPI can be unambiguously located by its strong electron density peak visible also at the contour level of 20 σ (red). The iodine of DPI is localized between Tyr398 (4.3 Å) and Tyr435 (3.5 Å). A putative halogen bond interaction between the iodine and a water molecule (red) is also observed.

Binding of DPI involves extensive Van der Waals interactions with the protein residues lining the active site cavity of MAO B (Figure 3B). Specifically, DPI establishes T-shaped π–π interactions that involve the two phenyl groups of the inhibitor with Phe343 and Tyr326, respectively. Moreover, the iodine atom is in van der Waals contact with the so-called aromatic cage, formed by the pair of residues (Tyr398–Tyr435) that bind the amino group of the MAO substrates. Iodine is generally considered to have the highest polarizability between monatomic ions, with this property being further associated to favorable interactions with aromatic groups.[18] The interactions between the aromatic cage side chains and the inhibitor are in agreement with this notion. It is of further notice that a conserved water molecule lays in proximity of the iodine atom. The observed distance between the halogen and the water molecule is 2.8 Å; the C–I···O angle is 152°. This geometry is compatible with the presence of a halogen bond between the inhibitor and the water (Figure 3B).[19]

The inhibitor extends towards to and is in contact with Ile199, known as the gating residue of the MAO B active site. We found that this side chain is in the so-called closed conformation, that seals the active site. This geometry follows the location of DPI in the innermost segment of the active-site cavity, close to the flavin ring (Figure 3B). This feature can be appreciated by the comparison with the structures of MAO B in complex with isatin (PDB ID: 1OJA) and methylene blue (PDB ID: 3ZYX; Figure 4). The latter inhibitor is particularly interesting because its tricyclic structure resembles that of DPI. In this regard, it is important to remark that the MAO B structure in complex with methylene blue was obtained with the I199A/Y326A double mutant that displayed enzymatic properties similar to human MAO A, being this isoform the preferred target of methylene blue.[20] Similar to isatin and methylene blue, DPI binds with its aromatic rings perpendicular to and in contact

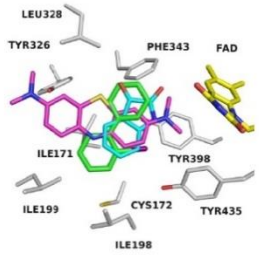

Figure 4. Comparison of MAO B–inhibitor complexes. The structure of DPI-bound MAO B (inhibitor carbons in green) is superimposed to the structures of MAO B in complex with isatin (cyan carbons, PDB ID: 1OJA) and methylene blue (magenta carbons, PDB ID: 3ZYX). For the sake of clarity, the flavin (yellow carbons) and side chains are shown only for the MAO B-DPI structure (carbon atoms in gray, sulfur atoms in light yellow).

with the flavin. Moreover, DPI binding does not perturb the protein residues lining the active site cavity, whose conformations are essentially identical in all three inhibitor-bound structures (atomic shifts <0.2 Å). Yet, despite these common features, the binding of the three multiring aromatic inhibitors is different (Figure 4). DPI is oriented with longest axis extending from Ile199 to Phe343, which is different from the orientation of methylene blue. Moreover, the less bulky (and lower affinity) isatin does not occupy the cavity space as efficiently as DPI. Thus, every inhibitor features a specific binding mode within the active site.

In summary, we were able to demonstrate that DPI competitively inhibits both MAO A and MAO B with K_i values in the low-/sub-micromolar range. The inhibition does not follow the mechanism postulated for the pan-flavoenzyme inhibitory

ChemMedChem | Communications doi.org/10.1002/cmdc.202000264 | Chemistry Europe European Chemical Societies Publishing

activity of DPI because it does not require the flavin to be reduced and does not result from a non-selective reactivity of the inhibitor with the reduced flavin. DPI rather features the properties of a classical and genuine MAO inhibitor. Its binding geometry involves multiple noncovalent interactions with the protein side chains and the flavin as well as a halogen bond with an ordered water molecule. These findings should be carefully considered whenever DPI is used as a modulator of ROS signaling and oxidative stress or as a NOX inhibitor. DPI should probably be viewed, above all, as a good MAO inhibitor.

Experimental Section

Experimental details for biochemical assays and X-ray crystallography can be found in the Supporting Information.

Acknowledgements

Research was supported by the Associazione Italiana per la Ricerca sul Cancro (AIRC; IG19808 and IG19162), PRIN 2015 (prot 20152TE5PK) and the "Dipartimenti di Eccellenza (2018–2022)". The project leading to these results has received funding from AIRC and from the European Union's Horizon 2020 research and innovation programme under the Marie Skłodowska-Curie grant agreement no 800924.

Conflict of Interest

The authors declare no conflict of interest.

Keywords: diphenylene iodonium · flavoenzyme · iodonium compounds · monoamine oxidases · reactive oxygen species

[1] a) J. Reis, M. Massari, S. Marchese, M. Ceccon, F. S. Aalbers, F. Corana, S. Valente, A. Mai, F. Magnani, A. Mattevi, *Redox Biol.* **2020**, *32*, 101466; b) J. Doussiere, J. Gaillard, P. V. Vignais, *Biochemistry* **1999**, *38*, 3694–3703; c) M. Goez, G. Eckert, U. Müller, *J. Phys. Chem. A.* **1999**, *103*, 5714–5721; d) S. Chakraborty, V. Massey, *J. Biol. Chem.* **2002**, *277*, 41507–41516; e) B. V. O'Donnell, D. G. Tew, O. T. Jones, P. J. England, *Biochem. J.* **1993**, *290*, 41–49; f) J. Covès, C. Lebrun, G. Gervasi, P. Dalbon, M. Fontecave, *Biochem. J.* **1999**, *342*, 465–472; g) J. Lu, P. Risbood, C. T. Kane, M. T. Hossain, L. Anderson, K. Hill, A. Monks, Y. Wu, S. Antony, A. Juhasz, H. Liu, G. Jiang, E. Harris, K. Roy, J. L. Meitzler, M. Konaté, J. H. Doroshow, *Biochem. Pharmacol.* **2017**, *143*, 25–38; h) F. Augsburger, A. Filippova, D. Rasti, T. Seredenina, M. Lam, G. Maghzal, Z. Mahiout, P. Jansen-Dürr, U. G. Knaus, J. Doroshow, R. Stocker, K.-H. Krause, V. Jaquet, *Redox Biol.* **2019**, *26*, 101272; i) M. M. Konaté, S. Antony, J. H. Doroshow, *Antioxid. Redox Signaling* **2020**; j) N. Suzuki, R. Mittler, *Free Radical Biol. Med.* **2012**, *53*, 2269–2276.

[2] J. Wen, R.-Y. Zhang, S.-Y. Chen, J. Zhang, X.-Q. Yu, *J. Org. Chem.* **2012**, *77*, 766–771.

[3] a) B. B. Paudel, J. E. Lewis, K. N. Hardeman, C. E. Hayford, C. J. Robbins, S. G. Codreanu, S. D. Sherrod, J. A. McLean, M. L. Kemp, V. Quaranta, *bioRxiv* preprint, **2019**, DOI: https://doi.org/10.1101/818989; b) S. J. Mandriota, C. Pyke, C. Di Sanza, P. Quinodoz, B. Pittet, M. S. Pepper, *Am. J. Pathol.* **2000**, *156*, 2077–2089; c) P. C. Holland, H. S. A. Sherratt, *Biochem. J.* **1972**, *129*, 39–54.

[4] a) H.-Q. Ju, H. Ying, T. Tian, J. Ling, J. Fu, Y. Lu, M. Wu, L. Yang, A. Achreja, G. Chen, Z. Zhuang, H. Wang, D. Nagrath, J. Yao, M.-C. Hung, R. A. DePinho, P. Huang, R.-H. Xu, P. J. Chiao, *Nat. Commun.* **2017**, *8*, 14437; b) M. Ogrunc, R. Di Micco, M. Liontos, L. Bombardelli, M. Mione, M. Fumagalli, V. G. Gorgoulis, F. d'Adda di Fagagna, *Cell Death Differ.* **2014**, *21*, 998–1012; c) P. S. Hole, J. Zabkiewicz, C. Munje, Z. Newton, L. Pearn, P. White, N. Marquez, R. K. Hills, A. K. Burnett, A. Tonks, R. L. Darley, *Blood* **2013**, *122*, 3322–3330.

[5] S. A. Sanders, R. Eisenthal, R. Harrison, *Eur. J. Biochem.* **1997**, *245*, 541–548.

[6] D. J. Stuehr, O. A. Fasehun, N. S. Kwon, S. S. Gross, J. A. Gonzalez, R. Levi, C. F. Nathan, *FASEB J.* **1991**, *5*, 98–103.

[7] A. Majander, M. Finel, M. Wikström, *J. Biol. Chem.* **1994**, *269*, 21037–21042.

[8] C. Riganti, E. Gazzano, M. Polimeni, C. Costamagna, A. Bosia, D. Ghigo, *J. Biol. Chem.* **2004**, *279*, 47726–47731.

[9] a) L. G. Iacovino, F. Magnani, C. Binda, *J. Neural Transm.* **2018**, *125*, 1567–1579; b) C. Binda, F. Hubálek, M. Li, D. E. Edmondson, A. Mattevi, *FEBS Lett.* **2004**, *564*, 225–228.

[10] a) A. Daiber, F. Di Lisa, M. Oelze, S. Kröller-Schön, S. Steven, E. Schulz, T. Münzel, *Br. J. Pharmacol.* **2017**, *174*, 1670–1689; b) M. Hancock, A. D. Hafstad, A. A. Nabeebaccus, N. Catibog, A. Logan, I. Smyrnias, S. S. Hansen, J. Lanner, K. Schröder, M. P. Murphy, A. M. Shah, M. Zhang, *eLife* **2018**, *7*, e41044; c) A. M. Brennan, S. Won Suh, S. Joon Won, P. Narasimhan, T. M. Kauppinen, H. Lee, Y. Edling, P. H. Chan, R. A. Swanson, *Nat. Neurosci.* **2009**, *12*, 857–863.

[11] C. Binda, A. Mattevi, D. E. Edmondson, *J. Biol. Chem.* **2002**, *277*, 23973–23976.

[12] a) D. E. Edmondson, C. Binda, J. Wang, A. K. Upadhyay, A. Mattevi, *Biochemistry* **2009**, *48*, 4220–4230; b) R. R. Rona, *Curr. Top. Med. Chem.* **2012**, *12*, 2189–2209.

[13] a) J. Reis, N. Manzella, F. Cagide, J. Mialet-Perez, E. Uriarte, A. Parini, F. Borges, C. Binda, *J. Med. Chem.* **2018**, *61*, 4203–4212; b) D. Knez, N. Colettis, L. G. Iacovino, M. Sova, A. Pišlar, J. Konc, S. Lešnik, J. Higgs, F. Kamecki, I. Mangialavori, A. Dolšak, S. Žakelj, J. Trontelj, J. Kos, C. Binda, M. Marder, S. Gobec, *J. Med. Chem.* **2020**, *63*, 1361–1387.

[14] W. J. H. van Berkel, in *Wiley Encyclopedia of Chemical Biology*, John Wiley & Sons, Inc. **2008**, pp. 1–11.

[15] J. Yu, N. Castagnoli, *Bioorg. Med. Chem.* **1999**, *7*, 231–239.

[16] P. Flaherty, K. Castagnoli, Y.-X. Wang, N. Castagnoli, *J. Med. Chem.* **1996**, *39*, 4756–4761.

[17] E. F. Garman, M. Weik, *J. Synchrotron Radiat.* **2019**, *26*, 907–911.

[18] A. Vergara-Jaque, P. Fong, J. Comer, *J. Chem. Inf. Model.* **2017**, *57*, 3043–3055.

[19] G. Cavallo, P. Metrangolo, R. Milani, T. Pilati, A. Priimagi, G. Resnati, G. Terraneo, *Chem. Rev.* **2016**, *116*, 2478–2601.

[20] E. M. Milczek, C. Binda, S. Rovida, A. Mattevi, D. E. Edmondson, *FEBS J.* **2011**, *278*, 4860–4869.

Manuscript received: April 23, 2020
Accepted manuscript online: May 27, 2020
Version of record online: June 10, 2020

ChemMedChem

Supporting Information

Diphenylene Iodonium Is a Noncovalent MAO Inhibitor: A Biochemical and Structural Analysis

Luca G. Iacovino[+], Joana Reis[+], Antonello Mai, Claudia Binda, and Andrea Mattevi*This article belongs to the Special Collection "NMMC 2019: DCF-SCI 40th Anniversary"

Author Contributions

L.I. Methodology:Lead; Writing - Original Draft:Equal; Writing - Review & Editing:Equal
J.R. Methodology:Lead; Writing - Original Draft:Equal; Writing - Review & Editing:Equal
A.M. Resources:Equal
C.B. Methodology:Equal; Supervision:Supporting; Writing - Original Draft:Supporting

Supporting Information

Table 1S. Data collection and refinement statistics for the crystal structures of human MAO B in complex with DPI.

Space group	C222
Unit cell axes (Å)	*a* = 128.5
	b = 222.5
	c = 85.6
Resolution (Å)	1.8
PDB code	6YT2
R_{sym} [a,b] (%)	14.8 (106.5)
$CC_{1/2}$ (%)	98.5 (55.3)
Completeness[b] (%)	98.7 (99.7)
Unique reflections	111,714
Redundancy	3.8 (3.7)
I/σ[b]	4.2 (1.7)
N° of non-hydrogen atoms	
protein/FAD	7948/2x53
inhibitor	2x13
detergent[c]/glycerol	26/2x6
water	649
Average B value for protein/inhibitor atoms (Å^2)	16.6/27.1
R_{cryst} [b,d] (%)	18.6 (31.6)
R_{free} [b,d] (%)	22.3 (35.9)
Rms bond length (Å)	0.012
Rms bond angles (°)	1.72

[a] $R_{sym}=\sum|I_i-\langle I\rangle|/\sum I_i$, where I_i is the intensity of i^{th} observation and $\langle I\rangle$ is the mean intensity of the reflection.

[b] Values in parentheses are for reflections in the highest resolution shell.

[c] As in previous human MAO-B structures, one molecule of the Zwittergent 3-12 detergent (used in crystallization experiments) is partly visible in the electron density of each of the two protein monomers present in the asymmetric unit [d] $R_{cryst}=\sum|F_{obs}-F_{calc}|/\sum|F_{obs}|$ where F_{obs} and F_{calc} are the observed and calculated structure factor amplitudes, respectively. R_{cryst} and R_{free} were calculated using the working and test sets, respectively.

Experimental Section

General Information **-** 1-methyl-4-(1-methyl-1H-pyrrol-2-yl)-1,2,3,6-tetrahydropyridine (MMTP) was synthetized as previously described by Jian Yu and Castagnoli[1]. All other reagents were purchased from Sigma-Aldrich except for detergents that were purchased from Anatrace (USA).

UV-visible spectra **-** The spectral properties of recombinant human MAO A and MAO B were measured at 25 °C with a diode-array UV Vis Spectrophotometer (Agilent 8453 HP G1103A). The enzymes (10 µM in 50 mM Hepes pH 7.5 and 0.25 % reduced Triton X-100) were incubated with different ligands.

Steady-state kinetics **-** All steady-state kinetic experiments were performed at 25 °C in 50 mM Hepes pH 7.5 containing 0.25 % reduced Triton X-100 using a Cary 100 UV/Vis spectrophotometer (Agilent). The rate of MMTP oxidation (ε_{420} = 25000 M^{-1} cm^{-1}) was monitored at different DPI concentrations (0 – 33 µM for MAO A and 0 – 6 µM for MAO B). The reaction was started by adding the enzyme at a final concentration of 0.07 µM. Visual inspection of the fitting curves and evaluation of the r^2 value were used to select the best fitting for determination of the inhibition constant using GraphPad (GraphPad Software Inc).

Protein Purification **-** Human recombinant MAO-A and MAO-B were expressed in *Pichia pastoris* and purified as previously described.[2,3] Purified protein samples were stored in 50 mM potassium phosphate buffer, pH 7.5, 0.8% (w/v) β-octylglucoside, 20% glycerol. Enzyme concentration was determined by measuring the absorbance UV/vis spectrum using a NanoDrop ND-1000 spectrophotometer (Thermo Scientific).

X-ray Crystallography **-** Human MAO-B in 50 mM potassium phosphate, pH 7.5, 8.5 mM Zwittergent 3-12 was cocrystallized with DPI by the sitting-drop vapor diffusion method following published protocols.[4] X-ray diffraction data were collected at the beamlines of the Diamond Light Source in Chilton (United Kingdom). For data collection, crystals were transferred into a mother liquor solution containing 18% (v/v) glycerol and flash-cooled in a stream of gaseous nitrogen at 100 K. Data processing and scaling (Table 1S) were performed using XDS[5] and the CCP4 package.[6] The coordinates of the MAO B - 4-oxo-4H-chromene-3-carboxamide derivative,[7] deprived of all water and inhibitor atoms, were used as initial model. The program Coot[8] was used for electron density inspection and model building, whereas crystallographic refinement was performed with the program REFMAC5.[9] Figures were generated by the program CCP4mg.[10]

References

1. J. Yu, N. Jr. Castagnoli, *Bioorg. Med. Chem.* **1999**, *7*, 231-239.

2. M. Li, F. Hubálek, P. Newton-Vinson, D. E. Edmondson, *Protein Expression Purif.* **2002**, *24*, 152−162.

3. P. Newton-Vinson, F. Hubalek, D. E. Edmondson, *Protein Expression Purif.* **2000**, *20*, 334−345.

4. C. Binda, F. Hubálek, M. Li, Y. Herzig, J. Sterling, D. E. Edmondson, A. Mattevi, *J. Med. Chem.* **2004**, *47*, 1767−1774.

5. W. Kabsch, *Acta Crystallogr. Sect. D: Biol. Crystallogr.* **2010**, *66*, 125−132.

6. The CCP4 Suite: Programs for Protein Crystallography. *Acta Crystallogr., Sect. D: Biol. Crystallogr.* **1994**, *D50*, 760−767.

7. J. Reis, N. Manzella, F. Cagide, J. Mialet-Perez, E. Uriarte, A. Parini, F. Borges, C. Binda, *J. Med. Chem.* **2018**, *61*, 4203−4212.

8. P. Emsley, B. Lohkamp, W. G. Scott, K. Cowtan, *Acta Crystallogr., Sect. D: Biol. Crystallogr.* **2010**, *66*, 486−501.

9. G. N. Murshudov, P. Skubak, A. A. Lebedev, N. S. Pannu, R. A. Steiner, R. A. Nicholls, M. D. Winn, F. Long, A. A. Vagin, *Acta Crystallogr., Sect. D: Biol. Crystallogr.* **2011**, *67*, 355−367.

10. S. McNicholas, E. Potterton, K. S. Wilson, M. E. M. Noble, *Acta Crystallogr., Sect. D: Biol. Crystallogr.* **2011**, *67*, 386−394

2. UDP-Glucuronic acid 4-epimerase

2.1 INTRODUCTION

Uridine 5'-diphosphate α-D-glucuronic acid (UDP-GlcA) represents a common substrate for C4-epimerases and decarboxylases releasing UDP-galacturonic acid (UDP-GalA) and UDP-pentose products, respectively. In particular, it acts as precursor of three important monosaccharides (D-galacturonic acid, D-xylose, D-apiose) required in cell wall polysaccharides biosynthesis (Reiter 2008, Reboul, Geserick et al. 2011). Besides their importance in cell biology, the sugar nucleotide syntheses from UDP-GlcA are of considerable interest also in biocatalysis (Meng, Du et al. 2019).

UDP-Glucuronic acid 4-epimerase (UGAepi), UDP-xylose synthase (UXS) and UDP apiose/xylose synthase (UAXS) are three enzymes yielding different products using UDP-GlcA as substrate (Fig. 14). They all belong to the Short Chain Dehydrogenase/Reductase (SDR) protein superfamily. Despite the low sequence identity between the SDR members (about 15-30%), the 3D structures show a conserved Rossmann-fold with highly similar α/β folding pattern and a central β-sheet. The general mechanism of reaction of SDR members superfamily involves a very conserved catalytic triad of Ser, Tyr, Lys residues and the nicotinamide ring (NAD^+) as cofactor. This triad forms the framework for a proton relay transfer including the 2'-OH of the NAD^+. UGAepi, UXS and UAXS's first catalytic step promotes the UDP-substrate oxidation catalysed by the proton abstraction of the Tyr at hydroxyl group at the position C4', and subsequent hydride transfer from UDP-GlcA to NAD^+. The UDP-4-keto-hexose-uronic acid generated is extremely instable and undergoes different pathways depending on the enzyme reaction. Among these, UGAepi is the only one able to prevent the substrate decarboxylation (Fig 14). Further, this enzyme catalyses the hydride re-addition at the C4' to achieve the UDP-Galacturonic acid switch in stereochemistry. While the mechanistic properties of UXS and UAXS have been studied in detail (Eixelsberger, Sykora et al. 2012, Eixelsberger, Horvat et al. 2017, Savino, Borg et al. 2019), the reaction catalyzed by UGAepi was still unexplored.

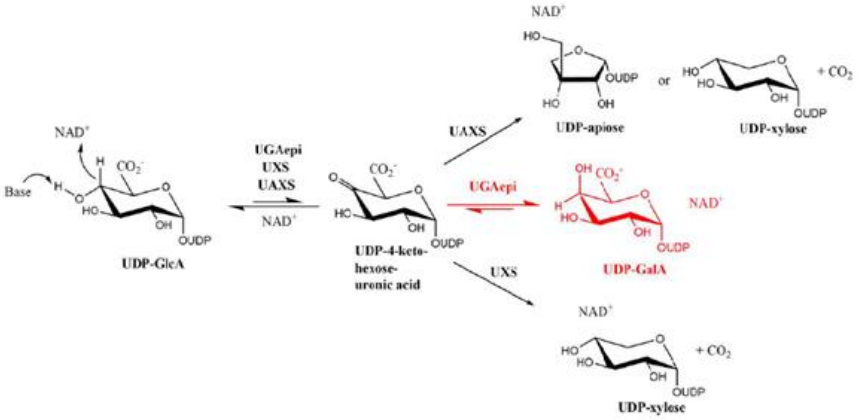

Figure 14. Reactions carried out by UDP-glucuronic acid epimerase (labelled UGAepi), UDP-xylose synthase (UXS) and UDP-apiose/xylose synthase (UAXS) using UDP-GlcA as substrate. The same 4-ketohexose-uronic acid intermediate yields different products that are specific for every enzyme (adapted from Iacovino et al. 2020).

The hypothesis that the UGAepi reaction occurs through the 4-keto-intermediate was supported by the inference to UDP-galactose 4-epimerase (GALE) reaction. GALE represents mechanistically the best characterized epimerase of SDR superfamily, the enzyme reaction promotes the interconversion of UDP-Glucose into UDP-Galactose. The epimerization mechanism occurs through a 180° degrees rotation of the 4-keto intermediate that shows the opposite face of the sugar for the second step of reduction by NADH (Thoden and Holden 1998). A similar rotation of the 4-keto intermediate was assumed also for UGAepi, but this has not been demonstrated so far.

Except for Ser/Tyr/Lys catalytic triad that are conserved residues of both UGAepi and UXS/UAXS decarboxylases, the other residues involved in substrate recognition are highly variable, despite sharing the same substrate. These enzymes have to face the challenge of combining substrate specificity with plasticity in properly positioning the 4-ketointermediate, thus implying a fine coordination of each chemical step of the enzymatic reaction to generate the different products. Another issue is to understand how UGAepi is able to preserve the very unstable 4-keto uronic acid intermediate from decarboxylation. Indeed, UGAepi substrate affinity analysis reveals that the C5' carboxylate group of UDP-GlcA is extremely important for substrate recognition. This observation represents an important point of divergency with GALE because it exhibits roughly the same binding

affinity with a variety of substrate analogues. Instead, UDP-sugar substrates without this carboxylate group are either inactive or give a strong decrease in the enzyme activity of UGAepi (Muñoz, López et al. 1999, Gu and Bar-Peled 2004, Broach, Gu et al. 2012).

Production of recombinant UDP-Glucuronic acid epimerases from plants and bacteria showed several difficulties (Feingold, Neufeld et al. 1958, Muñoz, López et al. 1999, Frirdich and Whitfield 2005), thus complicating their enzymatic characterization. Prof. Bernd Nidetzky at the University of Graz and his research group identified a new UDP-GlcA epimerase from *Bacillus cereus* HuA2-4 (BcUGAepi). Compared to other epimerases, this enzyme could successfully expressed in *E. coli* and represented the perfect candidate for a thorough biochemical characterization (Borg, Dennig et al. 2020). In our lab, we determined the crystal structure of BcUGAepi with different substrate analogs bound, which highlighted the enzymatic mechanism of the reaction. This work is described below and reported in detail in the article "Crystallographic snapshots of UDP-glucuronic acid 4-epimerase ligand binding, rotation and reduction" published in Journal of Biological Chemistry and attached at the end of this Chapter.

2.2 ELUCIDATION OF THE UDP-GLUCURONIC ACID 4-EPIMERASE MECHANISM OF REACTION

This work highlighted many aspects of UDP-glucuronic acid epimerases through a detailed crystallographic analysis of BcUGAepi elucidating the different steps of the reaction. The first crystal structure was solved in presence of NAD^+ (2.2 Å) (Fig. 15), tightly bound to the enzyme during the entire purification process, that acts as non-dissociable prosthetic group (Liu, Vanhooke et al. 1996, Kavanagh, Jörnvall et al. 2008, Eixelsberger, Sykora et al. 2012). As for other SDR family member, BcUGAepi is assembled as a homodimer stabilized by a hydrophobic patch of four adjacent α-helices (Gatzeva-Topalova, May et al. 2005, Savino, Borg et al. 2019). The N-terminal domain shows a typical Rossmann fold motif where NAD^+ is fully embedded within the protein, whereas the C-terminal domain provides the binding site for the UDP-GlcA substrate (Fig. 15). The active site is located at the interface between the NAD^+ and UDP-GlcA domains (Thoden, Frey et al. 1996, Thoden, Frey et al. 1996, Thoden, Frey et al. 1996).

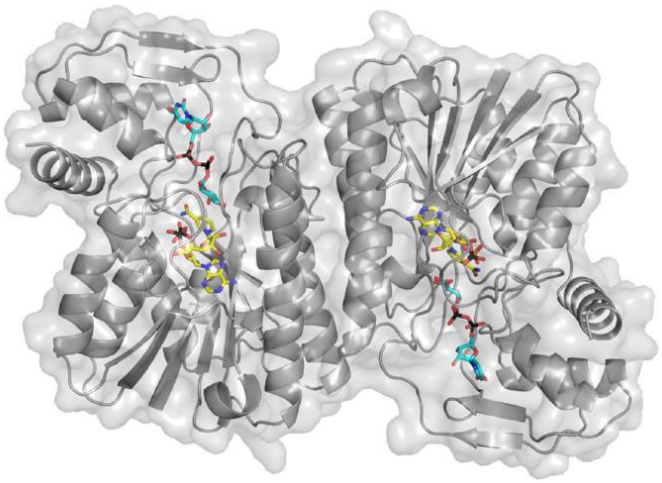

Figure 15. The overall structure of the dimeric UDP-glucuronic acid 4-epimerase from *Bacillus cereus*. The NAD^+ and UDP-GlcA carbons are in yellow and cyan, respectively. The backbone trace is shown as grey ribbon and semi-transparent protein surface (adapted from Iacovino et al. 2020).

In the free enzyme (i.e. no ligand bound), two loops (86-91 and 269-276) that belong to the C-terminal catalytic domain are totally disordered (Fig. 16 A). With its many hydrogen bonds, the UDP motif triggers the re-organization of these two loops and reveals the cavity where the sugar substrate will be hosted. This feature underlines that UDP is not only an accessory part of the substrate but it is fundamental in substrate recognition. Indeed, BcUGAepi is totally inactive with glucuronic acid as substrate. To inspect the binding mode of UDP-GlcA in the active site, BcUGAepi was co-crystallized in presence of an excess of the substrate (1.8 Å). The electron density clearly shows that the sugar motif laying on top of the nicotinamide ring., the fine geometry and the distance of 3.2 Å promotes the hydride transfer from NAD^+ to the C4' of UDP-GlcA (Fig. 16 A). Remarkably, the BcUGAepi active site is characterized by an extensive network of hydrophilic residues that have found the perfect counterpart with the 2'-OH, 3'-OH, 4'-OH hydroxyl groups and the 5' carboxyl group (Fig. 16 B-C). In particular, the 4'-OH is hydrogen bonded with Tyr149 that catalyses the proton abstraction and subsequent 4-keto-intermediate generation. Tyr149 mutation into phenylalanine (Y149F) causes a drastic drop of the epimerization activity (Liu, Thoden et al. 1997, Berger, Arabshahi et al. 2001) whereas it has a little impact on the sugar binding.

In this mutant, the tyrosine hydroxyl group is replaced by a water molecule. The negative charge of the 5' carboxyl group plays an active role in UDP-GlcA substrate recognition, indeed, other UDP-sugars like UDP-glucose, UDP-galactose, UDP-N-acetylglucosamine, and UDP-xylose are poorly active substrates or inactive against UDP-glucuronic acid 4-epimerases (Muñoz, López et al. 1999, Frirdich and Whitfield 2005, Borg, Dennig et al. 2020).

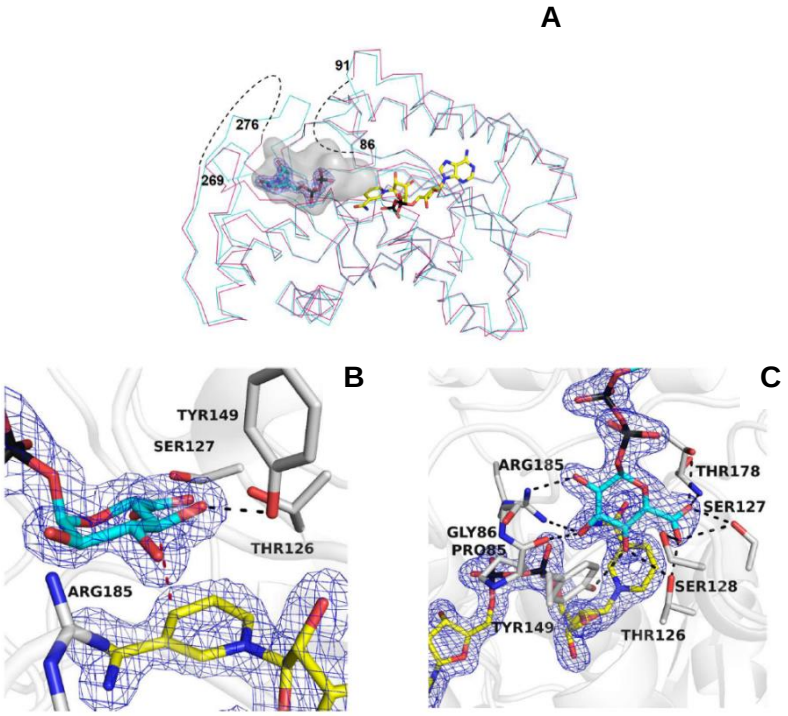

Figure 16. (A) Superposition between the Cα traces of the epimerase structures bound to NAD⁺ (purple) and NAD⁺/UDP (cyan). The loops 86-91 and 269-276 are disordered in the NAD⁺ complex (dashed lines). (B-C) Binding of the sugar moiety of the substrate (cyan carbons) in two orientations. The orientation of panel A outlines the binding of the substrate C4' at 3.2 Å distance from C4 of the nicotinamide (red dashed line) and the hydrogen bond between the sugar O4' and Tyr149 (black dashed line). All hydroxyl groups and the carboxylate of the glucuronic acid are engaged in hydrogen bonding interactions as shown in panel C (adapted from Iacovino et al. 2020).

After UDP-GlcA substrate oxidation (and subsequent NAD^+ reduction into NADH), the 4-ketointermediate is supposed to rotate within the active site, and the hydride transfer from NADH to the intermediate opposite face promotes the UDP-GalA production. To investigate further on the mechanism of the rotation induced by the 4-ketointermediate, BcUGAepi was co-crystallized in presence of an excess of UDP-GalA (1.5 Å). Remarkably, during the crystallization experiment, UDP-GalA was partially converted into UDP-GlcA, and the electron density shows a mixture of both substrate and product in chair conformation with ratio 1:1. This complex was defined "equilibrium" structure and interestingly shows the start and end points of the reaction (Fig. 17 A-B), highlighting two important aspects: substrate and product are bound with opposite orientations and the ligand rotation can take place almost without conformational changes since the "equilibrium" structure can be perfectly superimposed with the UDP-GlcA structure.

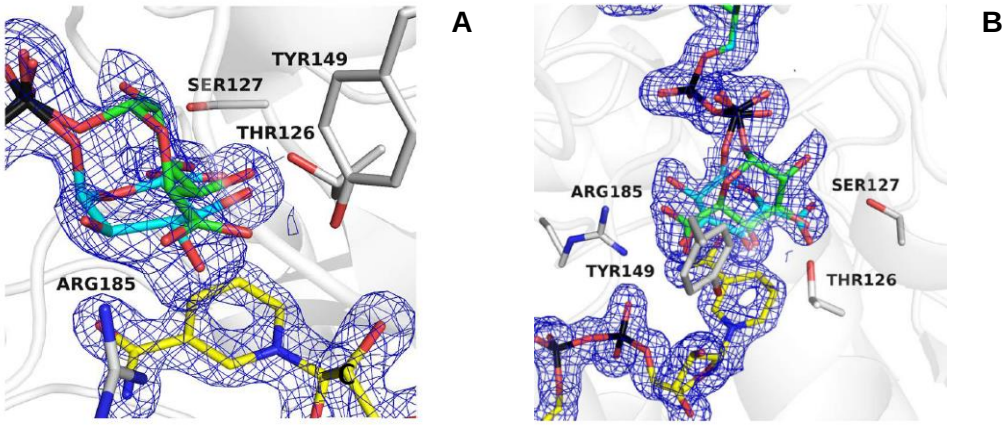

Figure 17 A-B. The equilibrium structure shows how the same active-site conformation accommodates substrate and product with their opposed chirality. Fitting of galacturonic (green carbons) and glucuronic (cyan carbons) moieties into the electron density shown with the same orientation as in Figure 16 B-C (adapted from Iacovino et al. 2020).

To better characterized the UDP-GalA binding mode, we performed several crystallization experiments trying to solve the crystal structure with the product alone. It turned out that a lower pH (6.5 instead of 8.0) and temperature (4°C instead of 20°C) represented very important parameters to modulate the enzyme reactivity and reduce the substrate/product

interconversion, isolating the UDP-GalA (1.85 Å) (Fig. 16 A-B). The UDP-GalA binding mode perfectly matches that observed in the equilibrium structure and the same active site configuration of the substrate complex is retained in the product complex. Strikingly, the C4' atom of UDP-GalA and UDP-GlcA holds exactly the same distance of 3.2 Å from NAD^+ and despite the rotation, the positions of the 3'-OH, 4'-OH, and 5'-carboxylate substituents of the glucuronic acid substrate overlap with those of the 5'-carboxylate, 4'-OH, and 3'-OH substituents of the galacturonic acid product. In other words, the extensive network of hydrogen bonds between these substituents and the surrounding residues are similar. This feature would explain why the enzyme can also catalyse the reverse reaction, namely the epimerization of UDP-galacturonic acid to UDP-glucuronic acid. These isolated structures clarified the mechanism behind the rotation of the 4-ketointermediate: a small torsional rotation of the β-phosphate (around 20-30° degrees) is coupled with 160° degrees rotation about the O1'-C1' bond that flips the sugar ring. This movement called "swing & flip" promotes the sugar rearrangement within the active site.

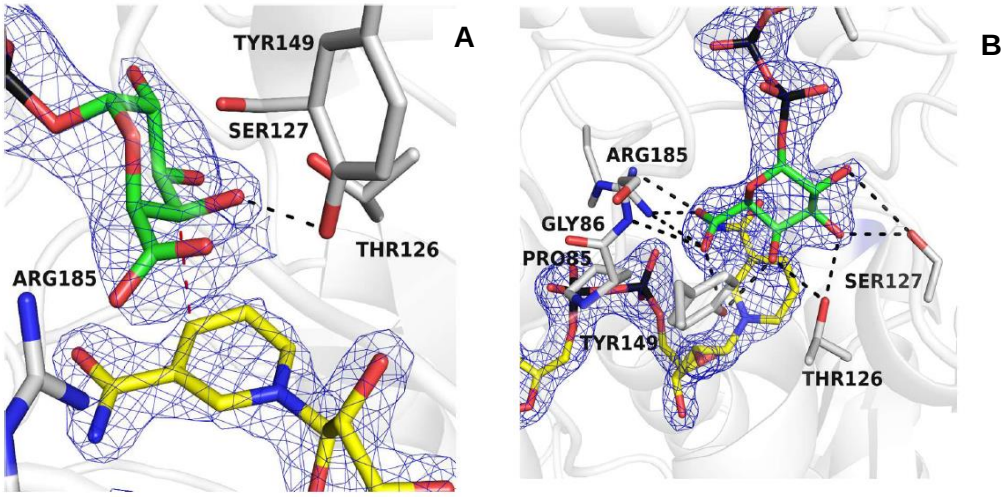

Figure 18 A-B. The crystal structure of BcUGAepi in complex with NAD^+ and UDP-galacturonic acid shown in two different orientations. Figure 18 A highlights the position of the C4' in proximity of the nicotinamide (red dashed line) and the hydrogen bond between the sugar O4' and Tyr149 (black dashed line). As shown in Figure 18 B, all hydroxyl groups and the carboxylate of the glucuronic acid are engaged in hydrogen bonding interactions with the protein. The orientations are the same as in Figure 16 B-C (adapted from Iacovino et al. 2020).

In summary, our work provided a detailed analysis of the BcUGAepi mechanism of reaction. All the crystallographic structures isolated of this enzyme gave a "crystallographic snapshot" of each reaction step. NAD^+ is anchored inside the N-terminal domain of the protein and represents a non-dissociable prosthetic group. In absence of the substrate, the active site is totally disordered and only the UDP binding promotes localized structural changes in the C-terminal domain where the substrate sugar ring will react with the NAD^+ cofactor. UDP-GlcA binding is favoured by a crown of hydrogen bonds with the surrounding hydrophilic residues of the active site. In this scenario, the C4' of the sugar ring is perfectly oriented towards the NAD that catalyses the hydride transfer and subsequent UDP-GlcA oxidation into 4-ketointermediate. With its trigonal carbon, the latter is ready to rotate in the active site. The rotation is promoted by the suboptimal interactions of the 4-ketointermediate with the active site residues and the spacious cavity accessible. Through a "swing & flip" movement the 4-ketointermediate shows the opposite face to the NADH which is ready to return the hydride and reduce the intermediate yielding UDP-GalA as product. Moreover, it is remarkable how the extensive network of hydrogen bonds interactions is able to protect the 4-ketointermediate from the decarboxylation, differently from decarboxylases of the same family as UXS and UAXS.

JBC Papers in Press. Published on July 13, 2020 as Manuscript RA120.014692
The latest version is at https://www.jbc.org/cgi/doi/10.1074/jbc.RA120.014692

Crystallographic snapshots of UDP-glucuronic acid 4-epimerase ligand binding, rotation and reduction

Luca Giacinto Iacovino[1], Simone Savino[2,4], Annika J.E. Borg[2], Claudia Binda[1], Bernd Nidetzky[2,3*], and Andrea Mattevi[1*]

[1]Department of Biology and Biotechnology "Lazzaro Spallanzani", University of Pavia, Via Ferrata 9, 27100, Pavia, Italy

[2]Institute of Biotechnology and Biochemical Engineering, Graz University of Technology, NAWI Graz, Petersgasse 12, 8010 Graz, Austria

[3]Austrian Centre of Industrial Biotechnology, Petersgasse 14, 8010 Graz, Austria

[4]Current address: Faculty of Science and Engineering Biotechnology, Gron Inst Biomolecular Sciences & Biotechnology, Nijenborgh 4, 9747 AG Groningen, The Netherlands

*Correspondence to bernd.nidetzky@tugraz.at and andrea.mattevi@unipv.it

Running title: Mechanism of UDP-glucuronic acid 4-epimerase

Keywords: SDR, short-chain dehydrogenase/reductase, epimerase, decarboxylase, catalytic intermediates, UDP-glucuronic acid, UDP-galacturonic acid, NADH, kinetic isotope effect

Abbreviations: SDR, short-chain dehydrogenase/reductase; BcUGAepi, UDP-glucuronic acid 4-epimerase from *Bacillus cereus*; UDP-GlcA, UDP-glucuronic acid; UDP-GalA, UDP-galacturonic acid.

Abstract

UDP-glucuronic acid is converted to UDP-galacturonic acid en route to a variety of sugar-containing metabolites. This reaction is performed by a NAD^+-dependent epimerase belonging to the short-chain dehydrogenase/reductase family. We present several high-resolution crystal structures of the UDP-glucuronic acid epimerase from *Bacillus cereus*. The geometry of the substrate-NAD^+ interactions is finely arranged to promote hydride transfer. The exquisite complementarity between glucuronic acid and its binding site is highlighted by the observation that the unligated cavity is occupied by a cluster of ordered waters whose positions overlap the polar groups of the sugar substrate. Co-crystallization experiments led to a structure where substrate- and product-bound enzymes coexist within the same crystal. This equilibrium structure reveals the basis for a "swing & flip" rotation of the pro-chiral 4-keto-hexose-uronic acid intermediate that results from glucuronic acid oxidation, placing the C4' atom in position for receiving a hydride ion on the opposite side of the sugar ring. The product-bound active site is almost identical to that of the substrate-bound structure and satisfies all hydrogen-bonding requirements of the ligand. The structure of the apo-enzyme together with kinetic isotope effect and mutagenesis experiments further outlines a few flexible loops that exist in discrete conformations, imparting structural malleability required for ligand rotation while avoiding leakage of the catalytic intermediate and/or side-reactions. These data highlight the double nature of the enzymatic mechanism: the active site features a high degree of precision in substrate recognition combined with the flexibility required for intermediate rotation.

Introduction

Nucleotide sugars are high-energy donor molecules that fulfil many roles, including contributing to cellular and tissue structural integrity (1-3), acting as molecular recognition markers for xenobiotic detoxification (4-6), and providing scaffolds for drug development (7). Among these metabolites, UDP-glucuronic acid (UDP-GlcA) represents a very versatile compound that undergoes a variety of enzymatic modifications. UDP-glucuronic acid 4-epimerase (EC 5.1.3.6), UDP-xylose synthase (EC 4.1.1.35), and UDP-apiose/xylose synthase (EC 4.1.1.-) modify UDP-GlcA through NAD^+-dependent redox chemistry, producing enzyme-specific sugar products (8-10). These structurally and functionally related enzymes belong to the family of the short-chain dehydrogenase/reductases (SDRs) (11). SDRs are characterized by a strictly conserved catalytic triad, Ser/Thr-Tyr-Lys. The tyrosine residue functions as the base that abstracts a proton from the substrate 4'-OH group and promotes C4' oxidation by NAD^+ (12-18). The generated 4-keto-hexose-uronic acid intermediate is unstable and converted into different products depending on the enzyme (**Scheme 1**). Because of their catalytic versatility, sugar-modifying SDR enzymes are increasingly recognized as valuable targets for many industrial biocatalytic applications.

As it can be seen from **Scheme 1**, the UDP-glucuronic acid 4-epimerase stands out for its ability to prevent decarboxylation at the C5' position of the 4-keto-hexose-uronic acid intermediate. This enzyme thereby efficiently interconverts UDP-GlcA into UDP-galacturonic acid (UDP-GalA) by inverting the configuration of the 4'-carbon. The strategies used by epimerases to invert the stereochemistry of UDP-sugar carbons have been subject of in-depth investigations (12). Among these, the structural features underlying the selective C4' epimerization by UDP-galactose 4-epimerase were extensively studied in the past few years (13,18,19). This enzyme is part of the Leloir pathway and interconverts UDP-galactose into UDP-glucose (20). It belongs to the SDR family, featuring the same Ser/Thr-Tyr-Lys catalytic triad as UDP-glucuronic acid 4-epimerase. The substrate is first oxidized at the C4' and the resulting 4-keto-hexose-uronic acid intermediate is thought to undergo a rotational movement within the active site. The intermediate is then reduced by NADH, leading to the inversion of the C4' configuration (18,21). The same catalytic strategy has been hypothesized also for the epimerases acting on UDP-GlcA (22). As demonstrated by recent work, these enzymes fine tune the rates of the individual redox steps to prevent the accumulation of the 4-keto-hexose-uronic acid, minimizing the undesired decarboxylation and/or release of this reactive intermediate (23).

While the catalytic mechanisms of UDP-xylose synthase and UDP-apiose/xylose synthase have been thoroughly elucidated (13,16,24), the epimerization reaction by UDP-glucuronic acid 4-epimerase remains partly unexplored. In this work, we carried out a comprehensive structural analysis of UDP-glucuronic acid 4-epimerase

from *Bacillus cereus* (BcUGAepi) by solving six high-resolution crystal structures that elucidate different steps along the reaction. The main aspects of these structures were compared with other SDR epimerases and decarboxylases. We also isolated a remarkable complex showing an equilibrium mixture of both substrate/product in approximate 1:1 ratio. We further used structural, kinetic isotope effect, and site-directed mutagenesis experiments to inspect the fine roles of catalytic residues. Our studies provide an overview of catalysis with critical insight into the mechanism of 4-ketose-uronic acid intermediate rotation and protection against intermediate decarboxylation. They further demonstrate that the UDP moiety is not only an accessory part of the molecule but it is fundamental for substrate recognition and active site configuration.

Results and discussion

Overall structure

The crystal structure of BcUGAepi co-purified with NAD^+ was initially solved at 2.2 Å resolution by molecular replacement (**Table 1**). The enzyme is composed of nine β-strands and eight α-helices assembled in two domains (13,25,26) (**Fig. 1**). The N-terminal domain is characterized by a Rossmann-fold motif comprising a core of seven β-strands surrounded by six α-helices. The NAD^+ cofactor is fully embedded within this domain while the smaller C-terminal domain provides the binding site for the UDP-GlcA substrate. The crevice between the two domains encloses the active site (27-29). As for other SDR family enzymes, two protein chains are arranged to form a tight homo-dimer (11,30,31) where each subunit (37 kDa molecular weight) interacts with two adjacent α-helices generating an extensively inter-molecular hydrophobic core of four α-helices (14,16) (**Fig. 1**). Structural comparisons using the Dali server (32) indicate that the overall structure of BcUGAepi is similar to the structures of UDP-galactose 4-epimerase from *Escherichia coli* (PDB entry 1UDA) (27-29) and MoeE5 (a UDP-glucuronic acid epimerase from *Streptomyces viridosporus*; PDB entry 6KV9) (22) with Z scores of 37.2 and 42.8 and sequence identities of 30% and 38%, respectively.

NAD^+ remains tightly associated to the enzyme during the entire purification process (**Fig. 2A**) (11,13,33). It is bound in an elongated conformation as typically observed in other SDR enzymes (21,26,34). Its binding is extensively stabilized through several interactions with residues of the Rossmann-fold domain. The amine group of the adenine ring hydrogen bonds to Asn101 and Asp62, the adenine-ribose hydroxyl groups interact with Asp32 and Lys43, the β-phosphate is ionically bound to Arg185, and the nicotinamide ribose is hydrogen bonded to Tyr149 and Lys153. These last two residues belong to the TyrXXXLys motif of the Ser/Thr-Tyr-Lys triad, the typical hallmark of SDR enzymes (30,35-37). This binding mode orients the *si*-face on the nicotinamide ring toward the substrate-binding site to cope with the sugar moiety and mediate hydride transfer.

On the structural roles of UDP

In the NAD^+ complex, two loops around the catalytic site (86-91 and 269-276) are disordered as gathered from the absence of well-defined electron density around them (**Fig. 2B**). The crystal structure of the enzyme bound to UDP (1.7 Å resolution; **Table 1**) reveals that these two loops become ordered in the presence of the mononucleotide. In particular, Glu276 anchors the hydroxyl groups of the nucleotide ribose whereas loop 86-91 lends more rigidity to the part of the cavity hosting the pyrophosphate (**Fig. 2B**-**C**). UDP binding affects the conformation of a third loop, formed by residues 204-214. This loop moves closer to the UDP-binding site so that Gln211 and Arg213 can hydrogen-bond to the UDP's ribose hydroxyl groups and the β-phosphate, respectively. Moreover, Phe206 is implicated in π-stacking with the uracil ring whereas Thr204 is hydrogen-bonded to the NH group of the base. This complex network of UDP-protein interactions is completed by loop 187-196. Here, Arg192 is engaged in a hydrogen bond with the uracil whereas the backbone N atom of Ala189 is hydrogen-bonded to the UDP pyrophosphate (**Fig. 2D**). Unlike residues 86-91, 204-214, 269-276, the conformation of loop 187-196 remains unaltered upon UDP ligation, being the only element of the apo-enzyme that is already pre-organized for nucleotide binding. These findings highlight the role of the UDP moiety of the nucleotide-sugar substrate. In the apo-enzyme, the binding site is open and can be readily accessed. With its many hydrogen binding groups, UDP triggers a few localized structural changes that collectively create the cavity where the sugar group binds and is modified (**Fig. 2B**). The nucleotide group of the substrate is therefore necessary to attain the catalytically competent conformation of the active site.

Structure of the Michaelis complex

The active site is located at the interface between the NAD^+ and the UDP domains (27-29). To visualize the mode of the sugar binding in this cavity, BcUGAepi was co-crystallized in presence of an excess of UDP-GlcA and the structure was solved at 1.8 Å resolution (**Table 1**). The electron density map shows the conformations of the sugar and nearby nicotinamide conformation with excellent clarity (**Fig. 3A**-**B**). In solution, the equilibrium of the reaction [UDP-GalA]/[UDP-GlcA] is 2.0 as measured using 1 mM UDP-GlcA at pH 7.6 (23). We hypothesize that crystal packing and the higher viscosity of the crystallization solutions, due to the relatively high PEG3350 concentrations (~20% w/v), may shift the equilibrium towards the substrate, UDP-GlcA. The glucuronic acid faces the nicotinamide ring of NAD^+ with a geometry that is perfectly suited for the hydride transfer and 4-keto-hexose-uronic acid intermediate generation (**Scheme 1**). As observed in MoeE5 (22), the sugar adopts the chair conformation to position its 4'-carbon at 3.2 Å distance from the C4 atom of the NAD^+. The substrate 4'-H atom is thereby predicted to point exactly towards the C4 of the nicotinamide ring (**Fig. 3A**). Moreover, Tyr149 properly interacts with the substrate to afford the deprotonation of the 4'-OH group (11). In essence, the co-crystallization experiment allowed us to capture the fine geometry of substrate binding in the Michaelis complex.

The sugar-binding cavity features a constellation of polar groups that are precisely positioned for hydrogen bonding to the hydroxyl and carboxylate groups of the substrate (**Fig. 3B**). The 4'-OH engages two residues of the SDR catalytic triad (Thr126 and Tyr149) whereas the 2'-OH and 3'-OH are hydrogen bonded to Arg185 and Pro85 (backbone oxygen). The 5'-carboxylate interacts with Thr126, Ser127, Ser128, and Thr178. Interestingly, Thr178 is the only residue in a disallowed region of the Ramachandran plot in all substrate/product-bound structures. Strained conformations have been often observed in enzyme active sites (38). In BcUGAepi, this strained backbone conformation is involved in the binding of the substrate carboxylate group whose negative charge is critical for recognition specificity. Indeed, UDP-glucose, UDP-galactose, UDP-N-acetylglucosamine, and UDP-xylose are poorly active substrates or inactive against UDP-glucuronic acid 4-epimerases (19,23,39-41).

The comparison between the structures of the enzyme bound to UDP and UDP-GlcA shows an interesting feature that further highlights this perfect complementarity between the sugar and its binding site. In the UDP complex, the sugar cavity is occupied by three ordered water molecules whose positions exactly overlap the 3'-OH, 4'-OH, and 5'-carboxylate groups of the substrate (**Fig. 3C**). Thus, the polar groups that decorate the cavity surface define a set of polar niches whose spacing matches the geometry of the polar substituents on the chair conformation of the glucuronic acid substrate.

These structural features were further explored in an experiment that probed the interactions at the 4'-OH locus of the substrate. The low-activity Y149F mutant (23) was co-crystallized with UDP-4-deoxy-4-fluoro-α-D-glucuronic acid, an inert substrate analogue where the 4'-OH is replaced by a fluorine atom. The structure (1.7 Å resolution; **Table 1**) shows the sugar ring with same orientation and interactions as previously described with UDP-GlcA structure (**Fig. 3D**). The 4'-carbon is at a slightly longer distance from the C4 of the nicotinamide (3.5 Å *versus* 3.2 Å observed in the substrate complex). Interestingly, the Y149F replacement gives room for the binding of an ordered water molecule that is absent in the structure of the wild type protein. Possibly, this water molecule may take over the role of the Tyr149 hydroxyl group, explaining the residual, yet significant activity of this mutant (23). Beside this variation in the water structure, the conformation of the active site, including the side chain at position 149, is essentially identical to that observed in the wild-type and remains unaffected by the mutation. These observations validate the conclusions inferred from the analysis of the UDP-GlcA complex and confirm that the OH group of the strictly conserved Tyr149 is above all critical for its role in acid-base catalysis (42,43) whereas it has little impact on the active-site and sugar conformation.

Capturing the rotation of the 4-keto-hexose-uronic acid intermediate

After the UDP-GlcA substrate is oxidized by NAD^+ (which is reduced to NADH), the 4-keto-hexose-uronic acid is thought to rotate inside the active site to favor the hydride transfer from NADH to the opposite face of the intermediate, therefore inverting the configuration of the C4' (see **Scheme 1**). To give evidence to this rotation mechanism, we co-crystallized BcUGAepi with an excess of the UDP-GalA product (1.5 Å resolution; **Table 1**). The multiple X-ray

diffraction data collected on several crystals grown in these conditions consistently led to electron density maps that were distinctly different from that observed in the substrate-bound enzyme. The maps could not be satisfactorily explained by the presence of a bound UDP-GalA as both modelling and crystallographic refinement systematically suggested the presence of residual density that could not be accounted for by the ligand. After various modelling experiments, we came to the conclusion that this extra density must be ascribed to a glucuronic acid molecule. In the course of crystallization, UDP-GalA is partly converted to UDP-GlcA so that the crystals contain an approximate equimolar content of GalA- and GlcA-bound crystalline enzymes (refined occupancies 0.5/0.5; **Fig. 4A**-**B**). This observation is line with the above-discussed idea that the crystallization conditions likely favor substrate accumulation. We define this complex as an "equilibrium" structure that is extremely interesting to visualize the start and end points of the reaction. Above all, this structure immediately suggests that the sugar rings of substrate and product bind with opposite orientations within the active site. Moreover, it reveals that ligand flipping can take place with almost no changes in the active site since the conformation of the equilibrium structure turned out to be virtually identical to that of the UDP-GlcA complex.

To confirm these findings and obtain further insight into the geometry of product binding orientation, we performed another crystallographic experiment to obtain the structure in complex with UDP-GalA alone. We reasoned that the ionizable group of Tyr149 and its function as active-site base could be highly sensitive to pH. Moreover, lowering of the temperature could further modulate the enzyme reactivity. Therefore, we performed the co-crystallization experiments with UDP-GalA at a lower pH (6.5 instead of 8.0) and temperature (4 °C instead of 20 °C). This strategy proved to be successful in that the crystal structure (1.85 Å resolution; **Table 1**) reveals very clear and unambiguous density for the GalA product bound to the active site (**Fig. 5**). Moreover, the GalA binding mode exactly matches that observed in the equilibrium structure, whose interpretation was thereby further validated by this experiment. The sugar of the UDP-GalA is flipped with respect to the orientation of the sugar of UDP-GlcA and is implicated in an intricate network of interactions. The three hydroxyl groups in position 1', 2', and 3' are H-bonded to Ser127, Thr126, and Tyr149 whereas the 5'-carboxylate is hydrogen-bonded to Tyr149, Gly86 (backbone N atom), and Arg185. Clearly, the BcUGAepi active-site can satisfy the hydrogen-bonding propensity of all polar (OH and carboxylate) groups of the sugar product despite its flipped orientation with respect to the substrate. The superposition of BcUGAepi/NAD^+/substrate and BcUGAepi/NAD^+/product complexes is particularly insightful to delve into these findings. The two complexes are nearly identical with a root-mean-square deviation of 0.33 Å for their α-carbons. Likewise, the binding of the UMP moiety of UDP-GalA is identical to that observed in the UDP-GlcA complex. Critical differences are instead observed for the β-phosphate and the sugar rings (**Fig. 6A**-**B**). Small 20-30° torsional rotations about the pyrophosphate's P-O-P bonds shift by 0.2 Å the position of the O1' atom bound to the β-phosphorous. This movement is coupled to a 160° rotation about the O1'-C1' bond that flips the sugar ring. Such a "swing & flip" movement re-orients and re-positions the sugar within the large active-site cavity (**Video S1**). Despite such a drastic alteration, both product and substrate sugars retain the same chair conformation. The positions of the 3'-OH, 4'-OH, and 5'-carboxylate substituents of the glucuronic acid substrate overlap with those of the 5'-carboxylate, 4'-OH, and 3'-OH substituents of the galacturonic acid product (**Fig 6B**-**D**). Strikingly, the C4' atom of UDP-GlcA and UDP-GalA holds exactly the same position at 3.2 Å distance from NAD^+ with the $C4_{nicotinamide}$-$C4'_{sugar}$ -$O4'_{sugar}$ angle measuring 106-107° in both structures (**Fig. 6E**). The only protein conformational change affects the peptide bond between Pro85 and Gly86 that has flipped orientation in the two structures; Pro85 oxygen (main chain) interacts with the 3'-OH of the substrate whereas Gly86 (main chain) interacts with the 5'-carboxylate of the product (**Fig. 6C**). Based on these observations, we surmise that after UDP-GlcA oxidation, the suboptimal interactions of the more rigid and distorted structure of the 4-keto-hexose-uronic intermediate promotes the "swing & flip" movement that is coupled to the flipping of the 85-86 peptide bond. The salt-bridge between Arg185 and the flipped 5'-carboxylate may be critical for holding the rotated intermediate and prevent its decarboxylation (**Fig. 6B** and **D**). With a firm grip on the flipped sugar, NADH can transfer its 4-hydride to the C4'of the keto intermediate affording the chirally-inverted product.

A flexible UDP-binding arginine promotes catalysis

Beside the highly ordered conformation of the active site as revealed by the crystal structure of the substrate and product complexes, the epimerization mechanism inherently entails a considerable degree of malleability of the active site to allow both UDP-GlcA binding and rotation of the keto intermediate. In this context, we were intrigued by the role of Arg88 at the entrance of the active site. This arginine residue is present only in BcUGAepi and MoeE5 (Arg94) (22). Other epimerases such as UDP-galactose 4-epimerase (21,27-29,34) have a glycine residue whereas other SDR decarboxylases (e.g. UAXS in **Scheme 1** (16)) show an alanine in the same position. Arg88 belongs to one of the above-described loops that become ordered only upon UDP binding (loop 86-91, see **Fig. 2B**). In the presence of glucuronic acid, the loop moves even further close to the UDP and the side chain swings into the active site interacting with the pyrophosphate and optimizing the shape of the substrate cavity (**Fig. 7A**). We hypothesized that this loop, with its multiple discrete conformations, could be instrumental to substrate binding and intermediate rotation occurring during catalysis. We therefore studied the R88A mutation that removes the long and flexible side chain at this position. The mutant enzyme was found to retain the capacity to generate UDP-GalA though with 8-fold lower catalytic rate (0.032 ± 0.002 s^{-1}; **Fig. 7B**) compared to 0.25 ± 0.01 s^{-1} of the wild type enzyme (23). We then turned to kinetic isotope effect (k_{cat}^{H}/k_{cat}^{D}) to probe the effects of the mutation using a C4'-deuterated substrate. We have previously shown that wild-type BcUGAepi shows a relatively low k_{cat}^{H}/k_{cat}^{D} of 2.0 (±0.1), due to a slow catalytically-relevant conformational change which partially masks the kinetic isotope effect (23). Conversely, we found that the R88A protein displays a more pronounced k_{cat}^{H}/k_{cat}^{D} of 4.2 (±0.3), a typical value for hydride transfer reactions. These data hint to a combination of factors affecting the properties of R88A. In the mutant, the sub-optimal position of the glucuronic acid substrate may impair hydride transfer whereas the more spacious and flexible active site can be less limiting for catalysis. As a result, the kinetic isotope effect appears to be largely unmasked in the mutant protein.

Conclusion

Our work illuminates many aspects of the epimerisation reaction catalyzed by UDP-GlcA epimerases. NAD^+ is fully embedded within the protein, functioning as non-dissociable prosthetic group. Conversely, the substrate binding site is lined by a set of flexible loops and side chains. Only upon UDP binding, these loops become ordered to create a cavity in front of the nicotinamide ring. The mononucleotide component of the substrate is therefore necessary for attaining the catalytically competent conformation. The active-site geometry features an exquisite complementarity to the sugar substrate. All the hydrogen-bonding groups of the glucuronic acid find a polar counterpart. Moreover, the 4'-carbon undergoing epimerization is precisely oriented for transferring a hydride to the nicotinamide. With its trigonal carbon, the resulting 4-keto-hexose-uronic acid intermediate may experience sub-optimal fitting and interactions inside the cavity. Through a "swing & flip" movement, the intermediate eventually rotates in the active site (**Video S1** and **Fig. 6E**). The spacious cavity of the enzyme is instrumental to this process. Consistently, its volume measures 990 $Å^3$ which is almost double that of the UDP-xylose and UDP-apiose/xylose synthases (500-600 $Å^3$; **Fig. 8**). Moreover, the very same loops that allow UDP-GlcA binding and active-site closure are likely to confer the malleability required for the intermediate rotation. The experiments on Arg88 support this notion. The flipped orientation positions the carbonyl group of the intermediate exactly as needed for the efficient hydride transfer from NADH which ultimately generates the chirally-inverted UDP-galacturonic acid product. Strikingly, the same active site configuration of the substrate complex (with the only exception of a peptide flip) is retained in the product complex. All polar groups of the galacturonic acid are indeed engaged in hydrogen-bond interactions with the protein. This feature explains why the enzyme can catalyze also the reverse reaction, namely the epimerization of UDP-galacturonic acid to UDP-glucuronic acid. Moreover, these precisely arranged hydrogen-bond interactions guarantee that the reactive keto intermediate is protected from the facile decarboxylation, differently from similar enzymes that modify UDP-GlcA through its decarboxylation.

Experimental section

Materials

All chemical reagents were purchased from Sigma-Aldrich, unless otherwise stated. The synthetic gene encoding for BcUGAepi was ordered in pET17b-expression vector (pET17b_BcUGAepi) from GenScript (USA) as a codon optimized gene for optimal expression in *E. coli* and with C-terminal Strep-tag for protein purification. For plasmid DNA isolation, the GeneJET Plasmid Miniprep Kit (Thermo Scientific; Waltham, MA, USA) was used. DpnI and Q5® High-Fidelity DNA polymerase were from New England Biolabs (Frankfurt am Main, Germany). Oligonucleotide primers were from Sigma-Aldrich (Vienna, Austria). *E. coli* NEB5α competent cells were from New England Biolabs (Frankfurt, Germany). *E. coli* Lemo21(DE3) cells were prepared in-house. DNA sequencing was performed by GATC (Konstanz, Germany). Uridine 5'-triphosphate (UTP, 98% purity) and adenosine 5'-triphosphate (ATP, 98% purity) were purchased from Carbosynth (Compton, UK). Deuterium oxide (99.96% 2H) was from Euriso-Top (Saint-Aubin Cedex, France). Calf intestinal alkaline phosphatase (CIP) was from New England Biolabs (Frankfurt, Germany) and D-lactate dehydrogenase from Megazyme (Vienna, Austria). Albumin Fraktion V (BSA) was from Roth (Karlsruhe, Germany). UDP-glucose pyrophosphorylase, inorganic pyrophosphatase and human UDP-glucose 6-dehydrogenase were expressed and purified according to previously described protocols (23). GalKSpe4 was expressed following a protocol from literature (44) and purified utilizing Strep-tag. UDP-Galacturonic acid and UDP-4-[^{2}H]-glucuronic acid were gently synthesized as previously described (23). The synthesis of UDP-4-deoxy-4-fluoro-α-D-glucuronic acid (4F-UDP-glucuronic acid) is described in the Supplementary Information.

Site-directed mutagenesis

BcUGAepi_R88A and BcUGAepi_Y149F variants were prepared using a modified QuikChange protocol as described previously (23). PCRs were carried out in the reaction volume of 50 µl using 20 ng of plasmid DNA as template and 0.2 µM of forward or reverse primer. Q5 DNA polymerase was used for DNA amplification.

Protein Expression and Purification

E. coli cells harboring pET17b_BcUGAepi (or pET17b_BcUGAepi_Y149F/pET17b_BcUGAepi _R88A) were grown in 10 ml of LB medium (50 µg/ml ampicillin and 35 µg/ml chloramphenicol) at 37 °C for 16 h. 2 ml of preculture were used to inoculate fresh LB medium (250 ml) supplemented with ampicillin (50 µg/ml) and chloramphenicol (35 µg/ml), and the cells were grown at 37 °C and 120 rpm. When the cell density (OD_{600}) reached a value of 0.8, isopropyl β-D-thiogalactoside (0.2 mM) was added to the culture media to induce gene expression. The cells were incubated at 18 °C and 120 rpm for 20 h. The cells were harvested by centrifugation (2800 g, 4 °C, 20 min), the pellet resuspended in 10 ml of Strep-tag loading buffer (100 mM Tris, 150 mM NaCl, pH 8) and the suspension was stored overnight at -20 °C prior to cell lysis. The cells were disrupted by sonication (pulse 2 sec on, 5 sec off, 70% amplitude, 5 min) and centrifuged (16100 g) at 4 °C for 45 min. The supernatant was collected and filtered (0.45 µm) prior to loading onto the StrepTrapTM HP column (5 ml resin, GE Healthcare Life Sciences) pre-equilibrated with the loading buffer (100 mM Tris, 150 mM NaCl, pH 8). The Strep-tagged protein was eluted with elution buffer (100 mM Tris, 150 mM NaCl, 2.5 mM D-desthiobiotin, pH 8) and re-buffered against the reaction buffer (50 mM Na_2HPO_4, 100 mM NaCl, pH 7.6) containing 10% glycerol using Amicon filter tubes (30 kDa cut-off). After buffer exchange, the protein was divided into aliquots, flash frozen in liquid nitrogen, and stored at -20 °C. Protein concentration was determined based on the absorption at 280 nm on a 24 Nanodrop spectrophotometer. Size and purity of the protein were confirmed by SDS-PAGE.

X-ray crystallography

Purified BcUGAepi was concentrated at 11 mg ml^{-1} in 20 mM Tris-HCl buffer at pH 8, 50 mM NaCl. Crystallization screenings were performed by vapor-diffusion sitting drop technique using commercial kits (Jena Bioscience and Hampton Research) and an Oryx 8 crystallization robot (Douglas Instruments, UK). Crystallization hits were optimized manually using the sitting-drop protocol. After optimization, the best diffracting crystals were found in a condition containing 200 mM potassium acetate and 14-24% PEG 3350 and the protein was co-crystallized in presence of 2 mM NAD^+ and 2 mM of different UDP ligands (**Table 1**). Crystals grew in 48 h from drops

prepared in a ratio of 1:1 BcUGAepi (11 mg ml^{-1}) and reservoir at 20 °C. Crystal grown in the presence of NAD^+/UDP-GalA were obtained at 4 °C using a BcUGAepi sample concentrated to 11 mg ml^{-1} in 20 mM Tris-HCl buffer at pH 6.5, 50 mM NaCl. Crystals were harvested from the mother liquor using nylon cryoloops (Hampton research, USA) and flash-cooled in liquid nitrogen after a short soak in a solution containing 26% v/v PEG 3350, 200 mM potassium acetate, 20% (w/v) glycerol, 2 mM NAD^+ and 2 mM ligand. X-ray diffraction data used for structure determination and refinement were collected at the PX beamline of the Swiss Light Source in Villigen, Switzerland (SLS). Data were scaled using the XDS (45) program and CCP4 (46) package for indexing and processing of the data. The space group symmetry together with final data-collection and processing statistics are listed in **Table 1**. The initial structure (NAD^+ complex) was solved with MOLREP (47) using the coordinates of NAD-dependent epimerase from *Klebsiella pneumoniae* (PDB: 5U4Q) as search model. Manual building, addition of water molecules, and crystallographic refinement were performed with COOT (48), REFMAC5 (49) and other programs of the CCP4 suite. Hydrogen atoms were added in the riding position following REFMAC5 protocols. Structure quality and validation were assessed using the wwPDB validation server. Figures were created with Pymol (50) and Maestro of the Schrödinger suite of programs (51) whereas cavity size were measured with Caver (52). Hydrogen bonds were inferred with Maestro using the default parameters (51).

Activity assays

The reaction mixture (200 µl final volume) contained 1 mM UDP-GlcA, 1 mM NAD^+ and 27 µM (1 mg/ml) purified recombinant BcUGAepi R88A in sodium phosphate buffer (50 mM Na_2HPO_4, 100 mM NaCl, pH 7.6). The reaction was incubated at 23 °C, quenched with methanol (50% (v/v) final concentration) at desired time points and the precipitated enzyme removed by centrifugation (16100 g, 4 °C, 30 min) prior to HPLC analysis. The initial rate was determined from the linear part of the time-course by dividing the slope of the linear regression (mM/min) by the enzyme concentration (mg ml^{-1}) giving the initial rate in µmol/(min mg protein). The apparent k_{cat} value (s^{-1}) was calculated as an average of four independent experiments from the initial rate with the molecular mass of the functional enzyme monomer (BcUGAepi R88A: 36918 g/mol).

Kinetic isotope effect measurement

The sugar nucleotides UDP-GlcA and UDP-GalA were separated with Shimadzu Prominence HPLC-UV system (Shimadzu, Korneuburg, Austria) on a Kinetex C18 column (5 µm, 100 Å, 50 x 4.6 mm) using an isocratic method with 5% acetonitrile and 95% tetrabutylammonium bromide buffer (40 mM TBAB, 20 mM K_2HPO_4/KH_2PO_4, pH 5.9) as mobile phase. UDP-sugars were detected by UV at 262 nm wavelength. For kinetic isotope effect measurements BcUGAepi concentration of 0.1 mg ml^{-1} (2.7 µM) was used and the reactions (30 µl final volume) were performed in quintuplicates for both UDP-GlcA and 4-^{2}H-UDP-GlcA (1 mM). The reaction mixtures were quenched (incubation in 50% (v/v) methanol) after 5 min and analyzed on HPLC. Initial reaction rates (V) were calculated from the linear dependence of the product formed and time used. The kinetic isotope effect was calculated from the ratio of the reaction rates (effectively, k_{cat}) for the unlabeled and deuterium-labeled substrate (KIE = $V_{unlabeled}/V_{labeled}$).

Data Availability: The structures presented in this paper have all been deposited in the Protein Data Bank (PDB) with the codes 6ZLA, 6ZL6, 6ZLD, 6ZLK, 6ZLJ, 6ZLL. All remaining data are contained within the article.

Funding
This work was supported by the Federal Ministry of Science, Research and Economy (BMWFW), the Federal Ministry of Traffic, Innovation and Technology (bmvit), the Styrian Business Promotion Agency SFG, the Standortagentur Tirol, and the Government of Lower Austrian and Business Agency Vienna through the COMET-Funding Program managed by the Austrian Research Promotion Agency FFG. Funding from the Austrian Science Funds (FWF; I-3247 to B.N. and A.J.E.B.) and by the Italian Ministry of Education, University and Research (MIUR): Dipartimenti di Eccellenza Program (2018–2022) – Department of Biology and Biotechnology "L. Spallanzani" University of Pavia, is acknowledged.

Author contributions
L.G.I. and S.S performed all crystallographic experiments. A.J.E.B. performed the mutagenesis, kinetics studies and synthesis of the ligands. C.B. supervised structure determinations. B.N. and A.M. designed and supervised the research. The manuscript was written with contributions from all authors.

Conflict of interest: The authors declare no conflicts of interest in regards to this manuscript.

References

1. Bethke, G., Thao, A., Xiong, G., Li, B., Soltis, N. E., Hatsugai, N., Hillmer, R. A., Katagiri, F., Kliebenstein, D. J., Pauly, M., and Glazebrook, J. (2016) Pectin Biosynthesis Is Critical for Cell Wall Integrity and Immunity in Arabidopsis thaliana. *Plant Cell* **28**, 537-556
2. Reboul, R., Geserick, C., Pabst, M., Frey, B., Wittmann, D., Lutz-Meindl, U., Leonard, R., and Tenhaken, R. (2011) Down-regulation of UDP-glucuronic acid biosynthesis leads to swollen plant cell walls and severe developmental defects associated with changes in pectic polysaccharides. *J Biol Chem* **286**, 39982-39992
3. Reiter, W. D. (2008) Biochemical genetics of nucleotide sugar interconversion reactions. *Curr Opin Plant Biol* **11**, 236-243
4. Bowles, D., Lim, E. K., Poppenberger, B., and Vaistij, F. E. (2006) Glycosyltransferases of lipophilic small molecules. *Annu Rev Plant Biol* **57**, 567-597
5. CE, B. N. H. (2015) *Carbohydrate metabolism II*,
6. Ritter, J. K. (2000) Roles of glucuronidation and UDP-glucuronosyltransferases in xenobiotic bioactivation reactions. *Chem Biol Interact* **129**, 171-193
7. Creuzenet, C., Belanger, M., Wakarchuk, W. W., and Lam, J. S. (2000) Expression, purification, and biochemical characterization of WbpP, a new UDP-GlcNAc C4 epimerase from Pseudomonas aeruginosa serotype O6. *J Biol Chem* **275**, 19060-19067
8. Kelleher, W. J., and Grisebach, H. (1971) Hydride transfer in the biosynthesis of uridine diphospho-apiose from uridine diphospho-D-glucuronic acid with an enzyme preparation of Lemna minor. *Eur J Biochem* **23**, 136-142
9. Moriarity, J. L., Hurt, K. J., Resnick, A. C., Storm, P. B., Laroy, W., Schnaar, R. L., and Snyder, S. H. (2002) UDP-glucuronate decarboxylase, a key enzyme in proteoglycan synthesis: cloning, characterization, and localization. *J Biol Chem* **277**, 16968-16975
10. Neufeld, E. F., Feingold, D. S., and Hassid, W. Z. (1958) Enzymatic conversion of uridine diphosphate d-glucuronic acid to uridine diphosphate galacturonic acid, uridine diphosphate xylose, and uridine diphosphate arabinose1,2. *Journal of the American Chemical Society* **80**, 4430-4431
11. Kavanagh, K. L., Jornvall, H., Persson, B., and Oppermann, U. (2008) Medium- and short-chain dehydrogenase/reductase gene and protein families : the SDR superfamily: functional and structural diversity within a family of metabolic and regulatory enzymes. *Cell Mol Life Sci* **65**, 3895-3906
12. Allard, S. T., Giraud, M. F., and Naismith, J. H. (2001) Epimerases: structure, function and mechanism. *Cell Mol Life Sci* **58**, 1650-1665
13. Eixelsberger, T., Sykora, S., Egger, S., Brunsteiner, M., Kavanagh, K. L., Oppermann, U., Brecker, L., and Nidetzky, B. (2012) Structure and mechanism of human UDP-xylose synthase: evidence for a promoting role of sugar ring distortion in a three-step catalytic conversion of UDP-glucuronic acid. *J Biol Chem* **287**, 31349-31358
14. Gatzeva-Topalova, P. Z., May, A. P., and Sousa, M. C. (2005) Structure and mechanism of ArnA: conformational change implies ordered dehydrogenase mechanism in key enzyme for polymyxin resistance. *Structure* **13**, 929-942
15. Samuel, J., and Tanner, M. E. (2002) Mechanistic aspects of enzymatic carbohydrate epimerization. *Nat Prod Rep* **19**, 261-277
16. Savino, S., Borg, A. J. E., Dennig, A., Pfeiffer, M., de Giorgi, F., Weber, H., Dubey, K. D., Rovira, C., Mattevi, A., and Nidetzky, B. (2019) Deciphering the enzymatic mechanism of sugar ring contraction in UDP-apiose biosynthesis. *Nat Catal* **2**, 1115-1123
17. Thibodeaux, C. J., Melancon, C. E., and Liu, H. W. (2007) Unusual sugar biosynthesis and natural product glycodiversification. *Nature* **446**, 1008-1016
18. Thoden, J. B., Henderson, J. M., Fridovich-Keil, J. L., and Holden, H. M. (2002) Structural analysis of the Y299C mutant of Escherichia coli UDP-galactose 4-epimerase. Teaching an old dog new tricks. *J Biol Chem* **277**, 27528-27534

19. Frirdich, E., and Whitfield, C. (2005) Characterization of Gla(KP), a UDP-galacturonic acid C4-epimerase from Klebsiella pneumoniae with extended substrate specificity. *J Bacteriol* **187**, 4104-4115
20. Holden, H. M., Rayment, I., and Thoden, J. B. (2003) Structure and function of enzymes of the Leloir pathway for galactose metabolism. *J Biol Chem* **278**, 43885-43888
21. Thoden, J. B., Wohlers, T. M., Fridovich-Keil, J. L., and Holden, H. M. (2001) Human UDP-galactose 4-epimerase. Accommodation of UDP-N-acetylglucosamine within the active site. *J Biol Chem* **276**, 15131-15136
22. Sun, H., Ko, T. P., Liu, W., Liu, W., Zheng, Y., Chen, C. C., and Guo, R. T. (2020) Structure of an antibiotic-synthesizing UDP-glucuronate 4-epimerase MoeE5 in complex with substrate. *Biochem Biophys Res Commun* **521**, 31-36
23. Annika J.E. Borg, A. D., Hansjörg Weber and Bernd Nidetzky. (2020) Mechanistic characterization of UDP-glucuronic acid 4-epimerase. *FEBS J submitted*
24. Eixelsberger, T., Horvat, D., Gutmann, A., Weber, H., and Nidetzky, B. (2017) Isotope Probing of the UDP-Apiose/UDP-Xylose Synthase Reaction: Evidence of a Mechanism via a Coupled Oxidation and Aldol Cleavage. *Angew Chem Int Ed Engl* **56**, 2503-2507
25. Gatzeva-Topalova, P. Z., May, A. P., and Sousa, M. C. (2004) Crystal structure of Escherichia coli ArnA (PmrI) decarboxylase domain. A key enzyme for lipid A modification with 4-amino-4-deoxy-L-arabinose and polymyxin resistance. *Biochemistry* **43**, 13370-13379
26. Polizzi, S. J., Walsh, R. M., Jr., Peeples, W. B., Lim, J. M., Wells, L., and Wood, Z. A. (2012) Human UDP-alpha-D-xylose synthase and Escherichia coli ArnA conserve a conformational shunt that controls whether xylose or 4-keto-xylose is produced. *Biochemistry* **51**, 8844-8855
27. Thoden, J., Frey, P., and Holden, H. (1996) High-resolution X-ray structure of UDP-galactose 4-epimerase complexed with UDP-phenol. *Protein Science* **5**, 2149-2161
28. Thoden, J., Frey, P., and Holden, H. (1996) Molecular Structure of the NADH/UDP-glucose Abortive Complex of UDP-galactose 4-Epimerase from Escherichia coli : Implications for the Catalytic Mechanism. *Biochemistry* **35**, 5137-5144
29. Thoden, J., Frey, P., and Holden, H. (1996) Crystal Structures of the Oxidized and Reduced Forms of UDP-galactose 4-Epimerase Isolated from Escherichia coli . *Biochemistry* **35**, 2557-2566
30. Jornvall, H., Persson, B., Krook, M., Atrian, S., Gonzalez-Duarte, R., Jeffery, J., and Ghosh, D. (1995) Short-chain dehydrogenases/reductases (SDR). *Biochemistry* **34**, 6003-6013
31. Persson, B., Kallberg, Y., Bray, J. E., Bruford, E., Dellaporta, S. L., Favia, A. D., Duarte, R. G., Jornvall, H., Kavanagh, K. L., Kedishvili, N., Kisiela, M., Maser, E., Mindnich, R., Orchard, S., Penning, T. M., Thornton, J. M., Adamski, J., and Oppermann, U. (2009) The SDR (short-chain dehydrogenase/reductase and related enzymes) nomenclature initiative. *Chem Biol Interact* **178**, 94-98
32. Holm, L. (2019) Benchmarking fold detection by DaliLite v.5. *Bioinformatics* **35**, 5326-5327
33. Liu, Y., Vanhooke, J. L., and Frey, P. A. (1996) UDP-galactose 4-epimerase: NAD+ content and a charge-transfer band associated with the substrate-induced conformational transition. *Biochemistry* **35**, 7615-7620
34. Thoden, J. B., and Holden, H. M. (1998) Dramatic differences in the binding of UDP-galactose and UDP-glucose to UDP-galactose 4-epimerase from Escherichia coli. *Biochemistry* **37**, 11469-11477
35. Jornvall, H. (1999) Multiplicity and complexity of SDR and MDR enzymes. *Adv Exp Med Biol* **463**, 359-364
36. Jörnvall, H., Höög, J.-O., and Persson, B. (1999) SDR and MDR: Completed genome sequences show these protein families to be large, of old origin, and of complex nature. *FEBS letters* **445**, 261-264
37. Rossman, M. G., Liljas, A., Brändén, C.-I., and Banaszak, L. J. (1975) 2 Evolutionary and Structural Relationships among Dehydrogenases. in *The Enzymes* (Boyer, P. D. ed.), Academic Press. pp 61-102
38. Herzberg, O., and Moult, J. (1991) Analysis of the steric strain in the polypeptide backbone of protein molecules. *Proteins: Structure, Function, and Bioinformatics* **11**, 223-229
39. Broach, B., Gu, X., and Bar-Peled, M. (2012) Biosynthesis of UDP-glucuronic acid and UDP-galacturonic acid in Bacillus cereus subsp. cytotoxis NVH 391-98. *Febs j* **279**, 100-112

40. Gu, X., and Bar-Peled, M. (2004) The biosynthesis of UDP-galacturonic acid in plants. Functional cloning and characterization of Arabidopsis UDP-D-glucuronic acid 4-epimerase. *Plant Physiol* **136**, 4256-4264
41. Munoz, R., Lopez, R., de Frutos, M., and Garcia, E. (1999) First molecular characterization of a uridine diphosphate galacturonate 4-epimerase: an enzyme required for capsular biosynthesis in Streptococcus pneumoniae type 1. *Mol Microbiol* **31**, 703-713
42. Berger, E., Arabshahi, A., Wei, Y., Schilling, J. F., and Frey, P. A. (2001) Acid-base catalysis by UDP-galactose 4-epimerase: correlations of kinetically measured acid dissociation constants with thermodynamic values for tyrosine 149. *Biochemistry* **40**, 6699-6705
43. Liu, Y., Thoden, J. B., Kim, J., Berger, E., Gulick, A. M., Ruzicka, F. J., Holden, H. M., and Frey, P. A. (1997) Mechanistic roles of tyrosine 149 and serine 124 in UDP-galactose 4-epimerase from Escherichia coli. *Biochemistry* **36**, 10675-10684
44. Chen, M., Chen, L. L., Zou, Y., Xue, M., Liang, M., Jin, L., Guan, W. Y., Shen, J., Wang, W., Wang, L., Liu, J., and Wang, P. G. (2011) Wide sugar substrate specificity of galactokinase from Streptococcus pneumoniae TIGR4. *Carbohydr Res* **346**, 2421-2425
45. Kabsch, W. (2010) Xds. *Acta Crystallogr D Biol Crystallogr* **66**, 125-132
46. Collaborative Computational Project, N. (1994) The CCP4 suite: programs for protein crystallography. *Acta Crystallogr D Biol Crystallogr* **50**, 760-763
47. Vagin, A., and Teplyakov, A. (1997) MOLREP: an Automated Program for Molecular Replacement. *Journal of Applied Crystallography* **30**, 1022-1025
48. Emsley, P., Lohkamp, B., Scott, W. G., and Cowtan, K. (2010) Features and development of Coot. *Acta Crystallogr D Biol Crystallogr* **66**, 486-501
49. Murshudov, G. N., Skubak, P., Lebedev, A. A., Pannu, N. S., Steiner, R. A., Nicholls, R. A., Winn, M. D., Long, F., and Vagin, A. A. (2011) REFMAC5 for the refinement of macromolecular crystal structures. *Acta Crystallogr D Biol Crystallogr* **67**, 355-367
50. DeLano, W. L. (2004) Use of PYMOL as a communications tool for molecular science. *Abstr. Pap. Am. Chem. Soc.* **228**, U313-U314
51. Schrödinger Release 2020-1: Maestro, S., LLC, New York, NY, 2020.
52. Chovancova, E., Pavelka, A., Benes, P., Strnad, O., Brezovsky, J., Kozlikova, B., Gora, A., Sustr, V., Klvana, M., Medek, P., Biedermannova, L., Sochor, J., and Damborsky, J. (2012) CAVER 3.0: a tool for the analysis of transport pathways in dynamic protein structures. *PLoS Comput Biol* **8**, e1002708
53. Karplus, P. A., and Diederichs, K. (2012) Linking crystallographic model and data quality. *Science* **336**, 1030-1033

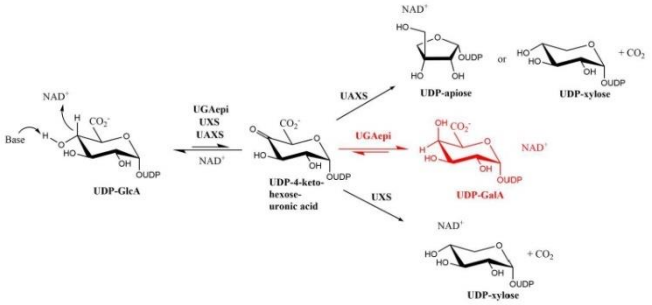

Scheme 1. Reactions carried out by UDP-glucuronic acid epimerase (labelled UGAepi), UDP-xylose synthase (UXS) and UDP-apiose/xylose synthase (UAXS) using UDP-GlcA as substrate. The same 4-keto-hexose-uronic acid intermediate yields different products that are specific for every enzyme.

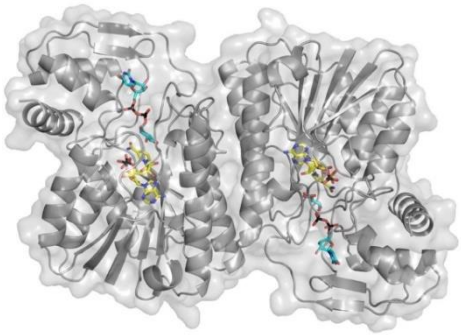

Figure 1. The overall structure of the dimeric UDP-glucuronic acid 4-epimerase from *Bacillus cereus*. The NAD^+ and UDP-GlcA carbons are in yellow and cyan, respectively. The backbone trace is shown as grey ribbon and semi-transparent protein surface.

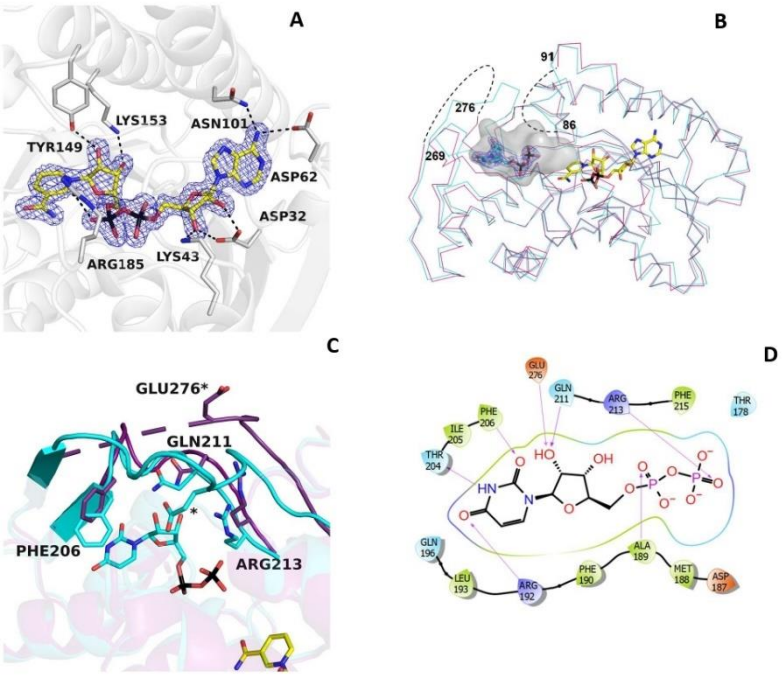

Figure 2. NAD^+ and UDP binding in BcUGAepi. (**A**) Weighted 2Fo-Fc electron density of NAD^+ in the epimerase/NAD^+ binary complex (subunit A). The contour level is 1.4 σ. Side chains involved in hydrogen-bonding and electrostatic interactions are shown (light grey carbons). Together with Thr126 (Figure 3), Tyr149 and Lys153 are part of the finger-print catalytic triad of the SDR family. (**B**) Superposition between the Cα traces of the epimerase structures bound to NAD^+ (purple) and NAD^+/UDP (cyan). NAD^+ carbons are in yellow and UDP carbons are in cyan. The electron density of UDP is shown with a contour level of 1.4 σ. The loops 86-91 and 269-276 are disordered in the NAD^+ complex (dashed lines). Upon UDP binding, both loops adopt an ordered conformation that defines a large cavity where the mononucleotide ligand binds. The large cavity space between the UDP pyrophosphate and the nicotinamide forms the sugar-binding site. (**C**) Ribbon diagram of the NAD^+ structure (purple) superposed onto the complex with NAD^+/UDP (cyan). In the absence of UDP, loop 269-276 is disordered. UDP binding reorganises this loop that, together with residues 204-214, wraps the UDP molecule. (**D**) Two-dimensional schematic diagram of the extensive interactions between UDP and the protein residues.

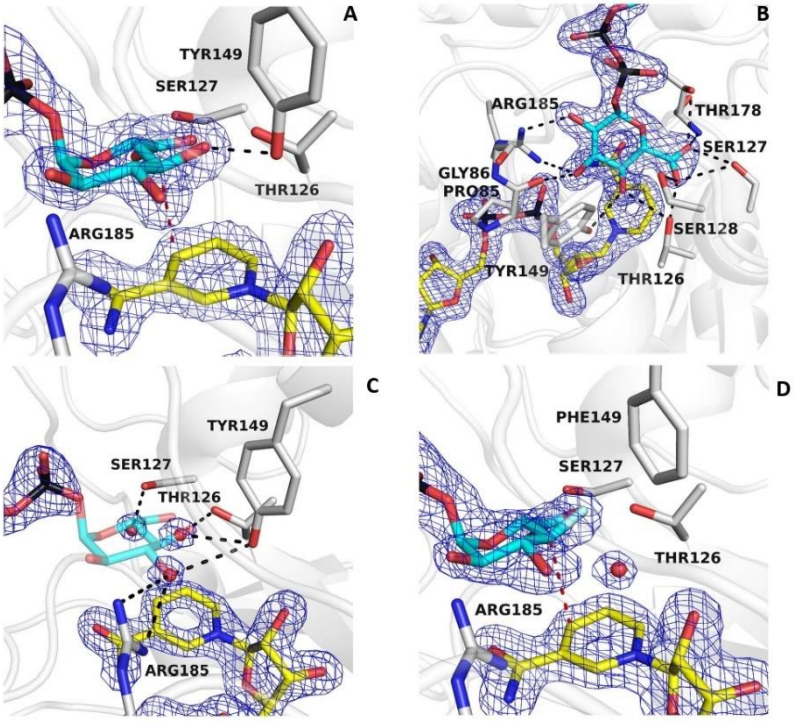

Figure 3. Binding of UDP-glucuronic acid. (**A**-**B**) Binding of the sugar moiety of the substrate (cyan carbons) in two orientations. The weighted 2Fo-Fc electron density for the NAD^+ (yellow carbons) and substrate is contoured at 1.4 σ (subunit A). The orientation of panel A outlines the binding of the substrate C4' at 3.2 Å distance from C4 of the nicotinamide (red dashed line) and the hydrogen bond between the sugar O4' and Tyr149 (black dashed line). All hydroxyl groups and the carboxylate of the glucuronic acid are engaged in hydrogen bonding interactions as shown in panel B. (**C**) A cluster of ordered water molecules are bound in the sugar-binding site of the UDP/NAD^+ complex. The positions of these waters exactly superpose onto the 3'-OH, 4'-OH, and 5'-carboxylate of the substrate sugar. The orientation is the same as in the left panel of 3A and the contour level of the density is 1.4 σ (subunit A). (**D**) Binding of UDP-4-deoxy-4-fluoro-α-D-glucuronic acid (fluorine in light cyan) to the Tyr149Phe mutant (subunit A). The structure is virtually identical to that of the ternary NAD^+/UDP-glucuronic acid complex (Fig. 3A). The hydroxyl group of Tyr149 is replaced by an ordered water molecule in contact with the fluorinated C4' atom.

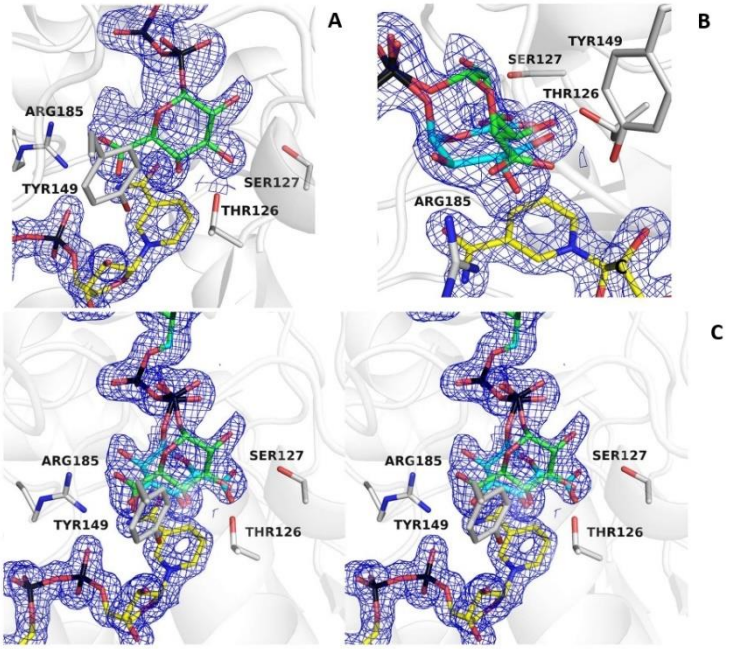

Figure 4. The equilibrium structure shows how the same active-site conformation accommodates substrate and product with their opposed chirality. (**A**) The weighted 2Fo-Fc map obtained from crystals grown in the presence of UDP-GalA can be nicely fit by this sugar (green carbons), but a significant portion of the density remains unoccupied (contour level 1.4 σ; subunit A). (**B**-**C**) Fitting of galacturonic (green carbons) and glucuronic (cyan carbons) moieties (0.5/0.5 occupancies) into the electron density shown with the same orientation as in Figure 3A-B. Figure 4C is in stereo.

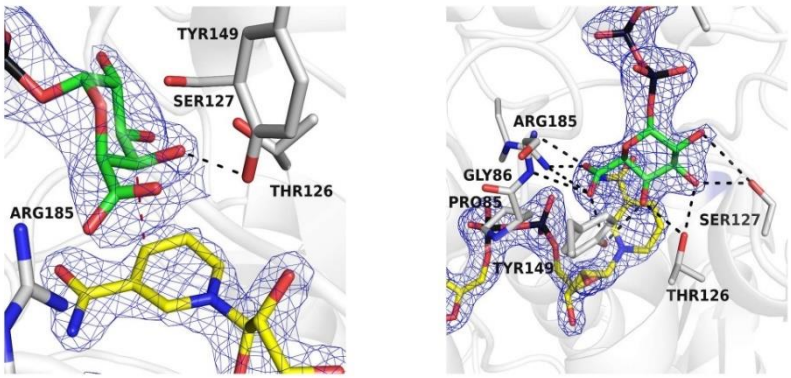

Figure 5. The crystal structure of BcUGAepi in complex with NAD^+ and UDP-galacturonic acid at pH 6.5 and 4 °C shown in two different orientations. The left-hand side panel highlights the position of the C4' in proximity of the nicotinamide (red dashed line) and the hydrogen bond between the sugar O4' and Tyr149 (black dashed line). As shown in the right-hand side panel, all hydroxyl groups and the carboxylate of the glucuronic acid are engaged in hydrogen bonding interactions with the protein. The orientations are the same as in Figure 3A-B. The contour level of the weighted 2Fo-Fc density 1.4 σ (subunit A).

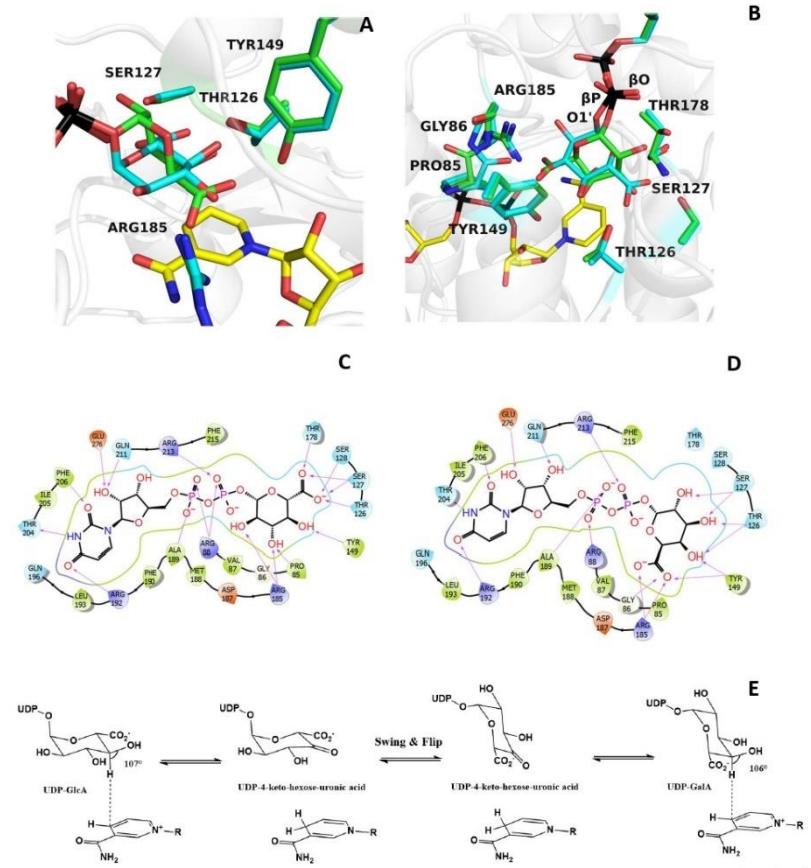

Figure 6. A detailed comparison of UDP-glucuronic and UDP-galacturonic acid binding. (**A-B**) The galacturonic acid (green carbons) can be moved on top of the glucuronic acid (cyan carbons) through a rotation of about 160° around the bond between the β phosphorous (βP) of UDP and O1' of the sugar combined with a smaller "swinging" 30° rotation around the bond between the β phosphorous and the pyrophosphate oxygen (βO) of UDP. These movements can be best appreciated in the orientation of the right-hand side panel. The orientations are the same as in Figure 3A-B. (**C-D**) Schematic two-dimensional overviews of the protein-ligand interactions. Despite their differing swing-rotated orientations, both sugars engage their polar groups in multiple hydrogen bonds with protein side chains. Only the 2'-carbon of glucuronic acid (B) is not hydrogen-bonded to the protein as it interacts with ordered waters. Moreover, the conformations of all active-site side chains remain virtually unaltered in the two complexes. (**E**) Scheme of the BcUGAepi reaction. The fine geometry of the $C4'_{sugar}$-$C4_{nicotinamide}$ contact allows C4' oxidation of glucuronate (forward reaction) and galacturonate (reverse reaction) acid.

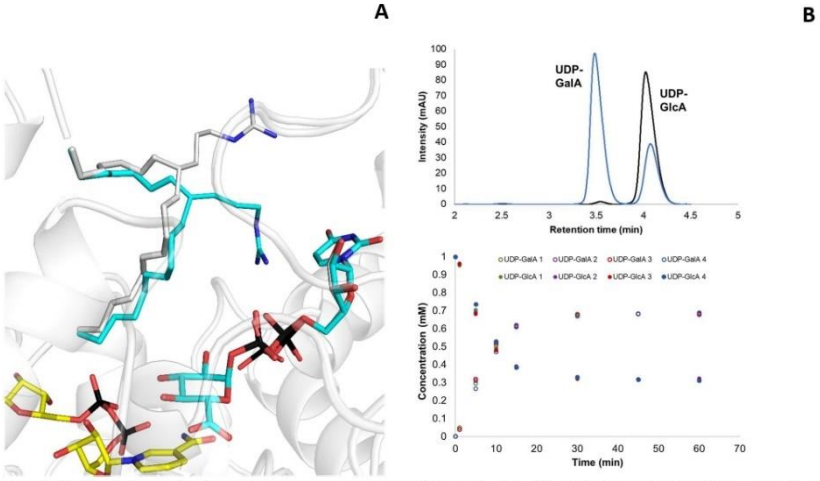

Figure 7. The role of Arg88. (**A**) In the presence of UDP-GlcA, loop 85-90 (shown as Cα trace; subunit A) closes over the substrate (cyan carbons) shifting its position as compared to the structure of the UDP-bound enzyme (grey carbons; subunit A). In particular, Arg88 changes its conformation to interact with the UDP pyrophosphate. (**B**) BcUGAepi R88A reaction with UDP-GlcA as substrate. The reaction mixture contained 1 mM UDP-GlcA, 1 mM NAD^+ and 27 µM (1 mg/ml) purified recombinant BcUGAepi R88A in sodium phosphate buffer (50 mM Na_2HPO_4, 100 mM NaCl, pH 7.6) in a final volume of 200 µl. The HPLC chromatograms after 1 min (black) and 60 min (blue) from the start of the reaction are shown in the top panel. The bottom panel depicts the time course of the depletion of UDP-GlcA (filled circles) and formation of UDP-GalA (open circles). Reactions were performed in quadruplicate and all the individual data points are shown.

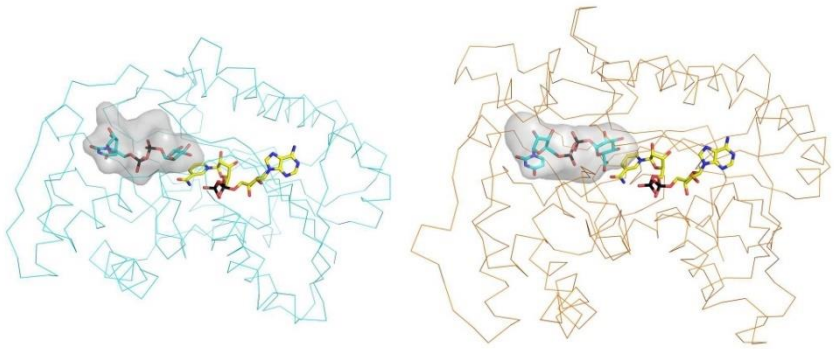

Figure 8. Comparison between the UGP-glucuronic binding sites of *Bacillus cereus* epimerase (left) **and *Arabidopsis thaliana* UDP-apiose/UDP-xylose synthase** (right, PDB entries 6H0N). The two enzymes share the same short-chain alcohol dehydrogenase site and catalytic (Ser/Thr-Tyr-Lys) triad. However, their sugar cavities have a different shape. The more spacious site of the epimerase is instrumental to a swing-rotation conformational change that the sugar undergoes after oxidation by NAD^+.

Table 1. Data collection and refinement statistics for the UGAepi crystal structures.

	NAD$^+$	**NAD$^+$/ UDP**	**NAD$^+$/ UDP-GlcA**	**NAD+/ UDP-GlcA/ UDP-GalA**	**NAD$^+$/ 4F-UDP-GlcA**	**NAD$^+$/ UDP-GalA**
Space group	C2	P1	P1	$P2_1$	P1	P1
Unit cell axes (Å)	214.5 78.5 87.9	42.5 58.6 64.9	42.4 58.4 64.7	53.7 124.3 98.4	42.2 58.2 64.4	56.8 62.7 105.8
Unit cell angles (°)	90.0 91.0 90.0	96.8 98.4 110.3	96.8 98.4 110.6	90.0 90.6 90.0	97.2 98.2 109.9	91.9 99.9 92.0
N° of chains /asym. unit	4	2	2	4	2	4
Resolution [a] (Å)	45.6-2.20 (2.25-2.20)	45.3-1.70 (1.74-1.70)	45.2-1.80 (1.84-1.80)	49.4-1.50 (1.53-1.50)	45.2-1.70 (1.74-1.70)	46.1-1.85 (1.89-1.85)
PDB code	6ZLA	6ZL6	6ZLD	6ZLK	6ZLJ	6ZLL
R_{sym} [a,b] (%)	4.6 (20.8)	6.5 (55.7)	8.4 (25.9)	8.3 (157)	13.7 (239)	11.6 (228)
$CC_{1/2}$ [a,c] (%)	99.9 (92.6)	99.7 (88.1)	99.7 (78.0)	99.5 (18.8)	99.6 (68.0)	99.7 (46.6)
Completeness [a] (%)	98 (92.6)	93 (91)	93.7 (92)	97.5 (97.5)	92.4 (90.8)	92.6 (83.6)
Unique reflections	72,646	58,368	49,095	190,286	57,074	113,316
Redundancy [a]	4.2 (3.2)	1.7 (1.7)	1.6 (1.7)	3.8 (3.9)	9.1 (9.5)	6.9 (6.4)
I/σ [a]	16.9 (4.6)	10.2 (1.2)	9.3 (2.5)	7.0 (1.0)	8.4 (1.5)	8.7 (1.1)
N° of non-hydrogen atoms						
protein	9714	4932	4934	9869	4930	9988
ligands	176	138	160	470	160	320
waters	243	251	298	695	170	242
Average B value for protein/ligand atoms (Å^2)	34.2/25.4	25.59/25.8	22.4/18.7	23.6/22.8	29.3/26.4	37.14/ 38.12
R_{cryst} [a] (%)	17.8 (21.5)	17.0 (28.6)	16.8 (24.8)	17.2 (32.2)	17.2 (29.7)	18.7 (32.2)
R_{free} [a] (%)	22.7 (26.5)	20.0 (30.7)	20.7 (27.1)	20.3 (30.9)	21.6 (30.7)	22.2 (34.0)
Root-mean-square deviations from standard values						
bond lengths (Å)	0.087	0.010	0.009	0.011	0.009	0.008
bond angles (°)	1.58	1.68	1.57	1.73	1.60	1.58
Ramachandran plot						
preferred (%)	97.5	98.0	98.0	97.7	98.0	97.3
allowed (%)	2.3	1.7	1.7	2.0	1.7	2.2
outliers (%)	0.2	0.3	0.3	0.3	0.3	0.4

[a] Values in parentheses are for reflections in the highest resolution shell.

[b] $R_{sym}=\sum|I_i-\langle I\rangle|/\sum I_i$, where I_i is the intensity of i^{th} observation and $\langle I\rangle$ is the mean intensity of the reflection.

[c] The resolution cut-off was set to $CC_{1/2}>0.3$ where $CC_{1/2}$ is the Pearson correlation coefficient of two 'half' data sets, each derived by averaging half of the observations for a given reflection. The data set for the equilibrium structure

feature some mild anisotropy. Following the resolution estimation given by the program Aimless (46) and based on the visual inspection of the electron density maps, only for this data set we included data with a somewhat lower $CC_{1/2}$ value (53).

Crystallographic snapshots of UDP-glucuronic acid 4-epimeraseligand binding, rotation and reduction

Luca Giacinto Iacovino, Simone Savino, Annika J.E. Borg, Claudia Binda, Bernd Nidetzky and Andrea Mattevi

J. Biol. Chem. published online July 13, 2020

Supplementary Information

Crystallographic snapshots of UDP-glucuronic acid 4-epimerase ligand binding, rotation and reduction

Luca Giacinto Iacovino[1], Simone Savino[2,4], Annika J.E. Borg[2], Claudia Binda[1], Bernd Nidetzky[2,3*], and Andrea Mattevi[1*]

[1]Department of Biology and Biotechnology "Lazzaro Spallanzani", University of Pavia, Via Ferrata 9, 27100, Pavia, Italy

[2]Institute of Biotechnology and Biochemical Engineering, Graz University of Technology, NAWI Graz, Petersgasse 12, 8010 Graz, Austria

[3]Austrian Centre of Industrial Biotechnology, Petersgasse 14, 8010 Graz, Austria

[4]Current address: Faculty of Science and Engineering Biotechnology, Gron Inst Biomolecular Sciences & Biotechnology, Nijenborgh 4, 9747 AG Groningen, The Netherlands

*Correspondence to bernd.nidetzky@tugraz.at and andrea.mattevi@unipv.it

Supplementary Video S1
The "swing & flip" movement as inferred from the structures of the enzyme bound to the substrate (UDP-glucuronic acid) and product (UDP-galacturonic acid). The orientations shown in videos S1A and S1B are the same as in Figures 3A and 5A and Figures 3B and 5B, respectively.

Synthesis of UDP-4-deoxy-4-fluoro-α-D-glucuronic acid
The synthesis strategy is indicated in **Scheme S1**. The reaction mixture (10 ml) contained 50 mM 4-deoxy-4-fluoro-α-D-glucose (91 mg, 0.5 mmol), 50 mM ATP (275.5 mg, 0.5 mmol) and 6 mM $MgCl_2$ (12.3 mg, 0.06 mmol) dissolved in 50 mM Tris/HCl buffer (pH 8). 4 mg/ml (86 µM) GalKSpe4 was added and the reaction mixture was incubated at 37 °C for 20 h. The progress of the phosphorylation reaction was analyzed on TLC (**Figure S1a**) by using a mixture of butanol, acetic acid and H_2O (2:1:1, respectively) as an eluent. The phosphorylated product was visualized by staining with a mixture consisting of thymol (0.5 w/v), ethanol (95 v/v) and concentrated H_2SO_4 (5 v/v). The nucleotidyl transfer reaction was initiated by adding 40 mM UTP (220 mg, 0.4 mmol), 1.3% (w/v) BSA, 0.42 mg/ml UGPase (6.4 mg) and 0.17 mg/ml iPPase (2.6 mg) and the reaction mixture was incubated at 30 °C for 4.5 h, until all the sugar 1-phosphate was converted to the corresponding UDP-sugar. The reaction mixture was analyzed on HPLC (**Figure S1b**). After confirming the completeness of the reaction on HPLC, the final oxidation step towards UDP-4-deoxy-4-fluoro-GlcA was initiated by the addition of 2 mM NAD^+ (13.2 mg, 0.02 mmol), 40 mM sodium pyruvate (44 mg, 0.4 mmol), 20 U/ml LDH (200 U) and 9 mg/ml hUGDH (90 mg), and the reaction was incubated at 37 °C for 24 h until no further conversion to UDP-4-deoxy-4-fluoro-GlcA was observed (followed on HPLC, **Figure S1c**). The enzymes were removed with Vivaspin Turbo centrifugal filter tubes (10 kDa cut-off, Sartorius) prior to column purification of the nucleotide sugar.
UDP-4-deoxy-4-fluoro-GlcA was separated from the other components by one enzymatic and four chromatographic purification steps. The first chromatographic purification was performed using ÄKTA FPLC system (GE Healthcare) connected to a 125 ml TOYOPEARL SuperQ-650M anion exchange column (GE Healthcare) and a 10 ml sample loop. 20 mM sodium acetate solution (pH 4.3) was used as

binding buffer. Compounds bound to the column were eluted with a step-wise gradient of 1 M sodium acetate buffer at pH 4.3. The steps were: 270 ml of 20 mM NaOAc, 200 ml of 300 mM NaOAc and 720 ml of NaOAc from 300 to 1000 mM with gradient for 240 min. Fractions containing the desired product were detected via UV absorption (ƛ = 254 nm), identified by HPLC and combined prior to concentrating under reduced pressure on a Laborota 4000 rotary evaporator (Heidolph, Schwabach, Germany) at 40 °C to a final volume of approximately 10 ml. UDP-4-deoxy-4-fluoro-GlcA was co-eluted with UTP and therefore further purification steps were needed. NaOAc was removed from the concentrated product mixture using an ÄKTA FPLC connected to Superdex G-10 size-exclusion column (GE Healthcare) and 5 ml sample loop. The product was detected based on its UV absorption at 254 nm and eluted with deionized water. The product-containing fractions were combined and concentrated under reduced pressure at 40 °C to a final volume of 6 ml. The pH of the product mixture was adjusted to 7.0 with NaOH and 10 U/ml CIP (60 U) was added to degrade the terminal phosphates (UTP) while leaving the nucleotide sugar intact. The dephosphorylation was performed at 30 °C and followed on HPLC every 2 h for 24 h, until all the UTP was degraded (**Figure S2**). The product mixture was subjected to a second round of anion exchange chromatographic purification (**Figure S3a**) with step-wise gradient: 20 mM NaOAc (until uridine eluted), 150 mM NaOAc (until UMP eluted) and 550 mM NaOAc (until UDP-4-deoxy-4-fluoro-GlcA eluted). The fractions containing the desired product were collected, concentrated in rotary evaporator and loaded into the size-exclusion column (for acetate removal, **Figure S3b**) as described above. Residual H_2O was removed by lyophilization (Christ Alpha 1-4 lyophilizer, B. Braun Biotech International, Melsungen, Germany), and the pure nucleotide sugar obtained as white powder. The purity and identity of UDP-4-deoxy-4-fluoro-GlcA were confirmed on HPLC (**Figure S4a**) and NMR (**Figure S4b,c**). The product was obtained in 66.2 mg (23%) yield and >95% purity.

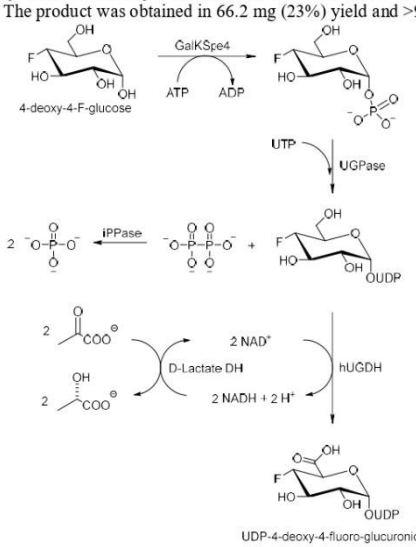

Scheme S1. Schematic representation of the one-pot synthesis of UDP-4-deoxy-4-fluoro-α-D-glucuronic acid starting from 4-deoxy-4-fluoro-α-D-glucose. ATP = adenosine-5'-triphosphate, ADP = adenosine-5'-diphosphate, UTP = uridine-5'-triphosphate, UGPase = UDP-glucose pyrophosphorylase, iPPase =

inorganic pyrophosphatase, hUGDH = human UDP-glucose 6-dehydrogenase, D-lactate DH = D-lactate dehydrogenase.

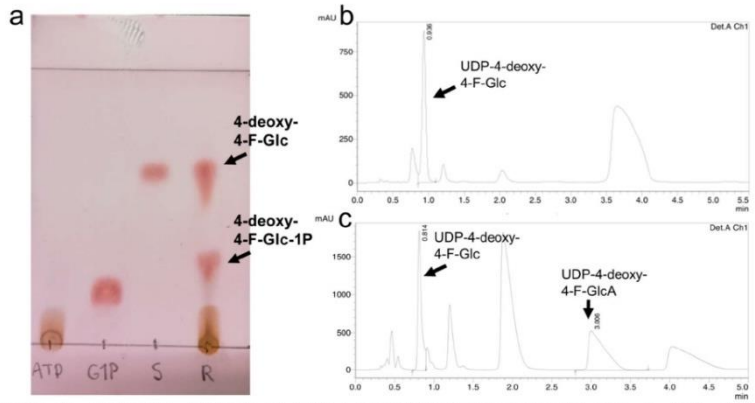

Figure S1. Three-step synthesis of UDP-4-deoxy-4-fluoro-α-D-glucuronic acid. **a**. TLC of the phosphorylation reaction of 4-deoxy-4-fluoro-Glc yielding 4-deoxy-4-fluoro-Glc-1-phosphate catalyzed by anomeric kinase GalKSpe4. **b**. HPLC chromatogram of the nucleotidyl transfer reaction forming UDP-4-deoxy-4-fluoro-Glc as a product. **c**. HPLC chromatogram of the oxidation of UDP-4-deoxy-4-fluoro-Glc to UDP-4-deoxy-4-fluoro-GlcA catalyzed by hUGDH.

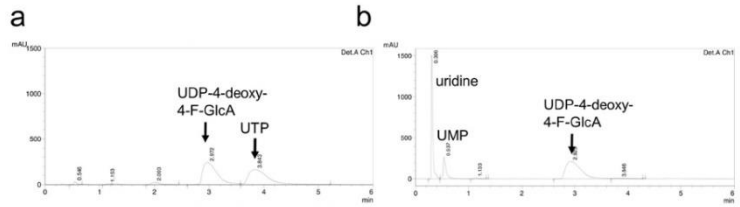

Figure S2. CIP digestion for UTP removal from the product mixture of UDP-4-deoxy-4-fluoro-GlcA. **a**. HPLC chromatogram after 1 min of CIP digestion. **b**. HPLC chromatogram after 24 h of CIP digestion.

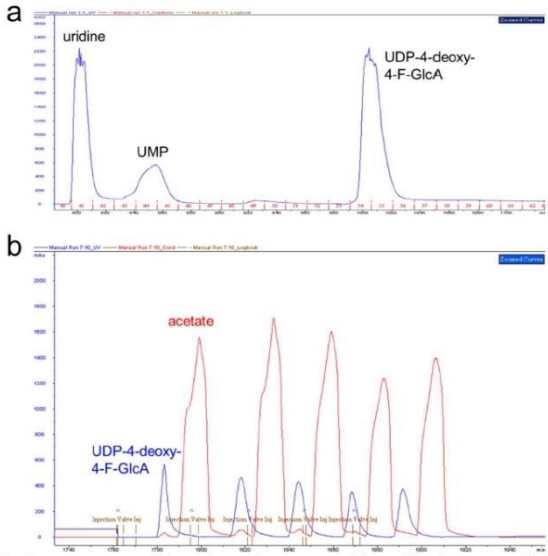

Figure S3. ÄKTA chromatograms of the column chromatographic purification steps of UDP-4-deoxy-4-fluoro-GlcA. **a**. Anion exchange chromatogram recorded during the purification of UDP-4-deoxy-4-fluoro-GlcA. The blue line corresponds to the UV signal at 280 nm. **b**. Chromatogram recorded during the desalting step of UDP-4-deoxy-4-fluoro-GlcA. The blue line corresponds to the UV-signal of the desired product (at 280 nm), the red line corresponds to the conductivity signal of acetate.

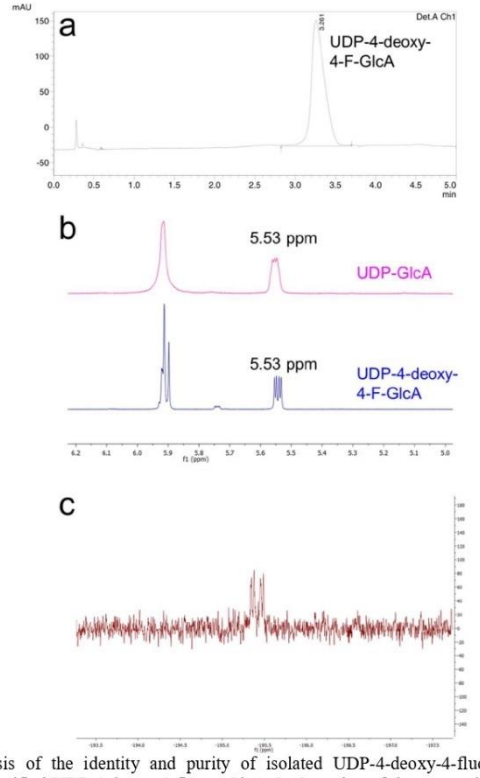

Figure S4. Analysis of the identity and purity of isolated UDP-4-deoxy-4-fluoro-GlcA. **a**. HPLC chromatogram of purified UDP-4-deoxy-4-fluoro-GlcA. **b**. Snapshot of the anomeric region of ^{1}H-NMR spectrum (D_2O, Varian INOVA 500-MHz NMR spectrometer) of UDP-4-deoxy-4-fluoro-GlcA (blue). UDP-GlcA is shown as a reference (pink). **c**. ^{19}F-NMR spectrum of UDP-4-deoxy-4-fluoro-GlcA confirming the attachment of fluorine at C4'.

REFERENCES

Akiyama, T. and T. Yamazaki (2001). "Myocardial interstitial norepinephrine and dihydroxyphenylglycol levels during ischemia and reperfusion." Cardiovasc Res **49**(1): 78-85.

Arslan, B. K. and D. E. Edmondson (2010). "Expression of zebrafish (Danio rerio) monoamine oxidase (MAO) in Pichia pastoris: Purification and comparison with human MAO A and MAO B." Protein Expression and Purification **70**(2): 290-297.

Beaulieu, J. M. and R. R. Gainetdinov (2011). "The physiology, signaling, and pharmacology of dopamine receptors." Pharmacol Rev **63**(1): 182-217.

Berger, E., A. Arabshahi, Y. Wei, J. F. Schilling and P. A. Frey (2001). "Acid-base catalysis by UDP-galactose 4-epimerase: correlations of kinetically measured acid dissociation constants with thermodynamic values for tyrosine 149." Biochemistry **40**(22): 6699-6705.

Binda, C., F. Hubálek, M. Li, Y. Herzig, J. Sterling, D. E. Edmondson and A. Mattevi (2004). "Crystal structures of monoamine oxidase B in complex with four inhibitors of the N-propargylaminoindan class." J Med Chem **47**(7): 1767-1774.

Binda, C., A. Mattevi and D. E. Edmondson (2011). "Structural properties of human monoamine oxidases A and B." Int Rev Neurobiol **100**: 1-11.

Borg, A. J. E., A. Dennig, H. Weber and B. Nidetzky (2020). "Mechanistic characterization of UDP-glucuronic acid 4-epimerase." Febs j.

Broach, B., X. Gu and M. Bar-Peled (2012). "Biosynthesis of UDP-glucuronic acid and UDP-galacturonic acid in Bacillus cereus subsp. cytotoxis NVH 391-98." Febs j **279**(1): 100-112.

Brooks, W. H., W. C. Guida and K. G. Daniel (2011). "The significance of chirality in drug design and development." Curr Top Med Chem **11**(7): 760-770.

Carlsson, A. (1959). "The occurrence, distribution and physiological role of catecholamines in the nervous system." Pharmacol Rev **11**(2, Part 2): 490-493.

Chaiyen, P., M. W. Fraaije and A. Mattevi (2012). "The enigmatic reaction of flavins with oxygen." Trends Biochem Sci **37**(9): 373-380.

Chakraborty, S. and V. Massey (2002). "Reaction of reduced flavins and flavoproteins with diphenyliodonium chloride." J Biol Chem **277**(44): 41507-41516.

Chaudhuri, K. R., D. G. Healy and A. H. Schapira (2006). "Non-motor symptoms of Parkinson's disease: diagnosis and management." Lancet Neurol **5**(3): 235-245.

Chaudhuri, K. R. and A. H. Schapira (2009). "Non-motor symptoms of Parkinson's disease: dopaminergic pathophysiology and treatment." Lancet Neurol **8**(5): 464-474.

Chiba, K., A. Trevor and N. Castagnoli, Jr. (1984). "Metabolism of the neurotoxic tertiary amine, MPTP, by brain monoamine oxidase." Biochem Biophys Res Commun **120**(2): 574-578.

Childs, B. G., D. J. Baker, J. L. Kirkland, J. Campisi and J. M. van Deursen (2014). "Senescence and apoptosis: dueling or complementary cell fates?" EMBO Rep **15**(11): 1139-1153.

De Colibus, L., M. Li, C. Binda, A. Lustig, D. E. Edmondson and A. Mattevi (2005). "Three-dimensional structure of human monoamine oxidase A (MAO A): relation to the structures of rat MAO A and human MAO B." Proc Natl Acad Sci U S A **102**(36): 12684-12689.

de Lau, L. M. and M. M. Breteler (2006). "Epidemiology of Parkinson's disease." Lancet Neurol **5**(6): 525-535.

Du, C. K., D. Y. Zhan, T. Akiyama, T. Inagaki, T. Shishido, M. Shirai and J. T. Pearson (2017). "Myocardial interstitial levels of serotonin and its major metabolite 5-hydroxyindole acetic acid during ischemia-reperfusion." Am J Physiol Heart Circ Physiol **312**(1): H60-h67.

Edmondson, D. E., C. Binda, J. Wang, A. K. Upadhyay and A. Mattevi (2009). "Molecular and mechanistic properties of the membrane-bound mitochondrial monoamine oxidases." Biochemistry **48**(20): 4220-4230.

Eisenhofer, G., P. Friberg, B. Rundqvist, A. A. Quyyumi, G. Lambert, D. M. Kaye, I. J. Kopin, D. S. Goldstein and M. D. Esler (1996). "Cardiac sympathetic nerve function in congestive heart failure." Circulation **93**(9): 1667-1676.

Eixelsberger, T., D. Horvat, A. Gutmann, H. Weber and B. Nidetzky (2017). "Isotope Probing of the UDP-Apiose/UDP-Xylose Synthase Reaction: Evidence of a Mechanism via a Coupled Oxidation and Aldol Cleavage." Angew Chem Int Ed Engl **56**(9): 2503-2507.

Eixelsberger, T., S. Sykora, S. Egger, M. Brunsteiner, K. L. Kavanagh, U. Oppermann, L. Brecker and B. Nidetzky (2012). "Structure and mechanism of human UDP-xylose synthase: evidence for a promoting role of sugar ring distortion in a three-step catalytic conversion of UDP-glucuronic acid." J Biol Chem **287**(37): 31349-31358.

Emerit, J., M. Edeas and F. Bricaire (2004). "Neurodegenerative diseases and oxidative stress." Biomed Pharmacother **58**(1): 39-46.

Fahn, S., D. Oakes, I. Shoulson, K. Kieburtz, A. Rudolph, A. Lang, C. W. Olanow, C. Tanner and K. Marek (2004). "Levodopa and the progression of Parkinson's disease." N Engl J Med **351**(24): 2498-2508.

Feingold, D. S., E. F. Neufeld and W. Z. Hassid (1958). "Enzymic synthesis of uridine diphosphate glucuronic acid and uridine diphosphate galacturonic acid with extracts from Phaseolus aureus seedlings." Arch Biochem Biophys **78**(2): 401-406.

FH, L. (1912). Paralysis agitans. . Handbuch der Neurologie (Lewandoski M, Hrsg). S. B. V. III.

Frirdich, E. and C. Whitfield (2005). "Characterization of Gla(KP), a UDP-galacturonic acid C4-epimerase from Klebsiella pneumoniae with extended substrate specificity." J Bacteriol **187**(12): 4104-4115.

Garman, E. F. and M. Weik (2019). "X-ray radiation damage to biological samples: recent progress." J Synchrotron Radiat **26**(Pt 4): 907-911.

Gatzeva-Topalova, P. Z., A. P. May and M. C. Sousa (2005). "Structure and mechanism of ArnA: conformational change implies ordered dehydrogenase mechanism in key enzyme for polymyxin resistance." Structure **13**(6): 929-942.

Gaur, S., M. E. Gross, C. P. Liao, B. Qian and J. C. Shih (2019). "Effect of Monoamine oxidase A (MAOA) inhibitors on androgen-sensitive and castration-resistant prostate cancer cells." Prostate **79**(6): 667-677.

Gu, X. and M. Bar-Peled (2004). "The biosynthesis of UDP-galacturonic acid in plants. Functional cloning and characterization of Arabidopsis UDP-D-glucuronic acid 4-epimerase." Plant Physiol **136**(4): 4256-4264.

Heikkila, R. E., A. Hess and R. C. Duvoisin (1984). "Dopaminergic neurotoxicity of 1-methyl-4-phenyl-1,2,5,6-tetrahydropyridine in mice." Science **224**(4656): 1451-1453.

Henderson Pozzi, M. and P. F. Fitzpatrick (2010). "A lysine conserved in the monoamine oxidase family is involved in oxidation of the reduced flavin in mouse polyamine oxidase." Archives of biochemistry and biophysics **498**(2): 83-88.

Henderson Pozzi, M. and P. F. Fitzpatrick (2010). "A lysine conserved in the monoamine oxidase family is involved in oxidation of the reduced flavin in mouse polyamine oxidase." Arch Biochem Biophys **498**(2): 83-88.

Herrera, A., P. Muñoz, H. W. M. Steinbusch and J. Segura-Aguilar (2017). "Are Dopamine Oxidation Metabolites Involved in the Loss of Dopaminergic Neurons in the Nigrostriatal System in Parkinson's Disease?" ACS Chem Neurosci **8**(4): 702-711.

Holland, P. C. and H. S. Sherratt (1972). "Biochemical effects of the hypoglycaemic compound diphenyleneiodonnium. Catalysis of anion-hydroxyl ion exchange across the inner membrane of rat liver mitochondria and effects on oxygen uptake." Biochem J **129**(1): 39-54.

Ju, H. Q., H. Ying, T. Tian, J. Ling, J. Fu, Y. Lu, M. Wu, L. Yang, A. Achreja, G. Chen, Z. Zhuang, H. Wang, D. Nagrath, J. Yao, M. C. Hung, R. A. DePinho, P. Huang, R. H. Xu and P. J. Chiao (2017). "Mutant Kras- and p16-regulated NOX4 activation overcomes metabolic checkpoints in development of pancreatic ductal adenocarcinoma." Nat Commun **8**: 14437.

Kasprzyk-Hordern, B. (2010). "Pharmacologically active compounds in the environment and their chirality." Chem Soc Rev **39**(11): 4466-4503.

Kavanagh, K. L., H. Jörnvall, B. Persson and U. Oppermann (2008). "Medium- and short-chain dehydrogenase/reductase gene and protein families : the SDR superfamily: functional and structural diversity within a family of metabolic and regulatory enzymes." Cell Mol Life Sci **65**(24): 3895-3906.

Kienzl, E., K. Jellinger, H. Stachelberger and W. Linert (1999). "Iron as catalyst for oxidative stress in the pathogenesis of Parkinson's disease?" Life Sci **65**(18-19): 1973-1976.

Kim, E. Y., J. Y. Koh, Y. H. Kim, S. Sohn, E. Joe and B. J. Gwag (1999). "Zn2+ entry produces oxidative neuronal necrosis in cortical cell cultures." Eur J Neurosci **11**(1): 327-334.

Langston, J. W. (2006). "The Parkinson's complex: parkinsonism is just the tip of the iceberg." Ann Neurol **59**(4): 591-596.

Langston, J. W., I. Irwin, E. B. Langston and L. S. Forno (1984). "Pargyline prevents MPTP-induced parkinsonism in primates." Science **225**(4669): 1480-1482.

Levin, J., T. Högen, A. S. Hillmer, B. Bader, F. Schmidt, F. Kamp, H. A. Kretzschmar, K. Bötzel and A. Giese (2011). "Generation of ferric iron links oxidative stress to α-synuclein oligomer formation." J Parkinsons Dis **1**(2): 205-216.

Li, M., C. Binda, A. Mattevi and D. E. Edmondson (2006). "Functional role of the "aromatic cage" in human monoamine oxidase B: structures and catalytic properties of Tyr435 mutant proteins." Biochemistry **45**(15): 4775-4784.

Linert, W., E. Herlinger, R. F. Jameson, E. Kienzl, K. Jellinger and M. B. Youdim (1996). "Dopamine, 6-hydroxydopamine, iron, and dioxygen--their mutual interactions and possible implication in the development of Parkinson's disease." Biochim Biophys Acta **1316**(3): 160-168.

Liu, Y., J. B. Thoden, J. Kim, E. Berger, A. M. Gulick, F. J. Ruzicka, H. M. Holden and P. A. Frey (1997). "Mechanistic roles of tyrosine 149 and serine 124 in UDP-galactose 4-epimerase from Escherichia coli." Biochemistry **36**(35): 10675-10684.

Liu, Y., J. L. Vanhooke and P. A. Frey (1996). "UDP-galactose 4-epimerase: NAD+ content and a charge-transfer band associated with the substrate-induced conformational transition." Biochemistry **35**(23): 7615-7620.

Lu, J., P. Risbood, C. T. Kane, M. T. Hossain, L. Anderson, K. Hill, A. Monks, Y. Wu, S. Antony, A. Juhasz, H. Liu, G. Jiang, E. Harris, K. Roy, J. L. Meitzler, M. Konaté and J. H. Doroshow (2017). "Characterization of potent and selective iodonium-class inhibitors of NADPH oxidases." Biochemical Pharmacology **143**: 25-38.

Mandriota, S. J., C. Pyke, C. Di Sanza, P. Quinodoz, B. Pittet and M. S. Pepper (2000). "Hypoxia-inducible angiopoietin-2 expression is mimicked by iodonium compounds and occurs in the rat brain and skin in response to systemic hypoxia and tissue ischemia." Am J Pathol **156**(6): 2077-2089.
Mann, D. M. and P. O. Yates (1983). "Possible role of neuromelanin in the pathogenesis of Parkinson's disease." Mech Ageing Dev **21**(2): 193-203.

Manni, M. E., M. Zazzeri, C. Musilli, E. Bigagli, M. Lodovici and L. Raimondi (2013). "Exposure of cardiomyocytes to angiotensin II induces over-activation of monoamine oxidase type A: implications in heart failure." Eur J Pharmacol **718**(1-3): 271-276.

Manzella, N., Y. Santin, D. Maggiorani, H. Martini, V. Douin-Echinard, J. F. Passos, F. Lezoualc'h, C. Binda, A. Parini and J. Mialet-Perez (2018). "Monoamine oxidase-A is a novel driver of stress-induced premature senescence through inhibition of parkin-mediated mitophagy." Aging Cell **17**(5): e12811.

Marsden, C. D. (1996). Movement disorders, Oxford University Press Inc.
Mason, P. (2011). Medical neurobiology.

Maurel, A., C. Hernandez, O. Kunduzova, G. Bompart, C. Cambon, A. Parini and B. Francés (2003). "Age-dependent increase in hydrogen peroxide production by cardiac monoamine oxidase A in rats." Am J Physiol Heart Circ Physiol **284**(4): H1460-1467.

Meng, D. H., R. R. Du, L. Z. Chen, M. T. Li, F. Liu, J. Hou, Y. K. Shi, F. S. Wang and J. Z. Sheng (2019). "Cascade synthesis of uridine-5'-diphosphate glucuronic acid by coupling multiple whole cells expressing hyperthermophilic enzymes." Microb Cell Fact **18**(1): 118.

Mialet-Perez, J., Y. Santin and A. Parini (2018). "Monoamine oxidase-A, serotonin and norepinephrine: synergistic players in cardiac physiology and pathology." Journal of Neural Transmission **125**(11): 1627-1634.

Müller, T., P. Riederer and E. Grünblatt (2017). "Determination of Monoamine Oxidase A and B Activity in Long-Term Treated Patients With Parkinson Disease." Clin Neuropharmacol **40**(5): 208-211.
Muñoz, R., R. López, M. de Frutos and E. García (1999). "First molecular characterization of a uridine diphosphate galacturonate 4-epimerase: an enzyme required for capsular biosynthesis in Streptococcus pneumoniae type 1." Mol Microbiol **31**(2): 703-713.

Oertel, W. H. (2017). "Recent advances in treating Parkinson's disease." F1000Res **6**: 260.

Ogrunc, M., R. Di Micco, M. Liontos, L. Bombardelli, M. Mione, M. Fumagalli, V. G. Gorgoulis and F. d'Adda di Fagagna (2014). "Oncogene-induced reactive oxygen species fuel hyperproliferation and DNA damage response activation." Cell Death Differ **21**(6): 998-1012.

Paudel, B. B., J. E. Lewis, K. N. Hardeman, C. E. Hayford, C. J. Robbins, S. G. Codreanu, S. D. Sherrod, J. A. McLean, M. L. Kemp and V. Quaranta (2019). "Disruption of Redox Balance Enhances the Effects of BRAF-inhibition in Melanoma Cells." bioRxiv: 818989.

Paudel, P., S. H. Seong, S. Shrestha, H. A. Jung and J. S. Choi (2019). "In Vitro and in Silico Human Monoamine Oxidase Inhibitory Potential of Anthraquinones, Naphthopyrones, and Naphthalenic Lactones from Cassia obtusifolia Linn Seeds." ACS Omega **4**(14): 16139-16152.

Pfeiffer, R. F. W., Z. K.; Ebadi, M. (2013). Parkinson's disease, Second Edition.

Pino, R., P. Failli, L. Mazzetti and F. Buffoni (1997). "Monoamine oxidase and semicarbazide-sensitive amine oxidase activities in isolated cardiomyocytes of spontaneously hypertensive rats." Biochem Mol Med **62**(2): 188-196.

Pönicke, K., U. Gergs, I. B. Buchwalow, S. Hauptmann and J. Neumann (2012). "On the presence of serotonin in mammalian cardiomyocytes." Mol Cell Biochem **365**(1-2): 301-312.

Ramsay, R. R. and A. Albreht (2018). "Kinetics, mechanism, and inhibition of monoamine oxidase." J Neural Transm (Vienna) **125**(11): 1659-1683.

Ramsay, R. R., C. Dunford and P. K. Gillman (2007). "Methylene blue and serotonin toxicity: inhibition of monoamine oxidase A (MAO A) confirms a theoretical prediction." Br J Pharmacol **152**(6): 946-951.

Reboul, R., C. Geserick, M. Pabst, B. Frey, D. Wittmann, U. Lütz-Meindl, R. Léonard and R. Tenhaken (2011). "Down-regulation of UDP-glucuronic acid biosynthesis leads to swollen plant cell walls and severe developmental defects associated with changes in pectic polysaccharides." J Biol Chem **286**(46): 39982-39992.

Reis, J., M. Massari, S. Marchese, M. Ceccon, F. S. Aalbers, F. Corana, S. Valente, A. Mai, F. Magnani and A. Mattevi (2020). "A closer look into NADPH oxidase inhibitors: Validation and insight into their mechanism of action." Redox Biology **32**: 101466.

Reiter, W. D. (2008). "Biochemical genetics of nucleotide sugar interconversion reactions." Curr Opin Plant Biol **11**(3): 236-243.

Rouzaud-Laborde, C., N. Hanoun, I. Baysal, J. S. Rech, C. Mias, D. Calise, P. Sicard, C. Frugier, M. H. Seguelas, A. Parini and N. Pizzinat (2012). "Role of endothelial AADC in cardiac synthesis of serotonin and nitrates accumulation." PLoS One **7**(7): e34893.

Savino, S., A. J. E. Borg, A. Dennig, M. Pfeiffer, F. de Giorgi, H. Weber, K. D. Dubey, C. Rovira, A. Mattevi and B. Nidetzky (2019). "Deciphering the enzymatic mechanism of sugar ring contraction in UDP-apiose biosynthesis." Nat Catal **2**(12): 1115-1123.

Schapira, A. H. (2007). "Future directions in the treatment of Parkinson's disease." Mov Disord **22 Suppl 17**: S385-391.

Sheikh, S., Safia, E. Haque and S. S. Mir (2013). "Neurodegenerative Diseases: Multifactorial Conformational Diseases and Their Therapeutic Interventions." J Neurodegener Dis **2013**: 563481.
Shih, J. C., K. Chen and M. J. Ridd (1999). "Monoamine oxidase: from genes to behavior." Annu Rev Neurosci **22**: 197-217.

Slotkin, T. A. (1999). "Mary Bernheim and the discovery of monoamine oxidase." Brain Res Bull **50**(5-6): 373.

Spillantini, M. G., M. L. Schmidt, V. M. Lee, J. Q. Trojanowski, R. Jakes and M. Goedert (1997). "Alpha-synuclein in Lewy bodies." Nature **388**(6645): 839-840.

Stefanis, L. (2012). "α-Synuclein in Parkinson's disease." Cold Spring Harb Perspect Med **2**(2): a009399.

Thoden, J. B., P. A. Frey and H. M. Holden (1996). "Crystal structures of the oxidized and reduced forms of UDP-galactose 4-epimerase isolated from Escherichia coli." Biochemistry **35**(8): 2557-2566.

Thoden, J. B., P. A. Frey and H. M. Holden (1996). "High-resolution X-ray structure of UDP-galactose 4-epimerase complexed with UDP-phenol." Protein Sci **5**(11): 2149-2161.

Thoden, J. B., P. A. Frey and H. M. Holden (1996). "Molecular structure of the NADH/UDP-glucose abortive complex of UDP-galactose 4-epimerase from Escherichia coli: implications for the catalytic mechanism." Biochemistry **35**(16): 5137-5144.

Thoden, J. B. and H. M. Holden (1998). "Dramatic differences in the binding of UDP-galactose and UDP-glucose to UDP-galactose 4-epimerase from Escherichia coli." Biochemistry **37**(33): 11469-11477.

Tysnes, O. B. and A. Storstein (2017). "Epidemiology of Parkinson's disease." J Neural Transm (Vienna) **124**(8): 901-905.

Villeneuve, C., C. Guilbeau-Frugier, P. Sicard, O. Lairez, C. Ordener, T. Duparc, D. De Paulis, B. Couderc, O. Spreux-Varoquaux, F. Tortosa, A. Garnier, C. Knauf, P. Valet, E. Borchi, C. Nediani, A. Gharib, M. Ovize, M. B. Delisle, A. Parini and J. Mialet-Perez (2013). "p53-PGC-1α pathway mediates oxidative mitochondrial damage and cardiomyocyte necrosis induced by monoamine

oxidase-A upregulation: role in chronic left ventricular dysfunction in mice." Antioxid Redox Signal **18**(1): 5-18.

Vojinović, V., A. M. Azevedo, V. C. B. Martins, J. M. S. Cabral, T. D. Gibson and L. P. Fonseca (2004). "Assay of H2O2 by HRP catalysed co-oxidation of phenol-4-sulphonic acid and 4-aminoantipyrine: characterisation and optimisation." Journal of Molecular Catalysis B: Enzymatic **28**(2): 129-135.

Westlund, K. N., R. M. Denney, L. M. Kochersperger, R. M. Rose and C. W. Abell (1985). "Distinct monoamine oxidase A and B populations in primate brain." Science **230**(4722): 181-183.

Wirdefeldt, K., H. O. Adami, P. Cole, D. Trichopoulos and J. Mandel (2011). "Epidemiology and etiology of Parkinson's disease: a review of the evidence." Eur J Epidemiol **26 Suppl 1**: S1-58.

Youdim, M. B., D. Edmondson and K. F. Tipton (2006). "The therapeutic potential of monoamine oxidase inhibitors." Nat Rev Neurosci **7**(4): 295-309.

Yu, J. and N. Castagnoli, Jr. (1999). "Synthesis and MAO-B substrate properties of 1-methyl-4-heteroaryl-1,2,3,6-tetrahydropyridines." Bioorg Med Chem **7**(2): 231-239.

Zecca, L., D. Tampellini, M. Gerlach, P. Riederer, R. G. Fariello and D. Sulzer (2001). "Substantia nigra neuromelanin: structure, synthesis, and molecular behaviour." Mol Pathol **54**(6): 414-418.

Zhao, G., R. C. Bruckner and M. S. Jorns (2008). "Identification of the oxygen activation site in monomeric sarcosine oxidase: role of Lys265 in catalysis." Biochemistry **47**(35): 9124-9135.

ABBREVIATIONS

5-HIAA: 5-Hydroxyindole Acetic Acid

AD: Alzheimer's Disease

ALDH: Aldehyde Dehydrogenase

BcUGAepi: UDP-Glucuronic Acid 4-epimerase from *Bacillus cereus*

CNS: Central Nervous System

COMT: Catechol-O-Methyltransferase

CVD: Cardiovascular Diseases

DA: Dopamine

DHPG: Dihydroxyphenylglycol

DOPAC: Dihydroxyphenylacetic Acid

DOPAL: 3,4-Dihydroxyphenylacetaldehyde

DPI: Diphenylene Iodonium

GALE: UDP-Galactose 4-Epiemerase

H_2O_2: Hydrogen peroxide

HF: Heart Failure

HRP: Horseradish Peroxide

HVA: Homovanillic Acid

L-DOPA: Levodopa

MAO: Monoamine Oxidase

MMTP: 1-methyl-4-(1-methyl-1H-pyrrol-2-yl)-1,2,3,6-tetrahydropyridine

MPTP: 1-methyl-4-phenyl-1,2,3,6-tetrahydropyridine

NAD^+: Nicotinamide Adenine Dinucleotide

ND: Neurodegenerative Disease

NET: Norepinephrine Transporter

NOX: NADPH Oxidase

PD: Parkinson's disease

ROS: Reactive species Oxygen

SAR: Structure activity relationship

SASP: Senescence-Associated Secretory Phenotype

SDR: Short Chain Dehydrogenase/Reductase

SN: Substantia Nigra

SNS: Sympathetic Nervous System

UAXS: UDP-Apiose/UDP-Xylose Synthase

UDP-GalA: UDP-Galacturonic acid

UDP-GlcA: UDP-Glucuronic acid

UGAepi: UDP-Glucuronic acid 4-epimerase

UXS: UDP-Xylose Synthase

α-syn: α-synuclein